Title: SMOS L2 OS Algorithm Theoretical Baseline Document

Doc code: SO-TN-ARG-GS-0007

Issue: 3

Revision: 7

Date: 22 June 2011

	Name	Function	Company	Signature	Date
Prepared	SMOS Team		Expert Support Laboratories		
Reviewed	P. Spurgeon	Project manager	ARGANS		
Approved	S. Lavender	Quality control	ARGANS		
Released	S. Delwart	Project manager	ESA		

Change Record

Issue	Revision	Date	Description	Approval
Draft	1	14-06-2005	Initial version at Software Requirement Review	
Draft	2	17-06-2005	Minor updates before SRR	
Draft	3	24-06-2005	Updates before Preliminary Design Review	
Draft	4	7-11-2005	Major revision after Preliminary Design Review	
Draft	5	20-12-2005	Revision before Critical Design Review	
Draft	6	23-01-2006	Update after CDR	
Draft	6.4	3-04-2006	Update after Mid Term Review	

	Page #	Section #	Comments	Date
issue 1.0		1.2	Updated list of variables	30-06-2006
	38	3.5	Updated mathematical description of sunglint and bistatic scattering coefficients	
	121	4.14.2.3	Section on parameter update during iterative retrieval scheme.	
	145	5	Update of the secondary neural network retrieval algorithm	
	194	Annex	Updated table of TBD / TBC	

	Page #	Section #	Comments	Date
issue 1.0b	4	1.2	Changed sea state flags	21-07-2006
	6	1.2	Definition of Resolution confirmed	
	7	1.2	σTb_model1, 2 and 3	
	14	1.2	Added Fg and Tg for high TEC gradient	
	14	1.2	Changed names for variables $\delta\tau_{GAS}$ κ_{GAS} τ_{GAS} Tb_{GAS} DT_{GAS}	
	16	1.2	Changed numbers of referred AGDP tables (error coming from old version)	
	17, 18	1.2	Corrected name of variables Dg_quality_SSSX (underscore missing)	
	17, 18	1.2	Corrected units in Tg and Dg for SSS	
	20	2.1.1	Two-scale is the default model	
	21	2.1.3	Corrected "decision tree" in figure	
	24	3.1	New flags for sea state development	
	39	4	Removed reference to non-standard document (its contents is in annex)	
	52	4.2.3	Removed reference to ECMWF current speed	
	88	4.8.2	Defined Fg and Tg for high TEC gradient	
	89-94	4.9	Major update of atmospheric section	
	117	4.14.2.2	Corrected name of variables Dg_quality_SSSX	
	118, 120	4.14.2.2	Added X to SSS variables names	
	122	4.15	Updated section on Tb42.5° computation	
	132	6	Updated description of Tb42.5° fields	

	133	6	Added Fg_quality_SSSX to UDP	
	134	6	Added Fg_TEC_gradient	
	136	6	ECMWF value and 999 for sigma in DAP when a parameter has not been retrieved	
	136	6	Added Tbgal, TBatm and tau to DAP	
	several		Comments on text removed (except in AGDP) and transfered to Pending Actions list when necessary	

issue 1.1	v-vii	Table of contents	False titles purged throughout the document	15-09-2006
	10 18	1.2	Fg_outsideLUT_M1 added. Fg_quality_SSSX description updated. Tg_quality_SSSX removed.	
	52	4.2.1.2	Definition of Fg_outsideLUT_M1 added.	
	82	4.6.1	Sentence added to introduce the new sky glitter corrections annex	
	97	4.10	Introduced void section for numbering coherence	
	111-112	4.14.1.1	Definition of $\sigma_{Tb\_model\_1}$ added.	
	121	4.14.2.2	New definition of Fg_quality_SSSX.	
	133	6.1	units for SST set to ºC instead of K	
	134	6.1	Fg_quality_SSSX description updated.	
	195-233	Annex	New annex on celestial sky glitter corrections	

issue 1.1b	1	1.1	New Reference and applicable documents section	14-12-2006
	3	1.2	Reference to SO-L2-SSS-ACR-013 for acronyms	
	3	1.2	New References list to Definitions section	
	19	1.3	Fm_RSC_FLAG removed from variables list	
	82	4.6.1	Sentence modified	
	87-124	4.7	Galactic noise 2 annex moved to new regular section	
	126	4.8	New Reference list to Faraday rotation section	
	135	4.10	New cardioid model section	
	144-145	4.13.1.1.1	Pseudo-Stokes instead of angle correction	
	149-152	4.14.1.1	Two cases considered in the iterative convergence approach (yes/no model error)	
	153	4.14.1.2	Text corrected accordingly	
	158	4.14.2	Introduced model uncertainty computation	
	166-169	4.17	New section on auxiliary data bias correction	
	179	6	Dg_QIX removed from UDP	
	182	6	Tbgal substituted by Tbgal_refl in DAP	
	183	6	Fm_RSC_FLAG removed from DAP	
	190	Annex 2	New Reference list to Annex 2	

issue 1.1c	13-14	1.3	Variables from 4.7 added to list	1-02-2007
	15	1.3	Variables from 4.10 added to list	

	52	4.2.1.2	Interpolation method updated for model 1 LUT, as well as out of LUT range flag	

issue 1.1d	many	several	All grid point flag names modified to include class (Fg_ctrl_..., Fg_sc_...)	1-6-2007
	5, 28, 30	1.3, 3.2, 3.3	L1c flags names modified	
	7	1.3	a_factor changed to nsig	
	8	1.3	Tm_angle_sun removed from variables list	
	8, 11, 13, 14	1.3	Out of LUT range flags in variables list	
	10	1.3	Thresholds for foam and roughness corrections added to variables list	
	11	1.3	Duplicated Tm_high_gal_noise removed	
	18	1.3	New cardioid variables	
	23	3	Explanation of code for flags classes	
	32	3.4	a_factor changed to nsig	
	40	3.5.4.3	Flags for out of Sunglint LUT range	
	55, 66, 73, 83, 84	4.2.2, 4.3.3, 4.4.3, 4.5.5	Switch for foam and roughness correction based on a threshold for wind speed value	
	55	4.2.1.2	Flags for out of Roughness 1 LUT range	
	66	4.3.2	Flags for out of Roughness 2 LUT range	
	83	4.5.4.3	Flags for out of Foam LUT range	
	90	4.6.2.3	New exception handling subsection	
	116	4.7.9.3	Exception handling for galactic noise 2	
	128	4.8.2	Corrected names for Fg and Tg_TEC_gradient	
	137-138	4.10	Modified cardioid model section	
	138	4.11	Comment on SBC implementation	
	148	4.13.1.2	Sentence modified	
	159, 161	4.14.1.2 , 4.14.2.2	New definition of Dg_chi2 and Dg_chi2_P	
	164	4.14.2.2	Dg_quality_SSSX definition updated with respect to Fg_sc_sea_state_X	
	181, 182, 184	6	Acard parameters in UDP	
	183, 184	6	Fg_sc_sea_state_X (1 to 6) in UDP instead of Fg_young_seas and Fg_old_seas	
	184	6	Fg_num_meas_low, min moved to confidence flags list	
	186	6	Acard parameters in DAP	
	186	6	Fm_L1c_sun included in DAP	
	187-188	6	Out of LUT range flags included in DAP	
	195	Annex	Added pending action on section 4.3 update Two actions removed	

issue 2.0	4, 26, 184	1.3, 3.1, 6	Fg_sc_in_clim_ice introduced	15-6-2007
	6, 28, 30	1.3, 3.2, 3.3	Tg_DT_ice changed to Tm_DT_ice	
	18, 138	1.3, 4.10	Thresholds for cardioid ice detection	
	20, 159	1.3, 4.14.1.2	Tg_lambda_diaMax introduced	
	20, 160, 183	1.3, 4.14.1.2, 6	Fg_ctrl_marq introduced	
	137, 190, 196, 197	4.10, Annexes	Numbered to Annex-1, 2 and 3	

	152	4.14.1.1	Added sentence on cardioid parameters to be retrieved	
	160-161	4.14.1.2	Further explanations on Dg_chi2_P_X	
	196	Annex-2	Slot to add Boutin et al. paper	
	197	Annex-3	New action on Out-of-LUT-range	

issue 2.0a	iv-v	Change log	Issues 2.0, 2.0a, 2.0b renumbered to 1.1c, 1.1d, 2.0 for coherence with delivery to ESA	19-07-2007
	18, 188	1.3, 6	T_{eff} corrected to T_eff	
	20-22	1.3	New cardioid variables and flags listed	
	27	3.1	If no ECMWF data, grid point not processed	
	162	4.14.2	The same iterative retrieval method used for SSS will be applied to cardioid model	
	182-183	6	Small typos corrected	
	183	6	All Fg_ctr from DAP moved to UDP	
	183	6	Process descriptor flags moved here	
	183	6	New Fg_ctr_no_aux_data	
	183	6	New flags for cardioid model	
	184	6	New quality descriptor for cardioid model	
	185	6	Process descriptors table removed	
	185	6	New Diff_TB_Acard[NM]	
	186-188	6	Placeholders for seven retrieved parameters for 3 roughness and cardioid models	
	188	6	T_eff and T_eff_sigma removed (included now in placeholders for cardioid model)	
	188-189	6	Grid point descriptors and Out-of-LUT-range flags moved to general DAP table	
	196	Annex 3	New action aded to update section 4.14 for pseudo-dielectric constant inversion	

issue 2.0b	3-4	1.3	New specific ECMWF flags for missing data. General flag removed	8-10-2007
	21	1.3	Tx and Ty at 42.5º in variables list	
	22	1.3	New flags for out-of-range values in AGDP LUTs	
	28	3.1	Tg_num_meas_valid is used only for warning	
	28	3.1	Control on missing ECMWF data separated for the 4 retrievals	
	29	3.2	Measurements outside AF_FOV might not be used for retrieval	
	31-32	3.3	Modified measurement selection diagrams	
	169	4.15	Tb at 42.5º at antenna level will be computed. Explanation on surface Tb study modified	
	174	4.17	Introduced new OoR LUT AGDP flags	
	184	6	ECMWF flags for missing data in UDP	
	184	6	Tx and Ty at 42.5º in UDP	
	190	6	OoR LUT AGDP flags in DAP	
	198	Annex	New action added to establish a method for not using or weighting points in the EAF-FOV	
	198	Annex	New action on changing 5 thresholds names	
	198	Annex	New action on missing flags for Tb_42.5	

	198	Annex	Removed redundant action item on 4.17	

issue 2.1	198	Annex	New action to confirm use of Fg_OoR_LUTAGDPT_param	9-10-2007

issue 2.2	5, 30, 32, 191	1.3, 3.2, 6	Fm_sun_limit introduced	10-12-2007
	5, 28, 31, 184	1.3, 3.1, 3.3, 6	Fg_ctrl_valid introduced	31-1-2008
	5, 6, 7, 28, 30, 32, 186, 187, 192	1.3, 3.1, 3.2, 3.3, 6	Measurement discrimation due to polarised galactic noise	29-1-2008
	7, 30, 32	1.3, 3.2, 3.3	Updated measurement selection due to galactic noise error (wind speed dependent)	12-12-2007
	20, 185	1.3, 6	Fg_ctrl_marq repeated 4 times (4 retrievals)	12-12-2007
	21, 169, 185	1.3, 4.15, 6	Introduced Fg_ctrl_no_surface	10-12-2007
	22, 183	1.3, 6	Introduced 3rd coordinate of grid point	
	28	3.1	Dg_num_outliers shall be divided by Dg_num_meas_l1c to compare with Tg_num_outliers_max%	10-12-2007
	29	3.2	L1 RFI flag : « TBD by L1 » removed	24-1-2008
	30	3.2	Definition of Fm_valid referred to diagram in page 32	10-12-2007
	71	4.4.1.2	Fg_ctrl_foam_M3 removed from text as it is not used	10-12-2007
	169	4.15	Typo corrected	10-12-2007
	184	6	3rd coordinate of grid point (altitude) in UDP	12-12-2007
	185	6	Fg_ctrl_no_aux_data removed (not used since issue 2.0b)	12-12-2007
	186	6	Excessive explanation removed from UDP	12-12-2007
	198	Annex	TBD/TBC column re-introduced in table	24-1-2008
	198	Annex	New action on generation of sky map	24-1-2008

	Page #	Section #	Comments	Date
issue 3.0	i, ii, all	cover, headings	Formatted to ARGANS version	9-6-2008
	vii	change log	Annotated missing change in issue 2.2	20-5-2008
	1	1	Change in annexes description	11-5-2008
	1	1.1	Updated applicable and reference documents	11-5-2008
	5, 6, 27, 28, 29	1.3	Several variables changed from percentage to fraction	7-5-2008
	8	1.3	New variables listed from 3.6 and 3.7	11-5-2008
	12, 69, 189	1.3, 4.3.2.3, 6	Fg_OoR_Rough2_dim5_Omega, not dim4	20-5-2008
	17, 19	1.3	Added missing units	11-5-2008
	17	1.3	Removed 4.11 variables from list	12-5-2008
	18	1.3	Introduced ECMWF codes in variables list	12, 22-5-2008
	19, 159, 184	1.3, 4.4.1.2, 6	Dg_num_iter is different for the 4 retrievals	20-5-2008
	20, 162	1.3, 4.14.2.2	Names for coefficients introduced in Tb sensitivity to SSS adjustment	7-2-2008
	several	1.3, 4.14, 4.17	AGDP renamed ECMWF Pre-Processing	7/12-5-2008
	21, 22	1.3	Completed variables list for 4.17 and 5	11-5-2008
	22, 182	1.3, 6	Grid point altitude removed from UDP	26-5-2008

	29	3.2	A switch to be implemented to optionally discard data outside the AF_FOV	14-5-2008
	43	3.6	Method to class sea state development	11-5-2008
	43, 44	3.7	Method to flag SST and SSS fronts	11-5-2008
	74	4.4.1.2	WC_U, WC_V changed to WSx, WSy	22-5-2008
	89	4.6	Galactic noise model 0 mentioned	8-2-2008
	142	4.11	Scene dependent bias section removed	12-5-2008
	154	4.14.1.1	Computation of theoretical uncertainties for retrieved parameters	12-5-2008
	155, 170	4.1.4.1.1.1, 4.17	Reference to SMOS ECMWF Pre-proc. doc.	11-5-2008
	156	4.14.1.2	Equation referred by number	12-5-2008
	173	4.17.3	New practical considerations section	12-5-2008
	184	6	Typos corrected in Dg_quality_SSSX	13-2-2008
	186	6	Lat, Long added to DAP	30-5-2008
	several	6	Merged cells in table (just aesthetics)	11-5-2008
	I, I-XVI, I	3 annexes	Pages renumbered to start at each annex	20-5-2008
	A1-I	Annex 1	Substituted by reference to Technical Note	20-5-2008
	A2-I - XVI	Annex 2	Added technical note on cardioid model	9/14-5-2008
	A3-I	Annex 3	New action to define Dg_quality_Acard	13-2-2008
	A3-I	Annex 3	Several pending actions closed	11/14-5-2008
	A3-I	Annex 3	New action on cross-checking ATBD-DPM variables names	18-5-2008
	9, 46	1.3, 4.1.1.1	Dielectric constant ε is expressed as $\varepsilon'+j\varepsilon''$	10-6-2008
	23	1.3	Dg_X_swath included in variables list	15-6-2008
	100, A3-I	4.7.2.2, A3	Removed TBD by N. Floury	1-7-2008
	173	4.17.3	New section on other auxiliary parameters bias removal (to match with TGRD)	1-7-2008
	A3-I	Annex 3	Removed action on checking SSA model	1-7-2008
	A3-I	Annex 3	New action on updating section 4.17	27-6-2008
	A3-I	Annex 3	Removed two completed actions and one comment	27-6/1-7-2008
	A1, A2, A3	Annex 1, 2 & 3	Added prefix to Annex page numbers	4-7-2008
	A3-I	Annex 3	Added new actions from AlgoVal#11	7-7-2008
	53, 99, A2-1	4.2, 4.6, Annex 2	Corrected missing references	8-7-2008
	1	1	Reference to annexes in introduction	30-9-2008
	145	4.13.1.1.1	Changes in text for coherence (word snapshot)	22-9-2008
	146	4.13.1.1.1	Strategy for Stokes 1 computation in full pol	19-9-2008
	155	4.14.1.1.1	Modified reference to ECMWF document	19-9-2008
	166	4.14.2.2	Dg_quality_Acard set to 0	19-9-2008
	166	4.14.3	Reference updated	22-9-2008
	A3-I - VII	Annex 3	New annex on Stokes 1 in full pol; previous Annex 3 becomes Annex 4	30-9-2008
	A4-I	Annex 4	Removed three pending actions	19-9-2008
	173	4.17.3	Added table of additional AGDP parameters	30-9-2008
	A4-I	Annex 4	Removed two pending actions	01-10-2008
	A4-I	Annex 4	Section 5: secondary Algorithm Description (neural network) moved to Annex 4; Annex 4 becomes Annex 5.	17-10-2008

	A5-I	Annex 5	Empty sections 4.7.9.2, 4.7.10 & four pending (obsolete) actions removed	17-10-2008
	175	5	SPH Quality Information Specification added	17-10-2008
	175	5	Edited SPH Quality Information Specification	27-10-2008

	Page #	Section #	Comments	Date
issue 3.1	147-150	4.13.1.1.2, 4.13.1	Corrections for galactic noise models behind a switch, updated dependencies table	21-01-2009

	Page #	Section #	Comments	Date
issue 3.2	22	1.3	Corrected Mean_Acq_Time definition & case: now called Mean_acq_time, as in IODD, code & product spec.	12-05-2009
issue 3.2	11, 67, 182	1.3, 4.3.3, 5	Corrected fg_oor_rough2_dim1..5 flags to match IODD LUT	22-05-2009
issue 3.2	4, 27, 31, 176	1.3, 3.1, 3.3, 5	Corrected meaning of fg_ctrl_ecmwf	27-05-2009

	Page #	Section #	Comments	Date
issue 3.3	18	1.3	Updated definitions of U* & WS	16-07-2009

	Page #	Section #	Comments	Date
issue 3.4	71-73	4.4.1	Roughness model 3 extended to cubic dependency on incidence angle	01-12-2009

	Page #	Section #	Comments	Date
issue 3.5		Annex 6	Added new Annex for OTTs	09-06-2010

	Page #	Section #	Comments	Date
issue 3.6		4.4	Complete rewrite of roughness model 3	07-12-2010
		4.3	Updated roughness model 2, especially 4.3.2	
		1.3	Renamed Fg_Oor_Roughx_xxx flags to Fg_Oor_Rough_dimx	

In the current issue

	Page #	Section #	Comments	Date
issue 3.7		3.4	Split into 3.4.1 (General approach for outlier detection) and 3.4.2 (RFI detection/mitigation)	27-04-2011
		3.1	Setting Fg_ctrl_suspect_RFI.true from Dg_RFI_L2	27-04-2011
		1.3	Added Tg_num_RFI_max, RFI_std RFI_nsig	27-04-2011
		3.3	Added Dg_RFI_L2, Fg_ctrl_suspect_RFI & Fm_L2_RFI; removed Dg_eaf_fov	27-04-2011
		3.3	Replaced Dg_L2_RFI by Dg_RFI_L2, JCD comment 9b(i)1 & 9d(i)	15-06-2011
	184	1.3, 3.2, table 1	Removed Dg_eaf_fov, JCD comment 9b(i)2	15-06-2011
		1.1	Changed test to "pertaining to this distribution", JCD comment 9c(i)	15-06-2011
			See Appendix of FAT minutes for JCD comments referenced above.	22-06-2011

	29	3.2	Updated setting Fm_L1c_sun (DPM PRP_1_3-4)	22-06-2011
		Annex 5	Added pending actions from DPM Table 2	22-06-2011

Table of contents

1. Introduction

The purpose of this Algorithm Theoretical Baseline Document is to establish the procedure that will be used in the SMOS mission to generate the Sea Surface Salinity data from brightness temperatures (Tb) recorded by the MIRAS radiometer. The output product (SMOS SSS Level 2 product) will consist on files containing half-orbit data (from pole to pole) on the ISEA grid defined at Level 1.

As it is not possible to transform the Tb into SSS through a univoque mathematical expression, two different approaches are proposed to retrieve SSS values from SMOS measurements. In the first one the L-band emission of the sea surface is computed using a series of mathematical models that have as independent variables the different geophysical parameters (including SSS) that determine this emission. These parameters are obtained from sources external to SMOS, and for SSS a guessed value is considered. The computed Tb, for all angular configurations that correspond to the specific satellite passage, are compared to the measured ones, and then the independent variables are modified in an iterative process until reaching the maximum similarity between both Tb values. The SSS that corresponds to this situation is considered to be the value retrieved from SMOS.

In the second approach, the relationship between measured Tb and sea surface conditions is established empirically through a neural network technique from a wide training data set. Once the method is efficiently operational, SSS in a grid point will be retrieved from Tb angular measurements at each satellite passage.

In section 2 an overview of the algorithm is presented, with a scheme of its application in the case of iterative retrieval. Section 3 describes the tests that have to be performed every time that the SSS retrieval is attempted, to select the measurements that are suitable to be used and flag any special conditions that may occur. Section 4 is a detailed description of all the parts of the algorithm, the different modules or sub-models that are used to compute the different contributions to sea surface Tb as well as the procedures to compare it with the measured Tb and the iterative convergence method. Section 5 describes the alternative approach based on neural networks. Section 6 presents the contents and structure of the output information after SSS retrieval. Five annexes provide additional information, as the geometry convention to relate Earth and satellite reference frames, the implementation of a pseudo-dielectric constant using the cardioid model, the possible strategies to compute the first Stokes parameter in full polarisation mode, the secondary algorithm, and a table summarising the parts of the ATBD that are still to be completed.

1.1 Reference and applicable documents

See the Software Release Document SO-RN-ARG-GS-0019 pertaining to this distribution.

1.2 Definitions, acronyms and abbreviations

- **Measurement:** brightness temperature measured in one MIRAS polarisation mode, along with relevant information (radiometric noise, observation conditions,

contributions as computed by the model, flags, polarisation direction). A measurement is associated with one Grid point, one Snapshot, one WEF and one Footprint .

- **Grid Point:** point on Earth surface where Measurements are available in SMOS L1c product.

- **Dwell line:** ensemble of Measurements at the same Grid Point available in SMOS L1c product.

- **SSS:** Sea Surface Salinity. Salinity of the upper fraction of the ocean that contributes to L-band emission (approx. 1 cm)

- **SST:** Sea Surface Temperature. When measured by SMOS it is the temperature of the upper fraction of the ocean that contributes to L-band emission (approx. 1 cm)

- **SSS spatial resolution** (or equivalent footprint diameter)**:** Diameter D of the equivalent circle, centred on a Grid Point, where SSS is retrieved. The area of the equivalent circle is equal to the mean area of the footprint ellipses of the Dwell line Measurements deemed valid for SSS retrieval D=sqrt(mean(axis1*axis2))

- **WEF:** 2D weighting function derived from synthetic antenna gain of MIRAS interferometer, apodization function used at reconstruction and fringe wash factor. Also termed synthetic antenna pattern or equivalent array factor. The two dimensions are differential cosines in the antenna reference frame.

- **Footprint:** 3db contour of WEF once WEF has been projected on Earth surface. Footprint is centred on a Grid point and defined by major and minor axes of an ellipse. Axes lengths are provided by SMOS L1c product.

- **DGG**: (Discrete Global Grid) **ensemble of Grid Points** on Earth Surface. Position of Grid Points are computed using hexagonal ISEA function with aperture 4 and resolution 9.

- **Snapshot:** Ensemble of measurements acquired at the same time. Distinction of snapshots per polarization is done.

- **Polarization direction**: axes of the polarization frames: **H** and **V** for the MIRAS antenna polarization frame (H is along SX axis, V is along SY axis of the figure in section 4.12), E_H and E_V for the target polarization frame at surface.

- **MIRAS Polarization mode**: MIRAS measures brightness temperatures in four polarization modes:
    - **HH** along polarization direction H.
    - **VV** along polarization direction V.
    - **HV:** one arm set to H, the two others set to V.
    - **VH:** one arm set to V, the two others set to H. HV and VH mode produce complex brightness temperatures that are complex conjugates. In L1C product, both HV and VH modes feed the HV brightness temperature data field with real and imaginary parts (see SO-TN-DME-L1PP-0024 and SO-IS-DME-L1PP-0002).

- **MIRAS operating mode**: MIRAS has two operating modes:
    - **Dual polarization mode**: measurement sequence is - HH – VV – HH – VV –HH – VV -…

- **Full polarization mode**: Measurement cycle is - HH – HV – VV – VH – HH – HV – VV – VH – HH - … (see SO-TN-DME-L1PP-0024)

- **Retrieval Polarization mode**: to derive SSS, one can use
  - Stokes 1 parameter, i.e. the sum of brightness temperatures in H and V polarization directions (**Stokes 1 retrieval mode**).
  - Brightness temperatures in H and V polarization directions (**dual pol retrieval mode**).
  - Brightness temperatures in H and V directions and real and imaginary part in HV (**full pol retrieval mode**).

- **Modified Stokes vector**: Full polarimetric set of temperatures proportional to modified Stokes parameters as defined by Ulaby, p. 1086

- **Prior values**: Values of the geophysical parameters, obtained from external sources, that are introduced, with their uncertainties, in the cost function, as reference information of the variability range during the iterative retrieval

- **First guesses**: Initial values of the geophysical parameters to be retrieved that are introduced in the first step of the minimisation process, and that will be successively modified during the iterations until achieving a retrieved value

See the Software Release Document for a list of acronyms.

1.3 List of variables

The modified Stokes vector in the antenna reference frame is [A1, A2, A3, A4] instead of $[T_{xx}, T_{yy}, T_{xy}]$ in level 1, with:

$A1 = T_{xx}$

$A2 = T_{yy}$

$A3 = 2\,Re(T_{xy})$

$A4 = 2\,Im(T_{xy})$

Variable name	Descriptive Name	Units	ATBD reference	Comment
General				
SSS	Sea surface salinity	psu		
SST	Sea surface temperature	K		
TEC	Total electron content	Tecu = 10^{16} m^{-2}		
Tb,p	Brightness temperature at p polarization (H,V)	K		
Th	Brightness temperature at H polarization in Earth reference frame	K		
Tv	Brightness temperature at V polarization in Earth reference frame	K		
T3	3rd Stokes parameter in Earth reference frame	K		

Variable name	Descriptive Name	Units	ATBD reference	Comment
T4	4th Stokes parameter of Tb in Earth reference frame	K		
A1	Brightness temperature, H pol, in antenna reference frame	K		
A2	Brightness temperature, V pol, in antenna reference frame	K		
A3	Third Stokes parameter in antenna reference frame	K		
A4	Fourth Stokes parameter in antenna reference frame	K		
3. Measurement discrimination				
Fg_sc_land_sea_coast1	land/sea	Y/N	3	
Fg_sc_land_sea_coast2	coast/no coast	Y/N	3	
Fg_sc_ice	Presence of sea ice in grid point	Y/N	3	
Fg_sc_suspect_ice	Grid point suspect of ice contamin.	Y/N	3	
Fg_sc_in_clim_ice	Gridpoint with maximum extend of sea ice accordy to monthly climatology	Y/N	3	
Fg_sc_rain	Heavy rain point	Y/N	3	
Fg_sc_low_SST	Low SST	Y/N	3	
Fg_sc_high_SST	High SST	Y/N	3	
Fg_sc_low_SSS	Low SSS	Y/N	3	
Fg_sc_high_SSS	High SSS	Y/N	3	
Fg_sc_low_wind	Low wind speed	Y/N	3	
Fg_sc_high_wind	High wind speed	Y/N	3	
Fg_sc_sea_state_1	Sea state development class 1	Y/N	3	
Fg_sc_sea_state_2	Sea state development class 2	Y/N	3	
Fg_sc_sea_state_3	Sea state development class 3	Y/N	3	
Fg_sc_sea_state_4	Sea state development class 4	Y/N	3	
Fg_sc_sea_state_5	Sea state development class 5	Y/N	3	
Fg_sc_sea_state_6	Sea state development class 6	Y/N	3	
Fg_sc_SST_front	Presence of a temperature front	Y/N	3	
Fg_sc_SSS_front	Presence of a salinity front	Y/N	3	
Fg_ctrl_ECMWF_1	No missing ECMWF data for SS1 retrieval	Y/N	3	
Fg_ctrl_ECMWF_2	No missing ECMWF data for SS2 retrieval	Y/N	3	
Fg_ctrl_ECMWF_3	No missing ECMWF data for SS3 retrieval	Y/N	3	
Fg_ctrl_ECMWF_4	No missing ECMWF data for Acard retrieval	Y/N	3	
Fg_ctrl_num_meas_low	Grid point with number of valid measurements below threshold	Y/N	3	
Fg_ctrl_num_meas_min	Grid point discarded due to very few measurements	Y/N	3, 4.14.3	
Fg_ctrl_many_outliers	Grid point with number of outlier measurements above threshold	Y/N	3	
Fg_ctrl_sunglint	Grid point with number of measurements flagged for sunglint above threshold	Y/N	3	
Fg_ctrl_moonglint	Grid point with number of measurements flagged for moonglint above threshold	Y/N	3	
Fg_ctrl_gal_noise	Grid point with number of measurements flagged for galactic noise above threshold	Y/N	3	

Variable name	Descriptive Name	Units	ATBD reference	Comment
Fg_ctrl_gal_noise_pol	Grid point with number of measurements flagged for polarised galactic noise above threshold	Y/N	3	
Fg_ctrl_valid	Grid point used in the retrieval	Y/N	3	
Fm_out_of_range	Tb out of range	Y/N	3	
Fm_resol	Measurement with spatial resolution (i.e. major axis length) above threshold	Y/N	3	
FmL1c_eaf_fov	Measurement outside EAF _FOV	Y/N	3	From L1
FmL1c_af_fov	Measurement outside AF _FOV	Y/N	3	From L1
FmL1c_border_fov	Border measurements	Y/N	3	From L1
FmL1c_RFI	Marked RFI by L1	Y/N	3	From L1
Fm_suspect_ice	Measurement above threshold in test for possible ice detection	Y/N	3	
Fm_outlier	Outliers measurements	Y/N	3	
Fm_L1c_sun	L1C information on sun contaminated measurements	Y/N	3	
Fm_low_sun_glint	After Sun glint IFREMER model	Y/N	3	
Fm_high_sun_glint	After Sun glint IFREMER model	Y/N	3	
Fm_sun_limit	Sun contamination above threshold	Y/N	3	
Fm_moon_specdir	Moon glint	Y/N	3	
Fm_gal_noise_error	Error in galactic map above threshold	Y/N	3, 4.6	
Fm_high_gal_noise	Measurements with specular direction toward a strong galactic source	Y/N	3, 4.6	
Fm_gal_noise_pol	Measurements with specular direction toward a polarised galactic source	Y/N	3	
Fm_valid	Measurement is valid	Y/N	3	
FmL1c_sun_tails	Flag comming from L1	Y/N	3	From L1
FmL1c_sun_glint_area	Flag comming from L1	Y/N	3	From L1
FmL1c_sun_glint_fov	Flag comming from L1	Y/N	3	From L1
Tg_dland1	Distance 1 (short) to land	Km	3	
Tg_dland2	Distance 2 (long) to land	Km	3	
Tg_ice_concentration	Threshold (fraction) in ECMWF ice concentration	dl	3	
Tg_low_SST_ice	Value of SST under which to perform ice test	K	3	
Tg_suspect_ice	Minimum fraction of measurements where ice test is positive to flag point	dl	3	
Tg_max_rainfall	threshold of maximum rain accepted	mm/h	3	
Tg_low_SST	Upper limit for very low SST	K	3	
Tg_medium_SST	Boundary between 'low SST' and 'medium SST'	K		
Tg_high_SST	Boundary between 'medium SST' and 'high SST'	K	3	
Tg_low_SSS	Upper limit for very low SSS	psu	3	
Tg_medium_SSS	Boundary between 'low SSS' and 'medium SSS'	psu	3	
Tg_high_SSS	Boundary between 'medium SSS' and 'high SSS'	psu	3	
Tg_low_wind	Upper limit for very low wind speed	m/s	3	
Tg_medium_wind	Boundary between 'low wind' and 'medium wind'	m/s	3	

Variable name	Descriptive Name	Units	ATBD reference	Comment
Tg_high_wind	Boundary between 'medium wind' and 'high wind'	m/s	3	
Dg_num_meas_l1c	Number of measurement available in L1C product	dl	3	
Dg_num_meas_valid	Number of valid measurements	dl	3	
Tg_ num_meas_valid	Threshold of number of valid measurements to flag	dl	3	
Tg_ num_meas_min	Minimum number of valid measurements to perform retrieval	dl	3, 4.14.3	
Dg_num_outliers	number of outlier measurements	dl	3.1, 3.2	
Tg_num_outliers_max	minimum fraction of outlier measurements to flag a grid point	dl	3.1, 3.4.1	
Tg_num_RFI_max	minimum fraction of RFI outlier measurements to flag a grid point	dl	3.1, 3.4.2	
Tg_sunglint_max	minimum fraction of measurements flagged for sunglint to flag a grid point	dl	3	
Tg_moonglint_max	minimum fraction of measurements flagged for moonglint to flag a grid point	dl	3	
Tg_gal_noise_max	min. fraction of measurements flagged for galactic noise to flag a grid point	dl	3	
Tg_gal_noise_pol_max	min. fraction of measurements flagged for polarised galactic noise to flag a grid point	dl	3	
Tm_out_of_range	threshold for Tb out of range	K	3	
Resolution	length of major axis of the measurement footprint	Km	3	
Dg_num_high_resol	number of measurements exceeding maximum allowed resolution	dl	3	
Tg_resol_max_ocean	maximum footprint resolution (i.e. major axis length) to be accepted for measurements in ocean points	Km	3	
Dg_af_fov	counter on number of measurements in alias free FOV	dl	3	
Dg_border_fov	counter on number of measurements on the border of FOV.	dl	3	
Dg_RFI_L1	number of measurements discarded due to being flagged RFI at L1	dl	3	
Tm_DT_ice	threshold for test on possible presence of ice	K	3	
Dg_suspect_ice	number of measurements suspect of being contaminated by ice	dl	3	
Dg_sunglint_L1	number of meas. with L1 sunglint flag	dl	3	
Dg_sunglint_L2	number of meas. with L2 sunglint flag	dl	3	
Tm_high_sun_glint	upper limit for very low sun_glint	K	3	
Tm_medium_sun_glint	boundary between 'low sun glint' and 'medium sun glint'	K	3	
Tm_low_sun_glint	boundary between 'medium sun glint' and 'high sun glint'	K	3	
Tm_sun_limit	limit of sun glint, between to process or not	K	3	
Dg_sun_fov	number of measurements affected by L1C flag SUN_FOV	dl	3	
Dg_sun_tails	number of measurements with SUN TAILS flag raised	dl	3	
Dg_sun_glint_area	number of measurements with SUN_GLINT_AREA flag raised	dl	3	

Variable name	Descriptive Name	Units	ATBD reference	Comment
Dg_sun_glint_fov	number of measurements with SUN_GLINT_FOV flag raised	dl	3	
Dg_moonglint	N. of meas. with L2 moonglint raised	dl	3	
Tm_angle_moon	angle between Target to Moon direction and specular direction	deg	3	
Tm_max_gal_noise_error	Threshold of the galactic noise error	K	3	
Tm_high_gal_noise	Definition of strong galactic source	K	3	
Q_CSWeF	Second Stokes parameter map weighted by a centrosymmetric WeF	K	3	
U_CSWeF	Third Stokes parameter map weighted by a centrosymmetric WeF	K	3	
Tm_gal_noise_pol	Definition of polarised galactic source	K	3	
Tg_WS_gal	Minimum WS to discard measurements contaminated by erroneous galactic noise	m/s	3	
Dg_gal_noise_error	Number of measurements with galactic noise error flag raised	dl	3	
Dg_gal_noise_pol	Number of measurements with specular direction toward a polarised galactic source	dl	3	
Dg_sky	Number of measurements with specular direction toward a strong galactic source	dl	3	
nsig	Factor to multiply σTb in outliers detection	dl	3.4.1	
RFI_std	Factor to multiply std_theory in RFI detection	dl	3.4.2	
RFI_nsig	Factor to multiply radiometric_noise in RFI detection	dl	3.4.2	
σTb_radiometric_noise	Radiometric noise of a single meas.	K	3	
σTb_model1	Model error estimate in outliers detection	K	3	roughness 1
σTb_model2	Model error estimate in outliers detection	K	3	roughness 2
σTb_model3	Model error estimate in outliers detection	K	3	roughness 3
3.5 Sunglint contamination				
dA	Area illuminated by sun glint	m^2	3.5	
$\vec{n}_s$	direction (incidence and azimuth s) of sun radiation at the considered earth surface position and time.	dl	3.5	
$\vec{n}_i$	direction (incidence and azimuth angles) of observation from MIRAS at target.	dl	3.5	
Tss	radiometric temperatures of scattered solar energy in area dA.	K	3.5	
$\overset{\circ}{\sigma}_{hh}$, $\overset{\circ}{\sigma}_{vv}$, $\overset{\circ}{\sigma}_{hv}$, $\overset{\circ}{\sigma}_{vh}$, also called $\overset{\circ}{\sigma}_{\alpha\alpha0}$	bistatic scattering coefficients of the sea surface	dl	3.5	
θ_s	scattering elevation angle	deg	3.5	
β_{sun}	2* angular radius of the sun as viewed from the earth.	deg	3.5	
T_{sun}	brightness temperature of the sun at 1.4GHz in the direction $\vec{n}_i$ and time t.	K	3.5	
T(φ,ψ,t)	position on the earth surface	(degN,degE,s)	3.5	

Variable name	Descriptive Name	Units	ATBD reference	Comment
ϕ	longitude of the observer	deg E	3.5	
ψ	latitude of the observer	deg N	3.5	
t	a given time	s	3.5	
q_k, q_i	vertical projections of the wave vectors	Rad m^{-1}	3.5	
$B\alpha\alpha_0$	geometric functions of the dielectric constant	dl	3.5	
h	surface elevation signal	m	3.5	
ρ	correlation function of roughness	m^2	3.5	
Ω_{sun}	solid angle intercepting the sun as seen from the earth	Sr	3.5	
φ_u	wind direction	deg	3.5	
θ_i, ϕ_i	local sun angles (incidence and azimuth) at the considered earth surface position and time	deg	3.5	
θ_s, ϕ_s	local observation angles (incidence and azimuth) from MIRAS antenna at target	deg	3.5	
Φ_{si}	angle of the difference between the scattered and incident wavevectors	deg	3.5	
Fg_OoR_Sunglint_dim2_ThetaSun	ThetaSun went out of LUT range during retrieval	Y/N	3.5.4.3	
Fg_OoR_Sunglint_dim3_Phi	Phi went out of LUT range during retrieval	Y/N	3.5.4.3	
Fg_OoR_Sunglint_dim4_Theta	Theta went out of LUT range during retrieval	Y/N	3.5.4.3	
Fg_OoR_Sunglint_dim5_WS	WS went out of LUT range during retrieval	Y/N	3.5.4.3	
3.6 Sea state developm.				
Hsw	Significant wave height of wind waves	m	3.6	
Tg_swell	Threshold for classification of sea state between swell or not swell dominated	dl	3.6	
Tg_old_sea	Upper limit of inverse wave age for old seas	dl	3.6	
Tg_young_sea	Lower limit of inverse wave age for young seas	dl		
3.7 SST and SSS fronts				
Radius_front	Radius to search for SST and SSS fronts	km	3.7	
Tg_SST_front	Threshold in SST gradient around a grid point to flag the presence of a SST front	K/km	3.7	
Tg_SSS_front	Threshold in SSS gradient around a grid point to flag the presence of a SSS front	psu/km	3.7	
4.1 Flat sea				
Tb flat, p	Brightness temperature in H and V pol due to a flat sea; p is polarization	K	4.1, 4.13	
Tb rough,p	Brightness temperature due to the roughness of the sea surface.		4.1, 4.13	
θ	Incidence angle	deg	4.1	
$\overrightarrow{P}_{rough}$	Vector of parameters that describes the roughness of the sea		4.1	
e	Emissivity of the sea	dl	4.1	

Variable name	Descriptive Name	Units	ATBD reference	Comment
$\Gamma_{h,v}$	Reflection coefficient in h / v polarization	dl	4.1, 4.2,4.3,4.4	
$R_{h,v\_}$	Flat sea reflection coefficient in h / v polarization	dl	4.1, 4.2,4.3,4.4	
ε	Complex dielectric constant	dl	4.1	
ε'	real part of dielectric constant	dl	4.1	
ε''	imaginari part of dielectric constant	dl	4.1	
$\mathcal{E}_\infty$	Electrical permittivity at very high frequencies	dl	4.1	
ε_s	Static dielectric constant	dl	4.1	
τ	Relaxation time	s	4.1	
σ	Ionic conductivity	Siemens	4.1	
ε_0	Permitivitty of the free space	Farads/m	4.1	
m	Coefficients vector for ε_s	dl	4.1.1.2	
t	Coefficients vector for τ	dl	4.1.1.2	
s	Coefficients vector for σ	dl	4.1.1.2	
4.2 Roughness model 1: Two-scales				
ϕ	Azimuth angle	rad	4.2.1.1	
a	Sea surface absorptivity		4.2.1.1	
Q	Second Stokes parameter	K	4.2.1.1	
U	Third Stokes parameter	K	4.2.1.1	
V	Fourth Stokes parameter	K	4.2.1.1	
λ_0	Radiometer wavelength	m	4.2.1.1	
λ_c	Cutoff wavelength	m	4.2.1.1	
S_x	Slope along the azimuth (Earth surface frame)	dl	4.2.1.1.1	
S_y	Slope across the azimuth (Earth surface frame)	dl	4.2.1.1.1	
$P(S_x,S_y)$	Probability density function of large waves	dl	4.2.1.1.1	
S_x'	Surface slope along the radiometer azimuth observation direction (radiometer frame)	dl	4.2.1.1.1	
S_y'	Surface slope across the radiometer azimuth observation direction (radiometer frame)	dl	4.2.1.1.1	
$T_{b,l}$	Local brightness temperature for a large wave	K	4.2.1.1.1	
θ_l	local incidence angle	rad	4.2.1.1.1	
ϕ_l	local azimuth angle	rad	4.2.1.1.1	
R_{ss}	reflectivity of small-scale roughness covered surface	dl	4.2.1.1.1	
R_c	coherent component of Rss	dl	4.2.1.1.1	
R_i	incoherent component of Rss	dl	4.2.1.1.1	
$\gamma_{m,n,p,q}$	Incoherent bistatic scattering coefficient, with (m,n,p,q)=(h,v) polarisations	dl	4.2.1.1.1	

Variable name	Descriptive Name	Units	ATBD reference	Comment
W_{ss}	sea surface power spectrum of small-scale roughness	dl	4.2.1.1.1	
k	Wavenumber	m^{-1}	4.2.1.1.1	
k_0	Radiometer wavenumber	m^{-1}	4.2.1.1.1	
k_c	Cutoff wavenumber	m^{-1}	4.2.1.1.1	
$R_{pp}^{(0)}$	Fresnel reflection coefficient (p=(h,v))	dl	4.2.1.1.1	
δR_{ss}	correction to Fresnel reflectivity induced by small-scale waves	dl	4.2.1.1.1	
$\delta R_{ss,0}$	omnidirectional component of δR_{ss}	dl	4.2.1.1.1	
$\delta R_{ss,2}$	second harmonic amplitude δR_{ss}	dl	4.2.1.1.1	
g_p	functions (p = v, h, 3 or 4) that account for both coherent and incoherent contributions to δR_{ss}	dl	4.2.1.1.1	
f	cosine function for Tv and Th, sine function for T3 and T4	dl	4.2.1.1.1	
$C(k, \phi)$	2D surface curvature spectrum	dl	4.2.1.1.1	
ξ	Ratio of k and k_0. Scattering weighting function given by *Johnson and Zhang* (1999)	dl	4.2.1.1.1	
$g'_{p,n}$	Ratio of $g_{p,n}$ and ξ. Scattering weighting function given by *Johnson and Zhang* (1999)	dl	4.2.1.1.1	
$W(k_p', \phi')$	2D surface power spectrum	dl	4.2.1.1.2	
Irough	First Stokes parameter due to the roughness of the sea surface	K	4.2.1.1.2	
z	Altitude	m	4.2.1.1.2	
u_c	Surface velocity	$m\ s^{-1}$	4.2.1.1.2	
κ	von Karman's constant	dl	4.2.1.1.2	
z0	roughness length	m	4.2.1.1.2	
L	Monin Obhukov length	m	4.2.1.1.2	
Ψ	function of the stability parameter z/L	dl	4.2.1.1.2	
C_D	drag coefficient	dl	4.2.1.1.2	
WSn	Neutral equivalent wind speed	$m\ s^{-1}$	4.2.1.1.2	
ϕ_w	wind direction, counted counterclockwise	rad	4.2.1.2	
ϕ_r	azimuthal observation angle of radiometer look direction, counted counterclockwise	rad	4.2.1.2	
ϕ_a	azimuth angle, counted counterclockwise, between wind direction and the azimuthal observation angle of radiometer look direction	rad	4.2.1.2	
Tp0	omnidirectionnal signal component (p polarization) of Tbrough	K	4.2.1.2	
Tp1	first harmonic component (p polarization) of Tbrough	K	4.2.1.2	
Tp2	second harmonic component (p polarization) of Tbrough	K	4.2.1.2	
U1	first harmonic component (3rd Stokes parameter) of Tbrough	K	4.2.1.2	
U2	second harmonic component (3rd Stokes parameter) of Tbrough	K	4.2.1.2	
V1	first harmonic component (4th Stokes parameter) of Tbrough	K	4.2.1.2	

Variable name	Descriptive Name	Units	ATBD reference	Comment
V2	second harmonic component (4th Stokes parameter) of Tbrough	K	4.2.1.2	
$\sigma_{Tb\ model}$	uncertainty of the model	K	4.2, 4.3, 4.4	
Tg_WS_roughness_M1	min. WS to apply roughness correction	m s^{-1}	4.2	
Fg_ctrl_roughness_M1	roughness correction applied	Y/N	4.2	
Tg_WS_foam_M1	minimum WS to apply foam correction	m s^{-1}	4.2	
Fg_ctrl_foam_M1	foam correction applied	Y/N	4.2	
Fg_OoR_Rough_dim1	Prior or retrieved SST went outside of LUT range	Y/N	4.2.1.2	
Fg_OoR_Rough_dim2	Prior or retrieved SSS went outside of LUT range	Y/N	4.2.1.2	
Fg_OoR_Rough_dim3	Prior or retrieved WS went outside of LUT range	Y/N	4.2.1.2	
Fg_OoR_Rough_dim4	Prior or retrieved Theta went outside of LUT range	Y/N	4.2.1.2	
4.3 Roughness model 2: SSA				
$\vec{k}$	surface wavenumber vector	rad m^{-1}	4.3	
W(k,φ)	sea surface directional waveheight wavenumber spectrum	m^4	4.3	
gγ	electromagnetic weighting functions	m^{-2}	4.3	
φ	Azimuthal direction relative to wind direction	deg	4.3	
Δeγ	wind-excess emissivity Stokes vector	dl		
Δeγ $^{(n)}$	nth azimuthal harmonics of the wind-excess emissivity stokes vector	dl		
γ	represent h, v, U or V depending on the case	dl		
Δe_B	residual Stokes vector of roughness impact	dl	4.3.2.1	
ε_{sw}	relative permittivity of sea water	dl		
Tg_WS_roughness_M2	min. WS to apply roughness correction	m s^{-1}	4.3	
Fg_ctrl_roughness_M2	roughness correction applied	Y/N	4.3.	
Tg_WS_foam_M2	minimum WS to apply foam correction	m s^{-1}	4.3	
Fg_ctrl_foam_M2	foam correction applied	Y/N	4.3	
Fg_OoR_Rough_dim1	Prior or retrieved WS went outside of LUT range	Y/N	4.2.1.2	
Fg_OoR_Rough_dim2	Prior or retrieved Omega went outside of LUT range	Y/N	4.2.1.2	
Fg_OoR_Rough_dim3	Prior or retrieved Theta went outside of LUT range	Y/N	4.2.1.2	
Fg_OoR_Rough_dim4	Prior or retrieved SSS went outside of LUT range	Y/N	4.2.1.2	
Fg_OoR_Rough_dim5	Prior or retrieved SST went outside of LUT range	Y/N	4.2.1.2	
4.4 Roughness model 3: Empirical				
WS	Wind speed	m/s	4.4	
φ	Azimuthal direction relative to wind direction	deg	4.4	

Variable name	Descriptive Name	Units	ATBD reference	Comment
Hs	Significant wave height	m	4.4	
Ω	Inverse wave age	dl	4.4	
Cp	Phase speed	m/s	4.4	
g	Gravity of the earth	m/s^2	4.4	
T_p	Mean period of wind waves	dl	4.4	
U*	Wind friction velocity	m/s	4.4	
C_d	Coefficient of drag	dl	4.4	
MSQS	Mean square slope of waves	dl	4.4	
Tg_WS_roughness_M3	min. WS to apply roughness correction	m s^{-1}	4.4	
Fg_ctrl_roughness_M3	Roughness correction applied	Y/N	4.4.	
Fg_OoR_Rough_dim1	Prior or retrieved Theta went outside of LUT range	Y/N	4.4.1.2	
Fg_OoR_Rough_dim2	Prior or retrieved WS went outside of LUT range	Y/N	4.4.1.2	
Fg_OoR_Rough_dim3	Prior or retrieved phi_wsn went outside of LUT range	Y/N	4.4.1.2	
Fg_OoR_Rough_dim4	Prior or retrieved Hs went outside of LUT range	Y/N	4.4.1.2	
4.5 Foam contribution				
F	Fraction of sea surface area covered by whitecaps	dl		
h	thickness of the white caps	m		
δ	thickness of the typical sea foam layer	m		
Ts	physical temperature of foam	K		
e^{typ}_{foam}	emissivity of typical sea foam-layer	dl		
r	radius of the coated bubbles	m		
ε_a	permittivity of the core of the bubbles made of air	dl		
ε_w	permittivity of the surrounded area (region 2)	dl		
$\varepsilon_{N\alpha}$	effective permittivity	dl		
d	thickness of the layer called region 1	m		
ψ	attenuation factor	dl		
R_p^{01}	Fresnel reflection coefficient between region 0 and 1, for p pol	dl		
R_p^{12}	Fresnel reflection coefficient between region 1 and 2, for p pol	dl		
N	volumetric concentration of bubbles	dl		
α	complex polarizability of a single bubble	dl		
k	packing coefficient or stickiness parameter	dl		
p_f	normalized probability distribution function	dl		
q	distribution of the bubble's filling factor	dl		
f	distribution of coating thicknesses	dl		
A	parameters of the distribution	dl		
B	parameters of the distribution	dl		
$\tilde{A}$		dl		
$\tilde{B}$		dl		
f_a	fraction of volume occupied by air bubbles	dl		

12

Variable name	Descriptive Name	Units	ATBD reference	Comment
Fc	coverage of actively breaking crests or active foam	dl		
Fs	coverage of passive foam or static foam	dl		
α_c	constant for 'crest-foam coverage'	dl		
β_c	constant for 'crest-foam coverage'	dl		
α_s	constant for 'static-foam coverage'	dl		
β_s	constant for 'static-foam coverage'	dl		
ΔT	air-sea temperature difference	ºC		
T_a	temperature of air	ºC		
$e^{typ}{}_{Bfp}$	???????????	dl		
Fg_OoR_Foam_dim1_WS	WS went out of LUT range during retrieval	Y/N	4.5.4.3	
Fg_OoR_Foam_dim2_TseaAir	TseaAir went out of LUT range during retrieval	Y/N	4.5.4.3	
Fg_OoR_Foam_dim3_SSS	SSS went out of LUT range during retrieval	Y/N	4.5.4.3	
Fg_OoR_Foam_dim4_SST	SST went out of LUT range during retrieval	Y/N	4.5.4.3	
Fg_OoR_Foam_dim5_Theta	Theta went out of LUT range during retrieval	Y/N	4.5.4.3	
4.6 Galactic noise contamination				
P	power	W	4.6.1.2.1	
k	Boltzmann constant	J K^{-1}	4.6.1.2.1	
ΔB	bandwidth	Hz	4.6.1.2.1	
v	velocity	m s^{-1}	4.6.1.2.1.a	
c	Light speed	m s^{-1}	4.6.1.2.1.a	
ν	Frequency associated with velocity v	Hz	4.6.1.2.1.a	
ν_0	Center frequency	Hz	4.6.1.2.1.a	
Pint	Integrated power	W	4.6.1.2.1.a	
ΔBsmos	SMOS radiometer bandwidth	Hz	4.6.1.2.1.a	
ϑ_i	incidence angle of one radiometer measurement	deg, rad	4.6.1.2.2	
φ_i	azimuth angle of one radiometer measurement (0 towards the north; positive westward)	rad	4.6.1.2.2	
ϑ_{igal}	Incidence angle of the incident galactic ray specularly reflected towards the radiometer	deg, rad	4.6.1.2.2	
Re	earth radius	km	4.6.1.2.2	
h_{rad}	altitude of the radiometer	km	4.6.1.2.2	
el	elevation angle (0 towards the horizon and positive above the horizon)	deg	4.6.1.2.2	
δ	declination	deg	4.6.1.2.2	
α	right ascension	deg	4.6.1.2.2	
T	sidereal time	deg	4.6.1.2.2	

13

Variable name	Descriptive Name	Units	ATBD reference	Comment
H	sidereal angle	deg	4.6.1.2.2	
Tbgal_refl	Galactic noise reflected towards the radiometer	K	4.6.1.2.2.a	
Tbgal	Effective brightness temperature of the galactic radiation	K	4.6.1.2.2.a	
Rrough	Roughness contribution to the reflection coefficient Γ	dl	4.6.1.2.2.b	
σ^0_{pp}	bistatic reflection coefficients (p=(h,v))	dl	4.6.1.2.2.b	
Tbgal_refl_lobe	reflected brightness temperature integrated over the antenna pattern	K	4.6.1.2.3	
Plobe	normalized power pattern of the antenna	W	4.6.1.2.3	
Fg_OoR_gam1_dim1_dec	Out of range flag raised if at least one of the measurements of a dwell has a declination value which falls outside the acceptable interval limits.	dl		
Fg_OoR_gam1_dim2_ra	Out of range flag raised if at least one of the measurements of a dwell has a right ascension value which falls outside the acceptable interval limits.	dl		
4.7 Galactic noise 2				
Ah_0	symmetric H-pol component	K		
Ah_2	$\cos(2\varphi_w)$ harmonic amplitude H-pol	K		
Av_0	symmetric V-pol component	K		
Av_2	$\cos(2\varphi_w)$ harmonic amplitude V-pol	K		
Bh_2	$\sin(2\varphi_w)$ harmonic amplitude H-pol	K		
Bv_2	$\sin(2\varphi_w)$ harmonic amplitude V-pol	K		
dec	Declination corresponding to specular reflection direction	°		
Fg_OoR_gam2_dec[Ngp]	Out of range flag raised if at least one of the measurements of a dwell has a declination value which falls outside the acceptable interval limits.	dl		
Fg_OoR_gam2_psi[Ngp]	Out of range flag raised if at least one of the measurements of a dwell has a psi angle value which falls outside the acceptable interval limits.	dl		
Fg_OoR_gam2_ra[Ngp]	Out of range flag raised if at least one of the measurements of a dwell has a right ascension value which falls outside the acceptable interval limits.	dl		
Fg_OoR_gam2_theta[Ngp]	Out of range flag raised if at least one of the measurements of a dwell has an incidence angle value which falls outside the acceptable interval limits.	dl		
Fg_OoR_gam2_WSn[Ngp]	Out of range flag raised if at least one of the measurements of a dwell has a wind speed value which falls outside the acceptable interval limits.	dl		
G	Sideral angle	°		

Variable name	Descriptive Name	Units	ATBD reference	Comment
h_hat_c[3]	Celestial basis vector. h component.	dl		
h_hat_u[3]	Upper hemisphere basis vector (topocentric frame). h component.	dl		
h_tild_u[3]	Upper hemisphere basis vector after Tac transformation. h component.	dl		
LUT_th_hc	$\widetilde{A}_h^{(2)} \; \cos(2\varphi_w)$ harmonic amplitude H-pol	K		
LUT_th_hs	$\widetilde{B}_h^{(2)} \; \sin(2\varphi_w)$ harmonic amplitude H-pol	K		
LUT_th_symm	$\widetilde{A}_h^{(0)}$ symmetric H-pol component	K		
LUT_tv_hc	$\widetilde{A}_v^{(2)} \; \cos(2\varphi_w)$ harmonic amplitude V-pol	K		
LUT_tv_hs	$\widetilde{B}_v^{(2)} \; \sin(2\varphi_w)$ harmonic amplitude V-pol	K		
LUT_tv_symm	$\widetilde{A}_v^{(0)}$ symmetric V-pol component	K		
nut	Nutation angle	°		
psi_uh	Orientation angle	°		
ra	Right ascension corresponding to specular reflection direction	°		
TB_gal[4]	Galactic TB contribution	K		
TB_gal_flat[2]	Galactic TB contribution given for a wind speed equal to 0 m/s	K		
TB_gal_rough[2]	Galactic TB contribution given for a wind speed of 3 m/s	K		
TB_roug[4]	Roughness TB contribution. TB_roug(1), TB_roug(2), TB_roug(3) and TB_roug(4) are respectively H, V polar and St3, St4	K		
v_hat_c[3]	Celestial basis vector. v component.	dl		
v_hat_u[3]	Upper hemisphere basis vector (topocentric frame). v component.	dl		
v_tild_u[3]	Upper hemisphere basis vector after Tac transformation. v component.	dl		
φ_relat	Wind speed direction given from incidence plan frame for one measurement.	°		
ɵ	Zenith angle of target to sensor direction	°		
4.8 Faraday rotation				
ω_{Fa}	Faraday	degrees	4.8.1.2	
TEC_n	Total Electron nadir columnar Content	1 TEC unit = 10^{16} m^{-2}	4.8.1.2	
B	Magnetic field vector	nanotesla	4.8.1.2	
U_{LS}	Unitary vector giving the direction of the line of sight (from target to spacecraft)	dl	4.8.1.2	
θ_g	Elevation away from the Oz axis	degrees	4.8.1.2	
φ_n	Azimuth from origin Ox (counter clockwise)	degrees	4.8.1.2	
Fg_sc_TEC_gradient	TEC gradient along dwell line for a grid point is above threshold	Y/N	4.8.2	
Tg_TEC_gradient	Threshold for TEC gradient	TECu	4.8.2	
4.9 Atmospheric effects				

Variable name	Descriptive Name	Units	ATBD reference	Comment
Tb_m	measured brightness temperature	K	4.9.1.1.1	
Tb_s	upwelling brightness temperature from the surface	K	4.9.1.1.1	
e_s	surface emissivity	dl	4.9.1.1.1	
Tb_{up}	brightness temperature self-emitted by the atmosphere upwards	K	4.9.1.1.1	
Tb_{down}	brightness temperature self-emitted by the atmosphere downwards	K	4.9.1.1.1	
Γ	surface reflection coefficient	dl	4.9.1.1.1	
τ	equivalent optical thickness of the atmosphere	dl	4.9.1.1.1	
κ	lineic absorption coefficient	dB/km	4.9.1.1.1	
z	Altitude	km	4.9.1.1.2	
$P(z)$	Pressure of the gas at the altitude z	hPa	4.9.1.1.2	
$T(z)$	temperature of the gas at the altitude z	K	4.9.1.1.2	
κ_{OX}	lineic absorption from oxygen at f=1.413 GHz	dB/km	4.9.1.1.2	
f	frequency	GHz	4.9.1.1.2	
$f0$	absorption line frequency	GHz	4.9.1.1.2	
γ	line width parameter	GHz	4.9.1.1.2	
γ_0	line width	GHz	4.9.1.1.2	
κ_{H2O}	water vapor absorption coefficient	dl	4.9.1.1.3	
κ_{22}	22.235 GHz absorption line	dl	4.9.1.1.3	
κ_r	residual term	dl	4.9.1.1.3	
ρ_v	water vapor density	$g\ m^{-3}$	4.9.1.1.3	
γ_1	line width parameter	GHz	4.9.1.1.3	
Tb_{atm}	brightness temperature self-emitted by the atmosphere	K	4.9.1.2.1	
τ_{atm}	total optical thickness of the atmosphere	dl	4.9.1.2.1	
δz	thickness of a slice of atmosphere	km	4.9.1.2.1	
$\delta\tau_{GAS}$	elementary optical thickness for each slice and for each component (G is replaced by either O2 or H2O)	dl	4.9.1.2.1	
κ_{GAS}	lineic absorption coefficient (G is replaced by either O2 or H2O)	dl	4.9.1.2.1	
ι	incidence angle	deg, rad	4.9.1.2.1	
τ_{GAS}	total optical thickness (G is replaced by either O2 or H2O)	dl	4.9.1.2.1	
Tb_{GAS}	radiative contribution (G is replaced by either O2 or H2O)	K	4.9.1.2.1	
T0	Surface atmospheric temperature	K	4.9.1.2.1	
P0	Surface pressure	hPa	4.9.1.2.1	
DT_{GAS}	difference between the equivalent layer temperature and the surface temperature (G is replaced by either O2 or H2O)	K	4.9.1.2.1	
τ_{O2}	O2 total optical thickness	dl	4.9.1.2.2	
DT_{O2}	difference between the equivalent layer temperature and the surface temperature for O2	K	4.9.1.2.2	
τ_{H2O}	H2O total optical thickness	dl	4.9.1.2.2	

16

Variable name	Descriptive Name	Units	ATBD reference	Comment
DT_{H2O}	difference between the equivalent layer temperature and the surface temperature for H2O	K	4.9.1.2.2	
WVC	Total precipitable water vapor	kg m^{-2}	4.9.1.2.2	
4.10 Cardioid model				
Acard	A coefficient for cardioid model	dl		
Bcard	constant for cardioid model	dl		
Ucard	U coefficient for cardioid model	°		
T_eff	Effective temperature retrieved with cardioid model	K		
Fg_sc_ice_Acard	Flag for ice detection with cardioid model	dl		
Tg_SST_ice_Acard	SST threshold for cardioid ice detection	K		
Tg_ Acard_ice	Acard threshold for cardioid ice detection	dl		
Tg_lat_ice_Acard	Latitude threshold for cardioid ice detection	º		
4.12 Transport ground to antenna				
θ	angle defined in 4.12	deg	4.12	
ϕ	angle defined in 4.12	deg	4.12	
ψ	angle defined in 4.12	deg	4.12	
ϕ_q	angle defined in 4.12	deg	4.12	
a	rotation angle	deg	4.12	
4.13 Sum of contributions				
θ_mean	mean incidence angle	deg	4.13	
θx	incidence angle acquired in x	deg	4.13	
θy	incidence angle acquired in y	deg	4.13	
Tb_{BOA}	Tb at bottom of the atmosphere, at earth reference frame	K	4.13	
$Tb_{reflected}$	All the tb contributions that are reflected at the sea	K	4.13	
Tb_{TOA}^{EARTH}	Tb at top of the atmosphere, at earth reference frame	K	4.13	
$Tb^{ANTENNA}$	Same as [A], Tb at antenna reference frame	K	4.13	
Tb_{foam}	Contribution of brightness temperature due to foam	K	4.13, 4.5	
F	Fraction of sea surface area covered by whitecaps	dl	4.13, 4.5	
4.14 Iterative scheme				
Tb^{mod}	Tb computed by a model	K	4.14	
Tb^{meas}	Measured Tb	K	4.14	
χ^2	Value of the cost function	dl	4.14	
$\sigma_{T\_meas}^2$	Variance of measured Tb given at different incidence angles	K	4.14	
$\sigma_{Tb\_model}^2$	Variance of modelled Tb given at different incidence angles	K	4.14,4.2,4.3,4.4	
σ_{pi}^2	A priori variance of different parameters to be retrieved	(several)	4.14	

Variable name	Descriptive Name	Units	ATBD reference	Comment
P_j^{prior}	A priori information of the value of the parameters to be retrieved	(several)	4.14	
$P_{j,first\ guess}$	Value of each parameter that will be used in the first iteration in the inversion algorithm	(several)	4.14	
$\sigma^2_{P\ retrieved}$	A posteriori variance of retrieved parameter	(several)	4.14	
$P_{j,retrieved}$	A posteriori value of the retrieved parameter	(several)	4.14	
SST	Sea surface temperature. ECMWF MARS table 128 code 34	K	4.14.1.1.1	
WSx	10 m neutral equivalent wind zonal component. ECMWF MARS table 228 code 131	m/s	4.14.1.1.1	
WSy	10 m neutral equivalent wind meridional component. ECMWF MARS table 228 code 132	m/s	4.14.1.1.1	
Φ	Wind direction computed from WSx and WSy	deg. met convention	4.14.1.1.1	
U*	Wind friction velocity derived by ECMWF pre-processor from codes 245 and 233 (table 140)	m/s	4.14.1.1.1	
Ω	Inverse wave age derived by ECMWF pre-processor from codes 245 and 236 (table 140)	ND	4.14.1.1.1	
WS	10 m wind speed from wave model. ECMWF MARS table 140 code 245	m/s	4.14.1.1.1	
Hs	Significant wave height. ECMWF MARS table 140 code 229	m	4.14.1.1.1	
MSQS	Mean square slope of waves. ECMWF MARS table 140 code 244	ND	4.14.1.1.1	
Np	Number of retrieved parameters	dl	4.14	
Nm	Number of different observations of a grid point	dl	4.14	
C_{Tb}	Variance-Covariance matrix of data	dl	4.14	
C_{Pj}	Variance-Covariance matrix for prior parameters	dl	4.14	
X	Data and priori parameter vector	(several)	4.14	
X_mod	vector of modeled Tb and parameter value at each iteration	(several)	4.14	
a	vector of parameters to be retrieved	dl	4.14	
d	gradient matrix	dl	4.14	
D	Hessian matrix	dl	4.14	
α	matrix derived from d	dl	4.14	
β	matrix derived from D	dl	4.14	
λ	Marquardt's diagonal amplifier	dl	4.14	
λ_{ini}	Initial Marquardt's diagonal amplifier	dl	4.14	
k_d	Factor for multiplying Marquardt's diagonal amplifier	dl	4.14	
δ_χ	Chi variance ratio for convergence test	dl	4.14	
Tb_lambda_diaMax	Threshold for Marquardt increment	dl	4.14	

Variable name	Descriptive Name	Units	ATBD reference	Comment
Fg_ctrl_marq_SSS1	Iteration stopped due to Marquardt increment too big for roughness 1	Y/N	4.14	
Fg_ctrl_marq_SSS2	Iteration stopped due to Marquardt increment too big for roughness 2	Y/N	4.14	
Fg_ctrl_marq_SSS3	Iteration stopped due to Marquardt increment too big for roughness 3	Y/N	4.14	
Fg_ctrl_marq_Acard	Iteration stopped due to Marquardt increment too big for cardioid	Y/N	4.14	
Tg_it_max	Maximum number of iterations allowed	dl	4.14	
Fg_ctrl_chi2_1	Poor fit quality using roughness model 1	Y/N	4.14	
Fg_ctrl_chi2_2	Poor fit quality using model 2	Y/N	4.14	
Fg_ctrl_chi2_3	Poor fit quality using model 3	Y/N	4.14	
Fg_ctrl_chi2_Acard	Poor fit quality using cardioid model	Y/N	4.14	
$Tg\_Q\chi$	Threshold to check the quality of the SSS retrieval	dl	4.14	
Dg_num_iter_1	Number of iterations using model 1	dl	4.14	
Dg_num_iter_2	Number of iterations using model 2	dl	4.14	
Dg_num_iter_3	Number of iterations using model 3	dl	4.14	
Dg_num_iter_Acard	Number of iterations using cardioid model	dl	4.14	
Fg_ctrl_reach_maxIter_1	Maximum number of iteration reached before convergence	Y/N	4.14	Roughness 1
Fg_ctrl_reach_maxIter_2	Maximum number of iteration reached before convergence	Y/N	4.14	Roughness 2
Fg_ctrl_reach_maxIter_3	Maximum number of iteration reached before convergence	Y/N	4.14	Roughness 3
Fg_ctrl_reach_maxIter_Ac	Maximum number of iteration reached before convergence	Y/N	4.14	Cardioid model
Tg_SSS_max	Maximum value of valid retrieved salinity	psu	4.14	
Tg_SSS_min	Minimum value of valid retrieved salinity	psu	4.14	
Tg_sigma_max	Maximum value of sigma of the retrieved salinity	psu	4.14	
Tg_Acard_max	Maximum value of valid retrieved Acard	dl	4.14	
Tg_Acard_min	Minimum value of valid retrieved Acard	dl	4.14	
Tg_sigma_Acard_max	Maximum value of sigma of the retrieved Acard	dl	4.14	
Fg_ctrl_range_1	Retrieved SSS is outside range	Y/N	4.14	Roughness 1
Fg_ctrl_sigma_1	Retrieved SSS sigma overpasses the accepted value	Y/N	4.14	Roughness 1
Dg_chi2_1	Retrieval fit quality index	dl	4.14	Roughness 1
Dg_chi2_P_1	chi2 high value acceptability probability	dl	4.14	Roughness 1
Dg_quality_SSS1	Descriptor of SSS1 uncertainty	psu	4.14.2	
Fg_ctrl_quality_SSS1	At least one critical flag was raised during SSS1 retrieval	Y/N	4.14.2	Roughness 1
Fg_ctrl_range_2	Retrieved SSS is outside range	Y/N	4.14	Roughness 2
Fg_ctrl_sigma_2	Retrieved SSS sigma overpasses the accepted value	Y/N	4.14	Roughness 2
Dg_chi2_2	Retrieval fit quality index	dl	4.14	Roughness 2

Variable name	Descriptive Name	Units	ATBD reference	Comment
Dg_chi2_P_2	chi2 high value acceptability probability	dl		Roughness 2
Dg_quality_SSS2	Descriptor of SSS2 uncertainty	psu	4.14.2	
Fg_ctrl_quality_SSS2	At least one critical flag was raised during SSS2 retrieval	Y/N	4.14.2	Roughness 2
Fg_ctrl_range_3	Retrieved SSS is outside range	Y/N	4.14	Roughness 3
Fg_ctrl_sigma_3	Retrieved SSS sigma overpasses the accepted value	Y/N	4.14	Roughness 3
Dg_chi2_3	Retrieval fit quality index	dl	4.14	Roughness 3
Dg_chi2_P_3	chi2 high value acceptability probability	dl		Roughness 3
Dg_quality_SSS3	Descriptor of SSS3 uncertainty	psu	4.14.2	
Fg_ctrl_quality_SSS3	At least one critical flag was raised during SSS3 retrieval	Y/N	4.14.2	Roughness 3
Fg_ctrl_range_Acard	Retrieved Acard is outside range	Y/N	4.14	Acard
Fg_ctrl_sigma_Acard	Retrieved Acard sigma overpasses the accepted value	Y/N	4.14	Acard
Dg_chi2_ Acard	Retrieval fit quality index	dl	4.14	Acard
Dg_chi2_P_Acard	chi2 high value acceptability probability	dl		Acard
Dg_quality_Acard	Descriptor of Acard uncertainty	dl	4.14	Acard
Fg_ctrl_quality_Acard	At least one critical flag was raised during Acard retrieval	Y/N	4.14	Acard
Tg_chi2_P_max	Maximum admisible value for Dg_chi2_P	dl		
Tg_chi2_P_min	Minimum admisible value for Dg_chi2_P	dl		
Fg_ctrl_chi2_P_1	Poor fit quality from test chi2_P	Y/N	4.14	Roughness 1
Fg_ctrl_chi2_P_2	Poor fit quality from test chi2_P	Y/N	4.14	Roughness 2
Fg_ctrl_chi2_P_3	Poor fit quality from test chi2_P	Y/N	4.14	Roughness 3
Fg_ctrl_chi2_P_Acard	Poor fit quality from test chi2_P	Y/N	4.14	Cardioid
dS_dT	Sensitivity of salinity to Tb	psu/K	4.14	Quality index
dT_dS_X X=0, 1	Coefficients for sensitivity adjustment	K/psu, 1/psu	4.14	Quality index
4.15 Brightness temperature at surface level				
$Tb_{42.5H}$	Computed surface Th at 42.5	K	4.15	
$Tb_{42.5V}$	Computed surface Tv at 42.5	K	4.15	
$\sigma_{Tb42.5H}$	Uncertainty of $Tb_{42.5H}$	K	4.15	
$\sigma_{Tb42.5V}$	Uncertainty of $Tb_{42.5V}$	K	4.15	
$Tb_{42.5X}$	Computed Tx at 42.5	K	4.15	
$Tb_{42.5Y}$	Computed Ty at 42.5	K	4.15	
$\sigma_{Tb42.5X}$	Uncertainty of $Tb_{42.5X}$	K	4.15	
$\sigma_{Tb42.5Y}$	Uncertainty of $Tb_{42.5Y}$	K	4.15	
Fg_ctrl_no_surface	No 42.5º angle along the dwell line	Y/N	4.15	

Variable name	Descriptive Name	Units	ATBD reference	Comment
4.16 Measurements selection				
Fm_lost_data	Flag for measurements not used in SSS retrieval due to lack of complementary polarisation	Y/N	4.16	
4.17 Geophysical parameters bias correction				
W_t	True wind speed	m/s	4.17	
φ	Wind direction	deg	4.17	
α_i	Wind speed gain	dl	4.17	
β_i	Wind speed bias	m/s	4.17	
n_{xi}, n_{yi}	Normally distributed noise with zero mean and unit amplitude	dl	4.17	
δ_i	Amplitude of the normally distributed random noise	m/s	4.17	
A	Scale parameter	dl	4.17	
C	Shape parameter	dl	4.17	
Fg_OoR_LUTAGDPT_lat	At least one measurement went outside of acceptable latitude limits	Y/N	4.17	
Fg_OoR_LUTAGDPT_lon	At least one measurement went outside of acceptable longitude limits	Y/N	4.17	
Fg_OoR_LUTAGDPT_month	The month value went outside of acceptable limits	Y/N	4.17	
Fg_OoR_LUTAGDPT_param	The parameter value went outside of acceptable limits	Y/N	4.17	
5. Secondary algorithm				
P	Auxiliary data vector			
g	Functional to be described with the NN algorithm			
X	Input layer			
Y	Network response			
W	Weights matrix			
b_0	Bias value associated to a single output neuron			
α_j	Interpolation angles			
β_k	Regression coefficients			
K	Epanechnikov kernel function that assigns weights to each point			
h	Bandwidth that controls the smoothing procedure			
I(t)	Step function			
Nc	Number of algorithms (or classes)			
Ns	Number of fixed angles			
θ_{min}, θ_{max}	Incidence angles that characterise a class			
Σ	Inverted of (p+1,p+1) matrix $\mathbf{X^T W X}$			

Variable name	Descriptive Name	Units	ATBD reference	Comment
6. Output Product				
Grid_Point_ID	Unique identifier of Earth fixed grid point.	dl		
Latitude	Geodetic latitude of grid point (WGS84)	dl		
Longitude	Geocentric longitude of grid point.	dl		
Mean_acq_time	Mean time of acquisition for all valid TB measurements of a DGG point. Expressed in EE CFI transport time format, defined as days since 2000/01/01.	s		
Equiv_ftprt_diam	Equivalent footprint diameter	km		
SSS1	Sea surface salinity using roughness model 1	psu		
σ_{SSS1}	Theoretical uncertainty computed for SSS1	psu		
SSS2	Sea surface salinity using roughness model 2	psu		
σ_{SSS2}	Theoretical uncertainty computed for SSS2	psu		
SSS3	Sea surface salinity using roughness model 3	psu		
σ_{SSS3}	Theoretical uncertainty computed for SSS3	psu		
A_card	Sea surface salinity using cardioid model	dl		
σ_{A_card}	Theoretical uncertainty computed for A_card	dl		
Diff_TB_1/3[NM]	Difference between Tb measurements and result of forward model 1 to 3. NM= Dg_num_meas_l1c <= 256. for two polarisations	K		
Diff_TB_Acard[NM]	Difference between Tb measurements and result of cardioid model. NM= Dg_num_meas_l1c <= 256. for two polarisations	K		
Param1/7_prior_M1/3, Ac	Prior of 7 parameters for retrieval with forward model 1 to 3, cardioid model			P_j^{prior} in 4.14
Param1/7_sigma_prior_M1/3, Ac	Sigma of prior of 7 parameters for retrieval with forward model 1 to 3, cardioid model			Similar in 4.14
Param1/7_M1/3, Ac	Retrieved value of 7 parameters using forward model 1 to 3, cardioid model			
Param1/7_sigma_M1/3, Ac	Theoretical uncertainty of 7 parameters retrieved with forward model 1 to 3, cardioid model			
Dg_X_swath	Distance between satellite track and grid point	km	6	

2. Algorithm overview

In the primary algorithm approach (iterative retrieval) a series of physical models (separate modules 4.1 to 4.10 in this ATBD) are applied to auxiliary data (SST, wind, etc.) and a first guess SSS, to compute the brightness temperature that should be measured at a specific polarization and geometric configuration. These values are transported to SMOS antenna level (module 4.12) and then compared to actually measured Tb. An iterative process (considering all measurements/views of a single grid point obtained in consecutive snapshots, module 4.14) allows minimization of the difference between modeled and measured values, until identifying a retrieved SSS for this grid point. Three different models are proposed for the effect of ocean surface roughness in L-band emissivity (modules 4.2 to 4.4) and then three retrieval processes will be run in parallel, and three SSS values provided in the L2 Output Product. A selection of the optimal method is expected to be achieved during SMOS commissioning phase and then implemented in the operational L2 processor.

An alternative approach (section 5) uses the neural network technique to retrieve SSS from SMOS measurements and a previous training data set.

The SSS retrieval algorithms described in this ATBD will be applied to all ISEA grid points included in a SMOS L1c product (half-orbit swath).

2.1 Sea Surface Salinity retrieval scheme

2.1.1 Iterative approach

Per ISEA grid point (once selected as coast/ocean or ocean) on each SMOS half-orbit:
- Get preprocessed auxiliary data (SST, wind, …)
- For all L1c Tb measurements available
    - Decision on processing/flagging according to several tests
    - Forward model for Tb at each angular measurement θ:
        - Emissivity of flat sea at θ with auxiliary SST and guessed SSS
        - Add roughness effects (3 model options + foam)
        - Add external noise (reflected signals: atmosphere, galactic, sun effects)
        - Add atmospheric atenuation and emision to antenna
    - Transport modeled Tb from TOA to antenna level
- Compare modelled with measured Tb
- Iterative convergente to retrieve SSS and adjust other parameters
- Output values: SSS, SST, roughness descriptors, TEC (depending on model options) corresponding to this specific gris point

As three different options are being studied to describe the effect of surface roughness on Tb, three SSS values will be retrieved at the end of the process. In some submodels, reference values for Tb are needed to compute flags. In this case one of the three roughness models will

be used as default for the computation. At Qualification Review 1 (19 July 2006) it was decided that Two-scale will be the default model.

2.1.2 Neural network approach

The iterative inversion is flexible and easy to develop and implement. However the main drawback is the need of a direct emissivity model. As any model, it simulates imperfectly the real brightness temperatures (many sources of yet badly known impact), and through the iterative process it directly affects the retrieved salinity. In order to avoid this dependency, a neural inversion can be developed just after launch without any need for direct models. The neural network algorithm will provide the best relation between SMOS measured brightness temperatures and collocated in-situ salinities. It is also a proper way to deal with remaining calibration errors. In the preparation phase of the mission, it is necessary to determine the structure of the algorithm, replacing SMOS brightness temperatures with simulated ones. Once SMOS in-flight, one only needs to update the algorithm coefficients to provide an accurate salinity. As there are different possibilities for direct models, different inversion method can be implemented in the L2 processor: one based on physical background (forward method+iterative inversion) with possible re-analysis of each geophysical source function and one purely empirical (NN method based on SMOS data alone versus collocated in-situ salinities and auxiliary data). It could be anticipated that a combination of both methods shall provide a robust algorithm with minimisation of risks for SSS retrieval accuracy.

2.1.3 General description
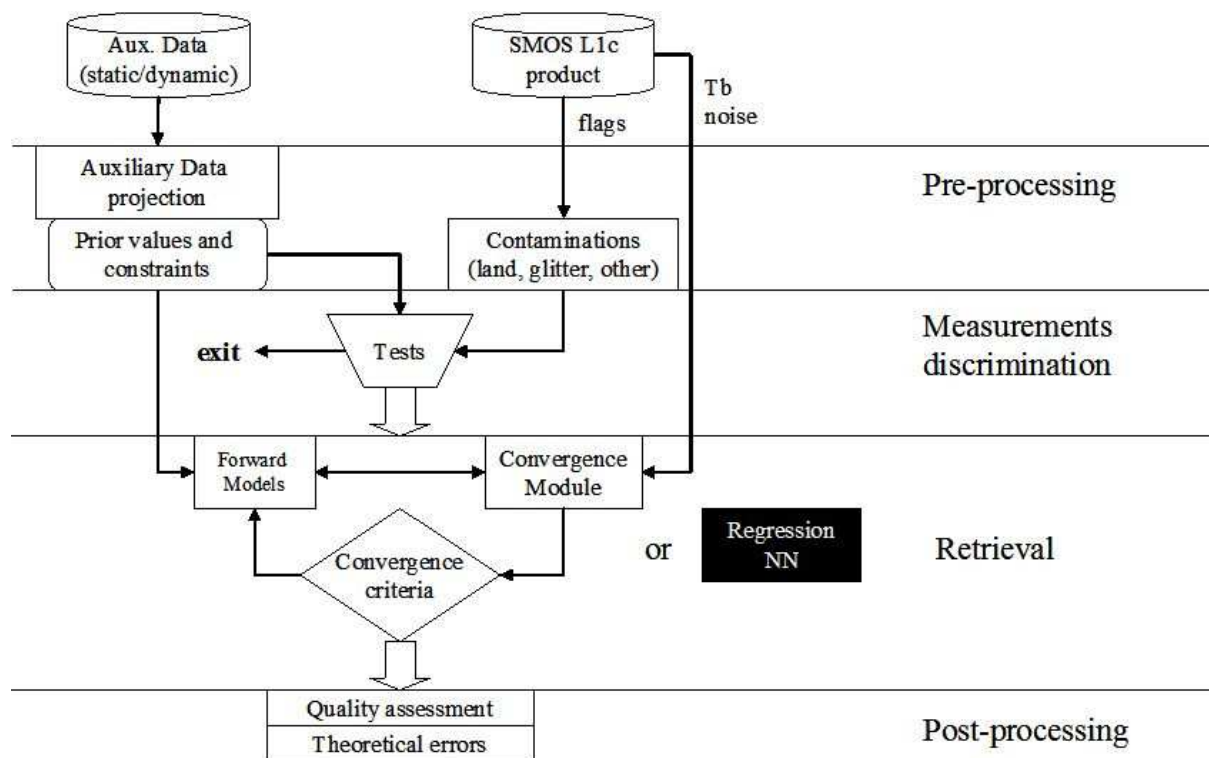
3. Measurement discrimination

The purpose of the measurement discrimination is to check the conditions of all the grid points and measurements coming from L1c to decide processing them or not to retrieve salinity. Additional information will be provided in the Output Product in terms of flags to describe some particular conditions that can rise warnings for some L3 applications or indicate that future specific reprocessing could be implemented.

A simple convention is proposed for naming flags:
Fx_class_name_of_flag
- F: the variable is a flag.
- x = **s**/**m**/**g**/**f**: Flag applies to **s**naphot, **m**easurement, **g**rid point, **f**ull half orbit.
- class= ctrl for control flag, sc for science flag
- name_of_flag.

A flag is a boolean (true/false). Numbers are descriptors (computed by the processor), named Dx_name_of_descriptor or thresholds (available in auxilary/configuration files), named Tx_name_of_threshold.

A series of tests, with defined threshold values, have to be run consecutively before applying the SSS retrieval algorithm to it:

3.1 Applied to grid points

Subject	Test	Threshold	Decision
Classification of grid points with respect to distance to land (4 categories)	Applying land mask based on distance of grid point to land.	1) Land: grid point inside land (coast line) 2) Coast/Land: grid point between coast and **Tg_dland1** 3) Coast/Ocean: grid point between Tg_dland1 and Tg_dland2 4) Ocean: grid point outside **Tg_dland2**	1) Land point. SSS retrieval is not performed 2) SSS retrieval is not performed and grid point is flagged as land contaminated 3) SSS retrieval performed, grid point flagged as Coast/ Ocean 4) SSS retrieval performed This classification will be implemented using two booleans for four states: (**Fg_sc_land_sea_coast1**; **Fg_sc_land_sea_coast2**) with (false;false)=Land (false;true)=Water, with distance to coast <= Tg_dland1 (true;true)=Water, with distance to coast <= Tg_dland2 and >Tg_dland1 (true;false)=Water, with distance to coast

			>Tg_dland2>Tg_dland1. Fg_sc_land_sea_coast1 defines the land contamination of the grid point and Fg_sc_land_sea_coast2 coastal grid points Note: both flags are computed offline and stored in an auxiliary file. If Tgdland1 and Tg_dland2 are modified too often, they will become processor configuration parameters and the processor will set both flags on the fly.
Presence of ice	Applying sea ice mask (evolving info.: ECMWF sea ice concentration + fixed info.: monthly extent climatology)	1) Grid point with ice concentration > **Tg_ice_concentration** 2) Grid point with ice concentration below threshold but within monthly climatological maximum extent of sea ice (**Fg_sc_in_clim_ice**) and (in case SSTprior < **Tg_low_SST_ice)** positive test for possible ice in at least **Tg_suspect_ice** of measures 3) Other grid points	1) Ice present. SSS retrieval is not performed (**Fg_sc_ice.true**) 2) Potencially sea ice contaminated. SSS retrieval is performed but point flagged (**Fg_sc_suspect_ice.true**) 3) No ice. SSS retrieval is performed
Heavy rain	Intense rainfall is reported in at least one of 4 ECMWF cells around the grid point	Rainfall above threshold **Tg_max_rainfall**	Process and flag as point affected by heavy rain (**Fg_sc_rain.true**)
Sea surface types	Build a descriptor (or several flags) to indicate different ocean surface conditions	1) SST. Four ranges of SST (very low, low, medium, high) can be defined using **Tg_low_SST**, **Tg_medium_SST** and **Tg_high_SST** 2) SSS. Four ranges of SSS using **Tg_low_SSS**, **Tg_medium_SSS** and **Tg_high_SSS** 3) Wind speed. Flag according to WS below/above neutral wind **Tg_low_wind**, **Tg_medium_wind** or **Tg_high_wind**	1) Two booleans for SST range (**Fg_sc_low_SST** and **Fg_sc_high_SST**) (false:false) SST <= Tg_low_ SST (true:false) Tg_low_SST < SST < =Tg_medium_ SST (true:true) Tg_medium_ SST < ST <= Tg_high_SST (false:true) SST > Tg_high_SST 2) Same for SSS range using (**Fg_sc_low_SSS** and **Fg_sc_high_SSS**) 3) Same for wind speed classification using (**Fg_sc_low_wind** and

		4) Sea state development. To distinguish between 6 different classes according to altimetry and ECMWF WAM model (see SMOS ECMWF PreProcessor) 5) Presence of SSS and/or SST fronts in (or around) the grid point	**Fg_sc_high_wind**) 4) Sea state development described (see section 3.6) by **Fg_sc_sea_state_X.true** (X 1 to 6) 5) Two flags (see section 3.7) **Fg_sc_SST_front** and **Fg_sc_SSS_front**
Number of valid measurements	Use the counter of measurements accepted for SSS retrieval in this grid point	If number of measurements used **Dg_num_meas_valid** < threshold **Tg_num_meas_valid** flag grid point If < **Tg_ num_meas_min** do not perform retrieval	Flag grid point with **Fg_ctrl_num_meas_low.true** if below Tg_num_meas_valid (just for warning) and **Fg_ctrl_num_meas_min. true** if retrieval not performed
Number of outlier measurements	Use the counter of measurements flagged as outliers in this grid point	If number of outliers Dg_num_outliers / Dg_num_meas_l1c > **Tg_num_outliers_max**	Flag grid point **(Fg_ctrl_many_outliers.true)**
Number of RFI outlier measurements	Use the counter of measurements flagged as RFI outliers in this grid point	If number of RFI outliers Dg_RFI_L2/ Dg_num_meas_l1c > **Tg_num_RFI_max**	Flag grid point **(Fg_ctrl_suspect_RFI.true)**
Number of measur. flagged for sunglint	Use the counter of measurements flagged for sunglint in this grid point	If Dg_sunglint_2 / Dg_num_meas_l1c > **Tg_sunglint_max**	Flag grid point **(Fg_ctrl_sunglint.true)**
Number of measur. flagged for moonglint	Use the counter of measurements flagged for moonglint in this grid point	If Dg_moonglint / Dg_num_meas_l1c > **Tg_moonglint_max**	Flag grid point **(Fg_ctrl_moonglint.true)**
Number of measur. flagged for galactic noise	Use the counter of measurements flagged for galactic noise in this grid point	If (Dg_gal_noise_error + Dg_sky) / Dg_num_meas_l1c > **Tg_gal_noise_max**	Flag grid point **(Fg_ctrl_gal_noise.true)**
Number of measur. flagged for polarized galactic noise	Use the counter of measurements flagged for polarized galactic noise in this grid point	If Dg_gal_noise_pol / Dg_num_meas_l1c > **Tg_gal_noise_pol_max**	Flag grid point **(Fg_ctrl_gal_noise_pol.true)**
Missing ECMWF data	Check that all the ECMWF data necessary for the four retrievals are made available to the OS processor	1) Some parameter neded for SSS1 retrieval is missing in the grid point 2) Some parameter neded for SSS2 is missing 3) Some parameter neded	1) SS1 retrieval not performed **(Fg_ctrl_ECMWF_1.false)** 2) SS1 retrieval not performed **(Fg_ctrl_ECMWF_2. false)** 3) SS1 retrieval not performed **(Fg_ctrl_ECMWF_3. false)**

		for SSS3 is missing 4) Some parameter neded for Acard is missing	4) SS1 retrieval not performed (**Fg_ctrl_ECMWF_4. false**)

All grid points that have successfully passed the tests described in 3.1 will be flagged with **Fg_ctrl_valid**

3.2 Applied to each measurement on a grid point

Subject	Test	Threshold	Decision
Tb out of range	Based on first comparison default model vs. measure	Abs(Tb measure – Tb model) (h or v) > threshold (**Tm_out_of_range**), then flag *See note 1*	Discard measurements flagged (**Fm_out_of_range.true**)
Footprint size	Check resolution (i.e. major axis length) of footprint	Only measurements with Resolution < **Tg_resol_max_ocean** are used in the retrieval. Flag others	SSS retrieval is performed with selected measurements (**Fm_resol.false**) Set counters for the measurements not used due to this excess of resolution **Dg_num_high_resol**
L1 flags: Grid points position within Field of View	Grid points are classified by L1 as belonging to Alias Free FOV, Extended AF FOV and (being inside) near the border of it The definition of border will be configurable. First approach considers 30 km	Three counters will allow knowing how many measurements of each type have been recorded for a grid point **Dg_af_fov** **Dg_border_fov**	1) Grid points outside EAF _FOV will not be processed (if any) (**FmL1c_af_fov.true**) 2) Measurements outside AF_FOV may not be used (**FmL1c_af_fov.false**). A switch is to be implemented for activation in case these measurements appear to be of too poor quality 3) Border measurements are rejected (**FmL1c_border_fov. true**)
L1 flag: RFI	L1 will not apply a RFI static mask (difficult due to being angle dependent) but build a table that will be further filled	Affected measurements will be flagged and a counter for the grid point incremented **Dg_RFI_L1**	Measurements will be marked with L1_RFI flag (**Fm_L1c_RFI.true**) but this will not be considered to discard data (done through outliers detection)
Possible presence of ice	Test applied to measures on grid points within monthly climatological maximum extent of sea ice and SSTprior < Tg_Low_SST_ice	If Tb > Tbflat + **Tm_DT_ice** then the measure is considered as possibly contaminated by ice	The measurement is flagged (**Fm_suspect_ice**) and a counter for the grid point is incremented (**Dg_suspect_ice**) to be used later in the percentage comparison to the threshold **Tg_suspect_ice**
Outliers	See description of test in	For each outlier	Outliers are flagged and not

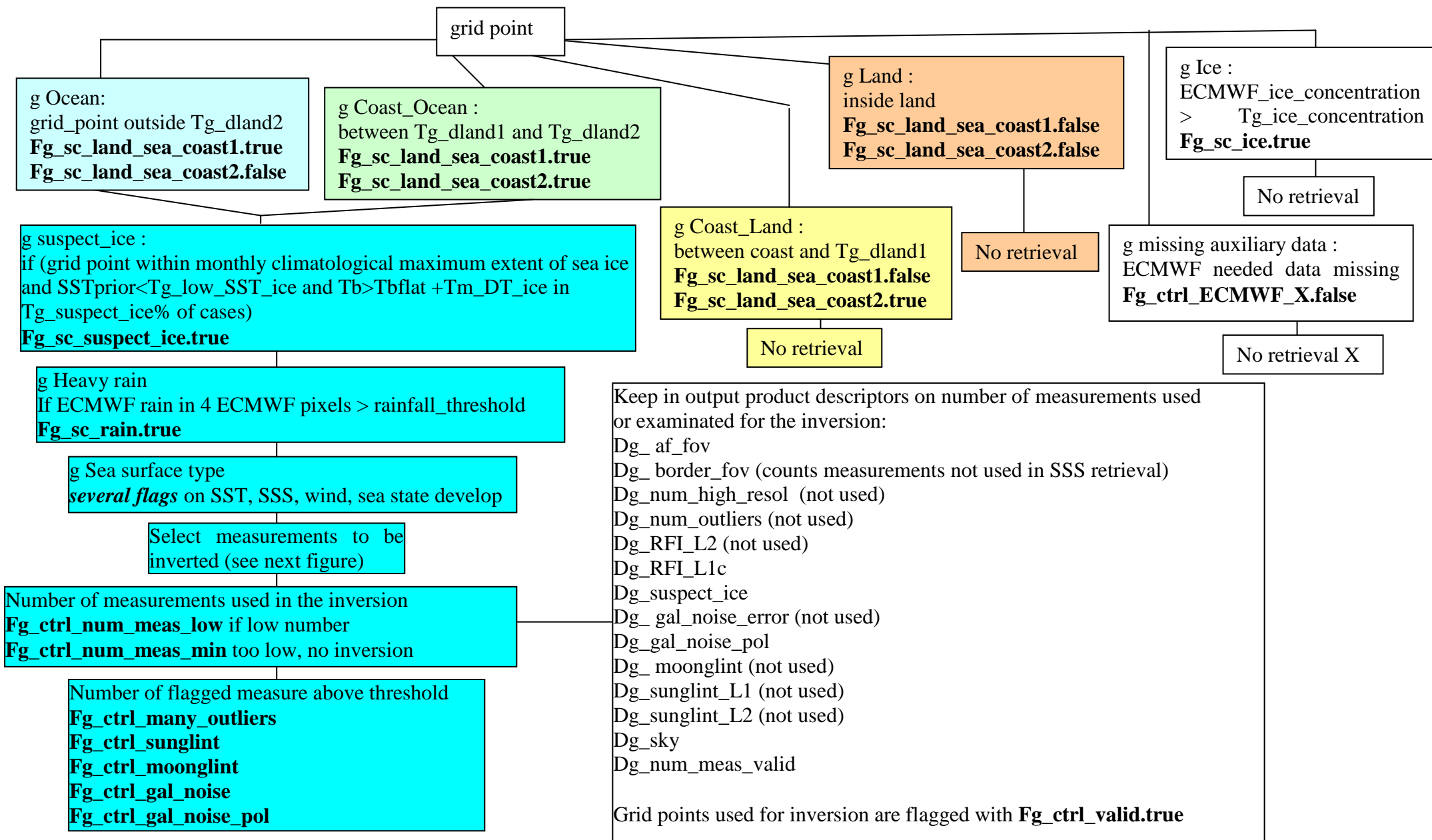|	section 3.4	measurement a counter is incremented for the grid point (**Dg_num_outliers**)	processed (**Fm_outlier.true**)
Sun contamination	L1C will provide information on sun contaminated measurements through the Fm_sun_fov and Fm_sun_point flags. These issummarized in a unique **Fm_L1c_sun.true** and counters set for the point Dg_sun_tails, Dg_sun_glint_area, Dg_sun_glint_fov	At L2 Sun glint IFREMER model will be applied and measurements will be classified as no glint, low glint, medium glint, high glint using two booleans **Fm_low_sun_glint Fm_high_sun_glint** and three thresholds (**Tm_high_sun_glint**, **Tm_low_sun_glint**, **Tm_medium_sun_glint**)	Measurements flagged with **Fm_L1c_sun.true** will not be processed Measurements classified at L2 as sun glint contaminated with intensity above **Tm_sun_limit** (that can coincide with the low, medium or high thresholds) will be flagged (**Fm_sun_limit.true**) and not processed Counters for discarded measurements as flagged in L1c and L2 **Dg_sunglint_L1, Dg_sunglint_L2**
Moon glint	Check angle between Target to Moon direction & specular direction	Flag if angle less than **Tm_angle_moon** and increment a counter **Dg_moonglint**	Not process flagged measurements (**Fm_moon_specdir.true**)
Galactic noise	Check galactic background error maps (potential error due to strong sources and error due to the centrosymmetrical WEF assumption), check convoluted polarization maps (Q_CSWeF & U_CSWeF)	1) If quadratic sum of all errors greater than **Tm_max_gal_noise_error** 2) If galactic noise greater than **Tm_high_gal_noise** 3) If |Q_CSWeF| greater than **Tm_gal_noise_pol** or |U_CSWeF| greater than **Tm_gal_noise_pol**	1) If wind speed is below Tg_WS_gal, flag and do not use measurement in the retrieval (**Fm_gal_noise_error. true**) and increment a counter **Dg_gal_noise_error** 2) Flag (**Fm_high_gal_noise.true**), and count (**Dg_sky**) measurements with specular direction toward a strong galactic source 3) Flag (**Fm_gal_noise_pol.true**) and count (**Dg_gal_noise_pol**) measurements with specular direction toward a polarized source.

All measurements that have successfully passed the tests described in 3.2 will be flagged with **Fm_valid** (see diagram in page 32) and used for the SSS retrieval in the concerned grid point. When the Measurement discrimination concludes that in a grid point no retrieval is performed, the corresponding fields in the Output Product will be set to default (clearly differentiated) values.

Note 1: In the three cases (Tb out of range, possible presence of ice, outliers detection) where measured Tb has to be compared with modelled values under the same configuration (viewing geometry, sea surface conditions) we have to deal with values at antenna level (measured) and values at surface (modelled). To simplify the tests we can just perform the tests with Th+Tv (first Stokes parameter) and using the default roughness model plus simplified corrections (atmospheric, galactic) that will allow a clear identification of measurements to be discarded, although not providing high quality modelled Th and Tv for SSS retrieval
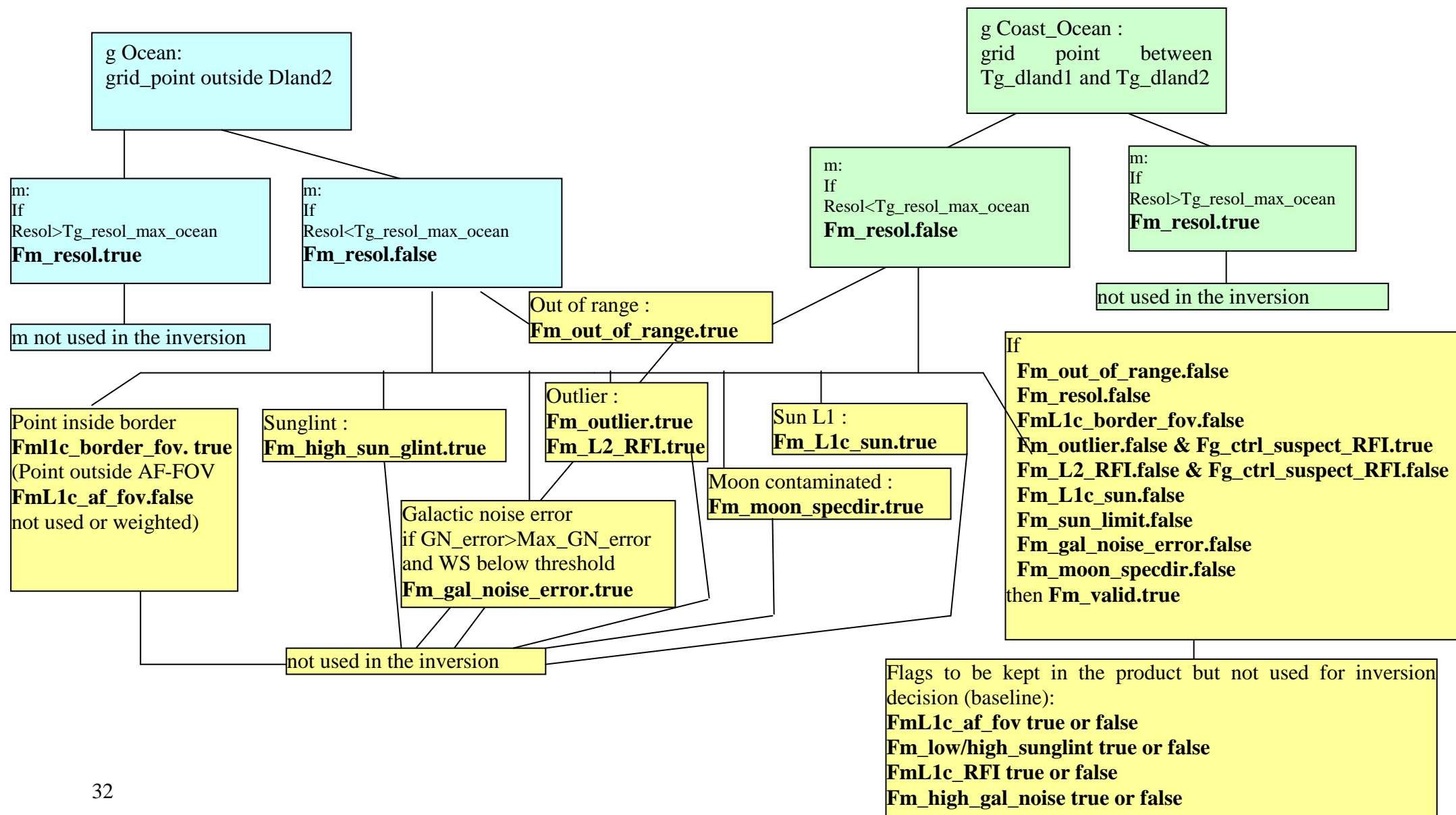
3.3 General diagram

In the following diagram the conceptual application of the measurement discrimination is schematised.

Classification of grid point:

grid point

g Ocean:
grid_point outside Tg_dland2
Fg_sc_land_sea_coast1.true
Fg_sc_land_sea_coast2.false

g Coast_Ocean :
between Tg_dland1 and Tg_dland2
Fg_sc_land_sea_coast1.true
Fg_sc_land_sea_coast2.true

g Land :
inside land
Fg_sc_land_sea_coast1.false
Fg_sc_land_sea_coast2.false

g Ice :
ECMWF_ice_concentration
>   Tg_ice_concentration
Fg_sc_ice.true

No retrieval

g suspect_ice :
if (grid point within monthly climatological maximum extent of sea ice and SSTprior<Tg_low_SST_ice and Tb>Tbflat +Tm_DT_ice in Tg_suspect_ice% of cases)
Fg_sc_suspect_ice.true

g Coast_Land :
between coast and Tg_dland1
Fg_sc_land_sea_coast1.false
Fg_sc_land_sea_coast2.true

No retrieval

g missing auxiliary data :
ECMWF needed data missing
Fg_ctrl_ECMWF_X.false

No retrieval

No retrieval X

g Heavy rain
If ECMWF rain in 4 ECMWF pixels > rainfall_threshold
Fg_sc_rain.true

g Sea surface type
several flags on SST, SSS, wind, sea state develop

Select measurements to be inverted (see next figure)

Number of measurements used in the inversion
Fg_ctrl_num_meas_low if low number
Fg_ctrl_num_meas_min too low, no inversion

Number of flagged measure above threshold
Fg_ctrl_many_outliers
Fg_ctrl_sunglint
Fg_ctrl_moonglint
Fg_ctrl_gal_noise
Fg_ctrl_gal_noise_pol

Keep in output product descriptors on number of measurements used or examined for the inversion:
Dg_ af_fov
Dg_ border_fov (counts measurements not used in SSS retrieval)
Dg_num_high_resol (not used)
Dg_num_outliers (not used)
Dg_RFI_L2 (not used)
Dg_RFI_L1c
Dg_suspect_ice
Dg_ gal_noise_error (not used)
Dg_gal_noise_pol
Dg_ moonglint (not used)
Dg_sunglint_L1 (not used)
Dg_sunglint_L2 (not used)
Dg_sky
Dg_num_meas_valid

Grid points used for inversion are flagged with **Fg_ctrl_valid.true**

Selection of measurements to be inverted:

g Coast_Ocean :
grid point between Tg_dland1 and Tg_dland2

g Ocean:
grid_point outside Dland2

m:
If
Resol>Tg_resol_max_ocean
Fm_resol.true

m:
If
Resol<Tg_resol_max_ocean
Fm_resol.false

m:
If
Resol<Tg_resol_max_ocean
Fm_resol.false

m:
If
Resol>Tg_resol_max_ocean
Fm_resol.true

m not used in the inversion

not used in the inversion

Out of range :
Fm_out_of_range.true

If
Fm_out_of_range.false
Fm_resol.false
FmL1c_border_fov.false
Fm_outlier.false & Fg_ctrl_suspect_RFI.true
Fm_L2_RFI.false & Fg_ctrl_suspect_RFI.false
Fm_L1c_sun.false
Fm_sun_limit.false
Fm_gal_noise_error.false
Fm_moon_specdir.false
then **Fm_valid.true**

Point inside border
Fml1c_border_fov. true
(Point outside AF-FOV
FmL1c_af_fov.false
not used or weighted)

Sunglint :
Fm_high_sun_glint.true

Outlier :
Fm_outlier.true
Fm_L2_RFI.true

Sun L1 :
Fm_L1c_sun.true

Moon contaminated :
Fm_moon_specdir.true

Galactic noise error
if GN_error>Max_GN_error
and WS below threshold
Fm_gal_noise_error.true

not used in the inversion

Flags to be kept in the product but not used for inversion decision (baseline):
FmL1c_af_fov true or false
Fm_low/high_sunglint true or false
FmL1c_RFI true or false
Fm_high_gal_noise true or false

3.4 Outliers detection

3.4.1. General approach for outlier detection

Measurement out of range: Detection of erroneous measurements (Tb) in a grid point.

Test : Comparison of each Tb measurement to one model and removal of Tb if:
abs((Tbmeas-Tbmodel) - median (Tbmeas-Tbmodel)) > *nsig* σTb

With: median computed using all Tb measured at same polarisation in the grid point
nsig typically equal to 5 (may be adjusted)
σTb=√ [(σTb_radiometric_noise)^{**2} + (σTb_model)$**2$]
σTb_model being an estimate of the error on the model
(first try: σTb_model =0.5 . Tbrough at nadir i.e. 50% error on roughness component; about 2K noise at 10m/s; a 0.2K increase of σTb for a 2.5K radiometric noise)

Advantages of this method:
-median is a robust estimator even with small number of measurements
-mean biases (model or intrument biases) removed
-Take into account corrections for atmosphere, galactic noise, incidence angle variations etc…

-When detecting Tg_num_outliers_max% of bad Tb in a grid point, flag the grid_point as 'possibly contaminated by land, ice or rain etc..' but do the SSS retrieval with the remaining Tb

3.4.2. RFI detection/mitigation

RFI over ocean areas (DEW line around the Arctic Circle, emissions from Island military bases such as Ascension Island, long range contamination from land based sources, etc) can have considerable impact on BT values. Detection of RFI outliers in the L2OS processor is performed by a two-step algorithm which first identifies grid points at risk of RFI contamination, and then applies a reduced outlier threshold to all measurements on these grid points. This algorithm is known to be sensitive to other sources of contamination (eg land and ice), and is therefore applied only in ocean areas far from land (>200 km). The RFI detection algorithm is applied independently for each measurement polarisation.

The standard deviation is computed over the whole dwell line and compared to 1.2 times of the theoretical standard deviation (i.e. the sum, over all measurements included in the dwell line, of the radiometric noise and the modelled error). The factor 1.2 corresponds to the 99% confidence interval. In case there is a risk of outlier, if the difference between the measured TB and the modelled TB are higher than 3 time of the radiometric noise, this measurement is discarded from the retrieval.

Step 1: identify for each grid point whether there is a risk of RFI outliers.

std_theory=$\sqrt{}$ (sum(radiometric_noise^2 + error_on_Tb_model^2) / number_meas)

risk_of_RFI = std(Tbmodel-Tbmeasurement) > *RFI_std* * std_theory

where *RFI_std* = 1.2 (estimated assuming we have 100 measurements, the 99% confidence interval on std_theory computed from these 100 stds would be 0.18 std_theory so putting a factor=1+0.2 seems reasonable).

Step 2: if risk_of_RFI:

for each measurement
   if abs(TBmodel[pol] - TBsmos[pol]) > *RFI_nsig* * radiometric_noise
      Fm_L2_rfi.true

where *RFI_nsig* = 3 (nsig is reduced from 5, non-RFI outlier detection threshold)

Dg_RFI_L2 = count(Fm_L2_rfi.true)
if (Dg_RFI_L2 / Dg_num_meas_L1c) > *Tg_num_RFI_max* then
   Fg_ctrl_suspect_rfi.true

where *Tg_num_RFI_max* = 50%

Following application of the RFI detection algorithm, measurement discrimination makes use of one of two outlier tests – this avoids false detection of RFI in areas where BT values are noisy (eg rain, near ice):

if Fg_ctrl_suspect_rfi.true then
   if Fm_L2_rfi then
      Fm_valid.false
else use non-RFI outlier test
   if Fm_outlier then
      Fm_valid.false

When detecting Tg_num_RFI_max% of bad Tb in a grid point, flag as 'possibly contaminated by RFI' but do the SSS retrieval with the remaining Tb.

3.5. Sunglint contamination

3.5.1. Theoretical description

3.5.1.1. Physics of the problem

Beyond geophysical sources of error, Yueh et al. [1] noticed that the solar radiations pose a significant challenge for the remote sensing of ocean surface salinity. The sun is indeed an extremely strong radiation source at L-band, exhibiting a time-dependent blackbody temperature that ranges between 100000 K and 10 million K, depending on the solar activity [2] and the next solar maximum is expected in 2010, that is 3 years after SMOS launch. Two distinct mechanisms may contribute to the solar radiation intercepted by a radiometer antenna: one is the reflection of sun radiations by the earth-surface (sunglitter effects) and the other is the direct leakage into the antenna. Here, we only focussed on the modeling for the reflected contamination over the ocean, direct contaminations being addressed by the Level 1 processor.

In [3a, 3b], it was shown that the centre of the sun's glitter pattern will never be located in the area of SMOS' synthesized field of view. However the expected range of surface wind speeds (zero wind is very uncommon) will cause the sun's glitter pattern to spread within the alias free field of view which might contamine the useful measured signals. More specifically, frequent pixel contaminations are expected around winter solstices when the the centre of the sun's glitter pattern will lye close to the right-hand border of the FOV.

Experimental evidences of the sunglitter strong impacts on the passive microwave sensing of the ocean using L-band radiometers was first given by Swift [4] in 1974, who analyzed the forward scattering of sun microwave radiations from the Cape Code Canal in Massachusetts. Data were collected at 1.4, 4.0, and 7.5 GHz for horizontal and vertical polarization at a fixed nadir viewing angle of 40°. As the sun passed through the main beam of the antennas, Swift found that the excess temperature due to reflected solar radiation increased dramatically with decreasing frequency and was polarization dependent. The sun was found to be such a dominating source at 1.4 GHz that the horizontally polarized component saturated the radiometer.

As shown by Wentz [5], these sun-glitter effects might be modelled using approximate scattering models to compute the forward scattering of the sun radiations from the rough water surface. Sun glitter does not occur frequently in practice. However, when it does, this phenomenon may have severe effects on the brightness temperature signals measured by spaceborne L- band radiometers.

If an incremental rough sea surface area dA located within the MIRAS antenna field of view is illuminated by the sun radiations along the direction of the unit vector $\vec{n}_i$, part of the intercepted energy might be scattered in the direction $\vec{n}_s$, i.e., toward the radiometer antenna. The solar energy scattered by dA in the direction $\vec{n}_s$ at time t is represented by the radiometric temperatures $T_{ss}(\vec{n}_s,t)$, given for h and v-polarization respectively by:

$$T_{ss}(\vec{n}_s, h, t) = \frac{1}{4\pi \cos\theta_s} \int_0^{2\pi} \int_0^{\beta_{sun}/2} \left[\sigma^o_{hh}(\vec{n}_s, \vec{n}_i) + \sigma^o_{hv}(\vec{n}_s, \vec{n}_i) \right] T_{sun}(\vec{n}_i, t) d\Omega_i$$

$$T_{ss}(\vec{n}_s, v, t) = \frac{1}{4\pi \cos\theta_s} \int_0^{2\pi} \int_0^{\beta_{sun}/2} \left[\sigma^o_{vv}(\vec{n}_s, \vec{n}_i) + \sigma^o_{vh}(\vec{n}_s, \vec{n}_i) \right] T_{sun}(\vec{n}_i, t) d\Omega_i$$

(1)

where $\sigma^o_{hh}, \sigma^o_{vv}, \sigma^o_{vh}$ and $\sigma^o_{hv,}$ are the bistatic scattering coefficients of the sea surface at 1.4 GHz for HH, VV, VH and HV polarizations, respectively, at scattered direction $\vec{n}_s$ and incident direction $\vec{n}_i$. The scattering elevation angle is denoted θ_s. The integration limits is over the solid angle subtented by the sun where $\beta_{sun}/2$ is the angular radius of the sun as viewed from the earth. At 1.4 GHz, $\beta_{sun}/2 \approx 0.293°$, which is 10% greater than the optical angular radius [6]. $T_{sun}(\vec{n}_i, t)$ is the brightness temperature of the sun at 1.4 GHz in the direction $\vec{n}_i$ and at time t.

Equations (1) show that in order to estimate the contamination due to sunglint temperature at a given SMOS pixel with node corresponding to position T on the earth surface, determined by the latitude ϕ and longitude ψ of the observer, and at a given time t, the following parameters are needed:

1) $\vec{n}_i$: the direction (incidence and azimuth angles) of sun radiations at the considered earth surface position and time T =(ϕ, ψ, t),

2) $\vec{n}_s$: the direction (incidence and azimuth angles) of observation from MIRAS at target T=(ϕ, ψ, t)

3) $T_{sun}(\vec{n}_i, t)$: the brightness temperature of the sun at 1.4 GHz in the direction $\vec{n}_i$ and at time t, and,

4) $\sigma^o_{hh}, \sigma^o_{vv}, \sigma^o_{vh}$ and $\sigma^o_{hv,}$: the bistatic scattering coefficients of the sea surface for HH, VV, VH and HV polarizations, respectively, at scattered direction $\vec{n}_s$, incident direction $\vec{n}_i$, and corresponding to the sea state conditions at target T=(ϕ, ψ, t).

Parameters 1) can be obtained from accurate ephemerides and parameters 2) are easily deduced from SMOS observation geometry. The main difficulties in estimating $T_{ss}(\vec{n}_s, t)$ therefore consist in providing accurate estimates for the brightness temperature of the sun at 1.4 GHz and for the sea surface bistatic coefficients at L-band. The brightness temperature of the sun at 1.4 GHz being considered here as an auxiliary parameter, we ony focussed on the physical description of the bistatic coefficients model.

In the present algorithm, the bistatic scattering coefficients of the rough sea surface needed in Equations (1) are estimated using the Small Slope Approximation theory ([7], [8]), which is known to work well from moderate to high incidence angles ($40° \leq \theta_i \leq 80°$). The lower order-approximation (referred to as the SSA-1) is used here and is appropriate for both large-

(the Kirchhoff regime) and small scale (the Bragg regime) roughness within a single theoretical scheme.

The calculation yields the following expression for a dimensionless scattering cross section $\sigma^{o}{}_{\alpha\alpha_{o}}$ for scattering of the wave of polarization α into the wave of polarization α_{o}:

$$\sigma^{o}{}_{\alpha\alpha_{o}}(\vec{n}_{s},\vec{n}_{i}) = \frac{1}{\pi}\left|\frac{2q_{k}q_{i}}{q_{k}+q_{i}}B_{\alpha\alpha_{o}}(\vec{n}_{s},\vec{n}_{i})\right|^{2}e^{-(q_{k}+q_{i})^{2}\rho(0)}\iint\left\{e^{\left[(q_{k}+q_{i})^{2}\rho(\vec{r})\right]}-1\right\}e^{\left[-i(\vec{n}_{s}-\vec{n}_{i})\cdot\vec{r}\right]}d\vec{r} \quad (2)$$

where (q_{k},q_{i}) represent the vertical projections of the wave vectors and the kernel functions $B_{\alpha\alpha_{o}}(\vec{n}_{s},\vec{n}_{i})$ are given in Appendix of [9]. These kernels are geometric functions of the dielectric constant: we used the Klein and Swift's model [10] to estimate the dielectric constant of sea water at L-band.

Here, the function $\rho(\vec{r})$ is defined by the relation:

$$\langle\exp[iQ(h(\vec{r}_{1})-h(\vec{r}_{2}))]\rangle = \exp[-Q^{2}(\rho(0)-\rho(\vec{r}_{1}-\vec{r}_{2}))]$$

where <…> means averaging over the space homogeneous statistical ensemble of sea surface roughness, described by the surface elevation signal $h(\vec{r}_{1})$, and $Q = q_{k}+q_{i}$. For Gaussian statistics ρ represents the correlation function of roughness and can be expressed strictly in terms of a roughness spectrum:

$$\rho(\vec{r}) = \int_{0}^{2\pi}\int_{0}^{\infty}W(\vec{k})\exp\left[i\,\vec{k}\cdot\vec{r}\right]d\vec{k}$$

where $W(\vec{k})$ is the directional wavenumber spectrum of the rough sea surface at surface wavenumber vector $\vec{k}$.

In the present work, sea surface statistics is assumed Gaussian and ρ is obtained from the sea surface spectrum model of Kudryavtsev al. [11]. In our approach, the calculation of $\sigma^{o}{}_{\alpha\alpha_{o}}$ is performed using an azimuthal harmonic decomposition for the autocorrelation function. Moreover, to calculate accurately the autocorrelation function, we introduced a sufficiently dense net on the surface wavenumber vector plane within the range $10^{-3} \leq k \leq 10^{3}$ rad/m, applying a uniform step with respect to *log(k)* rather than to *k*.

3.5.2. Mathematical description

3.5.2.1 Simplified scattered solar radiation contributions

An additional model simplification is used to estimate the amount of solar energy scattered by the sea surface and impinging the MIRAS antenna. We assumed than within the solid angle subtended by the sun as seen from any of the observed terrestrial targets, the local sun direction $\vec{n}_{i}$ is almost constant, so that, at any target *T*, the radiometric sunglint temperatures $T_{ss}(\vec{n}_{s},\alpha)$ of a sunglint Stokes vector component, can be approximated locally at polarization α, by:

$$T_{ss}(\vec{n}_s, t, \alpha) \approx \frac{T_{sun}(t)\,\Omega_{sun}}{4\pi \cos\theta_s} \left[\sigma^o_{\alpha\alpha}(\vec{n}_s, \vec{n}_i) + \sigma^o_{\alpha\alpha_o}(\vec{n}_s, \vec{n}_i) \right] \qquad (3)$$

where $\vec{n}_s$ and $\vec{n}_i$ are the local MIRAS observation and sun illumination directions at target T, respectively. Ωsun is the solid angle intercepting the sun as seen from the earth, and with $\beta_{sun}/2 \approx 0.293°$ at 1.4 GHz:

$$\Omega_{sun} = 2\pi \left[1 - \cos(\beta_{sun}/2) \right] = 8.2 \times 10^{-5}\ sr$$

To evaluate $T_{ss}(\vec{n}_s, \alpha)$ using equation (3) at a given earth position and time, one need the following parameters as inputs:

1) $[\theta_i, \phi_i]$ the local sun angles (incidence and azimuth angles) at the considered earth surface position and time, given by T =(ϕ, ψ, t);

2) $[\theta_s, \phi_s]$ the local observation angles (incidence and azimuth angles) from MIRAS antenna at target T=(ϕ, ψ, t)

3) $T_{sun}(t)$: the brightness temperature of the sun at 1.4 GHz and at time t,

4) the following ocean surface parameters at target T=(ϕ, ψ, t).:

   a) the prior sea surface salinity SSS [psu],
   b) the sea surface temperature SST [°C],
   c) the wind speed velocity at 10 meter height u_{10} [m/s], and,
   d) the wind direction φ_u [in rad].

Assuming that the main factors influencing the spread and intensity of the sunglint pattern will be the sun brightness temperature, the wind velocity and direction, we assume for the processor algorithm constant values for SSS=35 psu and for SST=15°C.

3.5.2.2 Efficient Implementation of Bistatic scattering coefficients at L-band

Bistatic scattering coefficients are functions of 6 variables:

• incoming radiation incidence angle θ_i

• incoming radiation azimuth angle ϕ_i

• outgoing azimuth angle ϕ_s

• outgoing incidence angle θ_s

• wind speed u_{10}

• wind direction φ_w (towards which the wind is blowing)

In the Level 2 processor, bistatic scattering coefficents are calculated based on Look-Up Tables (LUT). From LUT size and generation perspectives, it is impractical produce a LUT directly as a function of the six previously listed variables. Therefore, we make use of an

efficient implementaion of the lookup table for bistatic scattering coefficients in which we have separated the dependency on wind direction from the dependencies on other variables, without introducing further approximations. As detailed in [13], the 2-fold integration (2) can indeed be reduced to a 1D integral using azimuthal harmonics decomposition of the integrand in polar coordinates. Using harmonic decompositions of the bistatic scattering coefficients, we can write

$$\sigma_{\alpha\alpha_o}(\vec{n}_s,\vec{n}_i,u_{10},\varphi_w)=\sum_{m=0}^{\infty}\sigma_{\alpha\alpha_o}^m(\vec{n}_s,\vec{n}_i)\cos2m(\Phi_{si}-\varphi_w), \qquad (4)$$

where we have explicitly included the dependence of the final scattering coefficients on the wind speed u_{10} and wind direction φ_w and where the scattering coefficient harmonics $\sigma_{\alpha\alpha_o}^m(\theta_i,\phi_s-\phi_i,\theta_s,u_{10})$ are independent of wind direction. Moreover, these harmonics only depend on the incoming and scattered radiation incidence angles, the wind speed, and difference between the incoming and scattered radiation azimuth angles. The angle Φ_{si} is the angle of the difference between the scattered and incident wavevectors, and can be written as

$$\Phi_{si}(\theta_i,\phi_i,\phi_s,\theta_s)=\tan^{-1}\left(\frac{q_{Hy}}{q_{Hx}}\right)=\tan^{-1}\left(\frac{\sin\theta_s\sin\phi_s+\sin\theta_i\sin\phi_i}{\sin\theta_s\cos\phi_s+\sin\theta_i\cos\phi_i}\right).$$

Thus, switching from vector notation to angles, we can write the scattering coefficients as

$$\sigma_{\alpha\alpha_o}(\theta_i,\phi_i,\phi_s,\theta_s,u_{10},\varphi_w)=\sum_{m=0}^{\infty}\sigma_{\alpha\alpha_o}^m(\theta_i,\phi_s-\phi_i,\theta_s,u_{10})\cos2m(\Phi_{si}-\varphi_w), (5)$$

For processing issues, we provide a four dimension lookup table for the harmonic coefficients $\sigma_{\alpha\alpha_o}^m(\theta_i,\phi_s-\phi_i,\theta_s,u_{10})$ for even azimuthal wavenumbers m=0 through 10 on a discrete grid.

An interpolation method is then needed to infer the bistatic scattering coefficients harmonics from the LUT. It is found that linear interpolation introduces artifacts in all dimensions, but especially in incidence angle dimensions whereas a cubic Hermite interpolation method remove these problems. The basic idea behind the method is to ensure continuity of the first derivative of the interpolating function. To accomplish this, a four point stencil along each dimension surrounding the interpolation point is required, so in four dimensions we obtain a 256 point stencil, but the nature of the method is such that one can compute the coefficients once for all harmonics and reuse the weights, saving a large amount of processing time.

To implement the method, we apply the interpolation scheme separately along each of the four LUT dimensions and then combine all of the weights into a set of 256 weights. In a given dimension, we consider the four nearest points (i.e., the stencil) surrounding the point at which we desire a value, say x. We assume that these points can be written as x_{k-1}, x_k, x_{k+1}, and x_{k+2}, where x is between x_k and x_{k+1}. Next, we assume that our interpolating function is a cubic of the form

$$p(\mu)=a+b\mu+c\mu_2+d\mu_3, \qquad (1)$$

where

$$\mu=\frac{x-x_k}{x_{k+1}-x_k} \qquad (2)$$

and the coefficients depend upon the discrete function values at lookup table grid points. In the actual implementation, for a given interpolation location, a weight for each the

four stencil points is computed based on the value of μ, which by definition ranges from 0 to 1. If we define

$$a_o = 2\mu^3 - 3\mu^2 + 1$$
$$a_1 = \mu^3 - 2\mu^2 + \mu$$
$$a_2 = \mu^3 - \mu^2 ,$$
$$, a_3 = -2\mu^3 + 3\mu^2 \tag{3}$$

then the weights for the four surrounding points are

$$w_{k-1} = -\frac{1}{2}a_1$$
$$w_k = a_0 - \frac{1}{2}a_2$$
$$w_{k+1} = a_3 + \frac{1}{2}a_1 \tag{4}$$
$$w_{k+2} = \frac{1}{2}a_2$$

and the final expression for the interpolated value at point x is

$$p(x) = \sum_{j=k-1}^{k+2} w_j y_j, \tag{5}$$

where y_j are values from the lookup table along the given dimension.

Near boundaries, where the stencil exceeds the boundary of the lookup table, zero normal gradient extrapolation is applied along each of the four LUT dimensions, so that it is assumed that lookup table values extend beyond the table boundaries with the values at the boundaries.

As a final step, one need to implement the sum over the harmonics, given specific values for the incoming and scattered azimuths and wind direction. As it has been found that only the first few harmonics contribute significantly to the scattering coefficients, the sum is over only the first six even harmonics (including wavenumber 0), so that the processor shall computes

$$\sigma_{\alpha\alpha_o}(\theta_o,\phi_o,\phi_s,\theta_s,u_{10},\varphi_w) = \sum_{m=0}^{5} \sigma_{\alpha\alpha_o}^m(\theta_o,\phi_s-\phi_o,\theta_s,u_{10})\cos 2m(\Phi_{si}-\varphi_w).$$

3.5.3. Error budget estimates

Main sources of errors in the estimation of $T_{ss}(\vec{n}_s,\alpha)$ using Eq. (3) will be

✓ Errors on the estimation of the bistatic scattering coefficients of the sea surface at L-band, and

✓ Errors on the estimation of the sun brightness temperature at 1.4 GHz the SMOS time of acquisition.

An estimate of the errors on the modelling of the bistatic scattering coefficients of the sea surface at L-band can be based on the errors on the asymptotic electromagnetic, namely the SSA-1 approximation. SSA-1 gives qualitatively correct 3D bistatic scattering coefficient when compared to exact numerical simulation using the Method of Moment with a general

agreement between SSA-1 and MoM within 3dB in VV and within 1.5 dB in HH polarizations [12]. In average, SSA-1 overestimate HH and underestimates VV so that SSA-1 systematically overestimates the H/V ratio with a mean of order +20%. The errors on the sea surface roughness statistics are difficult to estimate but will clearly have an important impact as well.

A complete error budget estimate can not be provided without any estimate of the error on the auxiliary sun brightness temperature data at 1.4 GHz. If it comes out of L1 processor, we need an error budget on the estimate of that parameter from L1.

3.5.4. Practical considerations

3.5.4.1. Calibration and validation

Dedicated CAL/VAL activities should be envisaged for the SMOS sunglint model with two main components:

-an earth-based campaign aiming at measuring precisely the sunglint scattering at L-band (e.g., experiment similar to [4]), with high-quality concomitant auxiliary solar fluxes measurements at 21 cm as well as surface roughness information to calibrate and validate the bistatic-scattering coefficient models.

-a SMOS-data based analysis. Re-analysis of all flagged pixels and brightnesses for which good quality (close in time and space) co-localized auxiliary wind and solar flux data at 21 cm are available shall be performed to assess the efficiency of the model.

3.5.4.2. Quality control and diagnostics

Assuming the major source of error in the model shall be the estimation of the sun brightness temperature at 1.4 GHz, quality control and diagnostics will strongly depend on the accuracy for that auxiliary data.

If it comes out of L1 processor (without a priori geophysical input), a complementary quality check shall be performed for that auxiliary data using earth-based solar flux measurements available at 1.4 GHz. These are available from sun-tracker radiometers by the US Air Force, at Sagamore Hill (Massachusetts), since 1966. They can be obtained through the National Geophysical Data Center at Boulder, Colorado. These data sets also include other solar fluxes measurements conducted at 1415 MHz since 1988 from radiometers in Palehua (Hawaii), San Vito (Italy) and Learmonth (Australia), and 1GHz data are also collected daily at Nobeyama Radio Observatory (Japan). If high temporal resolution solar fluxes can be obtained, the closest data in time from SMOS acquisitions shall be used to monitor quality controls, as sun brightness temperature values might evolve very significantly over short time scales. The so-called R-components of the sun brightness temperature indeed consist of the second and minute-duration bursts produced by the active sun components: sunspots (manifestations of magnetically disturbed conditions at the sun's visible surface), flares (huge explosions on the surface of the sun) and other transient activity. This high-temporal varaibility of the sun signals might strongly affect the quality of the forward model estimates.

3.5.4.3. Exception handling

If there is no estimation of the sun brightness temperature at 1.4 GHz output from L1 processor (e.g., sun eclipsed by MIRAS), there is a need for other source of that auxiliary data.

If some parameter goes out of LUT range during the retrieval, a flag (Fg_OoR_Sunglint_dim2_ThetaSun, Fg_OoR_Sunglint_dim3_Phi, Fg_OoR_Sunglint_dim4 _Theta, Fg_OoR_Sunglint_dim52_WS) is raised. No extrapolation is done and the boundary value is taken.

3.5.5. Assumption and limitations

First assumption in the model is that within the solid angle subtented by the sun as seen from any of the observed terrestrial targets, the local sun direction $\vec{n}_i$ is almost constant. This is not a strong assumption. However, it is as well assumed that the sun brightness temperature at 1.4 GHz is not polarized and homogeneous within the solar disc. This is known to be unrealistic [2] and certainly will limitate somehow the applicability of the predicted sunglint pattern polarized features.

Another source of limitation is the bistatic coefficient modeling. The SSA-1 approximation is by essence a first-order small slope perturbation approach so that it is not expected to correctly estimate the roughness impact for sea surfaces exhibiting large slopes and most importantly, large curvature. Therefore, is it expected to fail in strong frontal conditions (strong wave-wave, wave-current or wind-wave interaction conditions) and does not account for breaking wave and foam impacts. Moreover, the sea surface state model (i.e. Kudryavtsev et al) is only accounting for wind seas and should be valid only for wind seas generated by winds stronger than about 2 m/s and less than 15 m/s. Out of these limits, it is not expected that the physics of air-sea interaction is correctly accounted for.

Therefore, we do not expect the model to perform well in presence of either strong swells, strong currents, very small and unsteady winds as well as stormy conditions. We expect however that accounting for the impact of waves on the drag coefficients will help better characterizing the impact of these parameters on roughness.

References

[1] S. H. Yueh, R. West, W. J. Wilson, F. K. Li, E. G. Njoku, and Y. Rahmat-Samii, Error sources and feasibility for microwave remote sensing of ocean surface salinity, *IEEE Trans. Geosci. and Remote Sens.*, vol. 39, no. 5, pp. 1049-1060, 2001.

[2] G. A. Duck and D. E. Gary, The sun at 1.4 GHz, *Astron. Astrophys.*, vol. 124, pp. 103-107, 1983.

[3a] N. Reul, WP1500: support for solar effects in "Retrieval Concept and Architecture Document for Sea Surface Salinity Retrieval for SMOS mission", ref. SMOS-TN-ACR-LOD-001, Issue 1, Revision 2, Dated 17/08/2004. Appendix A (contract CCN-2 of 16027/02/NL/GS)

[3b] B. Picard, N. Reul, P.Waldeufel, and E. Anterrieu, "*Impacts of Solar Radiations on sea surface salinity remote sensing from Synthetic Aperture Imaging Radiometers*", Proceedings of IGARRS 2004.

[4] C. T. Swift, Microwave radiometer measurements of the Cape Cod Cannal, *Radio Sci.*, vol. 9, no. 7, pp. 641-653, 1976.

[5] F. Wentz, The forward scattering of microwave solar radiation from a water surface, *Radio Sci.*, vol. 13, no. 1, pp. 131-138, 1978.

[6] J. Aarons, *Solar System Radio Astronomy*. Plenum, 1965.

[7] A. G. Voronovich, Small-slope approximation in wave scattering by rough surfaces, *Sov. Phys.-JETP*, vol. 62, pp. 65-70, 1985.

[8] A. G. Voronovich, Small-slope approximation for electromagnetic wave scattering at a rough interface of two dielectric half-spaces, *Waves in Random Media*, vol. 4, pp. 337-367, 1994.

[9] A. G. Voronovich and V. U. Zavorotny, Theoretical model for scattering of radar signals in ku and c-bands from a rough sea surface with breaking waves, *Waves in Random Media*, vol. 11, pp. 247-269, 2001.

[10] Klein L.A., and C.T. Swift, An improved model for the dielectric constant of sea-water at microwave frequencies, *IEEE Trans. Antennas and Propag.*, AP-25, 1043-111, 1977.

[11] Kudryavtsev V.N., Makin V.K. and Chapron B., Coupled sea surface-atmosphere model. 2. Spectrum of short wind waves, *J. Geophys. Res*, C4, 7625-7639, 1999.

[12] N Reul, CA Guerin, G. Soriano, E. Bachelier, P. Borderies, F. Mattia, C. Ruiz and N. Floury, "On the Use of Rigorous Microwave Interaction Models to Support Remote Sensing of Natural Surfaces" , ESA contract 17335/03/NL/AG, 2005.

[13] N. Reul, J. Tenerelli, B. Chapron and P. Waldteufel, « Modeling Sun glitter at L-band for the Sea Surface Salinity remote sensing with SMOS", submitted to IEEE TGRS, 2006.

3.6 Sea state development

The classification of sea state development at each grid point in 6 classes (Fg_sc_sea_state_X, X = 1 to 6) is indicated in section 3.1 to be done from altimeter data and ECMWF wave model. At present there is no established or tested methodology to derive this information and will be investigated in the framework of SMOS reprocessing.

As first approach the SMOS SSS L2 processor will implement a flag computation derived only from ECMWF data, using three of the auxiliary variables: significant wave height (Hs), significant wave height of wind waves (Hsw), and inverse wave age (Ω).

For each grid point the fraction of swell will be computed as (Hs-Hsw)/Hs. The highest value (1) would mean that there are no wind waves, then all the waves are due to presence of swell. The lowest value (0) corresponds to significant wave height only due to wind waves, then no presence of swell. Establishing a threshold value **Tg_swell**, for example equal to 0.5, allows classifying all grid points as swell dominated (fraction above threshold) or wind waves dominated (below threshold).

For the inverse wave age two thresholds (**Tg_old_sea** and **Tg_young_sea**) will allow classifying the wave age in three ranges: old, medium and young according to the parameter Ω being lower than Tg_old_sea, between Tg_old_sea and Tg_young_sea, or above Tg_young_sea.

Finally the combination of the two criteria allows the definition of the six classes of sea state development. The corresponding flags are set to true according to the table:

Flag set to true	Fraction of swell	Inverse wave age
Fg_sc_sea_state_1	below Tg_swell	below Tg_old_sea

Fg_sc_sea_state_2	above Tg_swell	below Tg_old_sea
Fg_sc_sea_state_3	below Tg_swell	between Tg_old_sea and Tg_young_sea
Fg_sc_sea_state_4	above Tg_swell	between Tg_old_sea and Tg_young_sea
Fg_sc_sea_state_5	below Tg_swell	above Tg_young_sea
Fg_sc_sea_state_6	above Tg_swell	above Tg_young_sea

3.7 Temperature and salinity fronts

The classification of grid points using science flags (see 3.1) requires a method to decide whether a grid point is on the vicinity of a temperature or salinity surface front. Different approaches can be used, and no preference has been selected during the development of the SMOS L2 SSS prototype processor.

A provisional solution is proposed in this section from the SST and SSS prior values used in the iterative convergence step (section 4.14):

A length scale is defined to calculate the horizontal gradient around each grid point (**Radius_front**) and two thresholds will indicate a strong gradient in SST and SSS values (**Tg_SST_front** and **Tg_SSS_front**).

1) Point flagged with presence of temperature front
For each grid point, the SST priors corresponding to all the DGG nodes, which centres are at less than Radius_front from the concerned point, are collected. The differences $|SST_i - SST_j|$ for all i,j pairs of collected values are computed and divided by the distance between centers d_{ij}. If at least one of these gradients is above Tg_SST_front then the grid point is considered to be near a temperature front and the flag Fg_sc_SST_front is raised.

2) Point flagged with presence of salinity front
The same procedure is applied collecting SSS values and using Tg_SSS_front as threshold. The points that have at least one difference above the threshold are classified as affected by a salinity front and Fg_sc_SSS will be raised.

4. Algorithm description

In the following sections it is necessary to take into account that polarised brightness temperature (of a plane wave measured by a radiometer) can be described through the polarisation vector $[T_b] = [T_{hh}, T_{hv}, T_{vh}, T_{vv}]$ in the Earth reference frame and $[T_{xx}, T_{xy}, T_{yx}, T_{yy}]$ in the antenna reference;

or through the Stokes vector $[I, Q, U, V]$, where:

I, first Stokes parameter, is the sum of both perpendicularly polarised T_b, H-pol + V-pol ($T_{hh}+T_{vv}$ or $T_{xx}+T_{yy}$, depending on the reference) and represents the total power transported by the wave

Q, second Stokes parameter, is their difference V-pol – H-pol ($T_{vv}-T_{hh}$ or $T_{yy}-T_{xx}$), and represents the linear polarisation oriented in the reference direction

U, third Stokes parameter, is the difference between linear polarisation components oriented in +45° and -45°; it is related to cross-polarisations by $U = T_{xy}+T_{yx} = T_{hv}+T_{vh}$

V, fourth Stokes parameter, is interpreted as the difference between left-hand and right-hand circularly polarised brightness temperature; all measurements indicate that it is negligible at L-band, so for most applications V is assumed to be 0.

Most of times, instead of the Stokes vector, the modified Stokes vector $[T_1, T_2, T_3, T_4]$ ($[T_{hh}, T_{vv}, U_{Earth}, V_{Earth}]$ or $[T_{xx}, T_{yy}, U_{antenna}, V_{antenna}]$) is used, as it is composed by the quantities actually measured by a fully polarised radiometer:

[modified Stokes vector] $= \lambda^2/kB\eta$ $[<|E_H|^2>, <|E_V|^2>, 2Re<E_V E_H^*>, 2Im<E_V E_H^*>]$

where λ is the radiometer's wavelength, k the Boltzmann constant, B the bandwidth, and η the medium impedance (air). E_H and E_V are the two orthogonal components of the plane wave.

To avoid any misunderstanding with other parameters used throughout this document we will designate the modified Stokes vector by [A1, A2, A3, A4] in the antenna reference (instead of Level 1 output[T_{xx}, T_{yy}, T_{xy}], with A1=T_{xx}, A2=T_{yy}, A3=2Re(T_{xy}), A4=2Im(T_{xy})) and [T_h, T_v, T_3, T_4] in the Earth reference (instead of [T_{hh}, T_{vv}, U_{Earth}, V_{Earth}]). This convention was adopted as part of the harmonisation activities in L2 processors development (see annex: SMOS L1c product requirements for sea surface salinity retrieval at level 2, 28/4/05).

4.1. Flat sea

4.1.1. Theoretical description

4.1.1.1. Physics of the problem

The brightness temperature can be expressed as the sum of two terms; the brightness temperature in the case of completely flat sea and the additional brightness temperature (ΔTb) due to the surface roughness, as follows:

$$[4.1.1] \quad T_{b,p}(\theta, SST, SSS, P_{rough}) = T_{b\ Flat,p}(\theta, SST, SSS) + \Delta T_{b\ rough,p}(\theta, SST, SSS, \overrightarrow{P_{rough}})$$

The first term is Tb due to the emission of a flat sea surface, which is well described by the Fresnel equations and is polarization dependent (p). The second term is the increment of brightness temperature due to sea roughness, which can be described through several parameters (P_{rough}) related to processes that modify this roughness. θ is the angle under which Tb is measured, SST is the sea surface temperature and SSS the sea surface salinity. ,

The brightness temperature is defined as:

$$T_b(\theta) = e(\theta) \cdot SST \qquad\qquad [4.1.2]$$

where $e(\theta)$ is the surface emissivity at L-Band which carries the major information regarding SSS. Assuming thermodynamical equilibrium, the Kirchoff laws applies and emissivity is considered equal to absorption, and equal to 1 – reflectivity.

It can be written, as follows:

$$e(\theta, \phi) = 1 - \Gamma(\theta, \varepsilon, \phi, roughness) \qquad\qquad [4.1.3]$$

where Γ is the reflectivity, which is dependent on the incident radiation nadir angle θ, on the complex dielectric constant of sea water ε ($\varepsilon'+j\varepsilon''$), the azimuth angle ϕ, the roughness and the polarisation.

In the case of a smooth surface sea, the reflectivity can be calculated straighforward using the Fresnel reflection laws, and providing an accurate dielectric constant model.

The Fresnel reflection coefficients R, for each polarisation, are defined as function of the sea water dielectric constant and the incidence angle, as follows:

$$Rh = \left| \frac{\cos\theta - \sqrt{\varepsilon - \sin^2\theta}}{\cos\theta + \sqrt{\varepsilon - \sin^2\theta}} \right|^2$$

$$Rv = \left| \frac{\varepsilon\cos\theta - \sqrt{\varepsilon - \sin^2\theta}}{\varepsilon\cos\theta + \sqrt{\varepsilon - \sin^2\theta}} \right|^2$$

[4.1.4]

Therefore Th and Tv for a flat surface are computed as:

$$Th_{flat}(\theta, SST, SSS) = (1 - Rh(\theta, \varepsilon)) \cdot SST$$
$$Tv_{flat}(\theta, SST, SSS) = (1 - Rv(\theta, \varepsilon)) \cdot SST$$

[4.1.5]

The complex dielectric constant of the sea water is dependent on temperature and on the concentration of salt. It can be calculated at any frequency, within the microwave band, from Debye (1929) expression:

$$\varepsilon = \varepsilon_\infty + \frac{(\varepsilon_s - \varepsilon_\infty)}{1 + i\omega\tau} - i\frac{\sigma}{\omega\varepsilon_0}$$

[4.1.6]

in which i is the imaginary number, ε_∞ is the electrical permittivity at very high frequencies, ε_s is the static dielectric constant, τ is the relaxation time, σ is the ionic conductivity, and ε_0 is the permittivity of free space. ε_s, τ and σ are functions of the temperature and salinity of sea-water, and have been evaluated by Klein and Swift (1977), Ellison et al. (1998) and Blanch and Aguasca (2004).

After some comparisons and analysis (Camps et al., 2004; Wilson et al., 2004), the Klein and Swift dielectric constant model has been agreed to be the model that better expresses this parameter and is the one presented here.

The term ΔTb_{rough} is described by 3 different models in sections 4.2, 4.3 and 4.4.

4.1.1.2. Mathematical description of algorithm

Some of the parameters in eq. 4.1.4 can be expressed through polynomial functions of salinity (SSS in the case of SMOS) in psu (practical salinity units, UNESCO, 1978) and water temperature in °C

$$\varepsilon_s = \left(m(0) + m(1)T + m(2)T^2 + m(3)T^3\right)$$
$$\left(m(4) + m(5)T \cdot SSS + m(6)SSS + m(7)SSS^2 + m(8)SSS^3\right)$$

[4.1.7]

$$\tau = \left(t(0) + t(1)T + t(2)T^2 + t(3)T^3\right)$$
$$\left(t(4) + t(5)T \cdot SSS + t(6)SSS + t(7)SSS^2 + t(8)SSS^3\right)$$

[4.1.8]

$$\sigma = SSS\big(s(0) + s(1)SSS + s(2)SSS^2 + s(3)SSS^3\big)$$
$$\exp((T - 25)(s(4) + s(5)(25 - T) + s(6)(25 - T)^2 \qquad\qquad [4.1.9]$$
$$- SSS(s(7) + s(8)(25 - T) + s(9)(25 - T)^2)))$$

The values of these parameters are provided in SMOS TGRD document. The present version considers the model provided by Klein and Swift (1977), but this will be modified if a more accurate model is available before SMOS launch

The dielectric constant ε is computed following equation [4.1.6] and a complex value results.

4.1.1.3. Error budget estimates (sensitivity analysis)

ε_∞ has an error of 20% but this is negligible at L-band.

Cox quotes that the ionic conductivity of the sea water, σ, has an error of ± 0.03% for salinities between 30 and 40 psu, which is also negligible.

The static permittivity, ε_s, has a maximum per cent error of 0.49 with respect the measurements, and an average per cent error of 0.11.

The relaxation time, τ, has been derived from measurement with an accuracy of $2.12*10^{-13}$ and this is the assumed error for that parameter.

Ho's estimated error for ε' is 0.2%.

Taking ε =75 + j42, which is the approximate value of the dielectric constant of the sea water at 1.43 GHz when SSS=20 psu and T=20ºC, it then follows that the error associated with this particular choice is:

δε ≅ 1.15(δε'+δε'')10^{-3}

Using the above mentioned values, δε' ≈ 0.15 and δε'' ≈ 0.13. Hence, the error in the brightness temperature with T=293K is

δTb = δe*T ≅ 0.09 K

4.1.2. Practical considerations

4.1.2.1. Calibration and validation

S. Blanch, from the Polytechnic University of Catalonia (UPC), is preparing a new laboratory experiment to compute the parameters that describe the dielectric constant following the Debye expression. Results of this experiment will be used to validate the Klein and Swift

model. If any change or tuning of the parameters is necessary this should be applied to the model, and the corresponding coefficients file modified accordingly.

4.1.2.2. Quality control and diagnostics

We expect that the SMOS Cal/Val activities will provide, after commissioning phase, further information on the quality of the model, and if necessary new values to improve it

4.1.2.3. Exception handling

There is no particular exception handling in the mathematical algorithm except if the following auxiliary data are not provided by the processor or exceed the ranges: SST, SSS, incidence angles at SMOS pixel. In that case the computation could not be done.

4.1.3. Assumption and limitations

The measurements on which the Klein & Swift model has been based, were obtained from NaCl solutions and some from real sea water samples. Few measurements were done on the salinity range from 30-40 psu, which are the most common values in the world's ocean. However the authors confirm that the model should be valid for sea waters that have a salinity range between 3 and 35 psu. However, until a new model is established and validated, the SMOS and Aquarius communities agreed on using Klein and Swift.

References

Blanch, S. and Aguasca, A. (2004). Seawater dielectric permittivity model from measurements at l-band. Proceedings of IGARSS 2004, Alaska.

Camps, A., Font, J., Gabarró, C., Miranda, J., Obligis, E., Labroue, S., Boone, C., Sabia, R., Vall-llosera, M., Reul, N., June 2004. WP1100, ESTEC ITT 1-4505/03/NL/Cb

Debye, P. (1929). Polar Molecules. New York: Reinhold.

Ellison, W., Balana, A., Delbos, G., Lamkaouchi, K., Eymard, L., Guillou, C., and Prigent, C. (1998). New Permittivity Measurements of Sea Water. Radio Science, 33(3):639–648.

Klein, L. and Swift, C. (1977). An Improved Model for the Dielectric Constant of Sea Water at Microwave Frequencies. IEEE Transactions on Antennas and Propagation, AP-25(1):104–111.

Swift, C. (1980). Passive Microwave Remote Sensing. Boundary-layer Meteorology, 18:25–54.

UNESCO (1981) The Practical Salinity Scale 1978 and the International Equation of State of Seawater 1980. 10th report of the Joint Panel on Oceanographic Tables and Standards. UNESCO Technical Papers in Marine Science, 36

Wilson, W., Yueh, S., Dinardo, S., and Li, F. (2004). High stability l-band radiometer measurements of saltwater. IEEE Transactions on Geoscience and Remote Sensing, 42(9):1829–1835.

4.2. Surface roughness 1: two-scale model

4.2.1. Theoretical description

For a complete description of the model, the reader should refer to (Yueh, 1997).

4.2.1.1. Physics of the problem

By definition, sea surface brightness temperature, T_b, in the direction defined by the incident angle θ and the azimuth angle ϕ is:

$T_b(\theta, \phi) = SST \cdot e(\theta, \phi)$,

where e is sea surface emissivity and SST is sea surface temperature. Assuming thermodynamical equilibrium, the Kirchhoff law applies and $e = a = 1 - \Gamma$, where a and Γ are sea surface absorptivity and reflectivity respectively. The so-called modified Stokes vector is written as

$$\overrightarrow{T_b} = \begin{bmatrix} Th \\ Tv \\ T3 \\ T4 \end{bmatrix} = SST. \left(\begin{bmatrix} 1 \\ 1 \\ 0 \\ 0 \end{bmatrix} - \vec{\Gamma} \right) \tag{1}$$

where Tv and Th are T_b in vertical and horizontal polarisations (hereafter V- and H-pol) respectively, related to first and second Stokes parameters by $I = Tv + Th$ and $Q = Tv - Th$ respectively, and $T3$ and $T4$ are the third (U) and fourth (V) Stokes parameters respectively. Due to the sea surface not being flat, scattering induced by sea waves slightly modifies the reflectivity from Fresnel's equations. Consequently, Γ depends not only on incidence angle θ and sea water dielectric constant (and in turn on SST and SSS) but also on ϕ and shape of the surface, i.e. the roughness.

The sea surface is never flat, with roughness at very different scales being created by local and instantaneous wind and/or distant wind (inducing swell), as well as by wave interactions. Roughness at sea surface scatters impinging electromagnetic waves and consequently modifies reflection from Fresnel's equation. Numerical rigorous solution of Maxwell's equations is not considered as they cannot be resolved explicitly. There is two widely-used approximated models, the two scales model and the so-called one-scale small slopes approximation. A simpler approach based on geometric optics (GO) (*Stogryn* (1967), *Prigent and Abba* (1990)) is discarded for use at low frequency. Indeed, whereas at high frequencies (i.e. in the millimeter domain) waves smaller than λ_0 (the radiometer wavelength) have a negligible contribution and all ocean waves can be considered as large-scale, simulations at 21 cm showed that a significant signal is induced by small scales and that a large part of roughness-induced signal is not predicted by GO (*Dinnat et al, 2002b*). Noticeably, GO predicts very small roughness effect on T_b at nadir and moderate incidence angles, in contradiction with observations from *Hollinger* (1971), *Swift* (1974), *Webster and Wilheit* (1976), *Camps et al.* (2004a) and *Etcheto et al.* (2004), as well as those from *Blume et al.* (1977) at 2.65 GHz. Note that it is very unlikely that the observed T_b variations correlated with wind speed variations are due to foam only, because they were observed also at small

wind speed WS and the trend was close to linear in WS (in the limit of measurements precision).

4.2.1.1.1. Electromagnetic model

In the two-scale model, surface is modelled as the superimposition of small waves upon large waves, roughness scales being parted into small and large scales by a cutoff wavelength λ_c. Small scales are sea waves whose height is small compared to λ_0 and large scales are waves whose curvature radius is large compared to λ_0. Below we summarize main elements of the two scale model of *Yueh* (1997). The reader should refer to the original paper for a complete description.

To derive Tb, one combines both large and small scales by integrating contributions of all large waves over the slopes domain (Sx, Sy) and weighting contributions by the slopes probability density function (PDF) of the large waves (P(Sx, Sy)). It follows that

$$\text{Tb sea}(\theta,\phi) = \iint T_{b,l}(\theta,\phi)P(S_x,S_y)(1 - S'_x \tan\theta)dS_x dS_y$$

where P is assumed to be Gaussian, and its width depends on the mean square slope (MSS) of the large-scale waves, S'x and S'y are the surface slopes along and across the radiometer azimuth observation direction, respectively. Local brightness temperature for a large wave ($T_{b,l}$) differs from Tb *flat* because (1) incidence and azimuth angles are modified because of the large wave's tilting, resulting in local incidence and azimuth angles (θ_i, ϕ_i), and (2) diffracting small-scale roughness is present on the large wave. Hence, Tb is expressed as

$$T_{b,l}(\theta_i, \phi_i) = SST \cdot (1 - R_{ss}(\theta_i, \phi_i)) \ . \ (6)$$

where R_{ss} = Rc+Ri is reflectivity of small-scale roughness covered surface, separated into a coherent (Rc) and an incoherent (Ri) component. The incoherent term, that accounts for waves impinging from non specular direction and scattered toward the radiometer, according to first order small-perturbation method (SPM1, *Rice* (1951)) is written as:

$$R_i(\theta_l,\phi_l) = \int_0^{\Pi/2} \sin\theta_\alpha \, d\theta_\alpha \int_0^{2\Pi} \frac{\cos\theta_\alpha}{4\Pi\cos\theta_l} \begin{bmatrix} \gamma_{hhhh} + \gamma_{hvhv} \\ \gamma_{vvvv} + \gamma_{vhvh} \\ 2\operatorname{Re}(\gamma_{vhhh} + \gamma_{vvhv}) \\ 2\operatorname{Im}(\gamma_{vhhh} + \gamma_{vvhv}) \end{bmatrix} d\varphi_\alpha \tag{2}$$

where γ functions are the bistatic scattering coefficients, dependent on sea surface power spectrum of small-scale roughness (W_{ss}).

The coherent term Rc, that expresses reflection and scattering of the power impinging from specular direction, is modeled using a second order small perturbation method (SPM2, *Yueh et al.* (1988)). Coefficients derived from SPM2 are (*Yueh,* 1997):

$$R_c(\theta,\phi) = \begin{bmatrix} \left|R_{hh}^{(0)}\right|^2 \\ \left|R_{vv}^{(0)}\right|^2 \\ 0 \\ 0 \end{bmatrix} + \int_0^{2\Pi} d\varphi_\alpha \int_0^\infty k_0^2 k_{\rho\alpha} W_{ss}(\vec{k_c}) \begin{bmatrix} 2\operatorname{Re}\{R_{hh}^{(0)*} g_{hh}^{(2)}\} \\ 2\operatorname{Re}\{R_{vv}^{(0)*} g_{vv}^{(2)}\} \\ 2\operatorname{Re}\{(R_{hh}^{(0)*} - R_{vv}^{(0)*})g_{vh}^{(2)}\} \\ 2\operatorname{Im}\{(R_{hh}^{(0)*} + R_{vv}^{(0)*})g_{vh}^{(2)}\} \end{bmatrix} dk_{\rho\alpha} \tag{3}$$

Johnson and Zhang (1999) introduce the unified equation that unifies R_i and R_c:

$$R_{ss} = \begin{bmatrix} \left|R_{hh}^{(0)}\right|^2 \\ \left|R_{vv}^{(0)}\right|^2 \\ 0 \\ 0 \end{bmatrix} + \underbrace{\int_0^\infty k_0^2 k_\rho' dk_\rho' \int_0^{2\Pi} W(k_\rho',\phi') \begin{bmatrix} g_h \\ g_v \\ g_3 \\ g_4 \end{bmatrix} d\phi'}_{\delta R_{ss}} = \begin{bmatrix} R_h(\theta_i,\phi_i) \\ R_v(\theta_i,\phi_i) \\ 0 \\ 0 \end{bmatrix} + \delta R_{ss} \qquad (4)$$

where the first term is the reflectivity of a flat sea, W is the surface power spectrum, $k_c = 2\Pi/\lambda_c$ is the cutoff wavenumber and g_p functions (p = v, h, 3 or 4) that account for both coherent and incoherent contributions to δR_{ss}, the correction to flat sea reflectivity induced by small-scale waves. Expanding physical quantities in a Fourier series with respect to azimuth direction, and under the assumption of even symmetry for surface roughness, one has:

$$\delta R_{ss} = \delta R_{ss,0} + \delta R_{ss,2} f(2\phi_0) \qquad (5)$$
$$C(k, \phi) = C_0(k) + C_2(k) \cos(2\phi_0) \qquad (6)$$
$$g_p = g_{p,0} + g_{p,2} f(2\phi_0) \qquad (7)$$

where f is cosine function for Tv and Th and sine function for T3 and T4, $C(k,\phi) = k^4 W(k,\phi)$ is the 2D surface curvature spectrum. Therefore, the omnidirectional component ($\delta R_{ss,0}$) and second harmonic amplitude ($\delta R_{ss,2}$) result from weighted integrals of the respective harmonics of the curvature spectrum:

$$\delta R_{ss,0} = \int_{kc/k0}^\infty C_0(k_\rho'). \begin{bmatrix} g'_{h,0} \\ g'_{v,0} \\ g'_{3,0} \\ g'_{4,0} \end{bmatrix} d\xi \qquad (8)$$

and

$$\delta R_{ss,2} = \int_{kc/k0}^\infty C_2(k_\rho'). \begin{bmatrix} g'_{h,2} \\ g'_{v,2} \\ g'_{3,2} \\ g'_{4,2} \end{bmatrix} d\xi \qquad (9)$$

where $\xi = k/k0$ and $g'_{p,n} = g_{p,n}/\xi$ are scattering weighting functions given by *Johnson and Zhang* (1999).

Dinnat and Drinkwater (2004) assessed the relative influence of the various scales on Tb from above weighting functions. Similarly to the radar case, there is a specific range of wavelengths (i.e. typically around λ_0) that contributes most to Tb, particularly when θ is small. However, significant additional contributions arise also from various scales especially at large θ. **Therefore, good knowledge of roughness is required over a wide range of scales (typically from 1 m to 2 cm).**

4.2.1.1.2. Sea surface roughness model

In the following Tb is decomposed as:

Tb=Tb flat + Tb rough   (10)

Where Tb flat is Tb modelled for a flat sea and Tb rough is the signal induced by the roughened sea.

Sea surface roughness is described using a 2D surface power spectrum $W(k_{p'}, \phi')$, i.e. a Fourier transform of the autocorrelation function of sea surface height, that appears in *Rc* and *Rss* equations and implicitly in *Ri*, or using 2D curvature spectrum $C(k, \phi)$ that appears in $\delta R_{ss,0}$ and $\delta R_{ss,2}$ equations. ψ is also used in the composite model to compute large-scale MSS that defines the slopes probability density function (PDF) of the large waves (P) used in Tb equation. There exists in literature many very different wave spectrum models (e.g. *Durden and Vesecky* (1985), *Donelan and Pierson* (1987), *Apel* (1994), *Yueh*(1997), *Elfouhaily et al.* (1997), *Lemaire* (1998), *Kudryavtsev et al.* (1999)...). In the following we focus on DV model as it has been widely used to simulate T$_{brough}$ at L-band and it simulates Tbrough in good agreement with campaign measurements provided it is multiplied by a factor2. Table 1 summarizes Irough (=Tb rough,v+Tb rough,h) sensitivity to wind speed, as found from 2-scale model and DV2 spectrum and derived from various campaigns:

Table 1 : Irough sensitivity to wind speed, for wind speed above 3m/s: theoretical models without foam and measurements

	dI/dWS	Incidence angle	Reference
SPM model + 2x Durden and Vesecki wave spectrum	0.45K/m/s	0-50°	ESA 14273/00/NL/DC study
Hollinger measurements	0.35K/m/s	20-70°	(Hollinger 1971)
WISE measurements	0.4K/m/s May decrease to 0.3K/m/s at 55° depending on wind height corrections (*Camps et al.*, 2004)	25-55°	(Etcheto, Dinnat et al. 2003; Camps, Font et al. 2004)
Eurostarrs measurements Mediterranean transit	0.5K/m/s Assuming dTh/dWS=dTv/dWS (NB: if it is not true, dI/dWS should be larger)	21.5 and 38.4°	(Etcheto, Dinnat et al. 2004)
Cape Cod Canal measurements	0.5K/m/s Assuming dTh/dWS=dTv/dWS (NB: if it is not true, dI/dWS should be lower)	23°	(Swift 1974; Sasaki, Asanuma et al. 1987)
JPL Gulf Stream Flights	0.6K/m/s	40°	(Yueh, West et al. 2001)

The *Durden and Vesecky* (1985) (hereafter DV) model is a semi-analytic spectrum, that relies onwork by *Pierson and Moskowitz* (1964) for gravity waves ranges, on *Phillips* (1977) for general form in equilibrium range, and that is fitted to HH-pol radar data at 13.9 GHz in order to account for deviation from the Phillips spectrum. The model is tuned to agree with *Cox and Munk* (1954) (hereafter CM) measured MSS. *Yueh* (1997) proposes to multiply the DV model by a factor 2 (hereafter DV2) to account for possible underestimation of MSS measured by *Cox and Munk* (1954), as suggested by *Donelan and Pierson* (1987) and *Apel*

(1994), and to better fit data at 19.65 and 37 GHz. It should be noted however that, if needed, the multiplying factor is quite uncertain, and Tbrough is directly proportional to this factor. Upwind/downwind T_b asymmetry is uncertain at L-band: using the empirical model for roughness asymmetry developed by *Yueh* (1997) from high frequency radiometric data, it is estimated to be up to ± 0.4 K at θ = 60° and WS = 8 m/s, and very small at moderate incidence angles. Upwind/crosswind asymmetry is very dependent on the spectrum model. Elfouhaily et al. (1998) model predicts asymmetry 3 times larger than DV2 model (and hence 6 times larger than DV), but still at most ± 0.3 K for WS = 10 m/s.

Sensitivity to roughness and model uncertainty studies are reported in *Dinnat et al.* (2003a). In this model, influence of roughness on Tb depends slightly on *SST* and *SSS*. Using a constant *SST* over the global ocean for estimating roughness effect would induce an error on retrieved *SSS* of the order of 0.5 psu between regions having SST differing by 30°C (the SSS effect is less important as a variation of 7 psu on SSS leads to a less than 0.1 psu error on retrieved *SSS*) (note that in reality, roughness and SST may be correlated especially close to fronts). **Therefore, $T_{b\,rough}$ dependence on *SST* should not be neglected in case of *SSS* retrieval in the context of largely variable *SST* , as for example for global ocean measurements** where there is a risk to introduce regional biases.
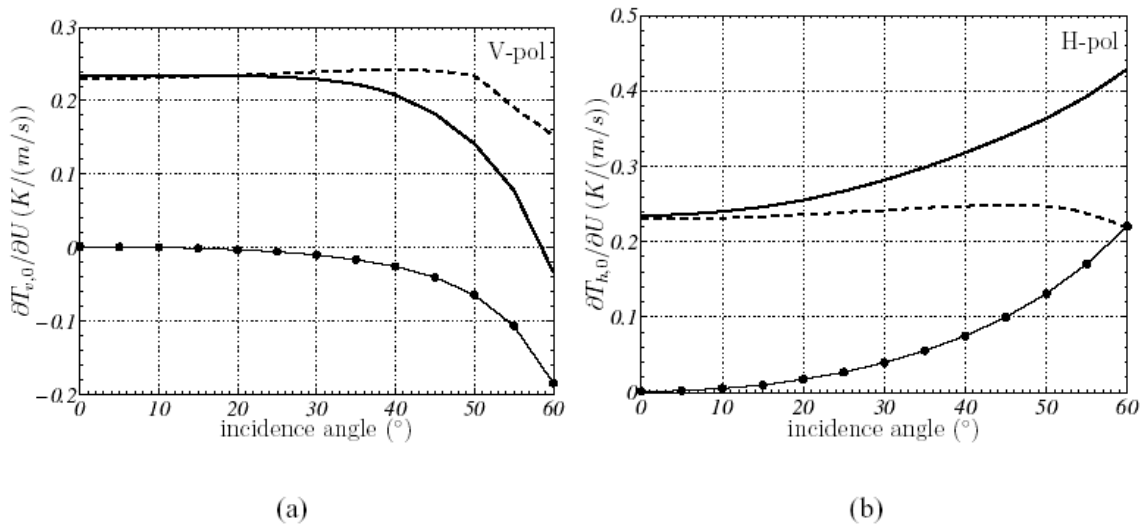
Figure 1: *Sensitivity of omnidirectional T_b to wind speed for (a) V-pol and (b) H-pol and SST = 15°C, SSS =36 psu, and WS = 8 m/s. Note that this sensitivity depends on WS, particularly for small wind speeds. Respective contribution of (dashed line) small and (dotted line) large scales to (plain line) total signal are illustrated. Model for sea spectrum is twice Durden and Vesecky (1985).*

Whatever the sea-surface spectrum model is, wind increases T_v and T_h for most incidence angles, by the order of a few tenths of a Kelvin per meter per second (see fig. 1 derived from DV2 spectrum). Sensitivity of T_v varies very slightly with θ up to 30°, where it starts to decrease to reach 0 close to 55°, and to become negative above. Sensitivity of T_h increases with incidence angle. These large sensitivity differences between V- and H-pol are due to the combination of large- and small-scale effect. Figure 1 also reports $T_{b\,rough}$ simulated taking into account only one of the two scales domain. Whereas the effect of small scales is an increase of roughly the same amount in T_v and T_h up to 50°, the effect of large scales is opposite in V and H-pol, and very dependent on θ. Therefore, the increase in T_h sensitivity with θ results from the addition of both scales effects, whereas the decrease in T_v sensitivity at large θ translates the increasing relative importance of large scales effects that counteract

small scales effect, θ ~55∘ being the incidence angle at which both scales effects cancel each other.

Nevertheless, it is of interest to note that **over most of the incidence angles measured by SMOS, the major contributors to Tb rough are the small scales.**

In the studies mentioned above, these small scales have been parametrized using WS assuming a neutral atmosphere (no air-sea temperature difference), i.e. a unique relationship between the friction velocity, U*, and WS. However this is usually not the case in the real world and atmospheric instability may create variations on the order of 5-10% on U*. Wind speed, WS, at an altitude z, and U* are classically related using the Monin-Obukhov equation:

$$WS(z) - u_c = \frac{U*}{\kappa}\left[\ln\left(\frac{z}{z0}\right) + \Psi\right]$$ (11)

where u_c is the surface velocity (i.e. the surface current), κ is von Karman's constant (normally assigned to a value of 0.4), z0 is the roughness length (often parametrized as a function of U* and possibly dependent on wave age, in meters), and Ψ is a function of the stabiility parameter z/L where L is the Monin Obhukov length that classically depends on temperature difference between air and sea, on SST and on relative humidity,

-or using a drag coefficient:

$$U*^2 / WS(10m)^2 = C_D$$ (12)

that depends on the above mentionned parameters.

In Dinnat's model, when looking at Tb rough as a function of WS or as a function of U* for variations of Cd of 5 to 12%, we observe that Tb rough better correlates to U* than with WS : on Figure 2 Tb rough simulations are presented for a 50° incidence angle (for which we expect the largest influence of both WS and U* because of the competitive effect of small and large scales (Fig.1)): nevertheless the correlation with U* is still much better than with WS and the scatter induced by the varying Cd is always less than 0.1K for a given U* (which is not true for a given WS).
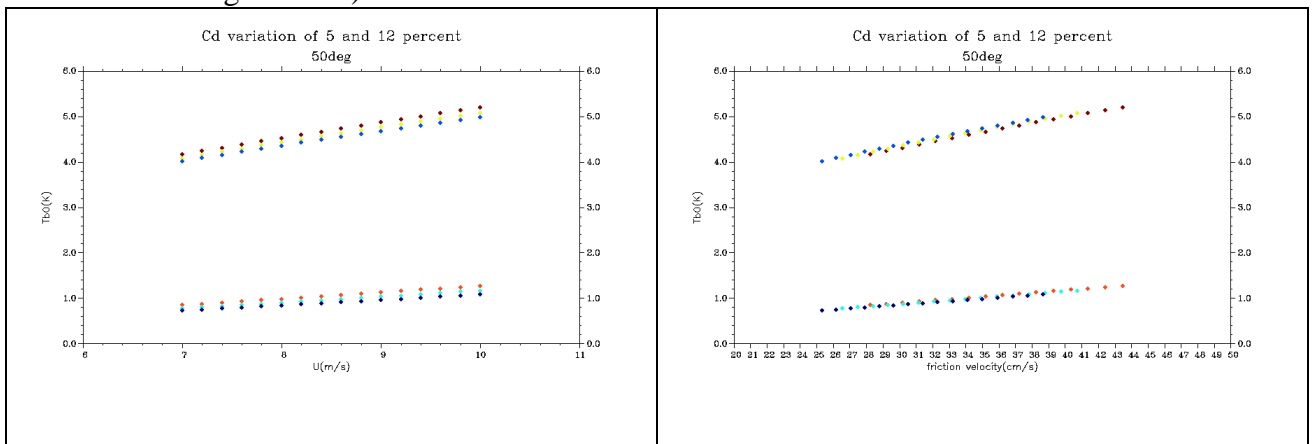
Figure 2: Tbrough0 (omnidirectional) at 50degree incidence angle in Vpol (bottom points) and Hpol(top points) as a function of wind speed (left) and as a function of U* (right) simulated for neutral conditions (blue points) and for Cd varying by 5% (yellow and light blue) and by 12% (red and brown).

Therefore, instead of parametrizing Tb rough variations as a function of WS only, we propose to relate them to U*, and to introduce the neutral equivalent wind speed parameter that is the parameter usually retrieved from scatterometer measurements.

Since scatterometer is primarily sensitive to U*, a neutral equivalent wind speed, WSn, has been introduced in the scatterometer community (Liu and Tang 1996) that represents the wind speed that would be measured at 10m height if the atmosphere were neutral and if the surface speed was zero:

$$WSn = \frac{U*}{\kappa}\left[\ln\left(\frac{10}{z0}\right)\right]$$ (13)

Given air-sea temperature differences and relative humidity observed over various regions of the open ocean, systematic differences of 0.5 to 1m/s over some particular regions may occur between WS and WSn (Liu and Tang 1996)(e.g. in the equatorial Pacific).

4.2.1.2. Mathematical description of algorithm

Since the model computation is very heavy, a tabulation of Tb rough will be provided. Tb rough is decomposed as the sum of an omnidirectionnal signal plus first and second harmonics:

$$Tb\ rough = \begin{bmatrix} Th0 + Th1\cos(\phi_a) + Th2\cos(2\phi_a) \\ Tv0 + Tv1\cos(\phi_a) + Tv2\cos(2\phi_a) \\ U1\sin(\phi_a) + U2\sin(2\phi_a) \\ V1\sin(\phi_a) + V2\sin(2\phi_a) \end{bmatrix}$$ (14)

where ϕ_a is the azimuth angle between wind direction (ϕ_w) and the azimuthal observation angle of radiometer look direction (ϕ_r): $\phi_a = \phi_w - \phi_r$ with all these angles counted counterclockwise, with origin on x axis (mathematical convention).

Tabulations of Th0, Th1, Th2, Tv0, Tv1, Tv2, U1, U2, V1 and V2 will be provided, as functions of incidence angle, SSS, SST, wind speed assuming a neutral atmosphere, WSn. We will assume that Tb rough can be entirely described using WSn In future versions, depending on:

-accuracy of ECMWF WS

-possibility of deducing a reliable U* from ECMWF WS and Tair-sea

-sensitivity of Tbrough to WS/U*

we could add dependency on WS.

It is proposed to use WSn components WSx and WSy from ECMWF to initialize the inversion. Wind speed and direction used to initialize Tb^{mod} values are deduced from WSx (positive eastward) and WSy (positive northward) as:

$$WSn = \sqrt{WSx^2 + WSy^2}$$

$\phi_w = \arctan(WSy/WSx)$

The tabulation will be provided for SSS between 30 and 40 psu, SST between 0 and 30°C, WSn between 2 and 30 ms^{-1}, and an incidence angle between 0 and 56 degrees. All the Tb rough are set to 0 for WSn=0. For the interpolation of the table, a switch allows to choose

between a linear interpolator (following the method described in TGRD) and a Hermite interpolator. The Hermite interpolation results in a continuous theoretical error on SSS, but is computationally heavy. The linear interpolation is faster, but it results in a discontinuity of the theoretical error on SSS, linked to the non-linearity of the model for wind speeds of 7 m/s.

If one of the prior values of the retrieved geophysical parameters is out of the LUT range, or if any retrieved geophysical parameters goes out of LUT range during the retrieval, different flags (Fg_OoR_Rough_dim1, Fg_OoR_Rough_dim2, Fg_OoR_Rough_dim3, Fg_OoR_Rough_dim4) are raised. No extrapolation is done and the boundary value is taken.

4.2.1.3. Error budget estimates (sensitivity analysis)

The advantage of retrieving WSn is that it is comparable to scatterometer derived wind speed. It would be of interest, before launch, to compare ECMWF WSn with scatterometer WS, in order to validate ECMWF WSn, and to decide the order of magnitude of differences between retrieved (from SMOS inversion) and first guess ECMWF WSn that are acceptable.

4.2.2. Practical considerations

4.2.2.1. Calibration and validation

It is likely that the factor 2 applied to the DV spectrum will need to be adjusted during the comissionning phase. Since Tb rough is proportionnal to this factor, the possibility of adjusting it should be kept.

Extrapolation of the tabulated values must be compared with model outputs to validate the extrapolation method.

4.2.2.2. Quality control and diagnostics

Values outside the min/max ranges given in the Tb rough tabulations should be deduced from a linear extrapolation of the two edge values of the tabulations (since most of the dependences are close to linear), except for low wind speed where Tb rough at WS between 0 and 2m/s should be deduced from a linear interpolation between 0 and Tb rough (2m/s). By default, the roughness correction is always applied (Fg_ctrl_roughness_M1.true). There is also the possibility (controlled by a switch based on a minimum wind speed Tg_WS_roughness_M1) that no roughness correction is applied in these low wind cases (due to lack of confidence in the model), and in such case a flag will be raised (Fg_ctrl_roughness_M1.false)

By default, no foam correction is applied and a flag is raised (Fg_ctrl_foam_M1.false). However, there is the possibility, controlled by a switch, that the foam correction is applied (Fg_ctrl_foam_M1.true). If wind speed is above a threshold (Tg_WS_foam_M1) the correction will be applied.

4.2.3 Assumption and limitations

In the present approach, surface speed (u_c) is neglected while studies like [*Kelly et al.,* 2001] evidence that current speed has an impact on scatterometer measurements in case of strong

currents gradients (equatorial Pacific); this issue will be studied in the future, including the best source for this auxiliar information.

Roughness is not necessarily related to local and instant wind only, and wind effects also imply its duration and action distance, as well as the presence of swell. These effects are not included in the present model but may be included in U* computation.
Additional phenomena are likely to cause noticeable modification of Tb. The first one is foam, that appears above a threshold wind speed, and whose permittivity largely differs from the one of sea water. During experimental campaigns it is very difficult to separate roughness and foam effect so that it is possible that the factor of 2 applied to DV spectrum is slightly overestimated but it was not possible using WISE and Eurostarrs data to demonstrate that dependence of Tb with respect to WS was non linear, implying that foam effect was weak. The second one, still to be investigated for L-band radiometry, is the presence of surface slicks of natural or non-natural origin. Slicks are known to damp roughness at specific scales, and their permittivity different from that of sea water might change T_b.

References

Blume, H.-J. C., A.W. Love, M. J. V. Melle, and W.W. Ho, Radiometric observations of sea temperature at 2.65 GHz over Cheasapeake Bay, *IEEE Transactions on Antennas and Propagation*, *AP-25*, 121–128, 1977.
Boutin, J., E. Obligis, and E. Dinnat, WP1120, Influence of Surface Roughness on Tb Simulated in L-Band by Yueh-LODYC Emissivity Model and by UCL Model - Analyse of the Differences, in*Scientific requirements and impact of space observation of ocean salinity for modeling and climate studies: final report*, NERSC technical report n_214 under contract n_14273/00/NL/DC European Space Agency, 2002.
Boutin, J., P. Waldteufel, N. Martin, G. Caudal, and E. Dinnat, Salinity Retrieved from SMOS Measurements over Global Ocean: Imprecisions Due to Surface Roughness and Temperature Uncertainties, *Journal of Atmospheric and Oceanic Technology*, *21*, 1432–1447, 2004.
Camps, A., et al., L-band sea surface emissivity: Preliminary results of the WISE-2000 campaign and its application to salinity retrieval in the SMOS mission, *Radio Science*, *38*, 2003.
Camps, A., et al., The WISE 2000 and 2001 field experiments in support of the SMOS mission: sea surface L-band brightness temperature observations and their application to sea surface salinity retrieval, *IEEE Transactions on Geoscience and Remote Sensing*, *42*, 804–823, 2004a.
Cox, C., and W. Munk, Measurement of the roughness of the sea surface from photographs of the sun's glitter, *Journal of the Optical Society of America*, *44*, 838–850, 1954.
Dinnat, E., J. Etcheto, J. Boutin, G. Caudal, A. Weill, A. Camps, J. Miller, and S. Contardo, Sea state influence on L-band emissivity in various fetch conditions, in *Geoscience and Remote Sensing Symposium,2002. IGARSS '02. 2002 IEEE International*, vol. 6, pp. 3632–3634, 2002a, tY - CONF.
Dinnat, E. P., De la d´etermination de la salinit´e de surface des oc´eans `a partir de mesures radiom´etriques hyperfr´equence en bande L, Ph.D. thesis, Universit´e Pierre et Marie Curie, Paris, France, 2003.
Dinnat, E. P., and M. Drinkwater, Optimizing the Active/Passive Synergy in the Frame of Sea Surface Salinity Retrieval from Microwave Measurements at L-Band, in *Proceedings MicroRad'04*, Rome, Italy, 2004.
Dinnat, E. P., J. Boutin, G. Caudal, J. Etcheto, and P. Waldteufel, Influence of sea surface emissivity model parameters at L-band for the estimation of salinity, *International Journal of Remote Sensing*, *23*, 5117–5122, 2002b.

59

Dinnat, E. P., J. Boutin, G. Caudal, and J. Etcheto, Issues concerning the sea emissivity modeling at L-band for retrieving surface salinity, *Radio Science*, *38*, 25–1–25–11, 2003a.

Dinnat, E. P., J. Boutin, G. Caudal, J. Etcheto, and S. Contardo, On the use of EuroSTARRS and WISE data for validating L-band emissivity models, in *First Results Workshop, EuroSTARRS/WISE/LOSACCampaigns, ESA SP-525*, pp. 117–124, ESTEC/European Space Agency, 2003b.

Donelan, M. A., andW. J. Pierson, Jr., Radar scattering and equilibrium ranges in wind-generated waves with applications to scatterometry, *Journal of Geophysical Research*, *92*, 4971–5029, 1987.

Donelan, M. A., F. W. Dobson, S. D. Smith, and R. J. Anderson, On the dependence of sea surface roughness on wave development, *Journal of Physical Oceanography*, *23*, 2143–2149, 1993.

Durden, S. L., and J. F. Vesecky, A physical radar cross-section model for a wind-driven sea with swell,*IEEE Journal of Oceanic Engineering*, *OE-10*, 445–451, 1985.

Etcheto, J., E. Dinnat, J. Boutin, A. Camps, J. Miller, S. Contardo, J. Wesson, J. Font, and D. Long,Wind Speed Effect on L-Band Brightness Temperature Inferred from EuroSTARRS and WISE 2001 Field Experiments, *IEEE Transactions on Geoscience and Remote Sensing*, *42*, 2206–2213, 2004.

Etcheto, J., E. Dinnat, J. Boutin, A. Camps, J. Miller, S. Contardo, J. Wesson, J. Font, and D. Long, Wind speed effect on L-band brightness temperature inferred from EuroSTARRS and WISE 2001 field experiments, *IEEE Transactions on Geoscience and Remote Sensing*, *42*, 2206-2214, 2004.

Hollinger, J. P., Passive microwave measurements of sea surface roughness, *IEEE Transactions on GeoscienceElectronics*, *GE-9*, 165–169, 1971.

Kelly, K.A., S. Dickinson, M.J. McPhaden, and G.C. Johnson, Ocean currents evident in satellite wind data, *Geophysical Research Letters*, *28*, 2469-2472, 2001.

Liu, W.T., and W. Tang, *Equivalent neutral wind*, 8 pp. JPL/NASA Publ. 96-17, 1 Aug. 1996.

Prigent, C., and P. Abba, Sea surface equivalent brightness temperature at millimeter wavelengths, *AnnalesGeophysicae*, *8*, 627–634, 1990.

Rice, S. O., Reflection of Electromagnetic Waves from Slightly Rough Surfaces, *Communications on Pure and Applied Mathematics*, *4*, 351–378, 1951.

Sasaki, Y., I. Asanuma, K. Muneyama, G. Naito, and T. Suzuki, The dependence of sea-surface microwave emission on wind speed, frequency, incidence angle and polarization over the frequency range 1 to 40 GHz, *IEEE Transactions on Geoscience and Remote Sensing*, *GE-25*, 138-146, 1987.

Stogryn, A., The apparent temperature of the sea at microwave frequencies, *IEEE Transactions on Antennas and Propagation*, *77*, 1658–1666, 1967.

Swift, C. T., Microwave radiometer measurements of the Cape Cod Canal, *Radio Science*, *9*, 641–653,1974.

Webster, W. J., Jr., and T. T. Wilheit, Spectral characteristics of the microwave emission from a winddriven foam-covered sea, *Journal of Geophysical Research*, *81*, 3095–3099, 1976.

Weill, A., T. Besnard, S. Contardo, J. Etcheto, and J. Boutin, WISE results from whitecapping andstereophotogrammetry: a tentative of superposition of topography and foam surface to retrieve active and fossil foam, in *First Results Workshop, EuroSTARRS/WISE/LOSAC Campaigns, ESA SP-525*, pp.89–94, ESTEC/European Space Agency, 2003.

Yueh, H. A., R. T. Shin, and J. A. Kong, Scattering of electromagnetic waves from a periodic surface with random roughness, *Journal of Applied Physics*, *64*, 1657–1670, 1988.

Yueh, S. H., Modeling of wind direction signals in polarimetric sea surface brightness temperatures, *IEEE Transactions on Geoscience and Remote Sensing*, *35*, 1400–1418, 1997.

Yueh, S. H., Estimates of Faraday rotation with passive microwave polarimetry for micrawave sensing of Earth surfaces, *IEEE Transactions on Geoscience and Remote Sensing*, *38*, 2434–2438, 2000.

Yueh, S. H., R. West, W. J. Wilson, F. K. Li, E. G. Njoku, and Y. Rahmat-Samii, Error sources and feasibility for microwave remote sensing of ocean surface salinity, *IEEE Transactions on Geoscience and Remote Sensing*, *39*, 1049–1060, 2001.

60

4.3. Surface roughness 2: Empirically modified SSA/SPM

4.3.1. Theoretical description

4.3.1.1. Physics of the problem

Polarimetric passive remote sensing involves measurement of all four modified Stokes parameters of the microwave thermal emission:

$$\begin{bmatrix} T_h \\ T_v \\ T_3 \\ T_4 \end{bmatrix} = T_s \left(\begin{bmatrix} 1-r_h \\ 1-r_v \\ -r_3 \\ -r_4 \end{bmatrix} \right) (1)$$

where T_h and T_v are the brightness temperatures measured by horizontally and vertically polarized antennas respectively, and T_3 and T_4 are proportional to the real and imaginary parts of the correlation between fields in horizontal and vertical polarizations respectively [1]. The second equality follows from Kirchhoff's Law, which relates the emissivity of a medium at constant temperature to the corresponding reflectivity (r_h, r_v, r_3 and r_4) multiplied with the surface physical temperature T_s. Reflectivities are calculated as an integral of bistatic scattering coefficients over the upper hemisphere in the reciprocal active scattering problem [2].

Particular interest in sea surface salinity remote sensing is given to brightness temperature variations with surface salinity and temperature when the sea surface is assumed smooth. In that case, it is straighforward to calculate reflectivities in Equation (1) at a given incidence angle using Fresnel reflection laws provided an accurate dielectric constant model is available at L-band. However, in the various discussions of the Sea Surface Salinity (SSS) retrieval schemes applied to spaceborne L-band radiometer data ([3]-[5]), it is clear that the major uncertainty in the required modelling is the effect of the wind and wave-generated roughness on the emissivity of the ocean's surface at L-band. The purpose of this section is to document one of the three forward models, namely the "SPM/small slope approximation (SPM/SSA)" that will provide roughness impact corrections in the version of the SSS retrieval algorithm used at launch of the ESA's Soil Moisture and Ocean Salinity (SMOS) satellite mission.

Analytical and numerical models for the calculation of the rough ocean surface polarimetric thermal emission have been developed [6]–[11], primarily through application of standard surface scattering approximate methods to calculate surface emissivity using Kirchhoff's law. Models based on both the small perturbation method (SPM) and the physical optics (PO) approximation has been presented. The physical optics (PO) approximation was shown to clearly underestimate the sea surface emissivity observations at L-band [12, 13], particularly in the low incidence angle range (less than about 20-30°). This is mainly because such model does not account for scattering on small roughness elements. Recent works [8-10] has further revealed that use of the SPM for emission calculations results in a small slope, rather than small height, emission approximation identical to that which would be obtained from the small slope approximation of [14], so that the SPM can provide accurate emission predictions even for surfaces with large heights in terms of the electromagnetic wavelength. Numerical tests of the SPM for a set of canonical periodic surfaces have confirmed this statement [15]. Moreover, the success of the SPM/SSA in matching measured brightness temperature [6,16-

19] has shown that the technique should be applicable for rough ocean surface brightness temperature predictions. These results motivate use of the SPM/small slope approximation (SPM/SSA) for the prediction of ocean polarimetric thermal emission at L-band.
The Stokes vector of sea surface brightness temperatures observed at radiometer frequency f, incidence angle θ_i and azimuth angle relative to wind direction ϕ_i can be written:

$$
\begin{bmatrix} T_h(f,\theta_i,\phi_i) \\ T_v(f,\theta_i,\phi_i) \\ T_3(f,\theta_i,\phi_i) \\ T_4(f,\theta_i,\phi_i) \end{bmatrix} = T_s \left(\begin{bmatrix} 1-\left|R_{hh}^{(o)}(f,\theta_i)\right|^2 \\ 1-\left|R_{vv}^{(o)}(f,\theta_i)\right|^2 \\ 0 \\ 0 \end{bmatrix} - \begin{bmatrix} \Delta e_h(f,\theta_i,\phi_i) \\ \Delta e_v(f,\theta_i,\phi_i) \\ \Delta e_3(f,\theta_i,\phi_i) \\ \Delta e_4(f,\theta_i,\phi_i) \end{bmatrix} \right) \quad (2)
$$

where T_s is the sea surface temperature. $R_\gamma^{(o)}(f,\theta_i)$ are the Fresnel reflection coefficients at polarization γ, and the $\Delta e_\gamma(f,\theta_i,\phi_i)$ are the first prediction of emissivity changes due to the rough sea surface. The physics of the forward problem here is to estimate accurately the wind-excess emissivity Stokes vector $\Delta e_\gamma(f,\theta_i,\phi_i)$ at f=1.4 GHz for the range of (θ_i,ϕ_i) values encountered in L1C SMOS data and for a range of wind and sea state conditions representative of the global ocean.

The SPM/SSA applies standard small perturbation theory to predict the bistatic scattering coefficients of a rough surface, and integrates these scattering coefficients over the upper hemisphere to obtain the reflectivities and hence brightness temperatures. The resonance behaviours observed in the critical phenomena region [20] produce a significant sensitivity of emission harmonics predicted by the SSA to ocean length scales of order equal to the electromagnetic wavelength. However, these emission harmonics are also sensitive (with the exception of the fourth Stokes parameter) to anisotropy in ocean length scale much larger than the electromagnetic wavelength. Use of the SPM/SSA up to 2nd order produces an expansion in surface slope, with zero order terms reproducing flat surface emission results, first order terms identically zero, and second order terms providing the first prediction of changes from flat surface brightnesses.

The second order terms take the form of an integral of a set of weighting functions over the surface directional spectrum, so that the wind-excess emissivity Stokes vector $\Delta e_\gamma(f,\theta_i,\phi_i)$ can be expressed as follows using the second order SPM/Small Slope Approximation theory (e.g., see [19]):

$$
\begin{bmatrix} \Delta e_h \\ \Delta e_v \\ \Delta e_3 \\ \Delta e_4 \end{bmatrix} = \int_0^\infty \int_0^{2\pi} kW(k,\phi) \begin{bmatrix} g_h(f,\theta_i,\phi_i;\varepsilon_{sw};k,\phi) \\ g_v(f,\theta_i,\phi_i;\varepsilon_{sw};k,\phi) \\ g_3(f,\theta_i,\phi_i;\varepsilon_{sw};k,\phi) \\ g_4(f,\theta_i,\phi_i;\varepsilon_{sw};k,\phi) \end{bmatrix} dkd\phi \quad (3)
$$

where $\vec{k}=(k,\phi)$ is a surface wavenumber vector, $W(k,\phi)$ is the sea surface directional waveheight wavenumber spectrum, ε_{sw} is the sea water dielectric constant and the g_γ kernels are electromagnetic "weighting" functions given explicitly in [19].

Note, that when deriving an asymptotic solution for EM scattering on the rough ocean surface, a key issue is to determine a tractable statistical description which specifies the sea surface geometry on a very wide range of scales (0.005-200 m). In most practical and/or theoretical studies, Gaussian statistics are assumed. Under such assumptions, the solution will then only depend upon the definition and the shape of the correlation function. Under Gaussian statistics assumption, which is used as well in the present SPM/Small Slope Approximation theory, the result can be expressed strictly in terms of a roughness spectrum. In the present algorithm, we used the Kudryatsev *et al* model [21] to estimate the sea surface roughness spectrum $W(k,\phi)$ in Equation (3), which was recently developed based on available field and wave-tank measurements, along with physical arguments concerning the dynamics of short-gravity waves. These scales indeed represent particularly important surface components for emissivity at 1.4 GHz, since they belong to the so-called "critical phenomena" region [20] within which surface components are dominant scatterers at L-band. It is important to note that this spectral model was developed without any relation to remote-sensing data. Moreover, by using the Kudryatsev *et al* spectral model, we avoided some deficiencies of the Elfouhaily et al spectral model as found by other (problems at the low to moderate wind speed transition).

In [19], it was shown that using a Fourier expansion in Eq (3), the wind-excess emissivity components can be separated out in individual emission azimuthal terms as follows:

$$\begin{bmatrix} \Delta e_h \\ \Delta e_v \\ \Delta e_3 \\ \Delta e_4 \end{bmatrix} = \begin{bmatrix} \Delta e_h^{(0)} + \Delta e_h^{(2)} \cos(2\phi_i) \\ \Delta e_v^{(0)} + \Delta e_v^{(2)} \cos(2\phi_i) \\ -\Delta e_3^{(2)} \sin(2\phi_i) \\ -\Delta e_4^{(2)} \sin(2\phi_i) \end{bmatrix} \quad (4)$$

where the $\Delta e_\gamma^{(n)}$ terms represent the nth azimuthal harmonics of the wind-excess emissivity.

Note that due to the assumption of gaussianity in the sea surface statistics, the solution can be expressed strictly in terms of a roughness spectrum. Properties of a directional spectrum result in no first azimuthal harmonic variations being obtained; introduction of non-gaussianity is required to obtain first azimuthal harmonics. As second azimuthal harmonics were measured to be already very small at L-band [22, 23], only the second order SSA/SPM expansion is considered here and no first azimuthal harmonic variations are neglected.

4.3.1.2. Mathematical description of theoretical SSA/SPM algorithm

The nth azimuthal harmonics of the wind-excess emissivity $\Delta e_\gamma^{(n)}$ terms in Eq (4) can be determined numerically by calculating integrals of the products of the nth azimuthal harmonics of the surface curvature spectrum $k^4 W(k,\phi)$ by the nth azimuthal harmonics of the electromagnetic weighting function g_γ.

Typically, the Kudryavtsev curvature spectrum model $k^4 W(k,\phi)$ is determined as function of the following geophysical parameters:

- The wind friction velocity U* [m/s],

- The inverse wave age parameter $\Omega = \dfrac{WS}{C_p}$ [dimensionless] for <u>the wind sea</u>, where *WS* is the wind speed module at 10 meter height [m/s] and C_p is the phase speed at the peak of the wind-sea spectrum [m/s]. Note that $\Omega = \dfrac{WS}{C_p} = \dfrac{2\pi WS}{gT_p}$ where g is the acceleration of gravity [m/s^2], and T_p is the peak period of wind-sea [s].

The electromagnetic weighting functions g_γ can be determined as function of

- the incidence angle θ_i at SMOS pixel, and,

- ε_{sw}, the complex sea water dielectric constant, which is itself function of Sea Surface Temperature T_s and Sea Surface Salinity *SSS*.

Therefore, the mathematical description of the SSA roughness brightness temperature corrections includes 4 major parts:

(1) A five-dimension Look-Up Table (LUT) of the $\underline{\Delta e_\gamma^{(n)}}$ coefficients.

Two options for the look-up table are possible as follows:

Option 1: LUT1 as function of

- the neutral equivalent wind speed WSn [m/s],

- the inverse wave age parameter Ω

- the incidence angle θ_i at SMOS pixel,

- the real part of ε_{sw}, and,

- the imaginary part of ε_{sw}.

Here the neutral equivalent wind speed is related to the friction velocity U* by

$$WSn = \frac{U*}{\kappa}\left[\ln\left(\frac{10}{z0}\right)\right],$$ where k is the von Karman constant and z0 is the roughness length.

Or

Option 2: LUT2 as function of

- the neutral equivalent wind speed WSn [m/s],

- the inverse wave age parameter Ω

- the incidence angle θ_i at SMOS pixel,

- the sea surface temperature T_s [K] and,

- the prior sea surface salinity SSS [psu].

Since ε_{sw} will be already calculated by the flat-sea surface module of the processor, it may seem advantageous to use the LUT dimensioned by the dielectric constant. However, the relationship of the dielectric constant to SSS and SST is such that for typical distributions of SSS and SST a large portion of the LUT will be unused and therefore it is not practical to use this approach. Therefore, for the processor we choose option 2 and discretize by SSS and SST, and use the same dielectric constant model as is used in the processor.

Parameter or variable ranges

- For the neutral equivalent wind speed WSn: 0$\rightarrow$ 40 [m/s],

- For the inverse wave age parameter for wind sea Ω: 0.5 $\rightarrow$ 2.5 [m/s],

- For the incidence angle θ_i at SMOS pixel [degrees]: 0$\rightarrow$ 75°

- For the sea surface temperature T_s : 269.15$\rightarrow$ 309.15 K

- For the prior sea surface salinity SSS : 0 $\rightarrow$ 40 psu

- For the azimuth angle relative to wind direction ϕ_i [in rad] : 0$\rightarrow$ 2π

- For the real part of the dielectric constant ε'_{sw} [no unit]: 65$\rightarrow$ 90

- For the imaginary part of the dielectric constant ε''_{sw} [no unit] 0$\rightarrow$100

(2) A multi-dimensional interpolation step.
Given the four values of the "geophysical" auxiliary parameters estimated at a given SMOS pixel, namely WSn_i, Ω_i, Real(ε_{sw}), Imag(ε_{sw}) where Real and Imag denote real and imaginary parts (respectively, $u*_i$, Ω_i, T_{si} and SSS_i), plus the series of incidence angles ($\theta_{i=1,...,N}$) associated to the L1C product considered, a linear interpolation is performed from LUT2 to evaluate the values of $\Delta e_{\gamma,i=1,...,N}^{(n)}$, the underlying multidimensional functions $\Delta e_{\gamma}^{(n)}$ at the pixel considered.

(3) Total roughness-induced emissivity correction.
From the value of azimuth angle relative to wind direction ϕ_i estimated at the pixel [in rad], the total wind-excess emissivity Stokes vector is calculated using Equation (4).

(4) Total roughness-induced brightness temperature correction.
From the estimated values of the total wind-excess emissivity Stokes vectors for each L1C incidence angles, the corresponding brightness temperature changes are derived by multiplying the results by the sea surface temperature at the pixel $T_{si.}$ [K].

4.3.1.3. Error budget estimates

In Figure 1, we show the comparison between currently available experimental data collected at L-band over water surfaces [4; 13; 22; 25-29] and the SSA/SPM model predictions of the wind speed sensitivity of surface emissivity at H and V polarization. The figures reveal that the model emissivity dependencies with wind speed are in agreement with the data to roughly

about $\pm 5 \times 10^{-4}$, in both vertical and horizontal polarizations. This translates into an error in brightness temperature of about 1 K at SST=15°C and WS =7 m/s. Note that this is a very maximized error estimate. In general, the model is found to correctly reproduce the averaged trends observed at both polarization also it often slightly underestimates the data, particularly in V-polarization and around nadir. Discrepancies might be due to either foam, currents, slicks and swell impacts not accounted for in the model or to radiometric uncertainties in the experimental data (see error bars given for some of the data). It is however expected that using auxiliary wind friction velocity data, a measure of wind stress that implicitly carries a response to near-surface phenomena, instead of wind speed at 10 meter height, shall improve the error budget estimate.

There is no evidence of clear azimuthal/wind direction related signatures in the few available measured brightness temperature signals at L-band [22, 23] so that it is now very difficult to estimate errors due to the wind stress directionality.

Therefore, we estimate an overall error budget on the roughness correction factor $\Delta e(\theta_i)$, as predicted by the SSA/SPM model (without accounting for wind direction impacts), of about:

$$\text{Error}\left(\begin{bmatrix} \Delta e_h(\theta_i) \\ \Delta e_v(\theta_i) \end{bmatrix}\right) = \pm 5 \times 10^{-4} \cdot U_{10}$$

An additional error will be introduced by the multi-dimensional interpolation scheme from the LUT table. The error is not provided yet in the draft ATBD but will be given later. Note that no error budget can be estimated for the third and fourth Stokes parameters as no data as function of wind speed are currently available for validation.
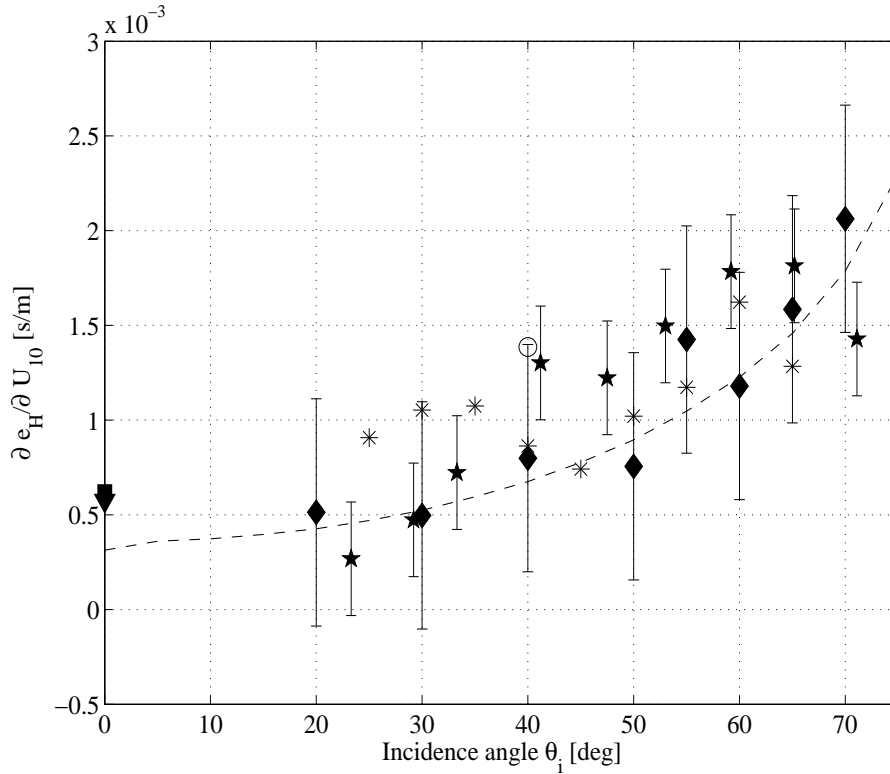
Figure 1a : for legend see next figure.
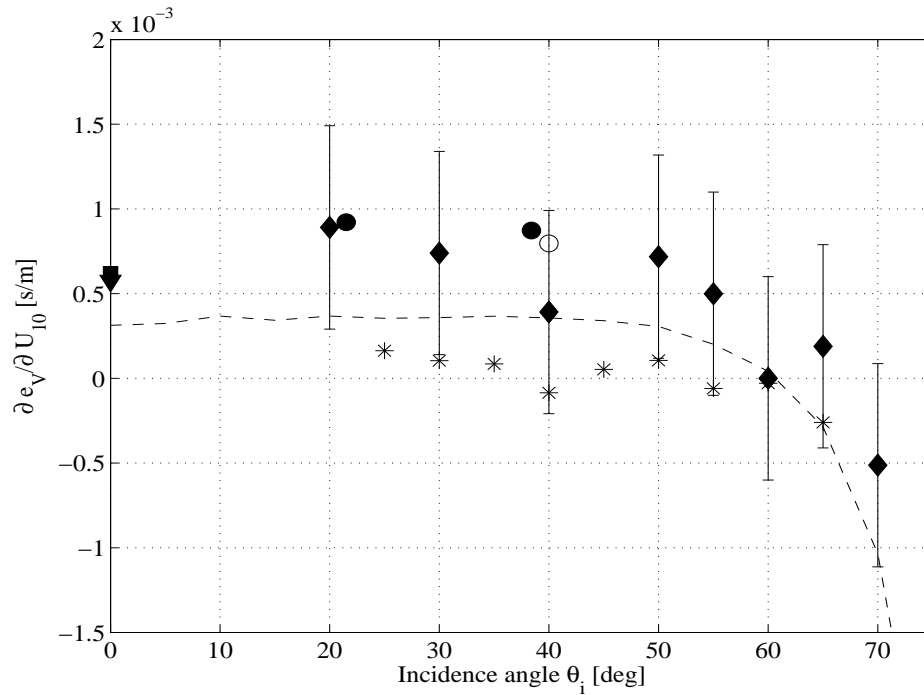
Figure 1b Comparison between measured and calculated sensitivities of the sea surface emissivity at L-band to wind speed at 10 meter height as function of incidence angle. Figure 1a: horizontal polarisation; Figure 1b: vertical polarisation. (★): Cape Code Canal data [13]; (■): Data from Skylab S-194 [25]; (✳): WISE 2000-2001 [22], [26]; (♦) : Argus Island Tower data [27]; (▼): Bering Sea Experiment [28]; (○): JPL experiment [4]; (●)EuroSTARRS [29]; (--): predictions from the SSA/SPM model at SST=15°C and SSS=35 psu. Error bars show uncertainties in the data of [13] and [27].

4.3.2. Practical considerations and introduction of empirical method

4.3.2.1. Calibration and validation

Calibration and validation of the forward SSA/SPM emissivity model for roughness correction will be done during the commissioning phase and later-on by perfoming residual analysis of the future SMOS measurements and using a formalism proposed for and applied to NASA scatterometer (NSCAT), Special Sensor Microwave Imager (SSM/I) and ESA/ERS scatterometer measurements [see 30].
Using in situ SSS, SST and wind (TAO, Argo drifter+ satellite SST and winds and ECMWF model winds) and SMOS co-localized data, the first step will be to remove the flat sea surface contribution from the SMOS surface brightness temperature data (i.e., corrected for atmospheric, ionospheric, galactic and sunglint contribution) in order to estimate the residual Stokes vector of roughness impact $\Delta e_B(\theta_i)$. The in situ and satellite SSS, SST and wind data will be the chosen reference. In addition, ECMWF analysis winds will be used as a thrid data source to completely determine the errors via a multiple collocation analysis. The main objective will be to present observed correlations between regional and seasonal model roughness correction factors $\Delta e_B(\theta_i)$ errors and nonwind oceanic and atmospheric factors such as the surface current and sea state. Following the methodology applied in [30], we shall explicitly take into account the errors in the reference datasets as well as in the roughness correction factors retrieved estimates. The gain shall come in more accurate assessment of

67

bias and variance and less possible systematic contamination that can obscur geophysically driven impacts not accounted for by the SSA/SPM model.

EMPIRICAL ADJUSTMENT OF ALGORITHM

On the basis of SMOS brightness temperatures obtained from March-October 2010, we have undertaken an initial evaluation of the SSA/SPM model described above, and on the basis of this evaluation we have introduced a new version of the roughness emission lookup table. In doing so we have maintained the same lookup table structure with the exception of replacing the friction velocity with the neutral equivalent wind speed at 10 m above the surface.

To perform the evaluation of the theoretical model, we collected a set of several hundred Pacific Ocean passes from March through October 2010, and we identified all snapshots for which boresight latitude lies between 55 degS and 30 degN. We then extracted all SMOS brightness temperatures within the extended alias-free field of view for which the x-component of the director cosine coordinates is smaller than 0.1 in magnitude and for which the y-component is equal to or larger than the value at nadir. This provides a manageable subset of data for which the polarization basis rotation required to transport the instrument basis brightness temperatures into surface basis components is generally small. More importantly, this subset of data can be transported to the surface basis in dual-pol mode away from nadir.

We used GPS-derived total electron content to compute the Faraday rotation and transported all brightness temperatures into the surface polarization basis. As the period considered included dual-pol and full-pol mode data, we chose to perform the rotation on (Tx,Ty) only, assuming that the third Stokes parameter in the surface basis is identically zero.

Before performing the rotation to the surface basis, we subtracted from the full brightness temperatures (Tx,Ty) our best estimate of all contributions to brightness except for surface roughness emission. These contributions included rough surface scattered celestial sky noise evaluated using the model described in this document and evaluated at a wind speed of 3 m/s.

Assuming that the residual brightness temperatures are associated zith surface roughness emission, we then binned the data by incidence angle and by surface wind speed. We used bin sizes of 5 deg for incidence angle and 1 m/s for wind speed. For neutral equivalent wind speed we used both ECMWF and NCEP winds in order to obtain a measure of possible uncertainty in the results. One might suppose that using buoy winds would yield better results, however in this case the aim is to obtain a roughness correction for SMOS as a function of the surface winds used in the processor.

The following figure shows the median residual brightness temperatures as a function of ECMWF and NCEP 10-m neutral equivalent wind speed for the smallest incidence angle bin. The solid curves show results for ascending passes while the dash curves show results for descending passes.

For comparison we have also plotted the isotropic components of the 2-scale model (green curves; Th=solid,Tv=dashed) and of the SSA/SPM model described here (black curves;

Th=solid,Tv=dashed). The median residual curves are slightly concave up with an overall impact of about 8 K at 25 m/s, so the overall sensitivity to wind speed of Th and Tv, based on the Pacific SMOS data, is about 0.3 K/(m/s) near nadir.

There is a slight difference between the NCEP and ECMWF results that amount to about 1 K at 25 m/s. Note that we have adjusted all curves to zero roughness emission at zero wind speed. More important differences exist between ascending and descending passes, with differences reaching 2 K at 25 m/s. This cannot be related to Faraday rotation because at this incidence angle Th and Tv are nearly equal for both ascending and descending passes (and they are exactly equal in the isotropic components of the theoretical model results).

Ascending/Descending Pass Roughness Emission at 0°
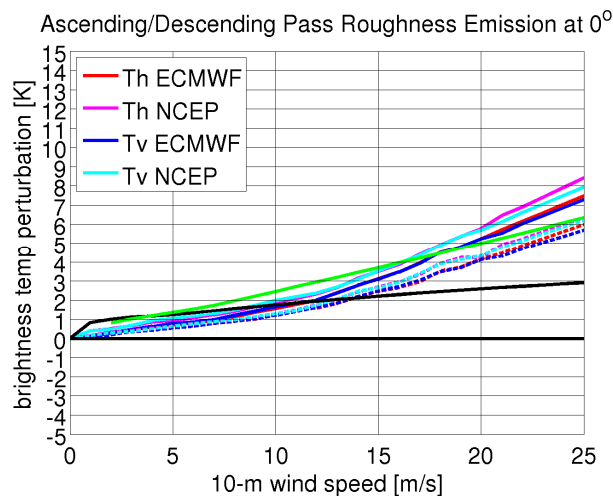
The results at 32 deg incidence angle, shown below, exhibit stronger sensitivity to wind speed (up to 10 K for Th at 25 m/s) than at nadir for Th and unchanged sensitivity for Tv. The increased sensitivity to wind speed for Th with increasing incidence angle and the unchanged sensivity in Tv is expected based upon the theoretical results shown earlier. However, we still see strong differences between ascending and descending passes (up to 2 K in Th at 25 m/s wind speed).

Both theoretical models clearly overestimate the roughness emission for Th and Tv below 10 m/s and underestimate roughness emission beyond 20 m/s.

Ascending/Descending Pass Roughness Emission Th at 32°
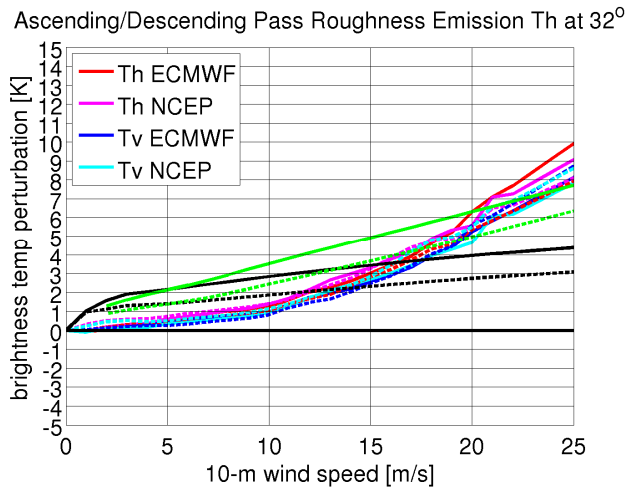
At a higher incidence angle, 61 deg, SMOS residuals show weak sensitivity of Tv to wind speed up to about 10 m/s followed by a linear increase from 0 to 6 K from 10 to 25 m/s. By contrast, Th increases nearly linearly from 0 to 13 K from 0 to 25 m/s, so the sensitivity of Th to wind speed reaches 0.5 K / (m/s). Both theoretical models greatly overestimate roughness emission in Th below 15 m/s and the 2-scale model underestimates roughness impact in Tv at all wind speeds.

Ascending/Descending Pass Roughness Emission at 61°
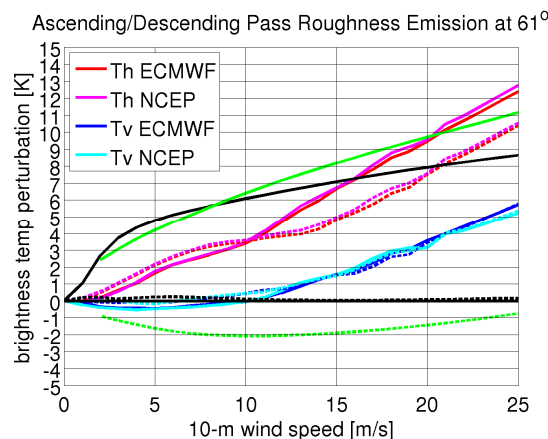
In order to examine the stability of the roughness residuals over time we have evaluated the residuals on two independence set of SMOS data: 'old' passes from March through May 2010 and 'new' passes from August through October 2010. The residuals at 61 deg incidence angle are shown below and reveal less than 1 K difference between the two sets of data at 25 m/s wind speed. This, along with the comparison between NCEP and ECMWF winds, provides an indication of the uncertainty of the roughness residuals.

Ascending Pass Roughness Emission at 61°
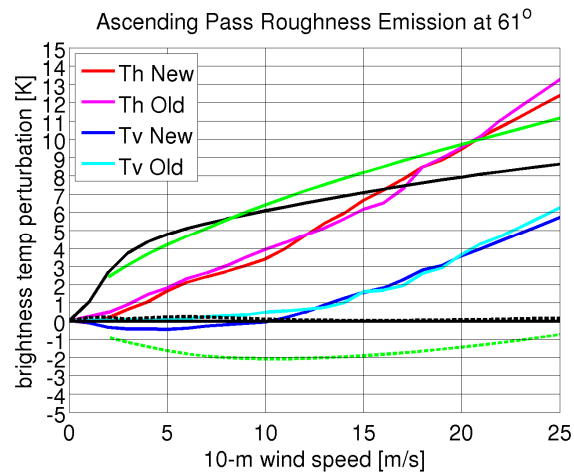
To assess the impact of using the empirically determined roughness residuals instead of the theoretical residuals, we collected a set of several hundred Pacific Ocean passes and evaluated the bias between the SMOS brightness temperatures and the complete theoretical and empirical models averaged over the alias-free field of view. We collected these biases in terms of (Tx+Ty)/2 and plotted them as a function of time and boresight latitude, and the results for descending passes from March 1 to November 1 2010 are shown below for the theoretical SSA/SPM model. Aside from the large negative bias in June and July, we can see areas of large negative biases associated with storms in the southern hemisphere. These biases correspond to roughness emission overestimation by the sum of the SSA/SPM and foam models.

AF-FOV Descending (Tx+Ty)/2 Bias [K]
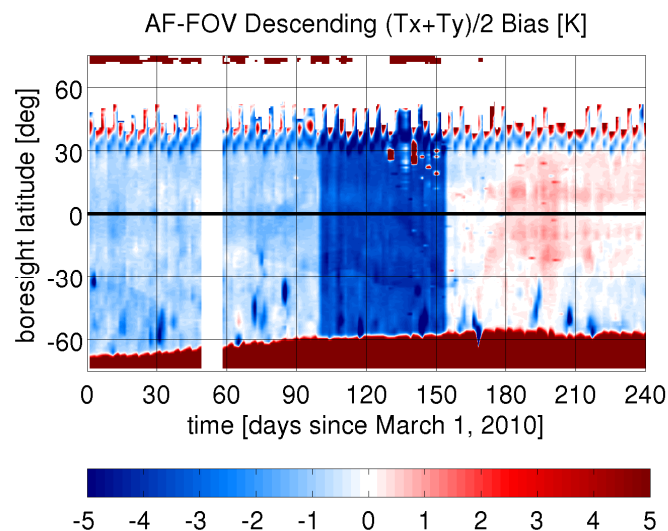
When we replace the SSA/SPM+foam model solutions with the empirical model described above, we obtain the following plot of bias in (Tx+Ty)/2 as a function of time and latitude.
Aside from an overall change in the bias level, the large biases associated with the high-latitude storms are less evident, which reflects a more accurate modeling of high wind rough surface excess emission.

AF-FOV Descending (Tx+Ty)/2 Bias [K]
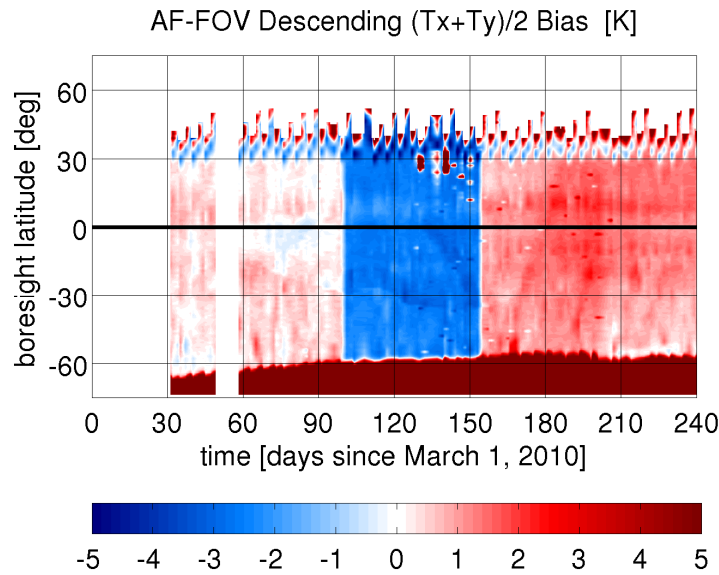
Although the empirical model does generally produce more accurate estimates of rough surface emission, the effectiveness of this approach is limited in situations in which the link between the sea surface roughness and model wind speed is affected by the strong temporal and spatial variations of wind speed, such as in the vicinity of midlatitude cyclones and hurricanes. In these situations two problems arise. First of all, in these situations the surface wind fields produced by the numerical weather prediction models such as ECMWF can suffer from significant errors in both the positions of the storm centers (and associated fronts) as well as the distribution of winds around the storms. Secondly, sea state can vary strongly for any given surface wind speed where the wind changes strongly in space and time, so that the emission prediction can be incorrect even if there is no error in the wind speed.

Finally, it should be noted, as discussed in the section describing the theoretical model, that there may be a dependence of the roughness emission on relative angle between emission direction and wind direction, but we have not been able to see a consistent azimuthal signal in the SMOS data as of this writing, and so we current set all azimuthal harmonic coefficients to zero identically.

4.3.2.2. Quality control and diagnostics

As explained in section 4.3.3 below, the SSA/SPM model is not expected to provide correct results for wind seas generated by winds less than about 2 m/s and larger than 15 m/s . This corresponds roughly to wind friction velocity u* less than 0.6 cm/s and larger than 0.5 m/s. The model can be applied as it is at launch for conditions out of this range however, we expect that the CAL/VAL activities will provide after commissioning phase a variability estimate at low winds and a residual foam impact at high winds which will be used to correctly tune the model.

4.3.2.3. Exception handling

There is no particular exception handling in the mathematical algorithm except if the following auxiliary data are not provided by the processor or exceed the ranges anticipated:

72

- the neutral equaivalent wind speed [m/s], (which can be estimated fromthe wind speed magnitude at 10 meter height, the roughness length, and the auxiliary parameter "Coefficient of drag with waves C_d "defined by : u*= $\sqrt{C_d} \times |U_{10}|$)

- the inverse wave age parameter Ω for <u>the wind sea</u> (which can be deduced from estimates of both U_{10} and the mean period of wind waves T_p: $\Omega = \dfrac{2\pi U_{10}}{gT_p}$),

- the incidence angles θ_i at SMOS pixel,

- the sea surface temperature T_s,

- the prior sea surface salinity SSS, and,

- the azimuth angle at SMOS pixel relative to wind direction ϕ_i.

If one of the prior values of the retrieved geophysical parameters is out of the LUT range, or if any retrieved geophysical parameter goes out of LUT range during the retrieval, different flags (Fg_OoR_Rough_dim1, Fg_OoR_Rough_dim2, Fg_OoR_Rough_dim3, Fg_OoR_Rough_dim4, Fg_OoR_Rough_dim5) are raised. No extrapolation is done and the boundary value is taken.

4.3.3. Assumption and limitations

As discussed above, the empirical model described above is expected to fail in strong storm and frontal conditions (strong wave-wave, wave-current or wind-wave interaction conditions). Furthermore, we do not expect the model to perform well in presence of either strong swells, strong currents, very small and unsteady winds where the link between surface roughness and wind speed is not direct. We expect however that accounting for the impact of waves on the drag coefficients will better characterize impact of these parameters on roughness.

References

[1] S. H. Yueh, R. Kwok, F. K. Li, S. V. Nghiem, and W. J. Wilson, "Polarimetric passive remote sensing of ocean wind vectors," *Radio Sci.*, vol. 29, pp. 799–814, 1994.

[2] L. Tsang, J. A. Kong, and R. T. Shin, *Theory of Microwave Remote Sensing*. New York: Wiley, 1985.

[3] G. S. E. Lagerloef, C. T. Swift, and David M. Le Vine, Sea surface salinity : The next remote sensing challenge, *Oceanography*, vol. 8, no. 2, pp. 44-49, 1995.

[4] S. H. Yueh, R. West, W. J. Wilson, Fuk K. Li, E. G. Njoku, and Y. Rahmat-Samii, Error sources and feasibility for microwave remote sensing of ocean surface salinity, *IEEE Trans. Geosci. and Remote Sens.*, vol. 39, no. 5, pp. 1049-1060, 2001.

[5] E. P. Dinnat, J. Boutin, G. Caudal, J. Etcheto, and A. Camps, Issues concerning the sea emissivity modeling in L-band for retrieving surface salinity, *Radio Sci.*, vol. 38, no. 4, 2003.

[6] S. H. Yueh, "Modeling of wind direction signals in polarimetric sea surface brightness temperatures," *IEEE Trans. Geosci. Remote Sensing*, vol. 35, pp. 1400–1418, 1997.

[7] D. B. Kunkee and A. J. Gasiewski, "Simulation of passive microwave wind direction signatures over the ocean using an asymmetric-wave geometrical optics model," *Radio Sci.*, vol. 32, p. 59, 1997.

[8] V. G. Irisov, "Small-slope expansion for thermal and reflected radiation from a rough surface," *Waves Random Media*, vol. 7, pp. 1–10, 1997.

[9] J. T. Johnson, ``A study of rough surface thermal emission and reflection using Voronovich's small slope approximation," IEEE Trans. Geosc. Rem. Sens., Feb 2005.

[10] A. B. Isers, A. Puzenko, and I. M. Fuks, The local perturbation method for solving the problem of di_raction from a surface with small slope irregularities," J. Electromagn. Waves Appl., vol. 5, no. 12, 1991.

[11] V. G. Irisov, "Microwave radiation from a weakly nongaussian surface," in *Proc. IGARSS'98* vol. 5, pp. 2329–2332.

[12] J. P. Hollinger, Passive microwave measurements of sea surface roughness, IEEE Trans. Geosci. Electron., vol. GE-9, no. 3, pp. 165-169, 1971.

[13] C. T. Swift, Microwave radiometer measurements of the Cape Cod Cannal, Radio Sci., vol. 9, no. 7, pp. 641-653, 1976.

[14] A. G. Voronovich, *Wave Scattering from Rough Surfaces*. Berlin, Germany: Springer-Verlag, 1994.

[15] M. Zhang and J. T. Johnson, "Theoretical studies of ocean polarimetric brightness signatures," in *Proc. IGARSS'98*, vol. 5, pp. 2333–2335.

[16] J. T. Johnson and Y. Cai, ``A theoretical study of sea surface up/down wind brightness emperature differences," IEEE Trans. Geosc. Remote Sens, 2002.

[17] J. T. Johnson, ``Comparison of the physical optics and small slope theories for polarimetric thermal emission from the sea surface," IEEE Trans. Geosc. Remote Sens, 2002.

[18] M. Zhang and J. T. Johnson, ``Comparison of modeled and measured second azimuthal harmonics of ocean surface brightness temperatures," IEEE Trans. Geosc. Remote Sens, 2001.

[19] J. T. Johnson and M. Zhang, ``Theoretical study of the small slope approximation for ocean polarimetric thermal emission," IEEE Trans. Geosc. Remote Sens., 1999.

[20] V. S. Etkin, N. N. Vorsin, Y. A. Kravtsov, V. G. Mirovskii, V. V. Nikitin, A. E. Popov, and I. A. Troitskii, Critical phenomena with the thermal radio irradiation of a periodically uneven water surface, *Izvestiya: Radiophysics and Quantum Electronics*, vol. 21, pp. 316-318, 1978.

[21] V. N. Kudryavtsev, V. K. Makin, and B. Chapron, "Coupled sea surface atmosphere model. 2. spectrum of short wind waves," J. Geophys. Res., vol. 104, no. C4, pp. 7625-7639, 1999.

[22] A. Camps, J. Font, M. Vall-llossera, C. Gabarro, R. Villarino, L. Enrique, J. Miranda, I. Corbella, N. Duo, F. Torres, S. Blanch, J. Arenas, A. Julia, J.Etcheto, V. Caselles, A. Weill, J. Boutin, S. Contardo, R. Niclos, R. Rivas, S. Reising, P. Wursteisen, M. Berger, and M. Martn-Neira, The WISE 2000 and 2001 Campaigns in support of the SMOS Mission: Sea surface L-band Brightness Temperature Observations and their application to Multi- Angular Salinity Retrieval, *IEEE Trans. Geosci. Remote Sensing*, vol. 42, no. 4, pp. 1039-1048, 2004.

[23] S. Sobjaerg and N. Skou, An Airborne Campaign measuring wind signatures from the Sea Surface using an L-band polarimetric radiometer, in *Proceedings of the International Geoscience and Remote Sensing Symposium, IGARSS*, Toulouse, 2003.

[24] L. A. Klein and C. T. Swift, ìAn Improved model of the dielectric constant of sea water at microwave frequencies,î *IEEE Trans. Antennas Propag.*, vol. AP-25, pp. 104-111, 1977.

[25] R. M. Lerner and J. P. Hollinger, ìAnalysis of 1.4 GHz Radiometric measurements from Skylab,î *Remote Sens. Environm.*, vol. 6, pp. 251-269, 1977.

[26] A. Camps, J. Font, J. Etcheto, V. Caselles, A. Weill, I. Corbella, M. Vall-llossera, N. Duffo, F. Torres, R. Villarino, L. Enrique, A. Julia, C. Gabarro, J. Boutin, E. Rubio, S. C. Reising, P. Wursteisen, M. Berger, and M. Martin-Neira, ìSea surface emissivity observations at L-band: First results of the wind and salinity experiment wise 2000, *IEEE Trans. Geosci. and Remote Sens.*, vol. 40, no. 10, pp. 2117-2129, 2002.

[27] J. P. Hollinger, Passive microwave measurements of sea surface roughness, *IEEE Trans. Geosci. Electron.*, vol. GE-9, no. 3, pp. 165-169, 1971.

[28] W. J. Webster, T. T. Wilheit, D. B. Ross, and P. Gloersen, Spectral characteristics of the microwave emission from a wind-driven covered sea, *J. Geophys. Res.*, vol. 81, no. 18, pp. 3095-3099, 1976.

[29] J. Etcheto, E. P. Dinnat, J. Boutin, A Camps, J. Miller, S. Contardo, J. Wesson, J. Font, and D. Long, Wind speed effect on L-band brightness temperature inferred from EuroSTARRS and WISE2001 field experiments, *IEEE Trans. Geosci. and Remote Sens.*, vol. 42, no. 10, pp. 2206-2213, 2004.

[30] Y. Quilfen, B. Chapron and D. Vandemark, "The ERS Scatterometer Wind measurement accuracy: evidence of seasonal and regional biases", *Journal of Atmopsheric and Oceanic Technology*, vol 18, p 1684-1697, 2001.

4.4. Surface roughness 3: empirical

4.4.1. Theoretical description

4.4.1.1. Physics of the problem

The brightness temperature can be expressed as the sum of two terms; the brightness temperature in the case of completely flat sea and the brightness temperature (ΔT_b) due to the surface roughness:

[4.4.1] $T_{b,p}(\theta_i, SST, SSS, P_{rough}) = T_{bflat,p}(\theta_i, SST, SSS) + \Delta T_{b\ rough,p}(\theta_i, SST, SSS, \overrightarrow{P_{rough}})$

where the first term is T_b due to specular reflection, which is well described by the Fresnel equations. The second term is the increment of brightness temperature due to sea roughness indicated here by a vector P_{rough}, which includes the effect of some of the parameters that modify the surface roughness, like wind speed (WS), significant wave height (Hs), inverse wave age (Ω)… Furthermore, T_b is polarization dependent.

Several models describe this increment on T_b in a theoretical basis as in the modules 2 and 3. However, these theoretical models are not fully well validated.

This module proposes to use an empirical model describing ΔT_b through several physically measurable parameters and coefficients which are derived from measurements.

The most important parameter that affects the roughness of the sea is the wind speed, due to the stress on its surface and then this is the main (and usually the only) parameter used in the description of the sea roughness. However, this impact is not linear with all wind speeds as shown in several works (Etcheto et al, 2004, Vall-llossera et al., 2003).

Miranda et al. (2003), using several wind speed sequences recorded during WISE 2000 and 2001 campaigns (Camps et al, 2004, Camps et al, 2002), found large differences between measured spectra and theoretical fully-developed spectra obtained with the measured local wind speed. This can produce errors on T_b of about a fraction of a Kelvin in both polarizations with opposite sign (therefore, these errors could be minimized by using the first Stokes parameter).

This is the case when swell is present, where some events of low local wind speed and high wave height are possible and therefore roughness can not be properly described only by the wind speed.

In Gabarró et al, 2004a, a new empirical model is proposed to describe the increment of T_b due to the roughness of the sea as function of wind speed and also significant wave height. That model is derived from WISE 2001 campaign measurements. Gabarró, 2004b compares the behaviour of this model with respect to other models which are only dependent on WS, and better performances are observed when the proposed model is used.

ARGANS ACRI ST	ICM-CSIC LOCEAN/SA/CETP IFREMER	SMOS L2 OS Algorithm Theoretical Baseline Document	Doc: SO-TN-ARG-GS-0007 Issue: 3 Rev: 7 Date: 22 June 2011 Page: 77

In Camps et al., 2004 authors have observed that azimuthal variations of the measured T_b during WISE 2000 at 25°, 35°, 45°, and 55° incidence angles, and at both polarizations, are within 0.5 K. However, they can be due to differences between calibrations, and the authors do not think there is any measurable azimuthal signature below 10 m/s. Only during very large storms (as the case of WISE2001, with a wind speed of 11m/s and very large waves (3 m < Hs < 5 m)), the azimuthal signature has been observed. However in Yueh et al. 2010, authors show a dependency of T_{bH} and T_{bV} on the wind direction at relatively high wind speeds (more than 14m/s) has been observed in a field campaign in North Atlantic. They say it can represent an increment of 1K at 14m/s and 2K at 24m/s.

A LUT is proposed to describe the $T_{b\,rough}$ as function of the parameters. This LUT depends on 4 parameters: θ (incidence angle), WSn (neutral wind speed from the WS components), ϕ_WS (wind direction) and Hs (wave height).

The model regression analysis will be performed with auxiliary data coming from ECMWF models since such data are globally available at high temporal frequency and can therefore maximize the collocation dataset of SMOS and auxiliary information. A comprehensive analysis of the different error contributions (notably measurement and auxiliary data errors, and fitting errors) will be carried out, as well as a correlation analysis among the different parameters (notably the roughness ones), to derive the most suitable model.

The Tb information to create the LUT is obtained from SMOS L1b and transformed to sea surface brightness temperature. The vector $\vec{p}$ can comprise any relevant geophysical parameters, for the implementations that we consider the follwing parameters will be used, namely incidence angle, wind speed (WS), wind direction (ϕ) and signicant wave height (Hs).

To diminish the impact of yet-unsolved processing problems owe to to first levels (correction of galactic noise, land contamination, TEC, Faraday rotation, etc) a very restrictive dataset of valid TB's will be considered; this gives more generality and stability to our results, so diminishing the expected impact on the GMF when a reprocessing is done. However, this also restricts the range of valid values for our LUT, and implies the necessity of implementing an extrapolation strategy to extend it out of the sampling range.

The tabulation of the LUT will be provided by incidence angle between 0 and 75º, WSn between 0 and 50 m/s, wind direction ϕ between 0 and 360º and HS between 0 and 15m. The outputs of the LUT are T_{bh}, T_{bv}, third stokes vector (U) and fourth stokes vector (V).

4.4.1.2. Mathematical description of algorithm

To permit a rapid computation of the Tb due to roughness a LUT has been created to determine the Tbrough empirically from SMOS L1b data and the geophysical parameters that describe this Tbrough.

The parameters used as input to the LUT are:
  - Incidence angle θi at SMOS pixel

- Neutral wind speed, WSn , computed from its components by:

$$WS_n = \sqrt{WS_x^2 + WS_x^2}$$

- Wind direction, obtained from the neutral components by : $\phi = \arctan(WS_x^2 / WS_y^2)$
- Wave Height (HS), obtained from the ECMWF wave model.

The outputs are:

$$Tb_{rough=} \begin{pmatrix} Tbrough\_h \\ Tbrough\_v \\ U \\ V \end{pmatrix}$$

where U is the thirds Stokes parameter and V the fourth Stokes parameter.

The parameters range as follows:

Dimension	Number of Values	Units	Coordinate Values
Radiometric Incidence angle	76	Deg	[0,1,2,3,….. Δ θ =1 …73,74,75]
Neutral Wind speed WSn	111	m/s	[0 …ΔWS=0.25 … 20][21 ... ΔWS=1…50]
Wind direction	36	Deg	[0…Δφ=10…..360]]
Significant Wave height - Hs	40	m	Hs (m) = [0 …ΔHs=0.25 … 8][9 ... ΔHs=1…15

Since the model is empirical the effect of foam is already included in the computed Tb, so the foam correction described in module 4.5 is never to be applied to roughness model 3.

Practical derivation of the empirical TB modulation

In spite of the apparent cumbersome mathematics, in practice the computation of E[Tb_p] is very easy: for each fixed value of $\vec{p}$ (vector of the geophysical parameters), all the values of Tb associated to that value of $\vec{p}$ are averaged together. This implies that an uncertainty or quantization range on the vector $\vec{p}$ must be given, as we cannot expect a precise value of $\vec{p}$ to be exactly repeated ever. Hence, a suitable quantization vector $\Delta\vec{p}$ must be constructed, which is defined as the quantization range for each of the components in $\vec{p}$.

The discretization shown above is based on considerations about the probability distribution of the geophysical parameters as well as about the tradeoff between lookup table size and resolution of nonlinear variations of emissivity corrections.

The values shown define the discretization ranges for each geophysical parameter p^a; we consider the n-th range of values of p^a, $C_{p^a}^n$, given by:

$$C_{p^a}^n \equiv \left[p_n^a - \Delta p_n^a, p_n^a + \Delta p_n^a \right]$$

where p_n^a is the n-th value that the parameter p^a can take, n = 1,…, N^a, and $\Delta p_n = (p_n - p_{n-1})/2$ (when sampling is not uniform this denition is modied to avoid overlaps). Given this discretization, the empirical estimate of the Tb modulation (i.e., empirical histogram) is then defined for those representative values P_n^a. We will denote the empirical Tb modulation by $\hat{T}b(\vec{p})$; it is given by:

$$\hat{T}b(\vec{p}_{\vec{n}}) = \frac{1}{N_{\vec{n}}} \sum_{\vec{p} \in C_{\vec{p}}^{\vec{n}}} Tb$$

where $\vec{n}$ designates the vector of discrete indexes for all geophysical parameters, and $N_{\vec{n}}$ stands for the number of points such that $\vec{p} \in C_{\vec{p}}^{\vec{n}}$.

Uncertainty on the empirical TB modulation

The quantization on the geophyisical vector $\vec{p}$ (that allows to pass from continuous $\vec{p}$ to a discrete collection $\vec{p}_{\vec{n}}$) will forcefully impact our estimate of Tb modulation. We can evaluate the impact of the quantizations by computing the conditioned standard deviation of Tb by $\vec{p}$, denoted by $\sigma_{Tb}(\vec{p})$, which is theoretically given by the following formula:

$$\sigma^2_{Tb}(\vec{p}_{\vec{n}}) = \int dTb \, Tb \, \rho(Tb|\vec{p}) - E\left[Tb|\vec{p}\right]^2$$

Again, the practical computation of the conditioned standard deviation $\sigma_{Tb}(\vec{p})$ is straightforward, as it just requires to computed the standard deviation of TB on $C_{\vec{p}}^{\vec{n}}$, namely:

$$\sigma_{Tb}(\vec{p}_{\vec{n}}) = \frac{1}{N_{\vec{n}}} \sum_{\vec{p} \in C_{\vec{p}}^{\vec{n}}} Tb - \hat{T}b(\vec{p}_{\vec{n}})^2$$

This conditioned standard deviation provides an accurate estimate of the marginal uncertainty on the value of the Tb as retrieved using the GMF LUT. It may happen, however, that the uncertainty is larger than what we would like. This would imply the necessity of improving the uncertainties of the geophysical variables. Notice, however, that even if the uncertainty on Tb may be large, as far as the amount of averaged data is large enough and the sampling errors are unbiased and independent, the quality of the LUT may still be good. So the key point is to know the signicance of the LUT.

4.4.1.3. Error budget estimates (sensitivity analysis)

In Camps et al., 2004, authors observe that the uncertainty of the brightness temperature sensitivity to wind speed is on the order of 0.1 K/(m/s) for all incidence angles, when using the model only dependent on WS. Therefore, for WS=10 m/s, the uncertainty of the brightness temperature T_b is about 1 K. Taking into account the brightness temperature sensitivity to SSS (0.35-0.8 K/psu at V-pol, and 0.20-0.6 K/psu at H-pol), it translates at 10 m/s into a ΔSSS within 1.2-5 psu.

4.4.2. Practical considerations

4.4.2.1. Calibration and validation

Roughness model 3 will be validated comparing SMOS SSS retrieved maps with this roughness model with SSS maps created with interpolated ARGO data.

4.4.2.2. Quality control and diagnostics

Because of its empirical derivation, the model's accuracy will be degraded for exceptional geophysical conditions, such as winds above 15m/s and wave height above 8m, for which very few SMOS observations are available.

4.4.2.3. Exception handling

There is no particular exception handling in the algorithm except if the following auxiliary data are not provided by the processor or exceed the ranges of the LUT:

- the wind speed, *WS*

- the significant wave height, *Hs*

- the incidence angles θ_i at SMOS pixel

If one of the prior values of the retrieved geophysical parameters is out of the LUT range, or if any retrieved geophysical parameter goes out of LUT range during the retrieval, different flags (Fg_OoR_Rough_dim1, Fg_OoR_Rough_dim2, Fg_OoR_Rough_dim3, Fg_OoR_Rough_dim4) are raised. No extrapolation is done and the boundary value is taken.

4.4.3. Assumption and limitations

When a significantly strong rain is present in the FOV, the model cannot be applied. This information will be known from the ECMWF data. Also in the case of presence of surface slicks, from natural or not natural origin, the model will not work properly.

There is the possibility (controlled by a switch) that no roughness correction is applied in wind speeds below Tg_WS_rougness_M3 (due to lack of confidence in the model), and in such case a flag will be raised (Fg_ctrl_roughness_M3.false). Elsewhere, the flag is set to true (Fg_ctrl_roughness_M3.true).

References

Camps, A., Font, J., Vall-llossera, M., Gabarró, C., Villarino, R., Enrique, L., Miranda, J., Corbella, I., Duffo, N., Torres, F., Blanch, S., Arenas, J., Julià, A., Etcheto, J., Caselles, V., Weill, A., Boutin, J., Contardo, S., Niclòs, R., Rivas, R., Reising, S., Wursteisen, P., Berger, M., and Martín-Neira, M. (2004a). The WISE 2000 and 2001 Campaigns in Support of the SMOS Mission: Sea Surface L-band Brightness Temperature Observations and their Application to Multi-Angular Salinity Retrieval. IEEE Transactions on Geoscience and Remote Sensing, 42(4):804–823.

Camps, A., Font, J., Etcheto, J., Caselles, V., Weill, A., Corbella, I., Vall-llossera, M., Duffo, N., Torres, F., Villarino, R., Enrique, L., Julià, A., Gabarró, C., Boutin, J., Rubio, E., Reising, S., Wursteisen, P., Berger, M., and Martín-Neira, M. (2002b). Sea Surface Emissivity Observations at L-band: First Results of the Wind and Salinity Experiment WISE-2000. IEEE Transactions on Geoscience and Remote Sensing, 40(10):2117–2130.

Camps, A., Font, J., Gabarró, C., Miranda, J., Obligis, E., Labroue, S., Boone, C., Sabia, R., Vall-llosera, M., Reul, N., June 2004. WP1100, ESTEC ITT 1-4505/03/NL/Cb

Camps, A., Vall-llossera, M., Villarino, R., Reul, N., Chapron, B., Corbella, I., Duffo, N., Torres, F., Miranda, J.J., Sabia, R., Monerris, A., and Rodríguez, R. (2005c). The Emissivity of Foam-Covered Water Surface at L-Band: Theoretical Modeling and Experimental Results From the Frog 2003 Field Experiment. IEEE Transactions on Geoscience and Remote Sensing, 43(5):925-937.

Etcheto, J., Dinnat, E., Boutin, J., Camps, A., Miller, J., Contardo, S., Wesson, J., Font, J., and Long, D. (2004). Wind speed effect on L-band brightness temperature inferred from EuroSTARRS and WISE 2001 field experiments. IEEE Transactions on Geoscience and Remote Sensing (in press).

Gabarró, C., Font, J., Camps, A., Vall-llossera, M., and Julià, A. (2004a). A New Emprical Model of Sea Surface Microwave Emissivity for Salinity Remote Sensing. Geophysical Research Letters, 31(L01309):1–5.

Gabarró, C. (2004b). Study of salinity retrieval errors for the SMOS mission. PhD thesis, Universitat Politècnica de Catalunya.

Miranda, J., Vall-llossera, M., Camps, A., Duffo, N., Corbella, I., and Etcheto, J. (2003). Sea State on the Sea Surface Emissivity at L-Band. IEEE Transactions of Geoscience and Remote Sensing, 41(10):2307–2315.

Yueh, S., Dinardo, S. J., Fore, A. F., Li, F.K. (2010). Passive and Active L-Band Microwave Observations and Modeling of Ocean Surfca eWinds. IEEE Transactions of Geoscience and Remote Sensing, 48(8):3087–3100.

Vall-llossera, M., Miranda, J., Camps, A., and Villarino, R. (2003). Sea Surface Emissivity Modeling At L-Band: An InterComparison Study. Proceedings of the WISE/LOSAC/EuroSTARRS campaigns Workshop. ESA, SP-525:143–154.

4.5. Foam Contribution

4.5.1. Theoretical description

4.5.1.1. Physics of the problem

Although foam generated by breaking waves typically covers only a few percent of the sea surface, it has a profound effect on the average microwave brightness of the ocean surface [1-8]. For surface wind speeds greater than 15 m/s, foam-induced effects may provide as much as half of the total sea surface signature to an orbiting microwave radiometer [9;10]. At L-band, WISE [11] and FROG [12] experiments have provided detailed L-band emissivity measurements of the sea foam over a wide range of incidence angles and salinities at both polarizations. Although foam as a weaker impact at 1.4 GHz than at higher frequencies, it was shown that the presence of foam also increases the emitted brightness temperature at L-band, since it acts as a transition layer that adapts the wave impedance of the two media: water and air. The increase depends on the fraction of the sea surface covered by foam and its thickness, which can be parameterized in terms of the local wind strength, but it depends as well on other factors, such as the air-sea temperature difference, the sea water temperature, the fetch, etc… FROG 2003 experiments revealed that at a salinity of 37 psu, the foam-induced emissivity increase is ~0.007 per mm of foam thickness (extrapolated at nadir), increasing with increasing incidence angles at vertical polarization, and decreasing with increasing incidence angles at horizontal polarization. According to the model developed by [13], for a 12 m/s wind speed, one should expect in average a coverage-weighted foam thickness of about 0.5 cm: this translates to an increase in brightness temperature of about 0.2 K at an SST of about 15°C. At 20 m/s, the calculation predicts a 0.5 K increases: this might have a non negligible impact for salinity retrieval accuracy.

In [12], it was shown that the emissivity model proposed by [14] correctly predicts the measured foam emissivities at L-band provided some auxiliary parameter describing the foam-water system are tuned. The purpose of this section is to document this forward foam emissivity model, which is used here to provide foam impact corrections in the version of the SSS retrieval algorithm used at launch of the ESA's Soil Moisture and Ocean Salinity (SMOS) satellite mission.

As proposed by [13], foam formations contribute to the total sea surface brigthness temperature measured by a radiometer as function of wind speed WS following:

$$T_{b,foam}(f, p, \theta_i, WS) = T_s \cdot \int e^{\text{typ}}{}_{\text{foam;p}}(f, p, \theta_i, h) \cdot F(WS, h) dh \quad (1)$$

where

- f, p and θ_i are the receiving electromagnetic frequency, polarization and incidence angle of the radiometer respectively,

- $F(WS, h)$ is the fraction of sea surface area covered by whitecaps with thickness h at wind speed WS,

- T_s is the physical tempearture of foam, usually assumed the same as the bulk sea surface temperature and,

- $e^{typ}{}_{foam}$ is the emissivity of typical sea foam-layer with thickness δ

This model is used in the present algorithm to provide foam impact corrections for SMOS. It contains two submodels: one to parametrize the emissivity of typical sea foam-layer with thickness h and the second to model the fraction of sea surface area covered by whitecaps with thickness h at wind speed *WS*. Both of them are successively detailed hereafter.

4.5.1.2. Emissivity modeling of the foam-water system

Following Guo et al. [6], it is assumed that foam on the ocean surface is composed of nearly spherical coated bubbles described by an outer radius r, made of an air core with permittivity ε_a, surrounded by a shell of sea water with thickness δ and permittivity ε_w. The foam covered ocean is modeled by the succession of three media: the air (region 0), a foam layer defined as a region of effective permittivity $\varepsilon_{N\alpha}$ with a layer thickness d (region 1), and the underlying seawater with some air bubbles (region 2) with permittivity ε_w. Boundaries between each region are assumed flat.

The emissivity of a typical foam-water system at incidence angle θ_i and polarization $p=$ h (horizontal) or v (vertical) is given by:

$$e^{\text{typ}}_{\text{foam;p}} = 1 - \left| R_p(\theta_i) \right|^2 \qquad (2)$$

where the coefficient R_p is the spectral reflection coefficient of the foam layer medium with the effective dielectric constant $\varepsilon_{N\alpha}$ and is given by

$$R_p(\theta_i) = \frac{R_p^{01}(\theta_i)e^{-j2\psi} + R_p^{12}(\theta_i)}{e^{-j2\psi} + R_p^{01}(\theta_i)R_p^{12}(\theta_i)}, \qquad (3)$$

where ψ is an attenuation factor that depends on the foam layer thickness d, the electromagnetic wavelength λ_0, and the effective permittivity $\varepsilon_{N\alpha}$:

$$\psi = \frac{2\pi d}{\lambda_0}\sqrt{\varepsilon_{N\alpha} - \sin^2\theta_i}, \qquad (4)$$

Note that for the foam-covered ocean, Stokes 3 and Stokes 4 = 0.

In Eq.(3), R_p^{01} are the Fresnel reflection coefficients between the air (region 0) and the foam (region 1):

$$R_h^{01}(\theta_i) = \frac{\cos(\theta_i) - \sqrt{\varepsilon_{N\alpha} - \sin^2\theta_i}}{\cos(\theta_i) + \sqrt{\varepsilon_{N\alpha} - \sin^2\theta_i}}, \qquad (5a)$$

and

$$R_v^{01}(\theta_i) = \frac{\varepsilon_{N\alpha}\cos(\theta_i) - \sqrt{\varepsilon_{N\alpha} - \sin^2\theta_i}}{\varepsilon_{N\alpha}\cos(\theta_i) + \sqrt{\varepsilon_{N\alpha} - \sin^2\theta_i}}, \qquad (5b)$$

and R_p^{12} are the Fresnel reflection coefficients between foam (region 1) and water (region 2):

$$R_h^{12}(\theta_i) = \frac{\sqrt{\varepsilon_{N\alpha} - \sin^2(\theta_i)} - \sqrt{\varepsilon_w - \sin^2\theta_i}}{\sqrt{\varepsilon_{N\alpha} - \sin^2(\theta_i)} + \sqrt{\varepsilon_w - \sin^2\theta_i}}, \qquad (6a)$$

and

$$R_h^{12}(\theta_i) = \frac{\varepsilon_w \sqrt{\varepsilon_{N\alpha} - \sin^2(\theta_i)} - \varepsilon_{N\alpha} \sqrt{\varepsilon_w - \sin^2 \theta_i}}{\varepsilon_w \sqrt{\varepsilon_{N\alpha} - \sin^2(\theta_i)} + \varepsilon_{N\alpha} \sqrt{\varepsilon_w - \sin^2 \theta_i}} . \tag{6b}$$

Region 2 consists of air bubbles embedded in the ocean background and is assumed to be absorptive. To solve the previous equations (2-6), one needs to define an effective permittivity for region 1, namely $\varepsilon_{N\alpha}$, and for region 2, namely ε_w.

The main parameter of the previous multi-layer emissivity model for foam is the effective permittivity $\varepsilon_{N\alpha}$ of the foam-layer considered. To define this parameter, the well-known *Lorenz-Lorentz* and *Hulst* equations can be used and modified for the poly-dispersed system of bubbles. The first formula takes into account *dipole interaction* of bubbles in a close-packed dispersed system (the quasi static approximation). The Hulst equations describe the contribution of the *multi-pole moment* of bubbles into effective permittivity of the system. Spectral calculations by Cherny and Raizer [15] show that first resonant electromagnetic effects by Hulst's mechanism occur for bubbles radius $a \approx \lambda_o/4$. At L-band ($\lambda_0 = 21$ cm), this corresponds to bubble diameters on order of 10 cm. Such very large bubbles are extremely rare at the sea surface and therefore, the multi-pole mechanism may be neglected at L-band for which the dipole term might be considered only. In the present work, we use the dipole approximation model developed by Dombrovskiy and Raizer [16] to describe the effective permittivity of the system. It involves the use of a modification of the Lorenz-Lorentz equation and yields to the following simple formula for the complex effective permittivity $\varepsilon_{N\alpha}$ of a foam-layer [15, 16]:

$$\varepsilon_{N\alpha} = \frac{1 + \frac{8}{3}\pi \overline{N\alpha}}{1 - \frac{4}{3}\pi \overline{N\alpha}}, \tag{7}$$

where

$$\overline{N\alpha} = \frac{\kappa \int \alpha(r) p_f(r) dr}{\frac{4}{3} \int r^3 p_f(r) dr}, \tag{8}$$

and N is the volumetric concentration of the bubbles, $\alpha(r)$ is the complex polarizability of a single bubble with external radius r, κ is the so-called packing coefficient or *stickiness parameter*, and $p_f(r)$ is the normalized probability distribution function of the bubbles' size.

In natural media such as foam, the densely packed particles can have adhesive forces that make them adhere to form aggregates. This effect is accounted for in the model by the *stickiness parameter* κ, which is inversely proportional to the strength of the attractive forces between bubbles [17].

According to Dombrovskiy and Raizer [16], the complex polarizability depends on the external radius of the bubbles r, the complex permittivity of the shell medium (salt water) ε_w, and the bubble's filling factor $q = 1 - \delta/r$ following

$$\alpha(r) = r^3 \frac{(\varepsilon_w - 1)(2\varepsilon_w + 1)(1 - q^3)}{(\varepsilon_w + 2)(2\varepsilon_w + 1)(1 - q^3) + 9\varepsilon_w q^3} . \tag{9}$$

85

Experimental measurements on stable foam reveal that the effective permittivity might be dependent on the vertical position within the foam layer, i.e., $\varepsilon_{N\alpha} = \varepsilon_{N\alpha}(z)$. In the simplest case, the foam-water system may be modeled as a succession of elementary foam-layers, each of them having a homogeneous effective dielectric constant. However, the exact dependence of such function with the vertical position, which depends on the vertical distribution of the bubble's size, is very poorly known. It is very likely that the vertical distribution of the bubble's size $p_f(r,z)$ is a function of the intensity and scale of the underlying breaking event. Moreover it will certainly strongly evolve during a transient breaking event. Nevertheless, in order to keep a tractable number of parameters in the present model, we choose to consider a uniform vertical distribution of bubbles sizes $p_f(r,z) = p_f(r)$ within the foam layer.

The foam void fraction (i.e., the ratio of the volume of air to the total volume of the foam) depends on the distribution of the bubble's filling factor q. Therefore, the distribution of bubbles radii $p_f(r)$ together with the distribution of coating thicknesses $f(\delta)$ determine the foam layer void fraction. In the present simplified model, we fixed the value of the shell thickness δ, but the outer bubble radius r is randomly distributed. According to Dombrovskiy [18], this approximation reflects an experimentally established fact for an emulsion layer of foam (young foam), but it requires verification for a foam with honeycomb structure (aged foam). Numerous observations of oceanic bubble size distributions are reported in the literature based on acoustic, photographic, optical, and holographic methods [19]. Currently, it is not clear how to parameterize the ocean surface bubble size distribution. Following Bordonskiy et al. [18] and Dombrovskskiy and Raizer [16], we used a Gamma distribution for the size distribution function of the bubbles:

$$p_f(r) = \frac{A^{B+1}}{\Gamma(B+1)} r^B e^{-Ar}, \qquad (10)$$

where A and B are parameters of the distribution defined with $r_p = A/B$ being the most probable radius. Finally, to calculate ε_w, a simple physical model based on induced dipoles is used. Let ε_{sw} denote the permittivity of the seawater at L-band, and f_a the fractional volume occupied by the air bubbles. Then, the effective permittivity ε_w, is given by the Maxwell-Garnett mixing formula [6]:

$$\varepsilon_w = \varepsilon_{sw} \frac{1 + 2 f_a y}{1 - f_a y}, \qquad (10)$$

where

$$y = \frac{1 - \varepsilon_{sw}}{1 + 2\varepsilon_{sw}}. \qquad (11)$$

Note that the effective permittivity ε_w here does not include scattering extinction, which is small due to the fact that the seawater is heavily absorptive.

According to our simplified model, the emissivity induced by a typical sea foam layer at L-band is a function of:

$$e^{typ}{}_{Bf} = function(\theta_i, p, T_s, r_p, \delta, \kappa, f_a, d, SSS, SST) \qquad (12)$$

where θ_i is the radiometer incidence angle, p is the polarization, T_s is the foam physical temperature, r_p is the most probable radius, δ is the bubble's water coating thickness, κ is

the bubble's packing coefficient, d is the foam layer thickness, f_a is the void fraction beneath the foam layer, and finally, SSS and SST are the sea surface salinity and temperature respectively.

4.5.1.3. Foam coverage Model

In [13], it was shown that the fractional sea surface covered by foam-layers with thicknesses between h and $h+dh$ at wind speed *WS,* namely, the term *F(WS,h)dh* in Equation (1), can be decomposed as follows:

$$dF(WS,h)=F(WS,h)dh= dF_c(WS,h)+ dF_s(WS,h) \qquad (13)$$

where $dF_c(WS,h)$ and $dF_s(WS,h)$ are the contributions to the coverage of actively breaking crests or active foam and of the passive foam, or static-foam formations (see [7] for detailed terminology), respectively.

The model which is used for these two terms is a modified form of that described in detail in [13], where the following empirical expression for $dF_c(WS,h)$ was derived:

$$dF_c(WS,h) = \left[2.9 \times 10^{-5} \cdot WS^3 \sqrt{h} \cdot e^{-4.48\sqrt{h}} dh \right] \times e^{(\alpha_c \Delta T - \beta_c)} \qquad (14)$$

where *WS* is the 10 meter height wind speed, α_c and β_c are numerical constants and ΔT is the air-sea temperature difference. Instead of using this form directly, however, we begin with empirical distribution functions for foam-generating breaker length per unit area per unit breaker speed interval as derived in [13] and then generalize these equations to accommodate improvement in the foam coverage distributions.

The breaker length distribution function is a modified form of that derived from measurements of Melville and Matusov (2002),

$$\Lambda(WS,c) = \tilde{A} \left(\frac{WS}{10} \right)^3 \times 3.3 \times 10^{-4} \cdot e^{-.64 \tilde{B} \left(\frac{c}{WS} \right)}$$

where $\tilde{A}$ and $\tilde{B}$ are constants to be specified. This distribution function differs from the empirical form of Melville and Matusov (2002) in that the exponent is a function of wave age rather than breaker phase speed.

Using the preceding formulation of the crest length distribution function, we can write the crest and static foam incremental coverages in terms of wind speed and breaker phase speed as

$$dF_c(WS,c) = \left[\frac{2\pi a_1}{g} c^2 \Lambda(WS,c) dc \right] \times e^{(\alpha_s \Delta T - \beta_s)}$$

and

$$dF_s(WS,c) = \left[\frac{2\pi a_2}{g} c^2 \Lambda(WS,c) dc \right] \times e^{(\alpha_s \Delta T - \beta_s)},$$

respectively. The final exponentials in the two previous equations are stability correction factors, which have a significant impact on the foam coverage. The free parameters in these correction factors are given fixed values. The constants a_1 and a_2 in the above equations are constants that reflect the persistence time of the foam layers, which is typically much larger for static than for crest foam.

In the modified formulation, we note that the incremental foam fractional coverage for both static and crest foam is a function of

- generating breaking front speed c,
- the 10 m wind speed, and
- the air-sea temperature difference.

The parameters α and β of the thermal correction factors were determined in [13] for both 'crest-foam' and 'static-foam' by best fitting the model to Monahan and Woolf [1989]'s empirical laws [19]. Using a least-square method, the determined numerical values for α and β are: $\alpha_c = 0.198$ and $\beta_c = 0.91$ for 'crest-foam coverage', and $\alpha_s = 0.086$ and $\beta_s = 0.38$ for 'static-foam coverage'.

To compute the total contribution of foam to the measured brightness temperature, we must determine the distribution of foam as a function of characteristic foam thickness, from which time dependence has been removed by assuming that foam layers associated with fronts moving at a given speed have equal probability of being at any stage of development. Using this assumption together with a simple model for the time dependence of foam layer depth, we obtain for crest foam the depth

$$\overline{\delta}_{\tau*}(c) = \frac{0.4c^2}{g},$$

and for static foam we obtain

$$\overline{\delta}_{\tau}(c) = \frac{0.4c}{2\pi a}\left[\frac{5c}{2g} + \tau'\left(1 - e^{-\frac{c}{g\tau'}(2\pi a - 5)}\right)\right].$$

In the above equations, g is the acceleration of gravity and c is the breaker phase speed, and τ' is the exponential decay time of the foam depth after the mean duration time of the breaking events (nominally taken to be 3.8 s for salt water). These expressions can be used to transform the differential foam coverage expressions into expressions for the incremental coverage per unit foam thickness.

4.5.2. Mathematical description

The total contribution of foam formations to the sea surface brigthness temperature measured at L-band as given in Eq. (1) will be mathematically expressed for implementation into the processor using:

1) Three Look-Up tables (LUTs) that will provide (1) the foam-induced sea surface brigthness temperature (one LUT1 for H and LUT2 for V polarization) and (2) an additional LUT (LUT3) that will also provide the total foam-coverage.

LUT1 and LUT2 will be provided as function of the following parameters (with associated ranges):

- the incidence angle θ_i at SMOS pixel [deg], (0 → 75°)

- the sea surface temperature T_s [K], (269.15 → 309.15 K)

- the prior sea surface salinity SSS [psu] (0 → 40 psu)

- the wind speed WS at 10 meter height [m/s],(0 → 30 m/s) and,

- the temperature difference between air at 2 m height and sea surface :
$\Delta T = T_s - T_a$, [°C]],(-30 → 30°C*)

LUT3 will be provided as function of the following parameters (with associated ranges):

- the wind speed WS at 10 meter height [m/s],and,

- the temperature difference between air at 2 m height and sea surface :
$\Delta T = T_s - T_a$, [°C]],(-30 → 30°C*)

LUT1 and LUT2 will provide directly Tb_foam (H or V) , expressed as the result of the integral in Eq. 1 times SST. The reason why we provide LUT3 as well is that in Eq 1, only incremental foam coverages dF as function of thickness are included and NOT the total foam coverage, namely F(U). However the processor will need the later to evaluate the total surface contribution including foam and no-foam surface contributions (flat+rough), as follows:

$$Tb_{surface} = (1-F)(Tb_{flat} + Tb_{rough}) + Tb_{foam}$$

Note that in the mathematical expression for $e^{typ}{}_{Bf,}$ the numerical values for r_p, the most probable bubble radius, for δ, the bubble's water coating thickness, for κ, the bubble's packing coefficient, and for f_a, the void fraction beneath the foam layer will be assigned constant values derived by best-tunning the model to the data observed during FROG campaign [12]. These values are not provided yet in the draft ATBD but will be given later.

2) Multi-dimensional interpolation schemes

Given the four values of the "geophysical" auxiliary parameters estimated at a given SMOS pixel, namely T_{si}, SSS_i, WS and ΔT, plus the series of incidence angles ($\theta_{i=1,...,N}$) associated to the L1C product considered, a multi-dimensional linear interpolation scheme will be applied to LUT1 ands LUT2 to evaluate, the values of $T_{Bf,i=1,...,N}{}^{(n)}$, at both H and V

polarization. An additional 2D cubic spline interpolation scheme will be applied to LUT3 as function of WS and ΔT, to determine the total foam coverage.

4.5.3. Error budget estimates

Inter-comparison between the FROG measurements [12] of the foam emissivities scaled at 100% coverage and the theoretical values computed with the model described above for $e^{typ}{}_{Bf}$ using as inputs the measured foam parameters have been perfomed in [12]. The values of the stickiness parameter κ, which were not measured during FROG, used in the model are the optimum ones found at each salinity, which in general increases with SSS as the bubbles are more densely packed.

The rms error between the measured data and the theoretical foam emissivity model was found to vary from 0.008 to 0.017 at H-polarization, and from 0.011 to 0.033 at V-polarization. In general the agreement is much better at H-polarization than at V-polarization. At V-polarization, the measured values show a larger variation with the incidence angle than the model predictions, which requires further analysis and refinement of the model. At H-polarization the agreement is excellent, except at low salinities, where there is a bias between the measured and predicted emissivites at all incidence angles.

A much higher uncertainty source in the model is the whitecap coverage model. Indeed, the model derived by [13] to parameterize $F(U,h)$ is constructed to match the empirical laws derived by [20]. Is is well known that extremeley large scatter in the whitecap coverage data as reported from one author to the other, which might yield to uncertainties of 100% to 600 % on empirical fits for $F(U,h)$. However, being the only source of validation we have, these empirical fits shall be used here as the basis for modeling.

Accounting for an error of 100% in the foam coverage and assuming a maximum coverage of 10%, we expect a maximum rms error budget on the foam emissivity contribution modelling of about:

$$Max(Rms\ error)\left(\begin{bmatrix} e^{typ}{}_{Bfh}(\theta_i) \\ e^{typ}{}_{Bfv}(\theta_i) \end{bmatrix}\right) \leq \begin{bmatrix} 1.7 \times 10^{-3} \\ 3.3 \times 10^{-3} \end{bmatrix}$$

This transaltes into about 0.5 K and 0.9 K maximal errors at H and V polarization, respectively.

4.5.4. Practical consideration

The model is not expected to provide significant contribution for wind speeds less than about 10 m/s. We could practically consider to perform that correction only for wind speeds more than that threshold value, using the measurement discrimination.

Note as well that when foam correction is applied to SMOS Tbs, the foam-free surface contribution (i.e. flat sea surface+ roughness correction) as to be weighted by 1-F(U), the free foam fractional surface so that F is an output of the present forward model.

4.5.4.1. Calibration and validation

Calibration and validation of the forward foam emissivity model for roughness correction will be done during the comissionning phase, and later-on, by perfoming residual analysis of the future SMOS measurements and using a formalism proposed for and applied to NASA scatterometer (NSCAT), Special Sensor Microwave Imager (SSM/I) and ESA/ERS scatterometer measurements [see 21].

Using in situ SSS, SST and wind (TAO, Argo drifter+ satellite SST and winds and ECMWF model winds) and SMOS co-localized data, the first step will be to remove the modelled flat sea surface and free-foam roughness contributions from the SMOS surface bightness temperature data (i.e., corrected for atmospheric, ionospheric, galactic and sunglint conribution) in order to estimate the residual foam impact. This shall be done in selected ocean area with strong winds (southern ocean and North seas). The in situ and satellite SSS, SST and wind data will be the chosen reference. In addition, ECMWF analysis winds will be used as a thrid data source to completely determine the errors via a multiple collocation analysis. The main objective will be to present observed correlations between regional and seasonal model predictions of the foam correction factors errors and nonwind oceanic and atmospheric factors such as the surface current and sea state. Following the methodology applied in [30], we shall explicitly take into account the errors in the reference datasets as well as in the foam correction factors retrieved estimates. The gain shall come in more accurate assessment of bias and variance and less possible systematic contamination that can obscur geophysically driven impacts not accounted for by the foam model.

4.5.4.2. Quality control and diagnostics

As explained in section 4.5.5 below, the foam correction model based on fixed geophysical parameters (bubbles radius, stickiness factors, etc ..) which might generate biases on the estimated correction.

The model can be applied as it is at launch but we expect that the CAL/VAL activities will provide after commissioning phase a possible tuning for these parameters.

4.5.4.3. Exception handling

In presence of very stormy conditions (Hurricane like situations) it is likely that high foam coverage will be associated with high rain rates. Foam correction in that case would be non-physical if no atmospheric correction to account for rain absorptivity is also provided by the processor.

If some parameter goes out of LUT range during the retrieval, a flag (Fg_OoR_Foam_dim1_WS, Fg_OoR_Foam_dim2_TseaAir, Fg_OoR_Foam_dim3_SSS, Fg_OoR_Foam_dim4_SST, Fg_OoR_Foam_dim5_Theta) is raised. No extrapolation is done and the boundary value is taken.

4.5.5. Assumption and limitations

*: Note that there is no impact of stratification when atmopshere is stable, i.e., $\Delta T < 0$ so that, the tables will be computed only for ranges where it has an impact and where the model is

thought to be valid, i.e., $\Delta T: 0 \rightarrow 15°C$. Out of this range, the LUTS will duplicate values at extreme borders of the validity range.

A strong limitation may come from the fact that the numerical values for r_p, the most probable bubble radius, for δ, the bubble's water coating thickness, for κ, the bubble's packing coefficient, and for f_a, the void fraction beneath the foam layer are assigned constant values derived by best-tunning the model to the data observed during FROG campaign [12]. This is a strong assumption, as these parameters clearly evolve as function of the synoptic wind and wave forcing conditions.

This foam contribution can be applied to the Tb roughness correction modelled according to modules 4.2 or 4.3 (it has no sense in the empirical option 4.4). A switch will be established for selection (based on a threshold for wind speed) and a flag raised to describe if foam contribution has been taken into account (Fg_ctrl_foam_MX.true, X=1,2).

References

[1] Rosenkranz, P. W., and D. H. Staelin, Microwave emissivity of ocean foam and its effect on nadiral radiometric measurements, J. Geophys. Res., 77, 6528-6537, 1972.

[2] Stogryn, A., The emissivity of sea foam at microwave frequencies, J. Geophys. Res., 779, 1658-1666, 1972.

[3] Ross, D. B., and V. Cardone, Observations of oceanic whitecaps and their relation to remote measurements of surface wind speed, J. Geophys. Res., 79, 444-452, 1974.

[4] Smith, P. M., The emissivity of sea foam at 19 and 37 ghz, IEEE Trans. Geosci. and Remote Sens., 26, 541-547, 1988.

[5] Kunkee, D. B., and A. J. Gasiewski, Simulation of passive microwave wind direction signatures over the ocean using an asymmetric-wave geometrical optics model, Radio Sci., 32, 59-78, 1997.

[6] Guo, J., L. Tsang, W. Asher, K.-H. Ding, and C.-T. Chen, Applications of dense media radiative transfer theory for passivemicrowave remote sensing of foam covered ocean, IEEE Trans.Geosci. and Remote Sens., 39, 1019-1027, 2001.

|7] Monahan, E., Oceanic whitecaps: Sea surface features detectable via satellite that are indicators of the air-sea gas transfer coefficient, in Proc. Indian Acad. Sci. (Earth Planet Sci.), vol.111, pp. 315-319, 2002.

[8] Anguelova, M., Whitecaps, sea-salt aerosols, and climate, Ph.D. thesis, Graduate College of Marine Studies, University of Delaware, Lewes, Delaware, 2002.

[9] Droppleman, J. D., Apparent microwave emissivity of sea foam, J. Geophys. Res., 79,696-698, 1970.

[10] Barber, R. P., and J. Wu, Sea brightness temperature effects of spray and whitecaps, J. Geophys. Res., 102, 5823-5827, 1997.

[11] A. Camps, J. Font, M. Vall-llossera, C. Gabarro, R. Villarino, L. Enrique, J. Miranda, I. Corbella, N. Duo, F. Torres, S. Blanch, J. Arenas, A. Julia, J.Etcheto, V. Caselles, A. Weill, J. Boutin, S. Contardo, R. Niclos, R. Rivas, S. Reising, P. Wursteisen, M. Berger, and M. Martn-Neira, The WISE 2000 and 2001 Campaigns in support of the SMOS Mission: Sea surface L-band Brightness Temperature Observations and their application to Multi- Angular Salinity Retrieval, *IEEE Trans. Geosci. Remote Sensing*, vol. 42, no. 4, pp. 1039-1048, 2004.

[12] A. Camps, M. Vall-llossera, R. Villarino, N. Reul, B. Chapron, I. Corbella, N. Duff, F. Torres'J. Miranda, R. Sabia, A. Monerris, R. Rodríguez, "The Emissivity Of Foam-Covered

Water Surface at L-Band: Theoretical Modeling And Experimental Results From The Frog 2003 Field Experiment", *IEEE Transactions on Geoscience and Remote Sensing*, vol 43, No 5, pp 925-937, 2005.

[13] N.Reul and B. Chapron, "A model of sea-foam thickness distribution for passive microwave remote sensing applications", *J. Geophys. Res.,* 108 (C10), Oct, 2003.

[14] N.Reul and B. Chapron, "Effects of foam on the emissivity of the sea surface at L-band", WP1300 Report, ESA contract N°15165/01/NL/SF, April 2001.

[15] V. Cherny and V. Y. Raizer, *Passive Microwave Remote Sensing of Oceans*, wiley-praxis series in remote sensing ed. Wiley, 1998.

[16] Dombrovskiy, L. A., and V. Y. Raizer, Microwave model of a two-phase medium at the ocean surface*, Izvestiya, Atmospheric and Oceanic Physics*, 28, 650-656, 1992.

[17] L. M. Zurk, L. Tsang, K. H. Ding, and D. P. Winebrenner, .Monte carlo simulations of the extinction rate of densely packed spheres with clustered and non-clustered geometries,. *J. Opt. Soc. America*, vol. 12, pp. 1772.1781, Aug. 1995.

[18] L. A. Dombrovskiy, .Calculation of the thermal radiation emission of foam on the sea surface,. *Izvestiya, Atmospheric and Oceanic Physics*, vol. 15, no. 3, pp. 193.198, 1979.

[19] J. Wu, .Variation of whitecap coverage with wind stress and water temperature. *J. Phys. Oceanogr.*, vol. 18, pp. 1448.1453, 1988.

[20] Monahan, E., and D. K. Woolf, Comments on variations of white-cap coverage with wind stress and water temperature, J. Phys.Oceanogr., 19, 706-709, 1989.

[21] Y. Quilfen, B. Chapron and D. Vandemark, "The ERS Scatterometer Wind measurement accuracy: evidence of seasonal and regional biases", *Journal of Atmopsheric and Oceanic Technology*, vol 18, p 1684-1697, 2001.

4.6. Galactic noise contamination 1

4.6.1. Theoretical description

This section has been written with the help of [*LeVine and Abraham,* 2004] and [*Delahaye et al.,* 2002] papers.

A new approach (Galactic noise 2) to the celestial sky glitter correction has been proposed in September 2006 and included as section 4.7. The simplistic case of a constant galactic noise of 3.7 K (Galactic noise 0) is also used in a milimalist model (see section 4.10).

4.6.1.1. Physics of the problem

At L-band, radiation from celestial sources is strong and spatially variable; they have been reviewed by *Delahaye et al.* (2002), *Le Vine and Abraham* (2004), and associated corrections needed to interpret L-band radiometric measurements have been thoroughly described by *Le Vine and Abraham* (2004). Radiation originates from three types of sources. The hydrogen line emission corresponds to a hyperfine atomic transition in neutral hydrogen: the radiation is maximum around the plane of the galaxy, most of the time less than 2 K. The cosmic background is a remnant signal of the origin of the universe and is almost constant in space and time (2.7 K). In addition to the almost constant cosmic background, a very variable (in space) continuum radiation (up to more than 10 K) is due to emissions from discrete radiosources.

As in the case of atmospheric emission, the cosmic background adds a contribution to the radiometric temperature that depends on the incidence angle linked to the reflection of the signal on the sea surface.

The two other types of sources add a signal that varies according to the incidence and azimuth angle of the measurement.

4.6.1.2. Mathematical description of algorithm

4.6.1.2.1. Data conversion

The common practice in passive microwave remote sensing of the earth is to consider equivalent brightness temperatures. Thence, for the purpose of L-band radiometry, it is common to present data from radioastronomy surveys in the form of equivalent black-body temperatures, i.e., as if they were from an equivalent thermal source with total power:

$$P = k\,Tb\,\Delta B \tag{1}$$

where k is the Boltzmann constant and ΔB is the bandwidth of the receiver used for the survey, or as a total power integrated over a frequency range as in the case of the hydrogen line emission.

a) Hydrogen Line emission:
The line emission has a relatively narrow spectrum. For hydrogen at rest, it occurs at a frequency associated with the hyperfine transition at 21.106cm. However the line is shifted by the motion of the hydrogen relative to the observer (Doppler shift) and spread by thermal

energy of the gas (collisions and vibrations). Nevertheless the spectrum is relatively narrow: Leiden/Dwingeloo survey (Hartmann and Burton 1997) in the Northern hemisphere and IAR survey in the southern hemisphere (Arnal, Bajaja et al. 2000) cover the velocity range from -450 to +400km/s which corresponds to a frequency range of 4.025MHz (see below) about the center frequency of 1.42GHz of hydrogen at rest. The integrated power reported in radioastronomy survey, P, is given in Kelvin kilometers per second (K-km/s). In order to convert it to a brightness temperature that will be recorded by a radiometer having a bandwidth ΔB, it is necessary to convert it in Kelvin-MHz using the line emission bandwidth and then to calibrate it with respect to the radiometer bandwidth.

Given the standard form for Doppler shift:

$$\nu = \nu_0 (1 - v/c) \tag{2}$$

with ν_0 the center frequency (1.42GHz), ν the frequency associated with the velocity v and c the light speed, a velocity range from -450 to +400km/s corresponds to a frequency bandwidth of 4.025MHz.

Thence the integrated power reported in radioastronomy survey corresponding to a velocity range of 850km/s, Pint, can be converted in Kelvin-MHz using:

$$\text{Pint(K-MHz)} = \text{Pint(K-km/s)} . 4.025/850 = \text{Pint(K-km/s)} . 4.735 \ 10^{-3} \tag{3}$$

Since the SMOS radiometer bandwidth, ΔBsmos in MHz, is well above 4MHz, this value can be converted to get an equivalent Tb for SMOS, as follows:

$$\text{Tb} = \text{Pint(K-MHz)}/\Delta\text{Bsmos} = \text{Pint(K-km/s)} . 4.735 \ 10^{-3} /\Delta\text{Bsmos} \tag{4}$$

b) Continuum radiation and cosmic background

These radiations are usually given in terms of effective brightness temperature, Tb, i.e. they include the correction for the bandwith of the survey (e.g. Reich and Reich maps). Thence, as these radiations are supposed to be homogeneous over the frequency range of SMOS bandwidth, there is no need to correct Tb deduced from radioastronomy surveys.

4.6.1.2.2. Galactic noise reflected towards the radiometer

In the following we will call the effective brightness temperature of the galactic radiation, Tbgal, as the sum of the hydrogen emission line plus the continuum radiation plus the cosmic background.

First it is necessary to determine the location in the celestial sky from which incident radiation will be reflected from one point in the field of view into the antenna. Given ϑ_i and φ_i respectively the incidence and the azimuth (0 towards the north; positive westward) angles of one radiometer measurement at this point, the incident galactic ray that will be specularly reflected towards the radiometer comes from an incidence angle, ϑ_{igal}:

$$\vartheta_{igal} = Arc\sin\left(\frac{\text{Re} + h_{rad}}{\text{Re}} \sin(\vartheta_i) \right) \tag{5}$$

where Re is the earth radius and h_{rad} is the altitude of the radiometer.

The elevation angle (in degrees; 0 towards the horizon and positive above the horizon) is defined as:

$$el = 90 - \vartheta_{igal} \tag{6}$$

Usually celestial maps are given in celestial coordinates system (declination, δ, and right ascension, α). It is therefore necessary to derive δ and α from the latitude, lat, longitude, lon, sideral time, T, ϑ_i and φ_i. This can be done by solving the following implicit equations:

$$\tan(\varphi) = \frac{-\sin(H)}{\tan(\delta)\cos(lat) - \cos(H)\sin(lat)} \tag{7}$$

$$\sin(el) = \sin(lat)\sin(\delta) + \cos(lat)\cos(\delta)\cos(H) \tag{8}$$

where H is the sidereal angle (see for instance Appendix C of *Le Vine and Abraham* (2004)) defined as:

H= T-lon-α

In the following we consider two cases:

a) a simple case assuming a rough sea and an homogeneous sky

b) a more complicated case where we take into account the sea surface roughness and the sky inhomogeneity.

In the following we will distinguish two polarizations for Tbgal. At present, existing galactic maps do not distinguish between V and H pol but there is suspicion about a possible polarization dependency.

a) Assuming an homogeneous sky:

In that case the contribution of roughness to the reflectance coefficient Γ, Rrough, computed for estimating Tbrough, can be used:

Tbgal_refl(lat,lon, T, ϑ_i , φ_i,p) =Tbgal(δ,α,p).(R(ϑ_{igal}, SSS, SST,p) +Rrough(ϑ_{igal} , SSS, SST,p)) (9)

where Rrough=-Tb rough/SST (Rrough is negative) (10)

If the sky were homogeneous, it is expected that the introduction of the roughness would have a small effect in most cases: for instance, for a 10m/s wind speed, (the reflection coefficient is modified by about 2.5% (at nadir)) and a galactic noise of 5K, neglecting the roughness effect would introduce an error of less than 0.08K.

b) Assuming an inhomogeneous sky:

Introducing bistatic reflection coefficients that can be extracted from 2-scale or from SSA models, σ_0 , in theory the galactic noise over the whole sky should be convoluted with these scattering coefficients. However since they are expected to decrease rapidly outside of the specular reflection, the integration could be done over an interval +/-dϑ_{igal} which value will be specified in the TGRD

$$\text{Tbgal\_refl(lat,lon, T, }\vartheta_1^a,\varphi_i,\text{v}) = \frac{1}{4\pi\cos(\vartheta_i)}$$

$$\int_0^{2\Pi} \int_{\vartheta_{igal}}^{\vartheta_{igal}+\delta\vartheta_s} \left(\sigma_{vv}^0(\vartheta_s,\varphi_s,\vartheta_i,\varphi_i)Tbgal(\vartheta_s,\varphi_s,\text{v}) + \sigma_{vh}^0(\vartheta_s,\varphi_s,\vartheta_i,\varphi_i)Tbgal(\vartheta_s,\varphi_s,\text{h}) \right)\sin(\vartheta_s)d\vartheta_s d\varphi_s$$

$$\text{Tbgal\_refl(lat,lon, T, }\vartheta_1^a,\varphi_i,\text{h}) = \frac{1}{4\pi\cos(\vartheta_i)}$$

(11)

$$\int_0^{2\Pi} \int_{\vartheta_{igal}}^{\vartheta_{igal}+\delta\vartheta_s} \left(\sigma_{hh}^0(\vartheta_s,\varphi_s,\vartheta_i,\varphi_i)Tbgal(\vartheta_s,\varphi_s,\text{h}) + \sigma_{hv}^0(\vartheta_s,\varphi_s,\vartheta_i,\varphi_i)Tbgal(\vartheta_s,\varphi_s,\text{v}) \right)\sin(\vartheta_s)d\vartheta_s d\varphi_s$$

Both cases a) and b) should be kept. A switch will allow to select the desired case.

4.6.1.2.3. Integration over the antenna beam

In addition it is necessary to integrate the reflected brightness temperature over the antenna pattern to obtain Tbgal_refl_lobe, which is the quantity measured by the radiometer:

$$\text{Tbgal\_refl\_lobe}(\vartheta_i,\varphi_i) = \int_0^{2\Pi} d\varphi_i \int_{\vartheta_i-\Pi/2}^{\vartheta_i+\Pi/2} d\vartheta_i' \int \text{Tbgal\_refl}(\vartheta_i')P_{lobe}(\vartheta_i'-\vartheta_i,\varphi_i)$$

(12)

where Plobe is the normalized power pattern of the antenna. In case Plobe is an axially symmetric pattern, according to *Le Vine and Abraham* (2004) it is possible to make the integration on δ and α and thence to precalculate galactic maps integrated over the antenna pattern before computing the reflection over the sea surface. Since the SMOS lobe varies accross the FOV and is not symmetric, it will be necessary to test if such an approximation is acceptable.

4.6.1.3. Error budget estimates (sensitivity analysis)

The main uncertainty is expected to come from inaccuracies of the galactic noise maps. (Reich and Reich 1986) estimate the accuracy on their maps (due to the calibration of the instrument) of 0.5K. From SRS study, a constant bias of 0.5K on galactic noise map will induce a mean bias on retrieved SSS of 1psu.
In addition to a constant bias, uncertainties are likely to appear on these maps close to the equatorial galactic plane. Comparisons between the maps derived from the Stokert survey, commonly called the Reich and Reich map, and the ones deduced from the Effelsberg survey are in progress to better apprehend the error on these maps. Both maps include the continuum radiation and the cosmic background; Stockert survey was performed with a 34mn angular resolution instrument while Effelsberg used a 9mn angular resolution instrument. Stockert map for the northern hemisphere and Effelsberg maps are available on the http://www.mpifr-bonn.mpg.de/survey.html site; the Stokert map for southern hemisphere was provided by ESA. Stockert maps are global but region around Cassiopeia is excluded (no data) and strong sources are suspected to be underestimated; Effelsberg survey is concentrated close to the equatorial plane (Cygnus excluded).

4.6.2. Practical considerations

4.6.2.1. Calibration and validation

As suggested before, it may be necessary to introduce a calibration factor proportional to Tbgal during the Cal/Val phase to correct for calibration and saturation problems of the existing surveys.

4.6.2.2. Quality control and diagnostics

Looking towards North (azimuth=0) with an incidence angle equal to the elevation of the observer, one looks towards the celestial North pole which location is invariant.

4.6.2.3. Exception handling

If a parameter goes out of LUT range during the retrieval, a flag (Fg_OoR_dim1_gam1_dec, Fg_OoR_gam1_ra) is raised. No extrapolation is done and the boundary value is taken.

4.6.3. Assumption and limitations

Depending on the reliability we can put on galactic noise maps, it could be necessary to discard some SMOS Tb affected by radiation coming from the galactic plane if it is demonstrated that this radiation is very badly known. Tests are in progress to estimate the impact of radiation errors in the galactic plane (as estimated from the difference between Effelsberg and Stockert surveys) on the retrieved SSS. Measurements affected by errors in the determination of the galactic noise will be flagged by Fm_gal_noise_error (if the error is above Tm_max_gal_noise_error). For further analysis, if necessary, measurements with high galactic noise (above Tm_high_gal_noise) will be flagged with Fm_high_gal_noise.

References

Arnal, E.M., E. Bajaja, J.J. Lararte, R. Morras, and W.J.L. Poppel, A high sensitivity HI survey of the sky at δ<=−25°, *Astron. Astrophys. Suppl. Series*, *142*, 35-40, 2000.

Delahaye, J.Y., P. Golé, and P. Waldteufel, Calibration error of L-band sky-looking ground-based radiometers, *RadioSci.*, *37*, 10.1029/2001RS002490, 2002.

Hartmann, D., and W.B. Burton, *Atlas of galactic neutral hydrogen*, 235 pp., Cambridge university press, New York, 1997.

LeVine, D.M., and S. Abraham, Galactic noise and passive microwave remote sensing from space at L-Band, *IEEE Transactions on Geoscience and Remote Sensing*, *42*, 119-129, 2004.

Reich, P., and W. Reich, A radio continuum survey of the northern sky at 1420 MHz, *Astron. Astrophys. Suppl. Ser.*, *63*, 205-292, 1986.

4.7 Galactic noise contamination 2

4.7.1. Overview of the Problem

Estimation of the down-welling celestial sky radiation at L-band that is scattered by the sea surface and sense by earth viewing radiometers, hereafter referred to as the *sky glitter* phenomenon, is of particular concern for the remote sensing of sea surface salinity (SSS)[1], [2], [3]. At L-band, celestial sky radiation originates from the uniform Cosmic Microwave Background (about 2.7 K), hereafter denoted *CMB*, the line emission from hydrogen and a continuum background [3], [4]. Sea surface scattered sky radiation might hamper accurate SSS retrievals from spaceborne measurements of up welling sea surface brightness temperatures at L-band mainly because of three factors:

First, the expected dynamical range of sea surface brightness temperature (T_b) change at L-band due to SSS variation is relatively small, being in average smaller than about 4 K for open ocean conditions. The T_b sensitivity to salinity indeed ranges from about 0.2 K to 0.8 K per psu in that microwave band [2] (depending on ocean surface temperature, considered incidence angle and polarization), and the open ocean salinities are generally in the range between 32 and 37 psu.

Second, although the sky glitter contribution to the effective brightness temperature measured by an L-band radiometer antenna depends on the sources intensity, the surface conditions, the observation geometry and the antenna characteristics (e.g., beam width, gain pattern), it can be of the same order or even greater than the surface salinity impact. For instance, it was found by [3] that the total effective background radiation (sum of line emission, continuum and CMB weighted by the antenna gain pattern) at the locus of the reflected rays on the sky, assuming a surface reflectivity of 1 and for a sun-synchronous orbiting antenna with a beam width on the order of 10°, an orbit inclination of 95° and a 6 A.M./6 P.M. equatorial crossing time, changes from a little less than 4 K to more than 9 K. The potential changes within that range are functions of the orientation of the sensor, the spacecraft location along the orbit and the time of year. Accounting for the fact that the actual ocean surface reflectivity may range from about 30 % to 80 % at 1.4 GHz (depending on the sea surface physical state, the polarization and bistatic configuration considered), celestial sky glitter contribution is expected to vary between about 1 to more than 7 K, which is very significant with respect to the surface salinity signature.

Third, the line emission from hydrogen and the continuum background exhibit sources that are spatially varying, being strongest in the direction of the plane of the galaxy and at several localized strong spots (Cassiopeia A, Cygnus A, ...). Given the relative motion between the sun-synchronous satellite's orbit, the earth and the celestial sky during a year, sky glitter contamination is expected to be geographically and seasonally variable. Corrections strategies for this contamination are therfore needed to be able retrieving unbiased large scale seasonal and geographical features of the global SSS field using the iterative optimization method.

For the SMOS mission, the multi-directional character of the surface brightness temperature

sensing and the large spatial extent of the swath reinforce the need to make accurate corrections for this contribution in the salinity data processing. Ideally, in order to reach 0.1 psu accuracy on the Level 2 retrieved salinity, the sky glitter contribution would need to be estimated with an uncertainty better than about 0.05 K. However, this represent a drastic constraint with regard to the respective accuracy of either the future SMOS radiometric measurements or the available sky brightness temperature maps. Rough sea surface-microwave interaction models at L-band is another important source of uncertainty in evaluating such contribution. Nevertheless, a physically based forward model is required to anticipate all major expected dependencies of the sky glitter contamination and *in fine* minimize potential biases in the SSS retrieval.

To correct for reflected sky noise in radiometric data acquired during scientific campaigns performed in the frame of the SMOS and Aquarius/SAC-D mission preparation, the perfectly smooth ocean surface assumption has been extensively used by authors ([11]-[14]). Same assumption was used in [2], [3] and [15] to provide preliminary estimate of the expected sky radiation contamination for the future Aquarius/SAC-D and SMOS missions, respectively. In such approach, the locii on the celestial sphere of the specular rays with respect to the radiometer observation direction within the antenna pattern are first determined. The high-resolution T_{sky} map is then weighted by the considered sensor antenna gain pattern, multiplied by the flat sea surface reflectivity computed from the observed Earth target salinity and surface temperature, polarization and incidence angle and finally integrated over the antenna pattern.

Over a flat sea surface, the L-band reflectivity varies from about 50 % to 80 % for incidence angles below 60°. Combining available radiometric data collected at L-band in that incidence angle range over water surfaces [12]-[14] (see figures in the ATBD section describing the SSA/SPM roughness correction), the absolute surface emissivity (and therefore reflectivity) sensitivity to wind speed is never observed to exceed about $2x10^{-3}$ /m/s at L-band. This translates, for a 10 m/s increase in wind speed, into a reflectivity decrease by less than 2 % compared to perfectly flat sea surface. Therefore, if the sky sources were assumed spatially uniform, sea surface roughness impact on the reflected sky contamination would be relatively small. However, sky radiation are not spatially uniform and as observed during the airborne LOSAC campaign [11], optimal correction of the radiometric data involved removing reflected galactic noise with an effective reflection coefficient varying between 0.6 and 0.9 times Fresnel coefficients for wind speeds from 20 to 0 m/s, respectively. This effect, which might correspond to up to a 40 % decrease in reflected signal intensity compared to a flat sea, is mostly a consequence of the angular spreading and associated attenuation of directional reflectivity in presence of roughness. Accounting for the roughness impact on the estimated reflected sky contamination is therefore an important issue for SSS remote sensing. In the following, we describe an efficient method for operational implementation of a correction taking into account the rough sea surface scattering impact.

We first recall the generation of the L-band Sky map to be used for SMOS data processing. This is basically a reproduction of the note by N. Floury. (This part might latter go in the TGRD section).

In order to place the scattering calculations in context, and to reveal any assumptions made in the development, in a second section, we first trace the path of the galactic radiation from the

source through the atmosphere to the scattering surface, and then back up to the radiometer. We summarize all of the transformations required to calculate the expected impact at the radiometer in terms of the incoming signal for the specific case of assumed unpolarized sky map. We then discuss integration of the signal over the antenna gain pattern. As part of this discussion, we review formulations of the sky glitter contribution for SMOS at antenna level assuming the surface is either rough or flat, since a specific transport processing is required for each case.

Next, we detail the rough surface and electromagnetic scattering models we employ in the calculations and review the geometry involved in the calculation. This is a key aspect of the development of the proposed efficient method for operational implementation of the correction.

The representation of the scattered signal, given the geometry of the problem is further described. In this context, we introduce a parametrization in terms of an orientation angle, ψ_{uh}, which, roughly speaking, is the orientation of the scattering upper hemisphere in the celestial frame. With this new variable, we detail a fast method of calculating the surface scattered signal in terms of zeroth and second harmonics of the wind direction given as input to the processor in precomputed Look up Tables. As demonstrated, due to the spatially nonhomogeneous sky, the latter wind direction harmonics can indeed have significant impact on the azimuthal behaviour of the overall L1C signal. We present an overview of the structure of the lookup tables to be used for the processing. The generation method for the LUTs is described in detail in the associated TGRD document.

Detail analysis of the sky glitter model features, comparison with flat sea surface model predictions for SMOS, accuracy of the approximate fast processing method, and expected seasonal and geographical contamination derived from orbit propagation simulation over a year are given in an Ifremer technical note that will be provided to the team soon (reference shall be updated as soon as done).

4.7.2. Generation of an L-band Sky map to be used for SMOS data processing

4.7.2.1 Overview

In [3], a method was presented to produce assumed unpolarized map of the equivalent brightness temperature of radiation at L-band from the *CMB* (herafter denoted T_{CMB}), from the Hydrogen line (T_{HI}), and from the continuum background (T_{cont}), based on recent radio astronomy surveys ([5]-[10]). In the following, we denote T_{sky} the sum of the three contributions. Such map for T_{sky} includes T_{HI} and T_{cont} contributions with sufficient spatial resolution (0.25°x0.25°) and radiometric accuracy to be relevant for remote sensing applications. Note that authors of the continuum radio astronomy surveys used in [3] mentioned that some strong sources were not included in their continuum map. This is for example the case of Cassiopeia A which peculiarities (high power flux) made it impossible to be measured accurately through the standard procedure. Nevertheless, it was shown in [4] that to first order, the model given in [3], is consistent with measurements made with several modern remote sensing instruments directly pointing towards the sky, although the data

suggest a slight polarization signature. The agreement is particularly good (RMS differences of 0.05-0.10 K) if small changes in the level (bias) of the radiometer measurements are permitted. Without such adjustments, agreement is obtained to within 0.5 K even in the worst case.

In the general context of the SMOS data processing, a sky brightness temperature map at L-band was generated using an approach similar to [3]. Missing data (e.g. Cassiopeia A area) and other strong sources into the Reich and Reich continuum map might however induce underestimation of the reflected sky noise corrections, particularly over calm sea surfaces. To alleviate this problem and flag associated potential errors in the estimation of the sky noise contribution, an additional error map using higher resolution surveys identifying celestial sphere position and values of sources, which intensity are under evaluated in the sky map is generated. The complete sky map and associated error field generated to flag missing strong sources is described in the following.

Three components are required to build a map of the sky emission at L-band [3]:

• the hydrogen HI line: this strong emitting line is centered at 1420.4058 MHz ($\pm$ additional Doppler). It is usually rejected by a band-stop filter in surveys of the continuum,

• the continuum at ~1.4 GHz includes a variety of emission mechanisms (other lines than HI, synchrotron, free-free, thermal, blended emission of discrete radio sources ...), and,

• the Cosmic Microwave Background (quasi constant value of 2.725 K)

The equatorial system of coordinates (right ascension, declination) is used here to define the domain covered by existing surveys. The reference system used here is B1950.

4.7.2.2 Main sources of data

To provide a coverage of the whole sky, the datasets must combine observations from both the North and the South hemispheres. It is assumed that experts took care of all the issues related to this combination (cross calibration, overlap, angular resolution, etc ...)

Continuum

The dataset identified here is a combination of the North Sky survey made with the Stockert radio telescope ([5]-[7]) and the South Sky survey made with the radio telescope of the Instituto Argentino de Radioastronomia [9]. When the bandwidth of the receiver was overlapping the HI emission, a stop-band filter centered over the HI line and 2MHz wide was applied to the measurement to reject it. Data are sampled with a 0.25°x 0.25° resolution in declination $\times$ right ascension (equatorial coordinates, B1950 system). The sensitivity (defined as 3 $\times$ rms brightness temperature noise) of the merged dataset is 0.05K. In the following, this dataset will be referred as the Reich and Testori map.

It is assumed that the "continuum" signal is broadband and does not vary in this region of the spectrum. Thus, one can combine surveys made at slightly different center frequencies and

with slightly different bandwidths. The "continuum" dataset includes the 2.725K cosmic background.

Hydrogen line

The Leiden-Argentina-Bonn (LAB) dataset was used here [21]. The LAB survey contains the final data release of observations of 21-cm emission from Galactic neutral hydrogen over the entire sky, merging the Leiden/Dwingeloo Survey ([10]) of the sky north of –30° with the Instituto Argentino de Radioastronomia Survey ([8]) of the sky south of –25°. The velocity spans a range between -450 km/s and +400 km/s, with a resolution of 1.3km/s. The rms brightness temperature noise of the merged dataset is 0.07-0.09K (for each 1.3 km/s layer). Data are sampled with a 0.5° x 0.5° resolution in latitude × longitude (galactic coordinates). This dataset will be referred in the following as the HI map.

Integration of HI into the continuum map

SMOS measures a bandwidth B_{SMOS} of 19MHz that includes the HI line (1420.4058 MHz) so that the latter has to be integrated into the continuum map in the context of SMOS data processing. The continuum signal is broadband, with almost constant brightness levels, herafter denoted T_{cont}, over SMOS bandwidth. It is understood that the data in (Reich & Testori) includes T_{cont} as well as the 2.725K cosmic background T_{CMB}, while HI data ([21]) does not include T_{CMB}.

To derive HI-line contribution over SMOS bandwith from HI line velocity range data, we used a Doppler relation between velocity range and frequency shift. The HI line frequency is f_o =1420.4058 MHz. The relation between frequency f and velocity v is given by the Doppler shift

$$f = f_o \left(\frac{c}{c+v} \right) \qquad (1)$$

with c the speed of light and v the speed of the source relative to the observer (positive away from observer). The stopband filter applied to the Reich & Reich measurements is centered on f_o and is B_{HI} =2MHz wide. This corresponds to a velocity range of [-211.2 km s_{-1}, +211.4 km s $_{-1}$]. Over this bandwidth, the contribution of HI signal is:

$$T_{HI}^{2MHz} = \frac{1}{(211.4+211.2)} \int_{-211.2km/s}^{211.4km/s} T_{HI}(v) dv \qquad (6)$$

Finally, the resulting sky noise to be taken into account in SMOS measurement is

$$T_{sky} = T_{CMB} + T_{cont} + T_{HI}^{2MHz} \frac{B_{HI}}{B_{SMOS}}. \qquad (7)$$

Gaps in the continuum survey: use of alternative surveys and source catalogs for missing data integration

Some areas of the Reich and Testori continuum survey are void of data; this is for example the case of Cassiopeia A which peculiarities (high power flux) made it impossible to be measured accurately through the standard procedure. Similarly, it may be that some strong

punctual sources are not properly taken into account in the continuum survey. Higher resolution surveys are available that can alleviate this problem by providing auxiliary 1.4GHz flux measurements for these problematic areas. These datasets usually come in two forms:

• higher resolution local sky maps where for a given area of the sky a radio flux is associated to each [right ascension, declination] cell. This enables to assess the slow variations of the background flux when it results from the combination of minor sources that cannot be individually identified. Once rescaled and converted to the proper geometry, these datasets can be used to patch the continuum map where data is missing.

• source catalogues that identify strong sources with small angular extensions and provide their total flux. These datasets can be useful to identify strong sources in otherwise quiet areas of the sky. Unfortunately, these high resolution surveys have still not been compiled into a global map of the radio sources of the sky. Several databases have thus been used here, with the related issues in terms of format / coordinate system / projection / units (main beam or full beam) and homogeneity of the available data. For example, the density of measurements available for the northern sky is larger than for the southern sky. See Appendix A for a discussion on the data from auxiliary surveys / catalogs used to generate the sky map.

1) Cassiopeia A area: In Reich and Testori map, the area around Cassiopeia has been left blank. There are two problems linked with this area:
• this remnant of a recent supernova presents a large angular extension, with a complex structure of its flux component,
• the measured flux varies in time Effelsberg survey [23], [24] was used here to give an idea of the spatial structure of the radio flux, but the complexity of this area and its temporal variations makes it unsuitable to accurate corrections without spending more effort on the analysis of the properties of this area (data are available on the temporal variation of the emission but are not considered in this algorithm). Consequently, the Reich & Testori map is complemented by the Effelsberg survey of the Cassiopeia area, rescaled (to the Tb for a 35 arcmin beam as in the Reich & Testori survey) and resampled (to the 0.25° pixel size). Moreover, an error Tb fields for the sky map was generated in which the Cassiopeia area is set to the rescaled and resampled value to flag the issue.

2) Other strong sources: One objective here is to check whether strong sources are properly taken into account in the Reich and Testori mapping. The authors mentioned that some strong sources (Orion A, Cygnus A, Taurus A, ...) were not included in the continuum map. In addition, it could be that measurement limitations or processing issues would reduce the intensity of some strong radio sources in the map. To check that the input of strong sources is well quantified, a map of strong sources is generated from L-band source catalogues [25], [26] and the corresponding brightness temperatures that would be collected by the Stockert/IAR radiotelescopes (35 arcmin beamwidth) is computed. These sources were extracted from the NVSS (North) and from the Parkes (South) catalogues. Here, individual sources stronger than 0.3 Jy are selected (such a flux would contribute to around 0.015K error in the Reich and Reich map). It is anyway expected that sources of this strength or fainter are taken into account in the continuum measurement. The resulting brightness temperatures were compared to the combination of the Reich and Testori and HI map. Most sources exhibit a Tb that is equal or smaller to the one of the continuum (as the sources are embedded into a strong emission area which is preponderant in the relatively large beam of the

telescope). However, some strong sources (Cassiopeia A,) can be identified. It is difficult to do a sensible modification of the Reich an Reich map as because of the large beamwidth - the angular area around the sources should also be corrected.

Hence, the values of Reich and Testori are left untouched in the final map for the sake of consistency.Most differences in flux are quite small and are expected to be smoothed out when SMOS beam is applied. The strongest discrepancies (several 100s of K) occur for Cygnus A and the area of Cassiopeia A. In the sky data generated for SMOS, the sky map itself is not corrected, but the value of the source (in K) is reported in the error field of the corresponding pixel, where a Stockert/Testori beam was approximately applied (resolution 35 arcmin, sampling 0.25 deg). Hot celestial sources can radiate downwards radiation with effective brigthness temperature up to about 400 K at L-band.

Some approximations had to be used at that stage to simplify the implementation. Note also, that as in [3], the sky map generated for SMOS and used here for the present version of the algorithm assumed unpolarized radiation.

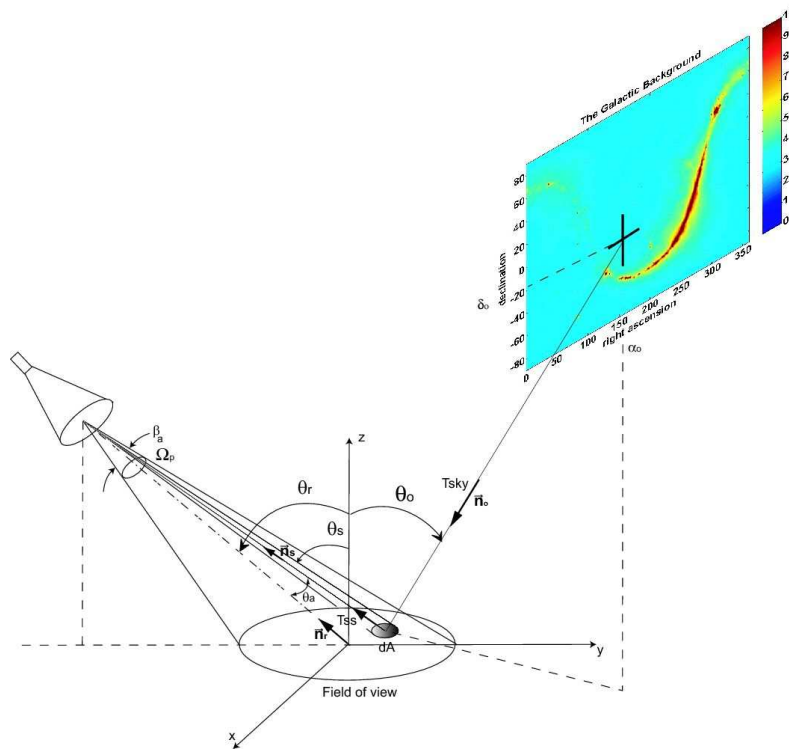### 4.7.3. Formulation of the Sky glitter contribution at surface level

Figure 2: Geometry of the sky-glitter problem

Figure (1) depicts a radiometer antenna of circular beamwidth β_a, viewing the surface at a boresight observation angle θ_r, and azimuthal angle Φ_r. An incremental sea surface area dA, located within the field of view, is illuminated by the sky along all directions $\vec{n}_o=(\theta_o,\Phi_o)$ within the solid angle Ω_s subtended by the upper hemisphere seen from dA (in Figure (1), only one particular sky illumination direction is plotted for illustration). Part of the intercepted energy is then scattered in the direction $\vec{n}_s=(\theta_s,\Phi_s)$, i.e., toward the radiometer

antenna. The sky energy scattered by dA in the direction $\vec{n}_s$ is represented by the radiometric temperature $T_p^s(\vec{n}_s)$. The **unpolarized** sky brightness temperature incident in the direction $\vec{n}_o$ is the sky brightness temperature $T_{sky}(\vec{n}_o)$, and is further attenuated along its downward path across the atmosphere. Assuming that the rough sea surface can be described by the surface wind speed vector alone, namely (u_{10}, φ_w), the surface *sky glitter brightness temperature* in the direction $\vec{n}_s$ and at polarization p, $T_p^s(\vec{n}_s)$, can be related to $T_{sky}(\vec{n}_o)$ by the following integral equation:

$$T_p^s(\theta_s,\phi_s,u_{10},\varphi_w)=\frac{1}{4\pi\cos\theta_s}\int_0^{\pi/2}\int_0^{2\pi}\left[\sigma_{pp}(\theta_o,\phi_o,\theta_s,\phi_s)+\sigma_{pq}(\theta_o,\phi_o,\theta_s,\phi_s)\right]T_{sky}(\theta_o,\phi_o)e^{-\tau\sec\theta_o}\sin\theta_o\,d\phi_o\,d\theta_o,$$ (4)

where the $\sigma_{pq}^o(\vec{n}_s,\vec{n}_o)$ are the bistatic scattering coefficients of the sea surface at scattered direction $\vec{n}_s$ and incident direction $\vec{n}_o$. The notation is such that the first subscript p refers to the polarization configuration of the scattered wave and the second subscript q refers to that of the incident wave. Note that the dependence of the cross sections on the wind speed and direction is implicit. τ is the atmospheric opacity at L-band.

Note also importantly that if the sky brightness temperatures were assumed polarized, i.e., $T_{sky}(\vec{n}_o)=T_{sky}^p(\vec{n}_o)$, the expression in (4) would be no more valid. Indeed, one would then need to additionally consider (i) polarisation basis rotation of the sky brightness temperature $T_{sky}^p(\vec{n}_o)$ signal between celestial frame and altitude-azimuth frame at earth target, (ii) Faraday rotation during the downward path across the ionosphere, and (iii) the use of a fully polarized Mueller scattering matrix to describe surface scattering.

Nevertheless, assuming unpolarized sky brightness temperature, equation (4) can be rewritten in Matrix form as follows:
$$T_p^s(\theta_s,\phi_s)=\frac{1}{4\pi\cos\theta_s}\int_{\Omega_s}\left(M_sA_d\right)T_{sky}d\Omega_s,$$

where $T_p^s(\vec{n}_s)$ is now the Stokes vector, M_s is the so-called Mueller scattering matrix for unpolarized incomming signals, in which all components but the upper left 2x2 matrix of entries are zero, so that we have
$$M_s=\begin{pmatrix}\sigma_{hh}(\theta_o,\phi_o,\theta_s,\phi_s) & \sigma_{hv}(\theta_o,\phi_o,\theta_s,\phi_s) & 0 & 0\\ \sigma_{vh}(\theta_o,\phi_o,\theta_s,\phi_s) & \sigma_{vv}(\theta_o,\phi_o,\theta_s,\phi_s) & 0 & 0\\ 0 & 0 & 0 & 0\\ 0 & 0 & 0 & 0\end{pmatrix};$$
and where A_d is a downward path atmospheric attenuation matrix given by
$$A_d=\begin{pmatrix}a_d^2 & 0 & 0 & 0\\ 0 & a_d^2 & 0 & 0\\ 0 & 0 & a_d^2 & 0\\ 0 & 0 & 0 & a_d^2\end{pmatrix},$$

with $a_d^2=e^{-\tau\sec\theta_o}$. Therefore, in our formulation of the sky glitter problem, only the first and second Stokes parameter in $T_p^s(\vec{n}_s)$ are non zero.

For later reference, it is also useful to define the total reflectivity at polarization p by

$$\Gamma_p = \frac{1}{4\pi\cos\theta_s} \int_0^{\pi/2} \int_0^{2\pi} \left[\sigma_{pp}(\theta_o,\phi_o) + \sigma_{pq}(\theta_o,\phi_o)\right] \sin\theta_o \, d\phi_o \, d\theta_o. \quad (5)$$

For a perfectly flat sea surface, this expression reduces to

$$|R_{hh}^{(0)}(S,T_S,\theta_S)|^2 = \left|\frac{\cos\theta_s - \sqrt{\varepsilon_{sw}(S,T_s) - \sin^2\theta_s}}{\cos\theta_s + \sqrt{\varepsilon_{sw}(S,T_s) - \sin^2\theta_s}}\right|^2$$

$$(6)$$

$$|R_{VV}^{(0)}(S,T_S,\theta_S)|^2 = \left|\frac{\varepsilon_{sw}(S,T_s)\cos\theta_s - \sqrt{\varepsilon_{sw}(S,T_s) - \sin^2\theta_s}}{\varepsilon_{sw}(S,T_s)\cos\theta_s + \sqrt{\varepsilon_{sw}(S,T_s) - \sin^2\theta_s}}\right|^2$$

where $\varepsilon_{sw}(S,T_s)$ is the dielectric constant for seawater given by the Klein and Swift model. S is the salinity and T_s is the sea surface temperature. Note there is no cross-pol reflectivity in the flat-surface case, and the reflected signal is

$$T_p^f(\theta_s) = \int_0^{\pi/2} \int_0^{2\pi} |R_{pp}^{(0)}(S,T_S,\theta_S)|^2 \, \delta(\theta_s - \theta_o, \phi_s - \phi_o + \pi) T_{sky}(\theta_o,\phi_o) e^{-\tau\sec\theta_o} \sin\theta_o \, d\phi_o \, d\theta_o \quad (7)$$

which simplifies to

$$\boxed{T_p^f(\theta_s) = |R_{pp}^{(0)}(S,T_S,\theta_S)|^2 \, T_{sky}(\theta_s, \phi_s - \pi) e^{-\tau\sec\theta_s}} \quad (8)$$

For typical ocean values of SST (0-38 °C) and SSS (20-40 psu), the sensitivity to SSS of the flat sea surface reflectivity at L-band vary from about 0.5×10^{-3}/psu to 3.5×10^{-3}/psu and its sensitivity to SST vary from about 0.2×10^{-3}/°C to 2×10^{-3}/°C, considering both linear polarizations and all incidence angles between 0 and 60°. Despite some previously listed very localized bright spots (Cassiopeia A, Orion A, Cygnus A, Taurus A, ...) for which the downwelling signal can reach up to about 400 K, the sky brightness temperature at L-band vary in general from 2.75 K to around 10 K. Assuming a 10 K bright source, the sensitivity of the specularly reflected celestial brightness temperature signals to SSS and SST might reach around 0.03 K/psu and 0.02 K/°C. These values are representative of an average worst case scenario since the surface reflectivity drops significantly in presence of roughness. To make possible the operational implementation of the sky glitter calculation, we nevertheless make the assumption that the sky glitter results at non zero wind speed weakly depend on these two surface parameters. We therefore selected ocean average values of T_s=15 °C and S=35 psu. For the flat sea surface cases, we however account for expected variations in these parameters.

4.7.4. Transport to antenna level and Integration over the Antenna Pattern

Although the focus of that part of the ATBD is on representing the sky scattered signal at surface level, we also discuss here issues related to the transport from the ground to the antenna and to the integration over the antenna pattern, as different processing are required wether the surface is rough or flat.

4.7.4.1. Tracing the galactic noise from surface to antenna level

Having derived the scattered signal at the surface, we then must apply attenuation on the upward path to the radiometer. We obtain

$$
\begin{pmatrix} T_{h}^{s'} \\ T_{v}^{s'} \\ U^{s'} \\ V^{s'} \end{pmatrix} = \begin{pmatrix} a_{u}^{2} & 0 & 0 & 0 \\ 0 & a_{u}^{2} & 0 & 0 \\ 0 & 0 & a_{u}^{2} & 0 \\ 0 & 0 & 0 & a_{u}^{2} \end{pmatrix} \begin{pmatrix} T_{h}^{s} \\ T_{v}^{s} \\ U^{s} \\ V^{s} \end{pmatrix} = A_{u} \begin{pmatrix} T_{h}^{s} \\ T_{v}^{s} \\ U^{s} \\ V^{s} \end{pmatrix},
\tag{9}
$$

where A_u is the upward path atmospheric attenuation matrix with $a_u^2 = \exp(-\tau \sec\theta_s)$. The upward signals are then subject to a Faraday rotation counterclockwise by angle ω_{fu}, across the ionosphere,

$$
\begin{pmatrix} T_{h}^{s''} \\ T_{v}^{s''} \\ U^{s''} \\ V^{s''} \end{pmatrix} = \begin{pmatrix} \cos^2\omega_{fu} & \sin^2\omega_{fu} & -\cos\omega_{fu}\sin\omega_{fu} & 0 \\ \sin^2\omega_{fu} & \cos^2\omega_{fu} & \cos\omega_{fu}\sin\omega_{fu} & 0 \\ \sin(2\omega_{fu}) & -\sin(2\omega_{fu}) & \cos(2\omega_{fu}) & 0 \\ 0 & 0 & 0 & 1 \end{pmatrix} \begin{pmatrix} T_{h}^{s'} \\ T_{v}^{s'} \\ U^{s'} \\ V^{s'} \end{pmatrix} = M_{fu} \begin{pmatrix} T_{h}^{s'} \\ T_{v}^{s'} \\ U^{s'} \\ V^{s'} \end{pmatrix},
\tag{10}
$$

and then rotation into the Ludwig-3 basis to correctly project the polarization basis onto the MIRAS antenna polarization basis vector,

$$
\begin{pmatrix} T_{h}^{s'''} \\ T_{v}^{s'''} \\ U^{s'''} \\ V^{s'''} \end{pmatrix} = \begin{pmatrix} \cos^2\Psi_l & \sin^2\Psi_l & -\cos\Psi_l\sin\Psi_l & 0 \\ \sin^2\Psi_l & \cos^2\Psi_l & \cos\Psi_l\sin\Psi_l & 0 \\ \sin(2\Psi_l) & -\sin(2\Psi_l) & \cos(2\Psi_l) & 0 \\ 0 & 0 & 0 & 1 \end{pmatrix} \begin{pmatrix} T_{h}^{s''} \\ T_{v}^{s''} \\ U^{s''} \\ V^{s''} \end{pmatrix} = M_{l} \begin{pmatrix} T_{h}^{s''} \\ T_{v}^{s''} \\ U^{s''} \\ V^{s''} \end{pmatrix},
\tag{11}
$$

Letting $T_p^a = (T_{he}^{'''s}, T_{ve}^{'''s}, U_e^{'''s}, V_e^{'''s})^T$ being the upward sky glitter brightness temperature Stokes vector at the antenna level, and combining all of the transformations from source to radiometer, we have for an unpolarized sky

$$
T_p^a = M_l M_{fu} A_u \int_{\Omega_s} (M_s A_d) T_{sky} d\Omega
\tag{12}
$$

It is usual to combine $M_l M_{fu}$ into one rotation matrix, M_α, so we have

$$
T_p^a = M_\alpha A_u \int_{\Omega_s} (M_s A_d) T_{sky} d\Omega
\tag{13}
$$

The Faraday rotation angle is a function of the total electron content (TEC) as well as the Earth's magnetic field, so that $M_\alpha = M_\alpha(\theta_s, \phi_s, TEC)$, but we will use the notation $M_\alpha(\theta_s, \phi_s)$ for simplicity.

4.7.4.2. Integration over the Antenna Pattern

To recapitulate the above results, accounting for the rough surface, the total upward scattered power normal to a unit area dA of sea surface impinging the antenna in the direction (θ_s, ϕ_s), after all transformations of the radiation from the source to the antenna, is as a function of angle (θ_a, ϕ_a) in the antenna spherical coordinate system,

$$
T_p^a(\theta_a, \phi_a) = (M_\alpha A_u) T_p^s = \frac{1}{4\pi\cos\theta_s} (M_\alpha A_u) \int_{\Omega_s} (M_s A_d) T_{sky} d\Omega_s,
\tag{14}
$$

where T_{sky} is the unpolarised sky brightness temperature given in the celestial frame. But this is the flux in some direction. To obtain the total power at a classical radiometer antenna, we must integrate this over all incident directions within the antenna pattern and weight the impinging signals by the antenna gain G, so that the total antenna temperature vector is

$$\overline{T}_p^a = \frac{1}{\Omega_p}\int_{\Omega_a} G(\Omega_a)T_p^a(\Omega_a)d\Omega_a = \int_{\Omega_a} G(\Omega_a)(M\alpha A_u)T_p^s\, d\Omega_a$$

(15)

where Ω_p is the vector antenna pattern solid angle, which simply normalizes the gain pattern weighting function G:

$$\Omega_p = \int_{\Omega_a} G\, d\Omega_a.$$

(16)

In the SMOS case, the antenna temperature is still given by an equation of the form (15), however, owing to the interferometric processing, the retrieved brightness temperature in direction (θ_a, ϕ_a) corresponds to an integral over a synthetic gain pattern centered at that direction.

Switching to director cosine coordinates, with

$$\xi = \sin\theta_a \cos\phi_a,$$

(17)

$$\eta = \sin\theta_a \sin\phi_a,$$

and with

$$d\Omega = \sin\theta_b\, d\theta\, d\phi = \frac{d\xi\, d\eta}{\cos\theta_b}, = \frac{d\xi\, d\eta}{\sqrt{1-\xi_2-\eta_2}}.$$

(18)

the synthetic antenna pattern, or Equivalent Array Factor (EAF), is

$$AF_{eq}(\xi,\xi',\eta,\eta') = \frac{\sqrt{3}}{2}d_2 \sum_m \sum_n W(u_{mn},v_{mn})\tilde{r}\left(-\frac{u_{mn}\cdot\xi + v_{mn}\cdot\eta}{f_o}\right)e^{j2\pi(u_{mn}\cdot(\xi-\xi') + v_{mn}\cdot(\eta-\eta'))}$$

(19)

where
• W is the apodisation function
• $\tilde{r}$ is the fringe-washing factor (FWF) which accounts for the spatial decorrelation between antennas.
• u, v are the baseline coordinates in the frequency domain
• d is the antenna element spacing (= 0.875)
• f_o is the central frequency (1413 MHz)
• ξ, η are the central director cosines (DC) coordinates; ξ', η' are running DC coordinates.

Defining $D = \{\xi,\eta : \xi^2 + \eta^2 < 1\}$ as the domain of integration, the rigorous expression for the polarized sky-glitter temperature contribution at antenna level expressed in the director cosines (DC) coordinates is given by

$$\overline{T}_p^a(\xi,\eta) = \iint_D \frac{AF_{eq}(\xi,\xi',\eta,\eta')}{\sqrt{1-(\xi'-\xi)^2-(\eta'-\eta)^2}}(M\alpha(\xi',\eta')A_u(\xi',\eta'))T_p^s(\xi',\eta')d\xi' d\eta'$$

(20)

The variations in atmospheric attenuation and geometrical rotation are sufficiently small within the narrow (2-3°) synthetic beam that these factors can be approximated by their values at the central director cosines (DC) coordinates (ξ,η), so that we have

$$\overline{T}^{a}_{p}(\xi,\eta)\approx\left(M\alpha(\xi,\eta)A_{u}(\xi,\eta)\right)\iint_{D}\frac{AF_{eq}(\xi,\xi',\eta,\eta')}{\sqrt{1-(\xi'-\xi)^{2}-(\eta'-\eta)^{2}}}T^{s}_{p}(\xi',\eta')d\xi'd\eta' \qquad (21)$$

As demonstrated in Ifremer's technical note, in presence of roughness, it turns out that the impact of the narrow synthetic antenna pattern is negligible assuming homogeneous roughness within the pixel. This is mainly due to the much larger angular spreading of the contributing part of the scattering coefficients compared to the narrow synthetic beam, which induces spatial uniformization of the scattered signal within the beam. Therefore, in the present algorithm, we neglect the array factor impact for rough sea surface conditions so that finally, the polarized sky-glitter temperature contribution at antenna level for rough sea conditions reads:

$$\boxed{\overline{T}^{a}_{p}(\xi,\eta)\approx\left(M\alpha(\xi,\eta)A_{u}(\xi,\eta)\right)T^{s}_{p}(\xi,\eta)} \qquad (22)$$

where T^{s}_{p} is given in equation (4).

However, as revealed in [15], in the case of a perfectly flat sea surface, i.e., wind speed equal zero m/s, the *EAF* factor impact is no more neglible considering a 0.25° resolution sky map. T^{s}_{p} is indeed replaced by $T^{f}_{p}(\theta_{s})$, and the integral becomes

$$\overline{T}^{fa}_{p}(\xi,\eta)\approx\left(M\alpha(\xi,\eta)A_{u}(\xi,\eta)\right)\iint_{D}\frac{AF_{eq}(\xi,\xi',\eta,\eta')}{\sqrt{1-(\xi'-\xi)^{2}-(\eta'-\eta)^{2}}}T^{f}_{p}(\xi',\eta')d\xi'd\eta'. \qquad (23)$$

But
$$T^{f}_{p}=\left|R^{(0)}_{pp}(S,T_{s},\theta_{s})\right|^{2}T_{sky}(\theta_{s},\phi_{s}-\pi) \qquad (24)$$
and so
$$\overline{T}^{fa}_{p}(\xi,\eta)\approx\left(M\alpha(\xi,\eta)A_{u}(\xi,\eta)\right)\times\iint_{D}\frac{AF_{eq}(\xi,\xi',\eta,\eta')}{\sqrt{1-(\xi-\xi')^{2}-(\eta-\eta')^{2}}}\left|R^{(0)}_{pp}(S,T_{s},\theta_{s}(\xi',\eta'))\right|^{2}T_{sky}(\xi',\eta')d\xi'd\eta'$$
$$\qquad (25)$$

It turns out that the Fresnel power reflection coefficients, like the atmospheric attenuation and geometrical rotation effects can be assumed to vary weakly over the significant portion of the synthetic beam, so that

$$\left|R^{(0)}_{pp}(S,T_{s},\theta_{s}(\xi',\eta'))\right|^{2}\approx\left|R^{(0)}_{pp}(S,T_{s},\theta_{s}(\xi,\eta))\right|^{2}, \qquad (26)$$
and
$$\overline{T}^{fa}_{p}(\xi,\eta)\approx\left(M\alpha(\xi,\eta)A_{u}(\xi,\eta)\right)\left|R^{(0)}_{pp}(S,T_{s},\theta_{s}(\xi,\eta))\right|^{2}\times\iint_{D}\frac{AF_{eq}(\xi,\xi',\eta,\eta')}{\sqrt{1-(\xi'-\xi)^{2}-(\eta'-\eta)^{2}}}T_{sky}(\xi',\eta')d\xi'd\eta'. $$
$$\qquad (27)$$

As derived in [15], further simplification can be made by noting that the Array Factor is a rather narrow, centro-symmetric function, independent of the location of the viewing point in the field of view, time independent 2-D pattern. The following analytical approximation has been tuned to the EAF with no FWF effect:

$$AF_{eq}(\xi,\xi',\eta,\eta')\cdot\approx F_{cs}(\rho(\xi,\xi',\eta,\eta'))=\max\left\{0,\left[\frac{\sin k_{f}\cdot\rho}{k_{f}\cdot\rho}\right]^{k_{k}}\frac{1}{1+k_{g}\cdot\rho_{k_{h}}}\right\} \qquad (28)$$

where $\rho=\sqrt{(\xi'-\xi)^2+(\eta'-\eta)^2}$ is the distance in director cosine coordinates, $k_f=73.30$, $k_g=524.5$, $k_h=2.1030$ and $k_k=1.4936$. Thus, switching to polar coordinates, we have

$$\bar{T}^{fa}_{P}(\xi,\eta)\cdot \approx \left(M_\alpha(\xi,\eta)A_u(\xi,\eta)\right)|R^{(0)}_{pp}(S,T_s,\theta_s(\xi,\eta))|^2 \iint_{D_\rho} \frac{F_{cs}(\rho)}{\sqrt{1-\rho^2}} T_{sky}(\xi,\eta,\rho,\phi)d\phi d\rho,$$ (29)

where $D_\rho=\{\rho,\phi:(\xi(\rho,\phi))_2+\eta((\rho,\phi))_2<1\}$ is the polar coordinated domain corresponding to D.

Equations (22) and (29) are the two quantities that have to be calculated by the processor to be used as final correction to the modelled Tbs at antenna level. Equation (21) shall be used in the rough sea surface cases, while Equation (28) shall be used in the purely flat sea surface cases.

In the flat sea surface case, we see that the sky map weighted by the centro symmetric WEF, used in (29), namely, $\bar{T}_{sky}$, can be precomputed using:

$$\bar{T}_{sky}=\iint_{D_\rho} \frac{F_{cs}(\rho)}{\sqrt{1-\rho^2}} T_{sky}(\rho,\phi)d\phi d\rho$$ (30)

4.7.5. Modelling the Scattering Cross Sections

A key submodel in the skyglitter evaluation in presence of roughness is the model for bistatic scattering coefficients of the rough sea surface at L-band. As anticipated, the intensity and spread of the skyglitter contamination will depend not only on the measurement geometry but also on the sea surface roughness conditions. Knowing that SMOS multi-angular capabilities range from 0° to about 60°, we seek to model scattering of radiation at directions varying almost from specular to grazing directions.

As mentioned, to compute the scattered signal at the Earth's surface, we need to obtain expressions for the scattering cross sections $\sigma_{pq}(\theta_o,\phi_o,\theta_s,\phi_s)$ in terms of known quantities. Clearly, these cross sections will depend on characteristics of the incident radiation and of the rough surface. In this section we briefly review the rough surface and electromagnetic models used in the algorithm.

4.7.5.1. Modelling the Rough Surface

In order to employ the electromagnetic scattering models, we need a model for the rough surface itself, in order to compute the correlation functions required for the scattering models. The choice for the sea surface spectrum model used in the calculation of the sky glitter is certainly an important issue. The surface correlation function $\rho(\vec{x})$ is defined by

$$\rho(x,y)=\int_{-\infty}^{\infty}\int_{-\infty}^{\infty} W(\xi_x,\xi_y)e^{i\vec{\xi}\cdot\vec{x}}d\xi_x d\xi_y,$$ (31)

where $W(\xi_x,\xi_y)$ is the directional wavenumber spectrum of the rough sea surface as a function of surface wavenumber vector in cartesian number wavespace $\vec{\xi}=(\xi_x,\xi_y)$. The sea surface elevation function is assumed here to be a Gaussian random process and ρ is obtained from the inverse Fourier transform of the sea surface spectrum as computed using the models of Kudryavtsev al. [1999]. This wave model produces spectra that depend primarily on the 10 m

wind speed u_{10} and inverse wave age Ω, so that

$$W=W(\xi_x,\xi_y;u_{10},\Omega). \qquad (32)$$

In the present algorithm, we only consider wind speed dependence, assuming the wind sea is fully developed (Ω=0.81) and we therefore refer to the spectrum using the notation $W(\xi_x,\xi_y)$, and we refer to the corresponding correlation function by $\rho(x,y)$. Also, since the directional wavenumber spectrum exhibits simpler structure in polar coordinates than in cartesian coordinates, and since the electromagnetic scattering problem is naturally expressed in spherical coordinates, it is expedient to introduce polar coordinates for both physical space and surface wavenumber space.

In cylindrical coordinates, the correlation function is decomposed into a zeroth and second harmonic:

$$\rho(r,\Phi)=\rho_0(r)-\rho_2(r)\cos2(\Phi-\varphi_w), \qquad (33)$$

where φ_w is the wind direction (towards which the wind is blowing), and where the isotropic part is given by $\rho_0(r)$ and the anisotropic azimuthal wavenumber 2 part is given by $\rho_2(r)$. These harmonics are used directly in the electromagnetic scattering model to compute harmonics of the scattering cross sections.

4.7.5.2. The Asymptotic Electromagnetic Scattering Models

Having introduced the generic approach for representing the rough surface, we now introduce the electromagnetic scattering models, the Kirchhoff (KA) model [] and the lowest-order model (SSA-1) based on the Small Slope Approximation theory []. The validity of KA approach is restricted to surfaces with large curvatures and to large Rayleigh parameters. The SSA has been proposed by Voronovich as an alternative to efficiently bridge Small Perturbation Model (SPM) and KA models. In particular, SSA at strictly meets SPM as the roughness goes to zero. Analytical expressions are in principle available for the SSA at all orders in slope. In practice, however, only the first two orders are tractable. The first-order SSA (SSA-1) implies the same single integral as in KA to determine a particular Fourier coefficient of the surface elevation coherence structure function with a different geometrical factor. The second order approximation (SSA-2), however, is a double oscillating integral, that is found very difficult to compute accurately, especially in the dielectric case where convergence problems and computational time demands become prohibitive. For the present algorithm, we thus consider first-order SSA (SSA-1) and the Kirchhoff approaches These two approaches can be considered to provide the asymptotic limits within a consistent framework of scattering slope expansions. Importantly, these two approaches lack taking into account directly the surface geometrical properties to predict the level of polarization. In particular, with the proposed models, this polarization level are independent of roughness states. SSA-1 is expected to exaggerate the polarization effects while KA will minimize them. Note as well, that at order 1, SSA-1 meets SPM only at order 1 while KA converge asymptotically up to second order in SPM. At the specular direction, which is the dominant contributor, both models gives however the same asymptotic solution.

To facilitate discussion we introduce a local cartesian coordinate system $(\hat{x},\hat{y},\hat{z})$ with basis vector $\hat{x}$ pointing eastward, basis vector $\hat{y}$ pointing northward, and basis vector $\hat{z}$ pointing upwards normal to the horizontal surface. For convenience of notation, we use incident and scattered wavevectors interchangeably with directions:

$$(\theta_o,\phi_o)\rightarrow\vec{k}_o$$

$$(\theta_s,\phi_s)\rightarrow\vec{k}_s. \qquad (34)$$

Application of either SSA-1 or the Kirchhoff approximation for scattering from the slightly rough ocean surface yields the following expression for a dimensionless bistatic scattering cross section $\sigma^O_{\alpha\alpha_o}$ for scattering of the incoming wave of polarization α_o into the outgoing wave of polarization α:

$$\sigma_{\alpha\alpha_o}(\vec{k}_s,\vec{k}_o)=\frac{1}{\pi}\left|\frac{2q_sq_o}{q_s+q_o}T_{\alpha\alpha_o}(\vec{k}_s,\vec{k}_o)\right|^2 e^{-(q_s+q_o)^2\rho(0)}\cdot I_K$$

$$(35)$$

where $T_{\alpha\alpha_o}(\vec{k}_s,\vec{k}_o)$ is a polarization-dependent kernel that is different for SSA-1 and the Kirchhoff models. I_K is often referred to as the Kirchhoff Integral and is given in cartesian coordinates by

$$I_K=\int_{-\infty}^{\infty}\int_{-\infty}^{\infty}\left\{e^{\left[(q_s+q_o)^2\rho(\vec{x})\right]}-1\right\}e^{\left[-i(\vec{k}_s-\vec{k}_o)\cdot\vec{x}\right]}dxdy, \qquad (36)$$

where we use the notation $\vec{x}$ to denote the horizontal displacement vector and the integral is evaluated over all possible displacements in the horizontal plane. In Eqs. (35) and (36), $(q_s,q_o)=(\hat{z}\cdot\vec{k}_s,-\hat{z}\cdot\vec{k}_o)$ represents the vertical projection of the wavevectors. As the kernel T depends on the dielectric properties of the scattering surface, we use the Klein and Swift's model to estimate the dielectric constant of sea water at L-band at SSS=35 psu and SST=15°C.

Using the harmonic decomposition of the correlation function as derived from the surface models, we can decompose the Kirchhoff integral into harmonics as well, so that in cylindrical coordinates we obtain

$$I_K=2\pi\int_0^\infty\left[J_0(q_Hr)(r)+I_0(a)J_0(b)e^{q_z^2\rho_0(r)}\right]rdr+\sum_{m=1}^\infty I_K^m\cos2m(\Phi_{si}-\varphi_w), \qquad (37)$$

where Φ_{si} is the angle of the difference between the scattered and incident wavevectors, and can be written as:

$$\Phi_{si}(\theta_o,\phi_o,\phi_s,\theta_s)=\tan^{-1}\left(\frac{q_{Hy}}{q_{Hx}}\right)=\tan^{-1}\left(\frac{\sin\theta_s\sin\phi_s+\sin\theta_o\sin\phi_o}{\sin\theta_s\cos\phi_s+\sin\theta_o\cos\phi_o}\right),$$

and where, for m from 1 to ∞,

$$I_K^m=4\pi\int_0^\infty I_m(a)J_{2m}(b)e^{q_z^2\rho_0(r)}rdr, \qquad (38)$$

is the coefficient of harmonic $2m$ in a cosine series decomposition of the Kirchhoff Integral. If we further let

$$I_K^0=2\pi\int_0^\infty\left[J_0(q_Hr)(r)+I_0(a)J_0(b)e^{q_z^2\rho_0(r)}\right]rdr \qquad (39)$$

then we see that

$$I_K=I_K(\Phi_{si}-\varphi_w)=\sum_{m=0}^\infty I_K^m\cos2m(\Phi_{si}-\varphi_w). \qquad (40)$$

In the above, $a(r)=q_z^2\rho_2(r)$ and $b(r)=q_Hr$. J_m is the Bessel function of the first kind and order m, and I_m denotes the modified Bessel function of the first kind and order m. We can incorporate the polarization-dependent coefficients multiplying the Kirchhoff Integral into

the sum over the Kirchoff Integral harmonics to obtain

$$\sigma_{\alpha\alpha_o}(\vec{k}_s,\vec{k}_o,u_{10},\varphi_w)=\sum_{m=0}^{\infty}\sigma_{\alpha\alpha_o}^{2m}(\vec{k}_s,\vec{k}_o)\cos 2m(\Phi_{si}-\varphi_w), \quad (41)$$

where we have explicitly included the dependence of the final scattering coefficients on the wind speed u_{10} and wind direction φ_w (towards which the wind is blowing), and where

$$\sigma_{\alpha\alpha_o}^{2m}(\vec{k}_s,\vec{k}_o)=\frac{1}{\pi}\left|\frac{2q_sq_o}{q_s+q_o}T_{\alpha\alpha_o}(\vec{k}_s,\vec{k}_o)\right|^2 e-(q_s+q_o)_2\rho(0)\cdot I_K^m$$

$$(42)$$

Note that the scattering coefficient harmonics are independent of wind direction. Moreover, these harmonics only depend on the incoming and scattered radiation incidence angles, the wind speed, and difference between the incoming and scattered radiation azimuth angles. Thus, switching from vector notation to angles, we can write the scattering coefficients as

$$\boxed{\sigma_{\alpha\alpha_o}(\theta_o,\phi_o,\theta_s,\phi_s,u_{10},\varphi_w)=\sum_{m=0}^{\infty}\sigma_{\alpha\alpha_o}^{2m}(\theta_o,\phi_s-\phi_o,\theta_s,u_{10})\cos 2m(\Phi_{si}-\varphi_w),}$$

$$(43)$$

4.7.6. Representation of the Scattered Galactic Noise Signal

As mentioned before, to obtain the total sky scattered signal in a given direction toward the radiometer defined by (θ_s, ϕ_s), we must integrate the brightness temperature contributions from waves incident at the target from all directions over the upper hemisphere, so that at polarization p, the total scattered signal is

$$T_p^s(\theta_s,\phi_s,u_{10},\varphi_w)=\frac{1}{4\pi\cos\theta_s}\int_{\Omega_s}[\sigma_{pp}+\sigma_{pq}]T_{sky}(\Omega_s)d\Omega_s \quad (44)$$

where Ω_s refers to angular position in the upper hemisphere.
Now, since the noise distribution over the upper hemisphere is a function of target position on Earth and time, the rough surface scattered galactic signal at polarization p, T_p^s, is a function of latitude ϑ_g, longitude φ_g, and time t as well as scattering incidence and azimuth angles, wind speed and wind direction, so that in general we have

$$T_p^s=T_p^s(\vartheta_g,\varphi_g,t,\theta_s,\phi_s,u_{10},\varphi_w). \quad (45)$$

The portion of the sky covered by the upper hemisphere is only a function of target latitude, longitude, and time. Moreover, changing the time or the target longitude only alters the right ascension of every point in the upper hemisphere by some constant independent of position in the upper hemisphere.

The upper hemisphere pole corresponds to the unit normal to the Earth surface at the target latitude and longitude. Denoting the right ascension and declination of the projection of this point in the celestial frame by (α_n,δ_n), we can remove the explicit dependence on time in (45) by introducing (α_n,δ_n) as independent variables and expressing the scattered galactic noise as

$$\overline{T}_p^s(\alpha_n,\delta_n,\theta_s,\phi_s,u_{10},\varphi_w).$$

However, this parametrization is not optimal for representing the functional dependence of

the scattered signal, since we know that the dominant source of scattered signal is associated with noise in the specular direction. Therefore, we seek to represent the scattered signal in terms of the location in the sky of the specular direction, which we denote $(\alpha_{spec}, \delta_{spec})$. In order to represent the scattering solution in terms of these variables, we must find a mapping between $(\alpha_{spec}, \delta_{spec})$ and (α_n, δ_n). This mapping will necessarily involve θ_s and ϕ_s, so that we can write the mapping function as

$$T:(\alpha_n, \delta_n, \theta_s, \phi_s) \rightarrow (\alpha_{spec}, \delta_{spec}, \theta_{spec}, \psi_{uh}), \qquad (46)$$

where θ_{spec} is the incidence angle of the specular direction in the upper hemisphere altitude-azimuth frame, and where we have introduced the angle ψ_{uh}, which represents the orientation of the upper hemisphere at the specular point $(\alpha_{spec}, \delta_{spec})$. The mapping operator T can be seen to be that function which rotates the unit normal vector in the upper hemisphere frame into the unit vector in the specular direction.

ψ_{uh} must be defined so as to allow construction of an inverse mapping operator T^{-1} that maps a specular direction $(\alpha_{spec}, \delta_{spec})$ uniquely into an upper hemisphere unit normal (α_n, δ_n). To facilitate a definition of ψ_{uh}, we first establish alt-azimuth coordinate systems and associated basis vectors in both the upper hemisphere and celestial frames along the line of sight in the specular direction. Detailed definitions of reference frames and associated transformation used in the derivation of ψ_{uh} are given in Appendix B. These transformation can be performed with the use of CFI. The basis vectors are analogous to horizontal and vertical polarization basis vectors used to describe electromagnetic plane waves. In the upper hemisphere frame, which is the topocentric frame whose origin is the surface target, also called the earth alt-azimuth frame, we define the 'horizontal' basis vector $\hat{h}_u = \hat{n}_u \times \hat{r} / \|\hat{n}_u \times \hat{r}\|$, where $\hat{n}_u$ is the unit normal to the surface at the target and $\hat{r}$ is directed outward towards the specular direction from the target. Next, we define a 'vertical' basis vector by $\hat{v}_u = \hat{h}_u \times \hat{r} / \|\hat{h}_u \times \hat{r}\|$.

If we let ϕ_{spec} and θ_{spec} be the specular azimuth and altitude, respectively, of $\hat{r}$ in the upper hemisphere frame, then we have

$$\begin{aligned} \hat{h}^u &= -\sin\phi_{spec}\hat{x}^u + \cos\phi_{spec}\hat{y}^u, \\ \hat{v}^u &= -\cos\phi_{spec}\sin\theta_{spec}\hat{x}^u - \sin\phi_{spec}\sin\theta_{spec}\hat{y}^u + \sin\theta_{spec}\hat{z}^u, \end{aligned} \qquad (47)$$

where $\hat{x}_u$, $\hat{y}_u$, and $\hat{z}_u$ are basis vectors for the topocentric Earth frame that determines the upper hemisphere. Analogous basis vectors can be defined in the celestial frame as

$$\begin{aligned} \hat{h}_c &= -\sin\alpha_{spec}\hat{x}_c + \cos\alpha_{spec}\hat{y}_c, \\ \hat{v}_c &= -\cos\alpha_{spec}\sin\delta_{spec}\hat{x}_c - \sin\alpha_{spec}\sin\delta_{spec}\hat{y}_c + \sin\delta_{spec}\hat{z}_c, \end{aligned} \qquad (48)$$

where α_{spec} and δ_{spec} are the specular right ascension and declination, respectively, of $\hat{r}$ in the celestial frame.

If we denote the components of a vector normal to the line-of-sight in the upper hemisphere alt-azimuth $(\hat{h}_u, \hat{v}_u)$ frame by (V_{hu}, V_{vu}), then its components in the celestial $(\hat{h}_c, \hat{v}_c)$ frame, denoted by (V_{hc}, V_{vc}), are

$$\begin{pmatrix} V^{hc} \\ V^{vc} \end{pmatrix} = \begin{pmatrix} \hat{h}^c \cdot \hat{h}^u & \hat{h}^c \cdot \hat{v}^u \\ \hat{v}^c \cdot \hat{h}^u & \hat{v}^c \cdot \hat{v}^u \end{pmatrix} \begin{pmatrix} V^{hu} \\ V^{vu} \end{pmatrix} \qquad (49)$$

It turns out that the preceding matrix is just a rotation matrix, so we can write this transformation as

$$\begin{pmatrix} V^{hc} \\ V^{vc} \end{pmatrix} = \begin{pmatrix} \cos\psi_{uh} & -\sin\psi_{uh} \\ \sin\psi_{uh} & \cos\psi_{uh} \end{pmatrix} \begin{pmatrix} V^{hu} \\ V^{vu} \end{pmatrix} \qquad (50)$$

where ψ_{uh} is the angle one must rotate a vector defined in the upper hemisphere alt-azimuth frame counterclockwise about the line-of-sight in the specular direction to obtain the vector components in the celestial sphere alt-azimuth frame. Equivalently, it is the angle one must rotate the alt-azimuth basis vectors at earth target clockwise to obtain the basis vectors for the celestial alt-azimuth frame. This angle is analogous to the Claassen angle in radiometry, and, referring to the previous equation, we see that an explicit expression for it is

$$\boxed{\Psi_{uh} = \tan^{-1}\left(\frac{-\hat{h}_c \cdot \tilde{v}_u}{\hat{h}_c \cdot \tilde{h}_u} \right)} \qquad (51)$$

where $\tilde{h}_u$ and $\tilde{v}_u$ are basis vectors for the upper hemisphere frame transformed into the celestial frame by applying the transformation matrix T_{ac} defined in Appendix B:

$$\boxed{\begin{aligned} \tilde{h}_u &= T_{ac}\hat{h}_u, \\ \tilde{v}_u &= T_{ac}\hat{v}_u, \end{aligned}} \qquad (52)$$

For convenience we repeat here the definition of T_{ac}, the transformation from alt-azimuth frame on earth, with origin at geodetic latitude ϑ_g and geodetic longitude φ_g, to the Celestial frame at time t:

$$T_{ac}(\vartheta_g, \varphi_g, t) = T_{ec}(H) T_{ae}(\vartheta_g, \varphi_g), \qquad (53)$$

where T_{ec} and T_{ae} are transformations from the Earth fixed frame to the Celestial frame and from the alt-azimuth frame to the Earth fixed frame, respectively. Both transformation are also completely defined in Appendix B. H is the Earth rotation angle, which in turns is the sum of G, the Greenwich sideral angle and a nutation angle μ. As shown in Appendix B, these transformat can be easily evaluated using Earth Explorer CFI.

Given the specular location in the celestial sphere, $(\alpha_{spec}, \delta_{spec})$, and given the incidence angle in the specular direction θ_{spec} at the earth target in the upper hemisphere along with the orientation angle ψ_{uh}, rotating a vector from the specular direction by θ_{spec} in the direction ψ_{uh} brings it into the direction normal to the target, for which the position in the celestial spherical coordinate system is (α_n, δ_n). Once this normal is computed, the latitude and longitude of the target is easily derived using the time t, and from this location together with the specular location in the sky given by $(\alpha_{spec}, \delta_{spec})$, the specular azimuth ϕ_{spec} can be computed. Therefore, at some specific acquisition time t, the inverse mapping operator T^{-1} maps a specular direction $(\alpha_{spec}, \delta_{spec})$ uniquely into an upper hemisphere unit normal (α_n, δ_n) and the complete representation of the scattering geometry is uniquely determined by the following set of variables

$$\{\alpha_{spec}, \delta_{spec}, \theta_{spec}, \psi_{uh}\} \qquad (55)$$

where we have omitted the geophysical variables u_{10} and φ_w that obviously enter into the full

scattering problem. A usefull representation of the functional form of the scattered signal in some scattering direction (θ_s, ϕ_s) is then

$$T_p^s \rightarrow T_p^s(\alpha_{spec}, \delta_{spec}, \theta_{spec}, \psi_{uh}, u_{10}, \phi_w). \tag{56}$$

4.7.7. Fast Implementation Method for Calculating Scattered Signal

Neglecting surface salinity and temperature dependencies in the rough sea surface reflectivity, we have seen that we can uniquely represent the scattered noise as a function of six variables:

$$T_p^s \rightarrow T_p^s(\alpha_{spec}, \delta_{spec}, \theta_{spec}, \psi_{uh}, u_{10}, \phi_w). \tag{57}$$

The total scattered signal, can, in turn, be represented as an integral over the upper hemisphere of the incoming noise,

$$T_p^s(\theta_s, \phi_s, u_{10}, \phi_w, \vartheta_g, \phi_g, t) = \frac{1}{4\pi\cos\theta_s} \int_0^{\pi/2} \int_0^{2\pi} \left[\sigma_{pp}(\theta_o, \phi_o, \theta_s, \phi_s) + \sigma_{pq}(\theta_o, \phi_o, \theta_s, \phi_s)\right] T_{sky}(\theta_o, \phi_o) e^{-\tau\sec\theta_o} \sin\theta_o d\phi_o d\theta_o, \tag{58}$$

where the portion of incomming sky is determined uniquely by the set $\{\alpha_{spec}, \delta_{spec}, \theta_{spec}, \psi_{uh}\}$.

To allow efficient implementation of the above equation, it is further assumed here that the atmospheric attenuation of celestial radiation during the downward path toward the surface is uniform within the upper hemisphere and set equal to its value at the specular direction, so that the term $\exp(-\tau\sec\theta_o)$ can be pulled out of the integral using:

$$T_p^s(\theta_s, \phi_s, u_{10}, \phi_w) \approx \frac{e^{-\tau\sec\theta_s}}{4\pi\cos\theta_s} \int_0^{\pi/2} \int_0^{2\pi} \left[\sigma_{pp}(\theta_o, \phi_o, \theta_s, \phi_s) + \sigma_{pq}(\theta_o, \phi_o, \theta_s, \phi_s)\right] T_{sky}(\theta_o, \phi_o) \sin\theta_o d\phi_o d\theta_o, \tag{59}$$

Now, we recall that the bistatic scattering cross sections have the form

$$\sigma_{\alpha\alpha_o}(\theta_o, \phi_o, \theta_s, \phi_s, u_{10}, \phi_w) = \sum_{m=0}^{5} \sigma_{\alpha\alpha_o}^{2m}(\theta_o, \phi_s - \phi_o, \theta_s, u_{10}) \cos 2m(\Phi_{si} - \phi_w). \tag{60}$$

where the variables have the standard meanings and the angle Φ_{si} is the angle of the difference between the scattered and incident wavevectors, defined in (38). As amplitudes for bistatic scattering cross sections harmonics greater than two have magnitudes at least about a factor of ten lower than the second harmonic, hereafter we only consider the zeroth and second harmonics. Retaining only the zeroth and second harmonics, and using the trigonometric identity $\cos(a+b) = \cos a \cos b - \sin a \sin b$ to factor out the wind direction ϕ_w from the above expression, we obtain :

$$\begin{aligned} \sigma_{\alpha\alpha_o}(\theta_o, \phi_o, \phi_s, \theta_s, u_{10}, \phi_w) = &\ \sigma_{\alpha\alpha_o}^{0}(\theta_o, \phi_s - \phi_o, \theta_s, u_{10}) \\ &+ \left[\sigma_{\alpha\alpha_o}^{2}(\theta_o, \phi_s - \phi_o, \theta_s, u_{10}) \cos(2\Phi_{si})\right] \cos(2\phi_w) \\ &+ \left[\sigma_{\alpha\alpha_o}^{2}(\theta_o, \phi_s - \phi_o, \theta_s, u_{10}) \sin(2\Phi_{si})\right] \sin(2\phi_w). \end{aligned} \tag{61}$$

As demonstrated in Appendix C, a usefull properties of the angle Φ_{si} is :

$$\Phi_{si}(\theta_o, \phi_o, \phi_s, \theta_s) = \Phi_{si}(\theta_o, \phi_o - \phi_s, 0°, \theta_s) + \phi_s = \Phi_{si}^{0}(\theta_o, \phi_o - \phi_s, \theta_s) + \phi_s. \tag{62}$$

since

$$\Phi_{si} - \varphi_w = \Phi_{si} - \phi_r - (\varphi_w - \phi_r), \tag{63}$$

and with $\Phi_{si} - \phi_r = \Phi_{si}^0$, we have

$$\Phi_{si} - \varphi_w = \Phi_{si}^0 - (\varphi_w - \phi_r) = \Phi_{si}^0 - \varphi_w^r \tag{64}$$

where φ_w^r is the now the wind direction (towards which the wind is blowing) relative to the radiometer azimuth. Using this result, we can redevelop the scattering coefficients in terms of Φ_{si}^0 and $\varphi_w^r = \varphi_w - \phi_r$, so that the modified scattering cross sections become

$$\sigma_{\alpha\alpha_o}(\theta_o,\phi_r,\phi_r,\theta_s,u_{10},\varphi_w) = \sigma_{\alpha\alpha_o}^0(\theta_o,\phi_s - \phi_r,\theta_s,u_{10})$$
$$+ \left[\sigma_{\alpha\alpha_o}^2(\theta_o,\phi_s - \phi_r,\theta_s,u_{10})\cos(2\Phi_{si}^0)\right]\cos(2\varphi_w^r) \tag{65}$$
$$+ \left[\sigma_{\alpha\alpha_o}^2(\theta_o,\phi_s - \phi_r,\theta_s,u_{10})\sin(2\Phi_{si}^0)\right]\sin(2\varphi_w^r).$$

For convenience, we now let

$$a_{\alpha\alpha_o}^{(0)}(\theta_o,\phi_s - \phi_r,\theta_s,u_{10}) = \sigma_{\alpha\alpha_o}^0(\theta_o,\phi_s - \phi_r,\theta_s,u_{10}),$$
$$a_{\alpha\alpha_o}^{(2)}(\theta_o,\phi_r,\phi_r,\theta_s,u_{10}) = \sigma_{\alpha\alpha_o}^2(\theta_o,\phi_s - \phi_r,\theta_s,u_{10})\cos(2\Phi_{si}^0), \tag{66}$$
$$b_{\alpha\alpha_o}^{(2)}(\theta_o,\phi_r,\phi_r,\theta_s,u_{10}) = \sigma_{\alpha\alpha_o}^2(\theta_o,\phi_s - \phi_r,\theta_s,u_{10})\sin(2\Phi_{si}^0)$$

By introducing Φ_{si}^0 and the wind direction relative to the radiometer azimuth φ_w^r, we have shifted all of the dependence on absolute radiometer azimuth and wind direction into the $\cos(2\Phi_{si}^0)$ and $sin(2\Phi_{si}^0)$ factors, and that the coefficients of these factors, $a^{(2)}$ and $b^{(2)}$, only depend on the relative azimuth $\phi_s - \phi_r$.

The total scattering coefficients can now be written as

$$\sigma_{\alpha\alpha_o}(\theta_o,\phi_r,\phi_r,\theta_s,u_{10},\varphi_w) = a_{\alpha\alpha_o}^{(0)} + a_{\alpha\alpha_o}^{(2)}\cos(2\varphi_w^r) + b_{\alpha\alpha_o}^{(2)}\sin(2\varphi_w^r). \tag{67}$$

Since we will be concerned with the polarized scattering of unpolarized incident radiation, we define the combined scattering cross section coefficients (including co-pol and cross-pol terms):

$$a_p^{(0)}(\theta_o,\phi_s - \phi_r,\theta_s,u_{10}) = a_{pp}^{(0)}(\theta_o,\phi_s - \phi_r,\theta_s,u_{10}) + a_{pq}^{(0)}(\theta_o,\phi_s - \phi_r,\theta_s,u_{10}),$$
$$a_p^{(2)}(\theta_o,\phi_r,\phi_r,\theta_s,u_{10}) = a_{pp}^{(2)}(\theta_o,\phi_r,\phi_r,\theta_s,u_{10}) + a_{pq}^{(2)}(\theta_o,\phi_r,\phi_r,\theta_s,u_{10}), \tag{68}$$
$$b_p^{(2)}(\theta_o,\phi_r,\phi_r,\theta_s,u_{10}) = b_{pp}^{(2)}(\theta_o,\phi_r,\phi_r,\theta_s,u_{10}) + b_{pq}^{(2)}(\theta_o,\phi_r,\phi_r,\theta_s,u_{10}),$$

and the combined scattering cross section as

$$\sigma_P(\theta_o,\phi_r,\phi_r,\theta_s,u_{10},\varphi_w) = \sigma_P^0(\theta_o,\phi_s - \phi_r,\theta_s,u_{10})$$
$$+ \left[\sigma_P^2(\theta_o,\phi_s - \phi_r,\theta_s,u_{10})\cos(2\Phi_{si}^0)\right]\cos(2\varphi_w^r) \tag{69}$$
$$+ \left[\sigma_P^2(\theta_o,\phi_s - \phi_r,\theta_s,u_{10})\sin(2\Phi_{si}^0)\right]\sin(2\varphi_w^r).$$

Now when we consider calculating the total scattered signal in the direction (θ_s,ϕ_s), we must integrate the product of these scattering cross sections with the incident power (assumed here to be unpolarized with brightness temperature T_{sky}) over the entire upper hemisphere, so that at polarization p the scattered signal is

$$T_p^s(\vartheta_g,\varphi_g,t,\theta_s,\phi,u_{10},\varphi_w)=\frac{\exp(-\tau\sec\theta_s)}{4\pi\cos\theta_s}\int_{\Omega_s}T_{sky}(\Omega_s)\sigma_p d\Omega_s \qquad (70)$$

where Ω_s refers to solid angle in the upper hemisphere. This can be written more explicitly as

$$T_p^s(\vartheta_g,\varphi_g,t,\theta_s,\phi,u_{10},\varphi_w)=\frac{\exp(-\tau\sec\theta_s)}{4\pi\cos\theta_s}\int_0^{\pi/2}\int_0^{2\pi}P(\theta_o,\phi,\vartheta_g,\varphi_g,\theta_s,\phi,u_{10},\varphi_w,t)\sin\theta_o d\phi d\theta_o. \qquad (71)$$

where

$$P(\theta_o,\phi,\vartheta_g,\varphi_g,\theta_s,\phi,u_{10},\varphi_w,t)=T_{sky}(\theta_o,\phi,\vartheta_g,\varphi_g,t)\sigma_p(\theta_o,\phi,\theta_s,\phi,u_{10},\varphi_w), \qquad (72)$$

and where the dependence of the incoming noise upon latitude ϑ_g and longitude φ_g of the target and time t is shown explicitly. Also,

$$\sigma_P(\theta_o,\phi,\phi,\theta_s,u_{10},\varphi_w)=a_P^{(0)}+a_P^{(2)}\cos(2\varphi_w^r)+b_P^{(2)}\sin(2\varphi_w^r). \qquad (73)$$

Since the dependence of the scattering cross sections on φ_w occurs alone as multiplicative harmonic factors, this dependence can be factored out of all integrals, so that we can write the total scattered signal at polarization p as

$$T_p^s(\theta_s,\phi,\vartheta_g,\varphi_g,t,u_{10},\varphi_w)=e^{-\tau\sec\theta_s}\Big[A_P^{(0)}(\theta_s,\phi,\vartheta_g,\varphi_g,t,u_{10})+A_P^{(2)}(\theta_s,\phi,\vartheta_g,\varphi_g,t,u_{10})\cos(2\varphi_w^r)+B_P^{(2)}(\theta_s,\phi,\vartheta_g,\varphi_g,t,u_{10})\sin(2\varphi_w^r).\Big]$$
$$(74)$$

where

$$A_P^{(0)}=\frac{1}{4\pi\cos\theta_s}\int_0^{\pi/2}\int_0^{2\pi}T_{sky}(\theta_o,\phi,\vartheta_g,\varphi_g,t)a_P^{(0)}\sin\theta_o d\phi d\theta_o,$$

$$A_P^{(2)}=\frac{1}{4\pi\cos\theta_s}\int_0^{\pi/2}\int_0^{2\pi}T_{sky}(\theta_o,\phi,\vartheta_g,\varphi_g,t)a_P^{(2)}\sin\theta_o d\phi d\theta_o, \qquad (75)$$

$$B_P^{(2)}=\frac{1}{4\pi\cos\theta_s}\int_0^{\pi/2}\int_0^{2\pi}T_{sky}(\theta_o,\phi,\vartheta_g,\varphi_g,t)b_P^{(2)}\sin\theta_o d\phi d\theta_o.$$

As noted previously, the above representation of the scattered signal harmonics is still not sufficiently convenient for fast implemenation, since much of the variation in scattered signal is expected to be related to changes in the specular location in the celestial sphere, and this specular location can change dramatically with changing radiometer incidence and azimuth angles. However, we can use the previously developed transformation involving the angle ψ_{uh}, and express the harmonic coefficients in terms of the specular location in the celestial sphere along with the orientation angle ψ_{uh}, so that we obtain the representation

$$\boxed{\begin{aligned}T_p^s(\alpha_{spec},\delta_{spec},\theta_{spec},\psi_{uh},u_{10},\varphi_w)=e^{-\tau\sec\theta_{spec}}[&A_P^{(0)}(\alpha_{spec},\delta_{spec},\theta_{spec},\psi_{uh},u_{10})\\ +&A_P^{(2)}(\alpha_{spec},\delta_{spec},\theta_{spec},\psi_{uh},u_{10})\cos(2\varphi_w^r)\\ +&B_P^{(2)}(\alpha_{spec},\delta_{spec},\theta_{spec},\psi_{uh},u_{10})\sin(2\varphi_w^r)]\end{aligned}} \qquad (76)$$

where the methodology to determine the angle ψ_{uh} is detailed in the previous section 6. Equation (76) provides a very usefull representation of the sky noise scattered signals at surface level to allow fast operationnal processing making use of pre-computed Look up tables for the coefficients $A_P^{(0)}$, $A_P^{(2)}$ and $B_P^{(2)}$. Readers may wonder why it is needed here to consider second wind direction harmonics of the sky scattered signals when it is already known that the second wind direction harmonics of the rough sea surface emissivity alone is relatively small at L-band. In fact, as demonstrated in Ifremer's technical note, it turns out that depending on the specular location in the celestial sphere, the amplitude of $A_P^{(2)}$ and $B_P^{(2)}$ can be as large as the surface emissivity second harmonics amplitude but with a phase that

can be very different due to the exitence of the $B_p^{(2)}$ term in (76), that is always zero for surface emissivity while it can be significant for the sky glitter signals. Although it needs further investigation, that term might be a plausible physical cause for wiggles observed during the airborne campaign LOSAC.

Making use of LUTS for the coefficients $A_p^{(0)}$, $A_p^{(2)}$ and $B_p^{(2)}$, the processor will only have to perform the following processing to evaluate surface scattered signals:

1) determine the following parameters for a given L1C data:

Parameter	Description
α_{spec}	Right ascension of the specular direction with respect to the radiometer look direction [deg]
δ_{spec}	Declination of the specular direction with respect to the radiometer look direction [deg]
θ_{spec}	Specular Incidence angle at target, which is directly the radiometer incidence angle at target
ψ_{uh}	Upper Hemisphere orientation angle
u_{10}	10 meter height wind speed at target
φ_w^r	Relative angle between the direction towards which the 10 meter wind is blowing and the scattering direction towards the radiometer.
τ	Atmospheric attenuation coefficient evaluated at target

2) Interpolate the coefficients $A_p^{(0)}$, $A_p^{(2)}$ and $B_p^{(2)}$ from the LUTs using a dedicated Hermite interpolation method described in detail in appendix D.

3) Evaluate the sum in equation (76)

The methodology we used to pre-compute the LUTS for the Sky glitter Harmonics coefficients, namely, $A_p^{(0)}$, $A_p^{(2)}$ and $B_p^{(2)}$ is described in detailed in the companion galactic noise TGRD note.

To construct these lookup tables, we discretized all five dimensions ($\alpha_{spec}, \delta_{spec}, \theta_{spec}, \psi_{uh}, u_{10}$) of the coefficients. By analyzing the dependence on each dimension, and weighing the accuracy constraint with constraints imposed by computational resources, we have determined that a reasonable discretization is the following:

$\{u_{10}\} = \{3,5,7,10,15,25\} m/s,$
$\{\theta_{spec}\} = \{0°,10°,20°,25°,30°,35°,40°,45°,50°,55°,60°,70°,80°\}$
The grid for ψ_{uh} is regular and defined (in degrees, mathematical convention) by the set
$\{-\psi_{uh}\} = \{22.5n\}$
where n is a integer ranging from 0 through 16. The grid for the specular right ascension α_{spec} is regular and defined (also in degrees) by the set
$\{\alpha_{spec}\} = \{3.75n\}$

where n is a integer ranging from 0 through 96. Finally, the grid for the specular declination δ_{spec} is regular and defined (in degrees) by the set

$$\{\delta_{spec}\} = \{3.75n\}$$

where n is a integer ranging from 0 through 96. It should be noted that the lookup table is defined in B1950 celestial coordintes, not the J2000 coordinate system. The lookup tables are stored in a MATLAB Version 7 file. The following table lists the correspondence between variable names and quantities described above.

Table 2: Mapping Between MATLAB Variable Names and Physical Quantities in the Lookup Tables

MATLAB Variable Name	Physical Quantity	Independent Variables
dec_b1950	B1950 declination δ_{spec} [deg]	δ_{spec}
ra_b1950	B1950 right ascension α_{spec} [deg]	α_{spec}
ws	10-m wind speed [m s^{-1}]	u_{10}
eia	radiometer incidence angle [deg]	θ_{spec}
psi	Upper Hemisphere orientation angle - ψ_{uh} [deg]	ψ_{uh}
th_symm	$\tilde{A}_h^{(0)}$: symmetric H-pol component [K]	$(\delta_{spec}, \alpha_{spec}, u_{10}, \theta_{spec}, \psi_{uh})$
tv_symm	$\tilde{A}_v^{(0)}$: symmetric V-pol component [K]	$(\delta_{spec}, \alpha_{spec}, u_{10}, \theta_{spec}, \psi_{uh})$
th_hc	$\tilde{A}_h^{(2)}$: $\cos(2\phi_w)$ harmonic amplitude H-pol [K]	$(\delta_{spec}, \alpha_{spec}, u_{10}, \theta_{spec}, \psi_{uh})$
th_vc	$\tilde{A}_v^{(2)}$: $\cos(2\phi_w)$ harmonic amplitude V-pol [K]	$(\delta_{spec}, \alpha_{spec}, u_{10}, \theta_{spec}, \psi_{uh})$
th_hs	$\tilde{B}_h^{(2)}$: $\sin(2\phi_w)$ harmonic amplitude H-pol [K]	$(\delta_{spec}, \alpha_{spec}, u_{10}, \theta_{spec}, \psi_{uh})$
th_vs	$\tilde{B}_v^{(2)}$: $\sin(2\phi_w)$ harmonic amplitude V-pol [K]	$(\delta_{spec}, \alpha_{spec}, u_{10}, \theta_{spec}, \psi_{uh})$

The Luts were derived for both the Kirchhoff or the SSA-1 scattering asympotic model, since it is not known which model perform the best at the moment. However, for the first operationnal implementation of the algorithm, we wish to employ the Kirchhoff approach as it minimizes errors in the predicted polarization ratios.

The scattering model is not expected to work properly in the range of wind speed strickly greater than zero and less than 3 m/s. In that range of wind speed, a "drop off" transition occurs in the scattering mechanism between purely specular reflection and rough sea surface scattering. It is expected that the threshold wind speed at which this drop off occur will be highly variable, depending on the low wind speed induced roughness variability within SMOS pixel. Therefore, the processing shall be based on three wind speed conditions based on the decision tree outputs:

        1)   if $u_{10} = 0$ m/s, than purely flat reflection model shall be implemented to evaluate surface signals with associated transport at antenna level (equation (29) above).

2) If $0 < u_{10} < 3$ m/s, although it is certainly not a physically based solution, we suggest at first to perform a linear interpolation between predictions of the flat reflection model at 0 m/s and the scattering model outputs at 3 m/s. Transport at antenna level shall then be perform using the rough sea case equation (equation (22) above).

3) If $u_{10} \geq 3$ m/s, apply the rough sea surface processing (equations (76) plus (22)).

In addition to the proposed corrections, a flag shall then be defined based on the the wind speed value conditions detailed above.

4.7.8. Error budget estimates

Main sources of errors in the estimation of the sky glitter contribution will be

✓ Errors on the estimation of the bistatic scattering coefficients of the sea surface at L-band, and

✓ Errors on the estimation of the sky brightness temperature at 1.4 GHz

An estimate of the errors on the modeling of the bistatic scattering coefficients of the sea surface at L-band can be based on the estimated errors of the asymptotic electromagnetic models, namely the SSA-1 and KA approximation. These two approaches can be considered to provide the asymptotic limits within a consistent framework of scattering slope expansions. Importantly, these two approaches lack taking into account directly the surface geometrical properties to predict the level of polarization. In particular, with the proposed models, this polarization level are independent of roughness states. SSA-1 is expected to exaggerate the polarization effects while KA will minimize them. SSA-1 overestimates HH and underestimates VV so that SSA-1 systematically overestimates the H/V ratio with a mean of order +20%. The errors on the sea surface roughness statistics, particularly those associated with the mean square slope and curvature levels within the spectrum are difficult to estimate but will clearly have an important impact as well.

In 90 % of the future SMOS measurements, we found that the numerical implementation method proposed here is in error with the exact asymptotic calculation with an error less than 0.1 K. Therefore errors associated with the use of our simplified numerical approach are expected to be of this order.

A specific case of importance in the scattering model error budget is very low wind speed conditions ($0 < u_{10} < 3$ m/s), where (i) the reflected signal energy are expected to be the highest, (ii) the surface variability will be very large and (iii) the proposed linear interpolation model is not physically based.

Another source of error might be the unpolarized sky assumption. Although the polarization signatures of sky radiations at L-band are expected to be less than about 0.1 K, we neglected signal polarization basis transformation and Faraday rotation during the sky radiation downward path as well as the complete polarized scattering mechanisms at the surface.

122

4.7.9. Practical consideration

4.7.9.1. Calibration and validation

Dedicated CAL/VAL activities should be envisaged for the SMOS skyglitter correction model with two main components:
- an Earth-based campaign aiming at measuring precisely the skyglitter scattering features at L-band (e.g., experiment similar to CoSMOS) with high-quality attitude control measurements as well as surface roughness information to calibrate and validate the bistatic-scattering coefficient models.
- a SMOS-data based analysis given the fact that the sky glitter will exhibit a predictable seasonal and geographical contamination. Re-analysis of the correction terms and measured brightnesses as function of position within the FOV, time of year, ascending or descending passes and wind speed for which good quality (close in time and space) co-localized auxiliary wind and surface roughness data are available shall be performed to assess the efficiency of the model.

4.7.9.3. Exception handling

If any parameter goes out of LUT range during the retrieval, different flags (Fg_OoR_gam2_dec, Fg_OoR_gam2_ra, Fg_OoR_gam2_WSn, Fg_OoR_gam2_theta, Fg_OoR_gam2_psi) are raised. No extrapolation is done and the boundary value is taken.

References

[1] C. T. Swift and R. E. McIntosh, "Considerations for microwave remote sensing of ocean-surface salinity," *IEEE Transactions on Geoscience and Remote Sensing*, vol. GE-21, no. 4, pp. 480–491, 1983.

[2] S. H. Yueh, R. West, W. J. Wilson, F. K. Li, E. G. Njoku, and Y. Rahmat-Samii, "Error sources and feasibility for microwave remote sensing of ocean salinity," *IEEE Trans. Geosci. Remote Sensing*, vol. 39, no. 5, pp. 1049–1060, May 2001.

[3] D. M. LeVine and S. Abraham, "Galactic noise and passive microwave remote sensing from space at L-band," *IEEE Trans. Geosci. Remote Sensing*, vol. 42, no. 1, pp. 119–129, Jan. 2004.

[4] D. M. LeVine, S. Abraham, Y. Kerr, W. Wilson, N. Skou, and S. Sobjaerg, "Comparison of model prediction with measurements of galactic background noise at L-band," *IEEE Trans. Geosci. Remote Sensing*, vol. 43, no. 9, pp. 2018– 2023, Sept. 2005.

[5] W. Reich, "A radio continuum survey of the northern sky at 1420 Mhzpart I," *Astron.Astrophys. Suppl. Series*, vol. 48, pp. 219–297, July 1982.

[6] P. Reich and W. Reich, "A radio continuum survey of the northern sky at 1420 mhz-part II," *Astron. Astrophys. Suppl. Series*, vol. 63, pp. 205– 292, July 1986.

[7] P. Reich, J. C. Testori, and W. Reich, "A radio continuum survey of the northern sky at 1420 mhz, the atlas of contour maps," *Astron. Astrophys.*, vol. 376, pp. 861–877, July 2001.

[8] E. M. Arnal, E. Bajaja, J. J. Larrarte, R. Morras, and W. G. L. P¨oppel, "A high sensitivity Hi survey of the sky at _ _ -25o," *Astronom. Astrophys. Suppl. Series*, vol. 142, pp. 35–40, Feb. 2000.

[9] J. C. Testori, P. Reich, J. A. Bava, F. R. Colomb, E. E. Hurrel, J. J. Larrarte, W. Reich, and A. J. Sanz, "A radio continuum survey of the southern sky at 1420 MHz. Observations and data reduction," *Astronomy and Astrophysics*, vol. 368, pp. 1123–1132, Mar. 2001.

[10] D. Hartmann and W. B. Burton, *Atlas of Galactic Neutral Hydrogen*. Atlas of Galactic Neutral Hydrogen, by Dap Hartmann and W. Butler Burton, pp. 243. ISBN 0521471117. Cambridge, UK: Cambridge University Press, February 1997., Feb. 1997.

[11] S. Schmidl Søbjærg, J. Rotbøll, and N. Skou, "Wind effects and angular dependence at L-band polarimetric data: first results of LOSAC," in *ESA SP-525: EuroSTARRS, WISE, LOSAC Campaigns. Proceedings of the First Results Workshop*, P. Fletcher, Ed., Mar. 2003, pp. 181–189.

[12] J. Etcheto, E. P. Dinnat, J. Boutin, A. Camps, J. Miller, S. Contardo, J. Wesson, J. Font, and D. Long, "Wind speed effect on L-band brightness temperature inferred from EuroSTARRS and WISE2001 field experiments," *IEEE Trans. Geosci. and Remote Sens.*, vol. 42, no. 10, pp. 2206–2213, 2004.

[13] A. Camps, J. Font, M. Vall-llossera, C. Gabarro, R. Villarino, L. Enrique, J. Miranda, I. Corbella, N. Duo, F. Torres, S. Blanch, J. Arenas, A. Julia, J.Etcheto, V. Caselles, A. Weill, J. Boutin, S. Contardo, R. Niclos, R. Rivas, S. Reising, P. Wursteisen, M. Berger, and M. Martn-Neira, "The WISE 2000 and 2001 Campaigns in support of the SMOS Mission: Sea surface L-band Brightness Temperature Observations and their application to Multi- Angular Salinity Retrieval," *IEEE Trans. Geosci. Remote Sensing*, vol. 42, no. 4, pp. 1039–1048, 2004.

[14] W. J. Wilson, S. H. Yueh, S. J. Dinardo, S. L. Chazanoff, A. Kitiyakara, F. K. Li, and Y. Rahmat-Samii, "Passive active l- and s-band (pals) microwave sensor for ocean salinity and soil moisture measurements," *IEEE Transactions on Geoscience and Remote Sensing*, vol. 39, no. 5, pp. 1039–1048, 2001.

[15] P. Waldteufel and S. Zine, "Impact of the variable angular apodization function on galactic contribution," CBSA, Tech. Rep., 2005.

[16] J. P. Hollinger, "Passive microwave measurements of sea surface roughness," *IEEE Trans. Geosci. Electron.*, vol. GE-9, no. 3, pp. 165–169,1971.

[17] C. T. Swift, "Microwave radiometer measurements of the Cape Cod Cannal," *Radio Sci.*, vol. 9, no. 7, pp. 641–653, 1976.

[18] W. J. Webster, T. T. Wilheit, D. B. Ross, and P. Gloersen, "Spectral characteristics of the microwave emission from a wind-driven covered sea," *J. Geophys. Res.*, vol. 81, no. 18, pp. 3095–3099, 1976.

[19] R. M. Lerner and J. P. Hollinger, "Analysis of microwave radiometric measurements from skylab," NRL, Tech. Rep., Apr. 1976, 93 p.

[20] A. Camps, J. Font, J. Etcheto, V. Caselles, A. Weill, I. Corbella, M. Vall-llossera, N. Duffo, F. Torres, R. Villarino, L. Enrique, A. Julia, C. Gabarro, J. Boutin, E. Rubio, S. C. Reising, P. Wursteisen, M. Berger, and M. Martin-Neira, "Sea surface emissivity observations at L-band: First results of the wind and salinity experiment wise 2000," *IEEE Trans. Geosci. and Remote Sens.*, vol. 40, no. 10, pp. 2117–2129, 2002.

[21] P. M. W. Kalberla, W. B. Burton, D. Hartmann, E. M. Arnal, E. Bajaja, R. Morras, and W. G. L. P̈oppel, "The Leiden/Argentine/Bonn (LAB) Survey of Galactic HI. Final data release of the combined LDS and IAR surveys with improved stray-radiation corrections," *Astronomy and Astrophysics*, vol. 440, pp. 775–782, Sept. 2005.

[22] E. Bajaja, E. M. Arnal, J. J. Larrarte, R. Morras, W. G. L. P̈oppel, and P. M. W. Kalberla, "A high sensitivity HI survey of the sky at –25° . Final data release," *Astronomy and Astrophysics*, vol. 440, pp.767–773, Sept. 2005.

[23] W. Reich, P. Reich, and E. Fuerst, "The Effelsberg 21 CM radio continuum survey of the Galactic plane between L = 357 deg and L = 95.5 deg," *Astronom. Astrophys. Suppl. Series*, vol. 83, pp. 539–568, June 1990.

[24] W. Reich, P. Reich, and E. Furst, "21cm radio continuum survey. I. (Reich+ 1990)," *VizieR Online Data Catalog*, vol. 408, pp. 30 539–+, Nov. 1997.

[25] A. Wright and R. Otrupcek, "Parkes Catalog, 1990, Australia telescope national facility." in *PKS Catalog (1990)*, 1990, pp. 0–+.

Appendix A: Auxiliary datasets used in the generation of the sky map

A. The Effelsberg survey

The Effelsberg survey [23,24] was conducted over the Galactic plane between $57^{o} \leq l \leq 95.5^{o}$ and $-4^{o} \leq b \leq 4.^{o}$ with the Effelsberg 100-m radio telescope. This survey covers the surroundings of the galactic plane. This survey is specifically used to complement the continuum survey around Cassiopeia A. Effelsberg survey does not include any data for Cygnus A.

Data provided in the Effelsberg survey can be converted to fit into the Reich continuum map. Indeed:
• The resolution of the 100m Effelsberg telescope (HPBW of 9.4') is higher than the one of the Stockert telescope used for the Reich continuum survey
• Data for Effelsberg survey are provided in main beam brightness temperature whereas Stockert data are provided in full beam brightness temperature.
An associated catalog of strong sources also exist

B. The NRAO VLA Sky Survey (NVSS).

Conducted by the National Radio Astronomy Observatory, the NRAO VLA Sky Survey (NVSS) is a 1.4 GHz continuum survey covering the entire sky north of -40 deg declination. A detailed description appears in [26]. In addition to the images, a source catalog was extracted by fitting elliptical Gaussians to all significant peaks. For more information, see http://www.cv.nrao.edu/nvss/. The sources flux proposed in NVSS are given an accuracy of 3% .

C. The Parkes survey

The Parkes database [25] consists of radio and optical data for 8264 radio sources. It covers essentially all the sky south of declination +27 degrees but largely excludes the Galactic Plane and the Magellanic Cloud regions. This survey is used for strong sources in the Southern sky.

D. Cross comparison NVSS-Effelsberg catalogues

A first check of the validity of the approach can be done by comparing integrated NVSS flux to the Effelsberg survey of sources in the galactic plane. The NVSS sources are extracted for the coordinates identified in the Effelsberg catalogue and their flux is integrated. Comparison in Figure 6 shows a rms error of around 0.5 Jy (0.25 Jy if the strongest source is not considered). This corresponds to approximately 0.5 K rms at the scale of the Reich and Reich continuum map and to 0.005 K at the scale of SMOS main beam. Some of the observed discrepancies come from the lack of compatibility between the protocols that describe the extraction of the sources from the catalogues (e.g. circular or square box). Only a few sources may contribute to a noticeable error at the scale of SMOS beam. For an error threshold selected at 0.05K, sources where discrepancies are larger than 5 Jy must be carefully considered.

E. Strong sources: Cassiopeia A, Cygnus A, Taurus A, Virgo A

Some very strong sources are present in the sky, which flux was measured at a range of frequencies. Among these, Cassiopeia A is characterised by a strong variation of its flux with time. Consequently, even if an estimation of its flux can be provided, it is not advised to use

it in any correction procedure. Virgo A is a small source which is surrounded by a halo which is a strong contributor in emission at low frequencies.

F. Calibration sources

An other set of sources is usually used for calibration purpose as their angular extension is very small and their flux is stable in time. The position / intensity of all these sources is found in literature and can be used to check the values of the sources extracted from the catalogue, as seen below where NVSS output is compared to what is found in literature. Discrepancies are mostly caused by the presence of a strong halo which is a strong contributor in emission; this is the case of Cassiopeia A and of Virgo A (at low frequencies).

Appendix B: Reference frames and transformation matrices

A. Reference frames

We begin by establishing several reference frames.

Earth Fixed Reference Frame

The first is the Earth Fixed Reference Frame, or E, centered at the center of the Earth Reference Ellipsoid, with cartesian basis $(\hat{x}_e, \hat{y}_e, \hat{z}_e)$.

  $\hat{x}_e$ points outward along the equatorial plane towards the Greenwich meridian,
  $\hat{y}_e$ points outward along the equatorial plane towards 90° E, and
  $\hat{z}_e$ points towards the North Pole.

Altitude-Azimuth frame

The second frame is the so-called alt-azimuth frame, or A, with cartesian basis $(\hat{x}_t, \hat{y}_t, \hat{z}_t)$, with

  $\hat{x}_t$ pointing eastward,
  $\hat{y}_t$ pointing northward, and
  $\hat{z}_t$ pointing upward (zenith).

This frame is the same as the topocentric frame defined in the EE CFI Mission Convention Document and is the natural frame in which to express the surface scattering problem since the scattering geometry is typically defined relative to the local surface orientation. Since this coordinate frame is defined relative to the location on the Earth's surface, the projection of the cartesian basis vectors for this frame in the Earth Fixed Coordinate System depends on latitude and longitude.

True of Date (TOD) Celestial Frame

The third frame is the True of Date (TOD) Celestial Frame, or C, with cartesian basis $(\hat{x}_c, \hat{y}_c, \hat{z}_c)$, in which the galactic noise map is provided. This frame is aligned with the Earth Fixed Frame except for a time-dependent rotation of $(\hat{x}_c, \hat{y}_c)$ relative to $(\hat{x}_e, \hat{y}_e)$. The center of the frame coincides with the center of the Earth, and the x-axis coincides with the direction of the true vernal equinox of date. This coordinate system's orientation accounts for the nutation of the Earth owing to a periodic effect of the gravitation fields of the moon and other planets acting on the Earth's equatorial bulge. Using the terminology in the EE CFI MCD, to transform a vector from the TOD Celestial Frame to the Earth Fixed Frame we apply a rotation about the $\hat{z}_e$-axis by the Earth rotation angle, H, which in turn is the sum of the Greenwich siderial angle G and a nutation angle μ.

B. Frames transformation

The transformation from one frame to another can be written as a 3×3 matrix, and we denote the transform from frame I to frame J as T_{IJ}. The matrices are built with the help of EE CFI. As mentioned above, the transformation from the Earth Fixed Frame to the TOD Celestial Frame, denoted T_{ec}, is a rotation about the $\hat{z}_e$-axis by an angle H. Introducing the rotation matrix R_z for a counterclockwise rotation by angle ϕ of the coordinate system about the $\hat{z}_c = \hat{z}_e$-axis

$$R_z(\phi) = \begin{pmatrix} \cos\phi & \sin\phi & 0 \\ -\sin\phi & \cos\phi & 0 \\ 0 & 0 & 1 \end{pmatrix}.$$

we can write the E to C transformation as

$$T_{ec} = R_z(-H) = R_z(-G-\mu), \tag{8}$$

Its inverse is

$$T_{ce} = T_{ec}^{-1} = R_z(H) = R_z(G+\mu). \tag{9}$$

G is a third-order polynomial in time. When G is expressed in degrees and T is the so-called Universal Time (UT1) expressed in the Modified Julian Day 2000 (MJD2000) date convention, the formula for G is

$$G = 99.96779469 + 360.9856473662860 T + 0.29079 \times 10_{-12} T_2. \tag{10}$$

Universal Time, UT1, is very close to the common Coordinated Universal Time (UTC), but differs slightly from it in that it does not differ from actual atomic clock time (TAI) by a constant integer number of seconds, whereas UTC time does. Since both UT1 and UTC are defined to be consistent with the mean diurnal motion of the Earth relative to the stars, they must be adjusted periodically, but the adjustment is accomplished differently in the two systems. For UT1 time this is done smoothly, whereas for UTC time this is accomplished by inserting leap seconds at scheduled times into UTC when it is predicted to lag behind UT1 time by a threshold (.9 s). This introduces discontinuities in UTC. In UT1, no discontinuities exist since the adjustment is continuous.

In the Modified Julian Day 2000 (MJD2000) J_m date convention time, either in the UT1 system or in the UTC system, is expressed as the interval of time in days (including fractional days) since midnight January 1, 2000. It differs from true Julian date J_d by a constant value

128

of 2451544.5 decimal days, so that in decimal days we have

$$J_d = J_m + 2451544.5. \tag{11}$$

As previously mentioned, the transformation between the alt-azimuth frame A and another frame is complicated by the fact that the alt-azimuth frame depends on location of the origin on the surface of the Earth, so that $A = A(\vartheta_g, \varphi_g)$, where ϑ_g is geodetic latitude and φ_g is the geodetic longitude. Here we take the geodetic longitude to be equal to the geocentric longitude. The geodetic latitude is the angle between the equatorial plane and the local normal to the Earth's surface at the point in question. It is related to the spherical coordinate latitude θ_s by the relation

$$\theta_s = \tan^{-1}\left((1 - e_2)\tan\vartheta_g\right), \tag{12}$$

where

$$e = \sqrt{\frac{A_e^2 - B_e^2}{A_e^2}}, \tag{13}$$

is the eccentricity of the ellipsoidal Earth, $A_e = 6378137$ m is the Earth's major axis (equatorial) radius and $B_e = 6356752.3142$ m is the Earth's minor axis radius. To determine explicitly the transformation from A to E we introduce a second rotation matrix that rotates the coordinate system counterclockwise about the x-axis,

$$R_x(\phi) = \begin{pmatrix} 1 & 0 & 0 \\ 0 & \cos\phi & \sin\phi \\ 0 & -\sin\phi & \cos\phi \end{pmatrix}; \tag{14}$$

To compute the composite transformation from A to E, we rotate the local alt-azimuth frame about the $\hat{x}_t$-axis by the angle $\phi = \vartheta_g - \frac{\pi}{2}$ to align $\hat{z}_t$ with $\hat{z}_e$, and then we rotate the resulting intermediate (primed) frame about the new $\hat{z}$-axis $\hat{z}_{t'}$ by the angle $-\varphi_g - \frac{\pi}{2}$ to align $\hat{x}_{t'}$ with x_e. The resulting composite transformation from A to E can be written as

$$T_{ae}(\vartheta_g, \varphi_g) = R_z\left(-\varphi_g - \frac{\pi}{2}\right) R_x\left(\vartheta_g - \frac{\pi}{2}\right) \tag{15}$$

and its inverse, mapping vectors from E to A, is simply

$$T_{ea}(\vartheta_g, \varphi_g) = R_x\left(-\vartheta_g + \frac{\pi}{2}\right) R_z\left(\varphi_g + \frac{\pi}{2}\right) \tag{16}$$

To organize the results of the scattering calculations and to compare results with specular reflection calculations, it is also useful to be able to compute the specular direction for a given incidence/azimuth angle. This can be accomplished by applying a transformation matrix T_{ref} which rotates a vector by 180° about the $\hat{z}_t$ axis in the alt-azimuth coordinate system:

$$T_{ref} = R_z(\pi). \tag{17}$$

The fourth frame is the Instrument Reference Frame, I. By our convention, cartesian basis vectors for this frame, denoted $(\hat{x}_i, \hat{y}_i, \hat{z}_i)$ are such that $\hat{x}_i$ points to the right of instrument motion, normal to the orbital plane, $\hat{y}_i$ points in the direction of spacecraft motion, and $\hat{z}_i$ points upward normal to the instrument plane containing $\hat{x}_i$ and $\hat{y}_i$. The sign convention we adopt here for $\hat{x}_i$ and $\hat{y}_i$ is opposite that in EE CFI, in which $\hat{y}_i$ is directed along spacecraft velocity vector towards the rear, while $\hat{x}_i$ is directed normal to the orbital plane to the left of

the spacecraft velocity vector. This reference frame is complicated by the fact that the spacecraft position and orientation, or attitude, are functions of time in E, so the transformation matrix between I and E is a function of time. Using CFI, at a particular time t (expressed in UTC) we obtain the transformation matrix $T_{ie}(t)$ transforming a vector from the instrument frame to the Earth Fixed Frame E and the inverse transform T_{ei}.

To find the transformation from the alt-azimuth frame to the celestial frame C, we first transform from alt-azimuth to the Earth Fixed Frame and then transform the resulting vector from the Earth fixed Frame to the celestial frame. The resulting transformation matrix is thus

$$T_{ac}=T_{ec}T_{ae}, \tag{18}$$

and its inverse, going from celestial coordinates to alt-azimuth coordinates, is

$$T_{ca}=T_{ac}^{-1}=T_{ea}T_{ce}. \tag{19}$$

In each of the above frames we can represent vectors in a spherical coordinate system, related to the corresponding cartesian coordinate system by the relations

$$\begin{aligned} x_k &= r_k \cos\theta_k \cos\phi_k, \\ y_k &= r_k \cos\theta_k \sin\phi_k, \\ z_k &= r_k \sin\theta_k, \end{aligned} \tag{20}$$

where k refers to the coordinate system, θ_k is the altitude (or latitude), ϕ_k is the azimuth, and r_k is range. In the Instrument Frame, we follow convention and introduce the additional director cosine representation of the spherical coordinates,

$$\begin{aligned} \xi &= \sin\theta_b \cos\phi, \\ \eta &= \sin\theta_b \sin\phi, \end{aligned} \tag{21}$$

where $\theta_b = \frac{\pi}{2} - \theta_i$ is the angle from boresight. In considering the finite beamwidth of the synthetic antenna we will need to integrate over the solid angle

$d\Omega = \sin\theta_b \, d\theta_b \, d\phi = \sin\theta_b J^{-1}(\theta_b,\phi)\, d\xi d\eta$ subtended by the beam, where J is the Jacobian of the transformation from (θ_b,ϕ) to (ξ,η). The Jacobian is

$$J(\theta_b,\phi)=(\xi,\eta)(\theta_b,\phi)=\begin{vmatrix} \xi\theta_b & \xi\phi \\ \eta\theta_b & \eta\phi \end{vmatrix}=\begin{vmatrix} \cos\theta_b\cos\phi & -\sin\theta_b\sin\phi \\ \cos\theta_b\sin\phi & \sin\theta_b\cos\phi \end{vmatrix}=\cos\theta_b\sin\theta_b=\sqrt{1-\xi^2-\eta^2}\sin\theta_b. \tag{22}$$

and so the transformed solid angle increment is

$$d\Omega=\sin\theta_b \, d\theta \, d\phi=\frac{d\xi d\eta}{\cos\theta_b},=\frac{d\xi d\eta}{\sqrt{1-\xi_2-\eta_2}}. \tag{23}$$

It should be noted that in the above transformations we are concerned about transforming directions rather than absolute positions, since we assume that the galactic signal is at such a large distance that origin shifts by distances on the order of the Earth diameter do not alter significantly the direction of a particular galactic source.

A fifth frame is termed the geographic frame, G. This frame is related to the instrument frame by a rotation about the $\hat{x}_i$ axis by a tilt angle t to align the instrument $\hat{z}_i$ axis with the $\hat{z}_t$ axis of the topocentric frame at the satellite subpoint $O=(\vartheta_{sp},\phi_{sp})$, $A_o=A(\vartheta_{sp},\phi_{sp})=G$. Thus, $\hat{x}_i$ is parallel to $\hat{x}_t(\vartheta_{sp},\phi_{sp})$.

As mentioned above, the alt-azimuth frame is the natural frame in which to perform bistatic scattering calculation, since in this frame relevant incidence and azimuth angles are readily

computed. Therefore, in performing scattering calculations for SMOS, we must establish a local alt-azimuth frame for every point in the FOV at which we wish to compute the scattered signal in the antenna frame. To this end, for each (ξ,η) in the director cosine coordinate system, we use CFI to determine the satellite location in E and we then determine the location on the Earth Reference Ellipsoid at which the line of sight (LOS) intersects the Earth. We let (x_t,y_t,z_t) be the unknown target location on the Earth's surface in E, (x_s,y_s,z_s) be the instrument location E, and we let (d_x,d_y,d_z) be the unit vector in the instrument look direction in E. Then if we let R be the range from instrument to the target, the target location is $(x_s+Rd_x, y_s+Rd_y, z_s+Rd_z)$, and it must satisfy the equation for an ellipsoid,

$$\frac{(x_s+Rd_x)^2}{A_e^2}+\frac{(y_s+Rd_y)^2}{A_e^2}+\frac{(z_s+Rd_z)^2}{B_e^2}=1. \qquad (24)$$

Expanding this equation and letting

$$A=\frac{d_x^2}{A_e^2}+\frac{d_y^2}{A_e^2}+\frac{d_z^2}{B_e^2},$$
$$B=\frac{2x_sd_x}{A_e^2}+\frac{2y_sd_y}{A_e^2}+\frac{2z_sd_z}{B_e^2},$$
$$C=\frac{x_s^2}{A_e^2}+\frac{y_s^2}{A_e^2}+\frac{z_s^2}{B_e^2}-1, \qquad (25)$$

the solution for R, the distance to the target, is

$$R=-\frac{B}{2A}\pm\frac{\sqrt{B^2-4AC}}{2A} \qquad (26)$$

If $B^2-4AC<0$ or if $R<0$ then the line of sight does not intersect the Earth surface, in which case the instrument receives radiation directly from space. In the case of multiple positive solutions, the smaller one corresponds the the first intersection of the line of sight with the Earth surface, and the other is on the other side of the the Earth.

Appendix C: Properties of the Angle Φ_{si}

Recalling the definition of Φ_{si},

$$\Phi_{si}(\theta_o,\phi_o,\phi_s,\theta_s)=\tan^{-1}\left(\frac{\sin\theta_s\sin\phi_s+\sin\theta_o\sin\phi_o}{\sin\theta_s\cos\phi_s+\sin\theta_o\cos\phi_o}\right)=\tan^{-1}\left(\frac{d_y}{d_x}\right), \qquad (27)$$

where
$$d_x=\sin\theta_s\cos\phi_s+\sin\theta_o\cos\phi_o,$$
$$d_y=\sin\theta_s\sin\phi_s+\sin\theta_o\sin\phi_o \qquad (28)$$

Now consider a change in ϕ_s by some amount $\Delta\phi_s$. Now let ϕ_o change by some amount, $\Delta\phi_o$. Then the new value of Φ_{si} is

$$\Phi_{si}'=\Phi_{si}(\theta_o,\phi_o+\Delta\phi_o,\phi_s+\Delta\phi_s,\theta_s)=\tan^{-1}\left(\frac{\sin\theta_s\sin(\phi_s+\Delta\phi_s)+\sin\theta_o\sin(\phi_o+\Delta\phi_o)}{\sin\theta_s\cos(\phi_s+\Delta\phi_s)+\sin\theta_o\cos(\phi_o+\Delta\phi_o)}\right)$$
$$=\tan^{-1}\left(\frac{\sin\theta_s(\sin\phi_s\cos\Delta\phi_s+\cos\phi_s\sin\Delta\phi_s)+\sin\theta_o(\sin\phi_o\cos\Delta\phi_o+\cos\phi_o\sin\Delta\phi_o)}{\sin\theta_s(\cos\phi_s\cos\Delta\phi_s-\sin\phi_s\sin\Delta\phi_s)+\sin\theta_o(\cos\phi_o\cos\Delta\phi_o-\sin\phi_o\sin\Delta\phi_o)}\right). \qquad (29)$$

Now if we choose $\Delta\phi_o=\Delta\phi_s$, then we obtain

$$\Phi_{si}'=\tan^{-1}\left(\frac{\sin\theta_s(\sin\phi_s\cos\Delta\phi_s+\cos\phi_s\sin\Delta\phi_s)+\sin\theta_o(\sin\phi_o\cos\Delta\phi_s+\cos\phi_o\sin\Delta\phi_s)}{\sin\theta_s(\cos\phi_s\cos\Delta\phi_s-\sin\phi_s\sin\Delta\phi_s)+\sin\theta_o(\cos\phi_o\cos\Delta\phi_s-\sin\phi_o\sin\Delta\phi_s)}\right). \qquad (30)$$

Collecting coefficients of $\cos\Delta\phi_s$ and $\sin\Delta\phi_s$, we have

$$\Phi_{si}' = \tan^{-1}\left(\frac{\cos\Delta\phi_s(\sin\theta_s\sin\phi_s + \sin\theta_o\sin\phi_o) + \sin\Delta\phi_s(\sin\theta_s\cos\phi_s + \sin\theta_o\cos\phi_o)}{\cos\Delta\phi_s(\sin\theta_s\cos\phi_s + \sin\theta_o\cos\phi_o) - \sin\Delta\phi_s(\sin\theta_s\sin\phi_s + \sin\theta_o\sin\phi_o)}\right), \tag{31}$$

or

$$\Phi_{si}' = \tan^{-1}\left(\frac{(\cos\Delta\phi_s)d_y + (\sin\Delta\phi_s)d_x}{(\cos\Delta\phi_s)d_x - (\sin\Delta\phi_s)d_y}\right). \tag{32}$$

Now defining

$$d_{x'} = (\cos\Delta\phi_s)d_x - (\sin\Delta\phi_s)d_y,$$
$$d_{y'} = (\sin\Delta\phi_s)d_x + (\cos\Delta\phi_s)d_y, \tag{33}$$

we have

$$\Phi_{si}' = \tan^{-1}\left(\frac{d_{y'}}{d_{x'}}\right), \tag{34}$$

where

$$\begin{pmatrix} d_{x'} \\ d_{y'} \end{pmatrix} = \begin{pmatrix} \cos\Delta\phi_s & -\sin\Delta\phi_s \\ \sin\Delta\phi_s & \cos\Delta\phi_s \end{pmatrix}\begin{pmatrix} d_x \\ d_y \end{pmatrix} \tag{35}$$

But this is just a counterclockwise rotation of $(d_x, d_y)^T$ by $\Delta\phi_s$, and so

$$\Phi_{si}' = \Phi_{si} + \Delta\phi_s, \tag{36}$$

or

$$\Phi_{si}(\theta_o, \phi_o + \Delta\phi_s, \phi_s + \Delta\phi_s, \theta_s) = \Phi_{si}(\theta_o, \phi_o, \phi_s, \theta_s) + \Delta\phi_s, \tag{37}$$

or

$$\Phi_{si}(\theta_o, \phi_o, \phi_s, \theta_s) = \Phi_{si}(\theta_o, \phi_o - \Delta\phi_s, \phi_s - \Delta\phi_s, \theta_s) + \Delta\phi_s. \tag{38}$$

In words, this equation states that the Φ_{si} function at $(\theta_o, \phi_o, \phi_s, \theta_s)$ is identical to the same function Φ_{si} evaluated at $(\theta_o, \phi_o - \Delta\phi_s, \phi_s - \Delta\phi_s, \theta_s)$, except that it will be everywhere shifted in value by $+\Delta\phi_s$. If we let $\Delta\phi_s = \phi_s$, then

$$\Phi_{si}(\theta_o, \phi_o, \phi_s, \theta_s) = \Phi_{si}(\theta_o, \phi_o - \phi_s, 0, \theta_s) + \phi_s, \tag{39}$$

so that $\Phi_{si}(\theta_o, \phi_o, \phi_s, \theta_s)$ may be obtained from Φ_{si} evaluated at zero ϕ_s merely by evaluating Φ_{si} at $\phi_o - \phi_s$.

Now let us define a reference Φ_{si}, say

$$\Phi_{si}^0(\theta_o, \phi_o, \theta_s) = \Phi_{si}(\theta_o, \phi_o, 0, \theta_s), \tag{40}$$

which is Φ_{si} evaluated at zero radiometer azimuth. Then from the ϕ_s translation property of Φ_{si} we have just established,

$$\Phi_{si}(\theta_o, \phi_o, \phi_s, \theta_s) = \Phi_{si}(\theta_o, \phi_o - \phi_s, 0, \theta_s) + \phi_s = \Phi_{si}^0(\theta_o, \phi_o - \phi_s, \theta_s) + \phi_s. \tag{41}$$

Recalling that the joint dependence of the second harmonic on Φ_{si} and φ_w is of the form $\cos 2(\Phi_{si} - \varphi_w)$, we have

$$\Phi_{si} - \varphi_w = \Phi_{si} - \phi_s - (\varphi_w - \phi_s), \tag{42}$$

but since $\Phi_{si} - \phi_s = \Phi_{si}^0$, we have

$$\Phi_{si} - \varphi_w = \Phi_{si}^0 - (\varphi_w - \phi_s). \tag{43}$$

Appendix D: Multi-dimensional Hermite Interpolation

Denote four successive gridpoints in one dimension by (x_0, x_1, x_2, x_3), and consider the problem

of interpolating some discrete function F_i, whose values are given at these gridpoints by (F_0, F_1, F_2, F_3), on the interval $[x_1, x_2]$. We wish this interpolating function to be continuous and to have continuous first derivatives on this interval. Noting that a cubic polynomial provides the freedom to enforce these contraints, we choose our interpolating function to be a cubic polynomial, and we determine coefficients for this polynomial to satisfy our contraints. Let

$$s = \frac{x - x_1}{x_2 - x_1}, \qquad (44)$$

and define the interpolating function on the interval $[x_1, x_2]$ by

$$p(s) = c_1 s^3 + c_2 s^2 + c_3 s + c_4. \qquad (45)$$

We wish this cubic interpolating polynomical $p(s)$ to pass through x_1 and x_2, so we must have

$$p(s=0) = c_4 = F_1,$$
$$p(s=1) = c_1 + c_2 + c_3 + c_4 = F_2. \qquad (46)$$

Additionally, we want the first derivatives of $p(s)$ to be contrained such that they are identical to the first derivatives of the corresponding $p(s)$ functions on the neighboring intervals. One way to accomplish this is to use centered differences to the define the derivatives at x_1 and x_2. Noting that

$$p_s = p_x x_s = (x_2 - x_1) p_x. \qquad (47)$$

we see that

$$p_s(s=0) = c_3 = \alpha(F_1 - F_0),$$
$$p_s(s=1) = 3c_1 + 2c_2 + c_3 = \beta(F_3 - F_1). \qquad (48)$$

where

$$\alpha = \frac{x_2 - x_1}{x_2 - x_0},$$
$$\beta = \frac{x_2 - x_1}{x_3 - x_1}. \qquad (49)$$

Arranging the preceding four constraints into a matrix equation, we have

$$M_1 F_i = M_2 c_i, \qquad (50)$$

where $F_i = (F_0, F_1, F_2, F_3)_T$ and $c_i = (c_1, c_2, c_3, c_4)_T$, and

$$M_1 = \begin{pmatrix} 0 & 1 & 0 & 0 \\ 0 & 0 & 1 & 0 \\ -a & 0 & a & 0 \\ 0 & -b & 0 & b \end{pmatrix} \qquad (51)$$

and

$$M_2 = \begin{pmatrix} 0 & 0 & 0 & 1 \\ 1 & 1 & 1 & 1 \\ 0 & 0 & 1 & 0 \\ 3 & 2 & 1 & 0 \end{pmatrix}. \qquad (52)$$

Now we can write the interpolating polynomial as

$$p(s) = (s^3, s^2, s, 1) \begin{pmatrix} c_1 \\ c_2 \\ c_3 \\ c_4 \end{pmatrix} \qquad (53)$$

But since

$$c_i = M_2^{-1} M_1 F_i, \qquad (54)$$

we have

$$p(s) = (s_3, s_2, s, 1) M_2^{-1} M_1 F_i, \qquad (55)$$

or

$$p(s) = \begin{pmatrix} -\alpha s_3 + 2\alpha s_2 - \alpha s \\ (2-\beta)s_3 + (\beta-3)s_2 + 1 \\ (\alpha-2)s_3 + (3-2\alpha)s_2 + \alpha s \\ \beta(s_3 - s_2) \end{pmatrix}^T \begin{pmatrix} F_0 \\ F_1 \\ F_2 \\ F_3 \end{pmatrix} \qquad (56)$$

Note that the weights are independent of the data F_i and depend only on the desired interpolation location s and the location of gridpoints x_i on which the discrete function is defined.

To interpolate in more than one dimension we simply apply the above formula along each dimension separately and then multiply the appropriate weights along each dimension to obtain the weights for a given point at which F is defined. The number of points in the interpolation stencil is 4_n, where n is the number of dimensions of the function F.

4.8 Faraday rotation computation from geomagnetic field

4.8.1 Theoretical description

4.8.1.1 Physics of the problem

The Faraday rotation is due to the effect of ionospheric electrons on the propagation of electromagnetic waves.

4.8.1.2 Mathematical description of algorithm

The Faraday angle ω_{Fa} for each view is provided by L1c data (field #09 or #10 in tables 26 or 27 of SO-IS-DME-L1PP-0002, depending on polarization mode), using auxiliary TEC_n (Total Electron nadir columnar Content) values. Therefore the description below need only be implemented when introduced in the direct model, in the case where TEC_n is retrieved.

Making use of the magneto-ionic theory and using the quasi longitudinal approximation as well as assuming a plane parallel ionosphere result in the following expression for L_band ((Le Vine and Abraham 2002; Waldteufel, Floury et al. 2004)):

$$\omega_{Fa} \approx 6950 * TEC_n * (\mathbf{B.U_{LS}}) / \cos(\theta_g) \ (°) \qquad \textbf{Eq 1}$$

Where:
- TEC_n is the total **vertical** electron content (TEC units; 1 TEC unit = 10^{16} m^{-2}); it is obtained from L1c field #15 for each view.. The range of TEC_n is about 5 to 50.
  If the TEC_n is retrieved, then a unique value for the DGG node is defined as initial value by selecting the median of the values for every view. Otherwise, every individual TEC_n value can be selected for computing ω_{Fa}.
- $(\mathbf{B.U_{LS}})$ is the scalar product of the magnetic field vector $\mathbf{B}$ by the unitary vector $\mathbf{U_{LS}}$ giving the direction of the line of sight (from target to spacecraft).
- The magnitude |B| of $\mathbf{B}$ (teslas) is obtained from L1c field #16 (expressed in nanotesla). The range of |B| is about 2 to 5 10^{-5} Tesla.

The vectors $\mathbf{B}$ and $\mathbf{U_{LS}}$ must be expressed in the same Euclidian reference frame.
- Concerning $\mathbf{B}$: The L1c provides (fields #17 and #18) the declination dec_B and inclination inc_B of B in a local geographical frame Oxyz (Ox towards East, Oy toward North, Oz upwards)
  In L1c data, dec_B is understood as the angle of $\mathbf{B}$ away from geographic North Oy, counted positive eastwards (clockwise); inc_B is understood as the angle of $\mathbf{B}$ away from the local horizontal plane Oxy, counted positive downwards.
  Every individual |B|, dec_B and inc_B value can be selected for computing ω_{Fa}.
- Concerning $\mathbf{U_{LS}}$: let us define polar geographical coordinates θ_g (elevation away from the Oz axis) and φ_n (azimuth from origin Ox, counter clockwise).
  Then :

B = [(cos(inc_B) sin(dec_B), cos(inc_B) cos(dec_B), -sin(inc_B)]

U$_{LS}$ = [sin(θ_g) cos(φ_n), sin(θ_g) sin(φ_n), cos(θ_g)];

(Note that φ_n differs from the relative azimuth defined in a frame linked to the spacecraft and introduced in the SM ATBD).

It is expected that the EE CFI may provide directly φ_n and θ_g. Alternatively, θ_g could be inferred from the incidence angle (provided by the L1c) through adding the Earth center angle; φ_n could be computed from the DGG node coordinates, assuming the coordinates of the subsatellite point are provided by the EE CFI.

The ω_{Fa} Faraday angle value is positive clockwise.

4.8.2 Assumptions and limitations

A single average magnetic field vector is used rather than altitude dependent values when carrying out an integration over the line of sight. The optimal value corresponds to altitudes which may vary between 350 and 400 km, depending on the ionospheric altitude profile. Considering the variation of B with altitude, resulting errors are not significant.

The TEC value is assumed constant over the area (up to about a 500 km size at ionospheric altitudes) concerned by a SMOS dwell line. This assumption may not be fully satisfactory in regions of strong ionospheric gradients.

It is useful to add an output flag (Fg_sc_TEC_gradient) in the User Data Product to warn against strong variations of the measured TEC over a dwell line. Every snapshot coming from L1 will carry its TEC value, but only a value (median from all snapshots) is used in the L2 computations at grid point level. When the difference between the maximum and minimum TEC values affecting a given DGG node is above a threshold (Tg_TEC_gradient) the flag will be rised. It is necessary to check if TEC data have the spatial resolution adequate for feeding such a flag.

References

DEIMOS Engenheria (2005) SMOS L1 Product Format Specification, SO-IS-DME-L1PP-0002 issue 1.4, 30 August 2005

4.9. Atmospheric effects

4.9.1. Theoretical description

This section of the ATBD takes advantage of the analysis reported in an ESA study [1: Peichl et al, 2004].

4.9.1.1. Physics of the problem

4.9.1.1.1. The radiative transfer equation

This section assumes a bare surface, and ignore the sky contribution as well as ionospheric effects. The geometrical rotation from the surface to the SMOS antenna is not considered either.

Several components of the atmosphere are radiatively active, which generates effects to be accounted for in the **radiative transfer equation** (RTE).

In the absence of atmosphere, the measured brightness temperature Tb_m is simply the upwelling brightness temperature from the surface Tb_s:

$Tb_m = Tb_s = SST\ e$	(1)

Where
- SST is the sea surface temperature
- e is the sea surface emissivity

Introducing the atmosphere, the RTE is written:

$Tb_m = Tb_s\ e^{-\tau_{atm}} + Tb_{up} + \Gamma\ Tb_{down}\ e^{-\tau_{atm}}$	(2a)

Where
- Tb_{up} is the brightness temperature self-emitted by the atmosphere upwards and attenuated along upward path
- Tb_{down} is the brightness temperature self-emitted by the atmosphere downwards and attenuated along downward path (In real case, when taking into account galactic noise, there is two terms (see sum of contribution equations))
- Γ is the surface reflection coefficient, with $\Gamma = 1 - e$, where e is computed for a rough surface $e=(Tb_{flat}+Tb_{rough})/SST$;
- τ_{atm} is the equivalent optical thickness of the atmosphere.

Comparing both equations, it is seen that the atmosphere will generate 3 corrective terms, which are best seen when writing equation (2) as follows:

$Tb_m = Tb_s\ +\ \mathbf{Tb_s\ (e^{-\tau_{atm}} - 1)} + \mathbf{Tb_{up}} + \mathbf{\Gamma\ Tb_{down}}\ \mathbf{e^{-\tau_{atm}}}$	(2b)

There are 4 atmospheric components to be considered: dry atmosphere, water vapor, clouds and rain. Ideally, the quantities to be known in equation (2) (τ_{atm}, Tb_{up}, Tb_{down}) are the sums of the 4 corresponding contributions.

In every case, the basic quantity from which atmospheric contributions can be estimated is normally the **lineic absorption coefficient κ**, generally expressed in dB/km.

4.9.1.1.2. Dry atmosphere

The radiatively active component in dry atmosphere is **<u>molecular oxygen</u>**.Oxygen molecules have a permanent magnetic moment; therefore absorption and radiation in the microwave region occur due to magnetic interactions with the incidence field. This interaction produces a family of rotation absorption lines in the vicinity of 60GHz (known as the oxygen complex) and an additional isolated line at 118.8GHz [Crane, 1971]. Due to pressure characteristics of the lower part of the Earth's atmosphere, pressure broadening causes the complex of lines to blend together to a continuous absorption band centered around 60GHz.

The oxygen absorption and radiation change due to changes in the meteorological parameters, and are dependent on the pressure $P(z)$ and the temperature $T(z)$ of the gas as a function of the height z.

A model for the absorption by oxygen for lower frequencies is described in [2: Ulaby, 1981]. For frequencies below 45GHz, the contribution from the 118.75GHz oxygen absorption line can be neglected, and thereby we only have the contribution from the 60GHz absorption line. Then the lineic absorption from oxygen at f=1.413 GHz can be written in dB/km as:

$$\kappa_{OX} = 1.1 \, 10^{-2} f^2 \left(\frac{P}{1013}\right)\left(\frac{300}{T}\right)^2 \gamma \left(\frac{1}{(f-f_0)^2 + \gamma^2} + \frac{1}{f^2 + \gamma^2}\right) \quad (3a)$$

where

- f is the frequency (1.413 GHz)
- f_0 is the absorption line frequency (60 GHz)
- P is the pressure in hectoPascal (hPa)
- T is the physical temperature in K
- γ is the line width parameter written in GHz as:

$$\gamma = \gamma_0 \left(\frac{P}{1013}\right)\left(\frac{300}{T}\right)^{0.85} \quad (3b)$$

Where the line width γ_0 is pressure dependent:

According to [1]: $\gamma_0 = 0.59$ above P = 333mb; $\gamma_0 = 1.18$ below 25mb, $\gamma_0 = 0.59$ [1+3.1 10^{-3} (333-P)] in between. However, more recent spectroscopic measurements [7] are better described when choosing $\gamma_0 = 0.59$ over the whole pressure range.

4.9.1.1.3. Water vapor

In the microwave region, water vapor has rotational absorption lines at 22.235 GHz and at 183.31 GHz. Furthermore there are also some absorption lines above this region, which contributes to the microwave absorption spectrum. For calculation of the absorption at L band one can, according to [Ulaby, 1981], group the contributions from the 183.31GHz and all the absorption lines above in a residual term through the use of low frequency approximation. The resulting absorption coefficient κ_{H2O} can then be written as a sum of the contribution from the 22.235 GHz absorption line κ_{22} and a residual term κ_r:

According to [Waters, 1976]:

$$\kappa_{22} = 2f^2 \rho_v \left(\frac{300}{T}\right)^{5/2} e^{-644/T} \left(\frac{\gamma_1}{(494.4 - f^2)^2 + 4f^2\gamma_1^2}\right)$$	(4a)

Where

- ρ_v is the water vapor density (gm^{-3})
- γ_1 is the line width parameter (GHz):

$$\gamma_1 = 2.85 \left(\frac{P}{1013}\right)\left(\frac{300}{T}\right)^{0.626}\left(1 + 0.018\frac{\rho_v T}{P}\right)$$	(4b)

Concerning the residual term, according to [2: Ulaby, 1981]:

$$\kappa_r = 2.4\,10^{-6} f^2 \rho_v \left(\frac{300}{T}\right)^{3/2}\gamma_1$$	(4c)

And finally:

$\kappa_{H2O} = \kappa_{22} + \kappa_r$	(4d)

4.9.1.1.4. Clouds

When electromagnetic radiation interacts with particles such as those in snow, clouds, fog and rain, it involves absorption and scattering. But if only drops, which have a diameter much smaller than the wavelength, are considered – which is the case for 1.4GHz - then scattering is unimportant, and the absorption coefficient can be calculated from the Rayleigh approximation.

The particles are assumed to be randomly distributed within the volume, and therefore the contribution of the individual particles can be summed assuming an incoherent process.

Furthermore, it is also assumed that the particles are spherical, which is a reasonably assumption for most atmospheric water and ice droplets. The scattering and absorption characteristics of a spherical particle are governed by three factors: electromagnetic wavelength, index of refraction, and particle radius.

Clouds are complex phenomena, which consists of water either in liquid or in frozen form. The amount of water and the phase of the water in the cloud depend on the altitude, the temperature and indirectly of the pressure. The clouds are described by cloud base, cloud top, the mass density of the liquid water in the cloud and principal composition of the cloud. The water content of a cloud is according to [Ulaby, 1981] typically less than 1g/m^3.

Radiative effects of ice clouds are negligible at L Band. Concerning liquid water clouds, according to [1] and [2], empirical expressions have been developed by [5: Benoit, 1968] for the lineic absorption coefficient. It appears that the only cases where the overall radiative effect at L Band might not be negligible concerns deep cumuli. However there is no reliable auxiliary data allowing select a depth for these clouds. In addition, they are mostly associated with rain events, which are dealt with next.

4.9.1.1.5. Rain

Physically, rain occurrence is similar to clouds. However the problem is complicated by several factors:

- Due to the size of raindrops, the Rayleigh approximation is no longer strictly valid, hence a dependence appears with the granulometry of rain, which is variable and not accurately known;
- Large raindrops are not spherical
- While ice particle do not contribute to atmospheric extinction, there is often a melting zone (just below the 0°C isotherm which is very poorly predicted and may not be negligible in terms of radiative effects
- Finally the rain is often expressed in rainfall intensity, whereas the relevant quantities are lineic densities (liquid water content) in the atmosphere.

For all these reasons, it does not seem practical to correct for rain. According to [1], rain in the atmosphere producing a non negligible radiative contribution when the rain intensity exceeds about 10 mm/hr; this is estimated to happen less than 0.2% of the time over all latitudes, up to less than 0.65% of the time over equatorial areas (these figures may be pessimistic for a 06h local time).

One should also mention the more in depth analysis carried out by Schultz [6].

Therefore rain occurrences are a matter for flagging rather than correcting. As stated above, the heavy clouds should be associated with rain events.

However, there are obviously cases for which rain attenuation effects will be significant. This will deserve further studies, including an attempt to build and a forward model for the rain contribution, an special attention for calibration operations. This is all the more true since rain is a major component of the global water cycle, in which the SMOS mission is expected to bring improved insights.

4.9.1.2. Mathematical description of algorithm

4.9.1.2.1. Ratiative transfer for gaseous components

From section 1.1, it is concluded that atmospheric contribution should be computed for oxygen and water vapor.

Numerical simulations show that, for L band, the Tb_{up} and Tb_{down} radiative contributions are extremely close one to each other and can be assumed equal to a single value Tb_{atm} in equation (2). Therefore what is needed is:

$\tau_{atm} = \tau_{O2} + \tau_{H2O}$	(5a)
$Tb_{atm} = Tb_{O2} + Tb_{H2O}$	(5b)

Equations (2a) and (2b) can be written again:

$Tb_m = Tb_s\, e^{-\tau atm} + Tb_{atm}\,(1 + \Gamma\, e^{-\tau atm})$	(5c)
$Tb_m = Tb_s\ + Tb_s\,(e^{-\tau atm} - 1) + Tb_{atm}\,(1 + \Gamma\, e^{\tau atm})$	(5d)

Contributions to absorption come from the whole thickness of the atmosphere. However, for oxygen it is not necessary to consider altitudes higher than a level ZM ≈ 30 km, where absorption becomes completely negligible. For water vapor, the altitude range to be considered is limited to ZM ≈ 10 km.

4.9.1.2.1.1 Multilayer model

Although this model will not be used in the prototype, we recall it here before describing the approximations that we will use (monolayer model).

Over the required altitude range, the exact computation requests knowledge of altitude profiles for T and P; then, the atmosphere is divided in slices δz. For each slice and for each component, the elementary optical thickness $\delta\tau_{GAS}$ (where GAS is replaced by either O2 or H2O) is computed from the lineic absorption coefficient (expressed in dB km^{-1}) κ_{GAS}:

$$\delta\tau_{GAS} = 1 - 1/10^{\kappa_{GAS}\ \delta z/10}$$	(6a)

The effect of **incidence angle** ι on optical thickness must be introduced in the above equation:

$$\delta z(\iota) = \delta z_{NADIR}/\cos(\iota)$$	(6b)

The total optical thickness τ_{GAS} is obtained by summing the $\delta\tau_{GAS}$ over the relevant altitude range:

$$\tau_{GAS} = \sum_{Z=0\rightarrow ZM}\delta\tau_{GAS}(z)$$	(6c)

The radiative contribution Tb$_{GAS}$ is (taking the upwelling case) computed as follows:

$$Tb_{GAS} = \sum_{Z=0\rightarrow ZM} T(z)\,\delta\tau_{GAS}(z)\exp[-\sum_{Z'=Z\rightarrow ZM}\delta\tau_{GAS}(z')]$$	(6d)

This formulation yields the upwelling oxygen contribution. As mentioned earlier, the downwelling contribution is found very close, with differences well below 0.01K.

Assuming the attenuation through an elementary layer is very small, and that the physical temperature variation at this scale is linear, the estimate for the physical temperature T(z) in (6d) can be taken as the **average** between T values for the bottom and the top of the elementary layer.

4.9.1.2.1.2. Monolayer model

For the purpose of SMOS data inversion, we show that multilayer model is not necessary to simulate atmospheric effects at L-band and we propose regressions to easily compute τ_{GAS} and Tb$_{GAS}$.

From equation (5c), it is seen that the 2 quantities linked to atmospheric radiative contributions τ_{atm} and Tb$_{atm}$ are fixed during the retrieval. Looking at equation (5d), it is seen however that the atmospheric contribution will vary with Tb$_s$ and Γ; therefore, strictly speaking, this contribution cannot be considered as a fixed additive correction.

The **oxygen** overall contribution is by far the largest atmospheric contribution. It may reach up to 6 K and beyond, as described in [1]. As shown above, after some simplifications, integrations along the vertical still remain necessary in the equations. Three ways are identified to compute τ_{GAS} and Tb$_{GAS}$:

1. Carry out the **integrations** as indicated in equations (6). The estimated necessary altitude range ZM are 20 km for O_2, 10 km for H_2O; the necessary resolution along the vertical is better than 100 m.
2. **Tabulate** the τ_{GAS} and Tb_{GAS} as functions of some parameters (e.g. surface atmospheric temperature T0, the surface pressure P0, some parameter describing the structure of the temperature profile, surface humidity,…) and then interpolate from these tables.
3. Build **empirical laws** to compute τ_{GAS} and Tb_{GAS}.

The most efficient (and physically meaningful) way to do this consists in writing the emission of each component as the product of optical thickness by an **equivalent layer (physical) temperature**, which is conveniently defined by its difference DT with the surface air temperature T0:

$Tb_{GAS} = (T0 - DT_{GAS})\, \tau_{GAS}$	(7)

For dry atmosphere, a **quadratic** fit to results obtained using the whole radiative transfer computation has been found necessary:

$\tau_{O2} = 10^{-6} \times$ (k0_tau_O2 + kT0_tau_O2 $\times$ T0 + kP0_tau_O2 $\times$ P0 + kT02_tau_O2 $\times$ T0^2 + kP02_tau_O2 $\times$ P0^2 + kT0P0_tau_O2 $\times$ T0 $\times$ P0) / cos(θ)	(8)

DT_{O2} = k0_DT_O2 + kT0_DT_O2 $\times$ T0 + kP0_DT_O2 $\times$ P0 + kT02_DT_O2 $\times$ T0^2 + kP02_DT_O2 $\times$ P0^2 + kT0P0_DT_O2 $\times$ T0 $\times$ P0	(9)

where
- θ is the incidence angle (radian)
- T0 is the near surface air temperature (Kelvin)
- P0 is the surface pressure (hectoPascal)
- τ_{O2} is obtained in neper; DT_{O2} is obtained in Kelvin

For the water vapour contribution, a **linear** fit is found adequate:

$\tau_{H2O} = 10^{-6} \times$ (k0_tau_H2O + k1_tau_H2O $\times$ P0 + k2_tau_H2O $\times$ WVC) / cos(θ) $\tau_{H2O} = \max(\tau_{H2O}, 0)$	(10)

DT_{H2O} = k0_DT_H2O + k1_DT_H2O $\times$ P0 + k2_DT_H2O $\times$ WVC	(11)

where
- **WVC** is the total precipitable water vapour content (kg m^{-2}), available from ECMWF data.
- τ_{H2O} is obtained in neper; DT_{H2O} is obtained in Kelvin

From values obtained for the DT and τ quantities:
- Tb_{O2} and Tb_{H2O} are obtained using eq. (7) respectively for O2 and H2O;
- Atmospheric term Tb_{atm} and τ_{atm} are obtained using eq. (5a) and (5b).

The numerical values for coefficients in eq. (8), (9), (10) and (11) are supplied in TGRD. These formulas were first written for land. For sea, the required accuracy is better than 0.05 K and this could be achieved using the same formulas but restricting the surface pressure range to [900 1100] hPa.

4.9.1.3. Error budget estimates (sensitivity analysis)

The method selected for computing gazeous radiative contributions has to be selected in such a way that the resulting error on upwelling brightness temperatures due to approximating the effect of physical atmospheric properties (pressure, temperature, water vapor concentration) never exceeds 0.05 K for SMOS operating conditions. It is expected that this goal is compatible with computing power/time requirements.

Then, the major error source will be due to estimates of absorption cross sections, which in turn reflect the uncertainty on spectroscopic measurements. This uncertainty is estimated around 5% .

4.9.2. Practical considerations

4.9.2.1. Calibration and validation

Since the uncertainty on absorption cross sections cannot be overcome, the resulting error will have to be corrected within the overall SMOS validation process. However, the variation with incidence angle offers a possibility to discriminate among other effects.

Assuming one succeeds in determining correctly the absorption cross sections, the resulting uncertainty would be permanently eliminated.

4.9.2.2. Quality control and diagnostics

In case a simplified algorithm is applied, care must be applied, based on considering a representative sample of experimental atmospheric data or analyses, in order to ensure that either tables or empirical laws cover the whole ranges of physical situations.

4.9.3. Assumption and limitations

Assumptions are related to laboratory knowledge of spectral properties of atmospheric gases.

Limitations concern the presence of liquid (cloud or rain) water in the atmosphere, for which a flagging approach is suggested rather than a correction.

References

[1]   M Peichl, V. Wittmann, E Anterrieu, B Picard, N Skou and S. Sobjaerg: Final report: SCIENTIFIC INPUTS FOR THE SMOS LEVEL 1 PROCESSOR DEVELOPMENT, in response to ESA contract No. 10508/02/NL/GS. The section referred to here was written by Skou and Sobjaerg.

[2]   Ulaby, Fawwaz T. and Richard K. More and Adrian K. Fung, (1981), "Microwave Remote Sensing – Active and Passive", Artech House Inc. , Vol. 1 & 3

[3]   Crane R.K. (1971).''Propagation Phenomena Affecting Satellite Communication Systems Operation in the Centimeter and Millimeter Wavelength Bands'', Proceedings of the IEEE, 59, pp 173-188.

[4]   Waters, J. W. (1976), "Absorption and Emission of Microwave Radiation by Atmospheric Gases", in Methods of Experimental Physics, M.L. Meeks, ed. 12, Part B, Radio Astronomy, Academic Press, Section 2.

[5]   Benoit, A. (1968) "Signal attenuation Due to Neutral Oxygen and Water Vapor, Rain and Clouds", Microwave Journal, 11, pp. 73-80

[6]   J. Schulz, in WP1200: "Impact of rain on sea surface brightness temperature", Scientific requirements and impact of space observations of ocean salinity for modeling and climate studies, ESA study 14273/00/NL/DC, 2002, p51-43.

[7]   Liebe, H. J., G. A. Hufford, M. G. Cotton, Propagation modeling of moist air and suspended water/ice particles at frequencies below 1000 GHz, in AGARD 52nd Specialists' Meeting of the Electromagnetic Wave Propagation Panel, pp. 3-1 - 3-10, Palma de Mallorca, Spain, 1993.

144

4.10 Cardioid model

As shown by Waldteufel et al. (2004), simultaneous retrieval of the real, ε', and imaginary part, ε'', of dielectric constant from SMOS Tb is an ill posed problem as the cost function, rather than a single minimum, exhibit a minimum valley, that can be represented analytically using a modified cardioid model. After carrying out the following change of variable:

$$\varepsilon' = A\_card \,(1 + \cos(U\_card)\,)\cos(U\_card) + B\_card$$

$$\varepsilon'' = A\_card \,(1 + \cos(U\_card)\,)\sin(U\_card)$$

[4.10.1]

which is equivalent to:

$$A\_card = m\_card^{\,2} / (m\_card + \varepsilon' - B\_card) \qquad U\_card = \tan^{-1}(\varepsilon''/(\varepsilon'-B\_card)\,)$$

$$\text{with: } m\_card = (\,(\varepsilon'-B\_card)^2 + \varepsilon''^2\,)^{1/2}$$

[4.10.2]

with B_card = 0.8, it is possible to retrieve the parameter A_card with good accuracy: a minimum of Chi2 is seen as a vertical line corresponding to a constant value of A_card and various values of U_card. Local minima of Chi2 are also observed for unrealistic negative values of A_card; as it will be described in the following, retrieval of such negative values are avoided by taking an error on prior A_card over the ocean of 20 units or by initiating the retrieval with low A_card value as low A_card are much better constrained.

With these definitions and considering direct emissivity models described above: for sea ice, A_card=1.2 (U_card=0); over a flat sea, A_card ranges between 48 and 67 depending on SSS and SST values and U_card between -0.9 and -0.5 radians.

It is clear that the minimization of Chi2 parameter does not allow to retrieve a single pair of $(\varepsilon', \varepsilon'')$ while it allows to retrieve a single value of A_card, U_card remaining undetermined. We found that initiating the retrieval with low A_card prior value (A_card^{prior} =1) and large error on A_card (σ_{A_card} =50) allows to avoid retrieval of negative A_card values while avoiding biases on low A_card values and gives the same result over ocean pixels as taking A_card^{prior} deduced from mean SSS and SST.

Details on cardioid computation over the ocean are given by Boutin et al (submitted, see Annex-2).

We suggest by default to use a minimalist model that includes the flat sea model plus atmospheric and constant galactic noise correction (GN=3.7K) reflected by a flat sea in order to minimize bias between effective A_card and A_card computed from retrieved SSS and SST. The relevance of including galactic noise and atmosphere correction in this minimalist model will be checked during AlgoVal tests.

Retrievals using the cardioid model use all the measurements available (including outliers, those affected by ice, sky radiation, sun glint, etc.). This implies the bypass of the measurement discrimination step.

In cold water, the use of the cardioid model should efficiently allow the detection of sea-ice: a flag (Fg_ice_Acard) is raised if the effective temperature T_eff<Tg_SST_ice_Acard and Acard<Tg_Acard_ice and abs(latitude) >Tg_lat_ice_Acard.

P. Waldteufel, J. L. Vergely, and C. Cot, "A modified cardioid model for processing multiangular radiometric observations," *IEEE Transactions on Geoscience and Remote Sensing*, vol. 42, pp. 1059-1063, 2004.

D. W. Marquardt, "An algorithm for least-squares estimation of non-linear parameters," *J. Soc. Ind. Appl. Math*, vol. 11, pp. 431-441, 1963.

J. Boutin, J.L. Vergely, P. Waldteufel, "On the use of an effective L-band pseudo-dielectric constant for qualifying SMOS measurements over the ocean," *submitted to IEEE Transactions on Geoscience and Remote Sensing*.

4.11. Bias correction

This section has been removed (issue 3.0) and left for the Reprocessing ATBD. The scene dependent bias correction will not be applied before having examined how it is corrected or mitigated at L1.

4.12. Transport ground level Tb to antenna level

4.12.1. Theoretical description

4.12.1.1. Physics of the problem

The iterative process to retrieve salinity from SMOS measurements requires comparing the measured data with Tb modeled through the algorithms described in this ATBD. All the different sub-models are describing the processes that contribute to sea surface L-band emission (flat sea, roughness, foam, …), the effects of incoming radiation that need to be added to this emission (atmospheric, cosmic and galactic background, …), plus the modifications to this radiation in its transit through the atmosphere. The result is the modeled value of Tb on top of the atmosphere expressed in the Earth reference frame.

The next step is to transport this Tb to the SMOS antenna reference frame, considering both the change in geometry and the ionospheric effects (Faraday rotation), to allow the comparison with the measured Tb.

4.12.1.2. Mathematical description of the algorithm

With the viewing geometry as defined in ACRI Reqts_L2Draft-2.doc (see figure and annex)
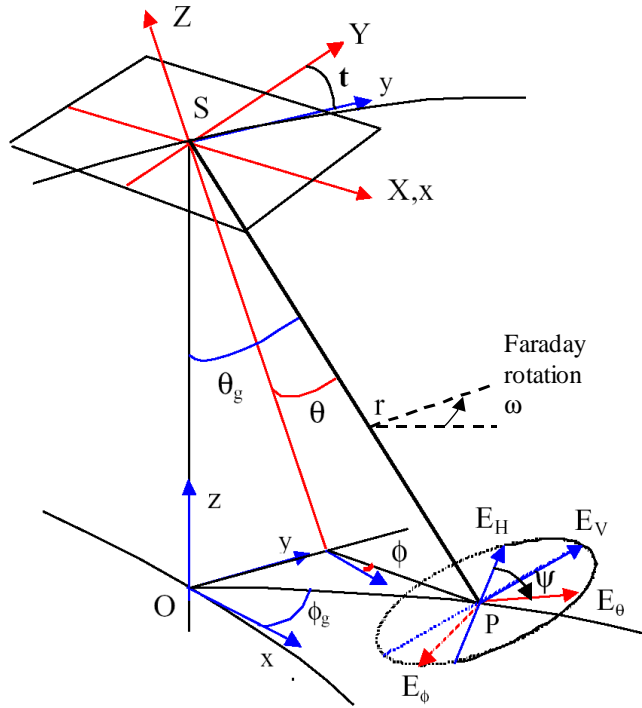
that follows the conventions described in Earth Explorer CFI Software Mission Convention Document (Deimos), we introduce the mathematical expressions for the angles to be used in the transport from ground to antenna reference frames.

$$\theta = Arc\cos\left[\sin t \sin\theta_g \sin\phi_g + \cos t \cos\theta_g\right]$$

$$\phi = -Arc\sin\left[\frac{-\sin t \cos\theta_g + \cos t \sin\theta_g \sin\phi_g}{\sin\theta}\right]$$

$$\psi = \pi - Arc\sin\left[\frac{\cos t \sin\theta_g - \sin t \cos\theta_g \sin\phi_g}{\sin\theta}\right]$$

for $-\pi/2 \le \phi_g \le \pi/2$:

for $\pi/2 \le \phi_g \le 3\pi/2$: ϕ has to be replaced by $\pi - \phi$ and ψ by $\pi - \psi$

We define the rotation angle $a = -\phi - \psi - \omega$, being ω the Faraday rotation angle. Then, following ACRI Reqts_L2Draft-2.doc

Dual polarization mode:

Direct transformation from surface reference frame to antenna reference frame is

148

$$\begin{bmatrix} A1 \\ A2 \end{bmatrix} = \begin{bmatrix} \cos^2(a) & \sin^2(a) & -\cos(a)\sin(a) \\ \sin^2(a) & \cos^2(a) & \cos(a)\sin(a) \end{bmatrix}\begin{bmatrix} T_H \\ T_V \\ T_3 \end{bmatrix} = [MR2]\begin{bmatrix} T_H \\ T_V \\ T_3 \end{bmatrix}$$

If T3 is assumed to be zero then the equation becomes:

$$\begin{bmatrix} A1 \\ A2 \end{bmatrix} = \begin{bmatrix} \cos^2(a) & \sin^2(a) \\ \sin^2(a) & \cos^2(a) \end{bmatrix}\begin{bmatrix} T_H \\ T_V \end{bmatrix} = [MR2]\begin{bmatrix} T_H \\ T_V \end{bmatrix}$$

There is a singularity problem if $\cos(a) = \sin(a)$, i.e. $a = \pm\,\pi/4$ or $\pm\,3\pi/4$. In such a configuration, $A1 = A2 = (T_H + T_V)/2$ and it is not possible to derive T_H and T_V from A1 and A2.

Full polarization mode:

$$\begin{bmatrix} A1 \\ A2 \\ A3 \\ A4 \end{bmatrix} = \begin{bmatrix} \cos^2(a) & \sin^2(a) & -\cos(a)\sin(a) & 0 \\ \sin^2(a) & \cos^2(a) & \cos(a)\sin(a) & 0 \\ \sin(2a) & -\sin(2a) & \cos(2a) & 0 \\ 0 & 0 & 0 & 1 \end{bmatrix}\begin{bmatrix} T_H \\ T_V \\ T_3 \\ T_4 \end{bmatrix} = [MR4]\begin{bmatrix} T_H \\ T_V \\ T_3 \\ T_4 \end{bmatrix}$$

No singularities appear in this mode.

As it has been shown by simulation studies and experimental data that over the ocean Thv ≈ Tvh ≈ 0, the third Stokes parameter at Earth reference frame is considered also to be 0 at first approximation. However, theoretical models provide non zero T3 and T4 so we recommend to keep the possibility of taking into account non zero T3, even in dual pol mode. Then the different sub-models provided in this SSS ATBD are valid either for dual-pol or full-pol formulation.

If the first Stokes parameter is used for the iterative retrieval I = A1 + A2 = Th + Tv and there is no need to apply any of the above described transformations.

References

Camps, A., M. Vall-llossera, N. Duffo, F. Torres, and I. Corbella (2005), Performance of Sea Surface Salinity and Soil Moisture retrieval algorithms with different auxiliary datasets in 2-D L-band aperture synthesis interferomètric radiometers, IEEE Trans. Geosci. Remote Sens., 43(5), May 2005

Claassen, J.P., and A.K. Fung, The Recovery of Polarized Apparent Temperature Distributions of Flat Scenes from Antenna Temperature Measurements, IEEE Transactions on Antennas and Propagation, AP-22 (3), 433-442, 1974.

Waldteufel, P. et Caudal, G. Off-axis Radiometric Measurements; Application to Interferometric Antenna Design. IEEE TGARS, 40, 6, juin 2002, 1435-1439

Waldteufel, P, Floury, N., Dinnat, E., Caudal, G., Ionospheric Effects for L-abnd "-D Interferometric Radiometry, IEEE TGARS, 42, 1, janvier 2004, 105-118

4.13. Sum of contributions

4.13.1. Theoretical description

4.13.1.1. Physics of the problem

This module consists in the addition of all the sub-models used to compute the brightness temperature of a specific ocean grid point at antenna level. Then it includes the forward model for L-band emissivity of a flat sea, plus correction for surface roughness (3 different options are considered by now, that can incorporate additional terms for foam, swell effects or others), the introduction of galactic noise contamination, atmospheric effects, and finally transport from ground level to antenna level. With the present development, measurements affected by sun glint and moon contamination are flagged and discarded for retrieval. However, if in the future algorithms to adequately correct for these effects can be obtained, the measurements will be kept and the corresponding corrections will be introduced in the sum of contributions.

The input to module 13 are the equations provided by modules 1 to 12 and will be applied to those grid points that have been selected as adequate for SSS retrieval in the Measurement discrimination step.

4.13.1.1.1. Note on first Stokes parameter computation

As information to the rest of modules, we indicate here the detail of the first Stokes parameter ($I=Th+Tv=A1+A2$) computation from a complete SMOS measurement (2.4 s), in fact a pair of two consecutive measurements in orthogonal polarisations:

As A1 and A2 are measured in two consecutive (in case of dual-pol) 1.2 s snapshots, the incidence angle for a specific grid point is not exactly the same for both, but will differ (in case of dual-pol) in some 0.6º (approx. 8 km displacement at 756 km height). A little bigger in case of full-pol.

Then a correction was assumed to be done routinely by shifting both measurements to a value that corresponds to the angle that is just in the middle of θx and θy ("mean angle"). To do that, we planned to add to each A the difference between modelled values for the two angles. However, the modelisation of both polarisations at the antenna reference frame requires introducing the Faraday rotation angle. And this is the step we want to avoid by computing the first Stoke parameter. Moreover, this correction would be for sure much below the noise of the measurement, and then was not expected to have a very significant impact.

Consequently it was decided (October 2006) not to perform any correction to A1 and A2 but to compute directly a 'Pseudo' First Stokes parameter:

$I(\theta\_mean)=A1(\theta x)+A2(\theta y)$

where $\theta\_mean=(\theta x+\theta y)/2$

We call it 'pseudo' first Stokes, since both measurements have not been acquired at the same time and therefore with the same incidence angle. This parameter will be a little bit sensitive to TEC but it does not represent a significant problem.

The way to extract proper measurements is described in the Measurements Selection section (4.16).

In case of full polarisation mode, the generation of the 'pseudo' Stokes parameter is not so straightforward, and a specific strategy has to be drawn (see Technical Note by ACRI, 15/09/08). According to « SMOS L1 Full Polarisation Data Processing » (ref : SO-TN-DME-L1PP-0024. Issue : 1.6. Date : 16/07/07. ESA/DEIMOS) the measurement cycle consists on 26 steps spread over four 1.2 s snapshots:

Snapshot	Step	arm pol	measurements	
1	1	XXX	XX	
2	2	YYX	YY, XY, YX	repeated 4 times
	3	XYY	YY, XY, YX	
	4	YXY	YY, XY, YX	
3	1'	YYY	YY	
4	2'	XXY	XX, XY, YX	repeated 4 times
	3'	YXX	XX, XY, YX	
	4'	XYX	XX, XY, YX	

Three different strategies to compute the pseudo-I are proposed for implementation in the processor to be further tested during commissioning phase to make a decision on the optimal one:

1) To use the closest A1 (XX) and A2 (YY) pairs, as in dual pol case, even they have different integration times (1.2 s in snapshots 1 and 3, 0.4 s in 2 and 4) and consequently very different radiometric noises that anyway will be added in the quadratic form explained in section 4.16. If the time interval between the two members of a pair is above a specified threshold (due to missing measurements) the pseudo-I will not be computed.

2) To add all XX and YY measurements of a full cycle. This way both components are acquired during 4/3 of a snapshot integration time. In case of absence of one measurement, either the measurements of the whole cycle are not processed (and then discarded), or else they are processed following different procedures according to the missing measurement within the cycle (see details in the TN mentioned above).

3) To use only A1 and A2 acquired respectively in snapshots 1 and 3. This third strategy discards measurements made when the three arms are not in the same polarisation, to avoid problems that may arise during these complex steps of the full pol mode.

4.13.1.1.2. Sum of modules

The iterative method for salinity retrieval requires computing Tb with expected SST, SSS and roughness descriptors values at the adequate incidence angle, add the effect of all envisaged contaminations (galactic, sun, moon and atmospheric), and transport the resulting value to antenna level for comparison with the measured Tb (level 1c) previously corrected for bias, if necessary. This series of computations will be made following the different sub-models described in sections 4.1 to 4.12 of this ATBD.

When an angular dependence is present, the computations are made for θ_mean.

1- Tb_1 = Tb_flat computed with equation described in 4.1
2- Tb_2 = Tb_1 + Tb_rough computed with surface roughness sub-model described in 4.2, 4.3 or 4.4. It is clear that from this step three versions of the Tb exist in parallel
3- Tb_3 = Tb_2 with corrections for foam if applicable, following sub-model described in 4.5
4- Tb_4 = Tb_3 modified for reflected galactic noise contamination as described in 4.6 or 4.7, which is attenuated by the atmosphere, when down-welling (described in 4.9).
5- Tb_5 = Tb_4 modified by the reflected down-ward atmospheric emission as described in 4.9.
6- Tb_6= Tb_5 attenuated by the atmosphere when travelling along the antenna-surface path (described in 4.9).
7- Tb_7=Tb_6 modified by the atmosphere self emission direct to antenna (described in 4.9).
8- Tb_8 = Tb_7 transported from ground to antenna level as described in 4.12 (geometry and Faraday rotation)

This Tb_8 is the brightness temperature that has to be included as "Tb mod" in the iterative convergence module (4.14) where it is compared with the "Tb meas" measured by SMOS

We have to indicate that the choice of retrieving SSS using I or using Th and Tv separately does not affect modules 4.1 to 4.11, that are mathematically described using Th and Tv. It is only in step 8 above when either the Tb to be transported is Th+Tv (then equal to A1+A2) or both components are transported separately and then the Faraday rotation has to be taken into account.

4.13.1.2. Mathematical description of algorithm

The Sum of contributions can be expressed mathematically as follows:

Firstly the brightness temperature of the sea at the bottom of the atmosphere is computed. Latter the atmosphere and extraterrestrial sources are applied, and finally the transport from ground to antenna is considered.

The brightness temperature at the ground level (BOA) due to sea surface emission *(at BOA there is also the reflection of atm. signal + galactic signal etc)* is as follows (steps 1 to 3):

$$Tb_{sea} = (Tb_{flat} + Tb_{rough})(1 - F) + Tb_{foam} \qquad [4.13.1]$$

Tb_{flat} is the Tb for a flat sea, as described in module 1, and Tb_{rough} is the contribution of the roughness of the sea, with 3 different options described in 4.2, 3 and 4. F is the fraction of sea foam coverage that mainly depends on the wind speed (WS) and is given in module 5. Tb_{foam} is the brightness temperature due to the foam and described also in module 5. If flag Fg_ctrl_foam_MX is set to false, then F and Tb_{foam} must be set to 0. This will always happen with the empirical roughness model since it takes already indirectly into account the foam effect. The effect of foam is only appreciable for wind speeds higher than 12 m/s. However, the terms envolving the foam contribution (F and Tb_{foam}) should be applied always, unless otherwise specified through a switch (see sections 4.2 and 4.3), and it is already considered in the definition of F and Tb_{foam} in module 5. When roughness models 4.2 and 4.3 are applied, Tb_{rough} and Tb_{foam} can be set to 0 according to sea surface conditions (behind a switch).

Then atmosphere and extraterrestrial sources are considered (steps 6 and 7)

$$Tb_{BOA} = Tb_{sea} + Tb_{reflected} = Tb_{sea} + (Tb_{DN}\Gamma + (Tgal\_refl)e^{-\tau_{atm}}) \qquad [4.13.2]$$

where $Tb_{reflected}$ is the radiometric temperature from the sky and atmosphere scattered by the surface, which is the addition of two terms; the downward emitted atmospheric radiation (Tb_{DN}) and the brightness due to extraterrestrial sources. The extraterrestrial sources considered here (Tgal_ref) are the hydrogen line, the cosmic and galactic contribution already reflected on the sea surface, as explained in section 4.6 and 4.7 of this document. Tgal_ref is multiplied by an attenuation factor due to the atmosphere, since its formulation is at top of the atmosphere. A switch will be available to choose between galactic noise contamination 1 (section 4.6) or 2 (section 4.7) to computed the reflected noise (at the moment, the semi-empirical model will only use the galactic noise contamination 1 module). The atmospheric contribution term (Tb_{DN}) is multiplied by Γ, that is the reflection coefficient

To compute Tb at top of the atmosphere (without considering Faraday rotation, for practical reasons) in the Earth reference frame (steps 8 and 9):

$$Tb_{TOA}^{EARTH} = Tb_{BOA}\ e^{-\tau_{atm}} + Tb_{UP} \qquad [4.14.3]$$

where Tb_{UP} is the atmospheric self emission direct to the antenna (but computed at TOA and with Earth reference frame) and $e^{-\tau_{atm}}$ is the attenuation produced by the atmosphere. Section 4.9 specifies that Tb_{UP} and Tb_{DN} are very close, and considered equal to Tbatm, which is defined in that section.

Finally to compute this temperature at the antenna reference frame, the geometrical transformation and the ionospheric effect should be considered, following module 12, as (step 10):

$$Tb^{ANTENNA} = [MR4] \cdot Tb_{TOA}^{EARTH} \qquad [4.13.4]$$

where MR4 is the matrix that describes the geometrical transformation plus the Faraday rotation

4.13.1.3. Error budget estimates (sensitivity analysis)

The addition of the different modules implies an analysis of the impact of the individual errors on the overall error budget. This was planned in the ESL proposal as WP2600 and expected to be finished by the end of the study.

4.13.2. Practical considerations

4.13.2.1. Calibration and validation

The validation of this module can be done by running some tests cases with exactly the same configuration (in terms of sub-models switched on and use of auxiliary data) with the summation module used in the SRS study and the equivalent used by UPC from SEPS, to check that the result is the same

4.13.2.2. Quality control and diagnostics

The range of validity of this module comes from the intersection of the corresponding ranges for all sub-models.

4.13.3. Assumption and limitations

The module has to be applied to all grid points selected as good for salinity retrieval at the Measurement discrimination.

Dependencies table

The following table describes the dependencies between modules. In particular, what modules should be applied or not to the different roughness models. In some cases, a switch will be required to allow using or not the module, and therefore to test if using the module is beneficious or not.

	Roughness model 1 -2-Scales	Roughness model 2 -SSA	Roughness model 3 - empirical
Flat sea	Y	Y	Y

Rough mod 1	Y	N	N
Rough mod 2	N	Y	N
Rough mod 3	N	N	Y
Foam contrib.	S	S	N
Galactic noise 1	S (by default)	S (by default)	Y (by default)
Galactic noise 2	S	S	N
Galactic noise 0	S	S	S
Atmos. Effects	Y	Y	Y
Bias corr	S	S	S
Tranport ground to antenna	Y	Y	Y
Sum of contributions	Y	Y	Y
Iterative scheme	Y	Y	Y

Y = Yes, apply
S = Behind a switch
N = Not apply

4.14. Iterative Scheme

4.14.1. Theoretical description

4.14.1.1. Physics of the problem

The iterative Levenberg and Marquard method is choosen to be used in the inversion algorithm. This method was already implemented in the simulator for soil moisture study and gives very similar results to the [*Jackson*, 1972] method used in SR1600. The mathematical problem is described below in detail.

Two cases are considered here: in case 1 the model error is neglected, while in case 2 it is taken into account.

- Case 1 – Model error neglected

In this case the model error is considered negligible and not taken into account.

The set of measurements are brightness temperatures Tb_i^{meas} observed for a single grid point at different incidence angles, θ_i. These data need to be fitted into a direct model to find the solution of the parameters.

$$T_b^{mod} = f(\theta, SSS, SST, P_{rough})$$

where P_{rough} is a vector that includes the parameters used in each model to describe the sea roughness.

This implies minimization of the following constrained cost function :

$$\chi^2 = \sum_{i=0}^{Nm-1} \frac{\left[T_{bi}^{meas} - T_{bi}^{mod}(\theta, P) \right]^2}{\sigma_{T_{b_i}}^2} + \sum_{j=0}^{Np-1} \frac{\left[P_j - P_j^{prior} \right]^2}{\sigma_{P_j}^2} \qquad [4.14.1]$$

being P_j, the j parameters that influence the T_b: SSS, SST, WS (or other wind descriptors), and depending on the cases, also significant wave height Hs, wind direction ϕ, inverse wave-age Ω, and TEC parameter in case of not using first Stokes, etc. θ is the incidence angle of measurements from nadir. In case of cardioid retrieval, the P_j parameters are Acard and the surface temperature.

$P_{j\ prior}$ is a value of parameter P_j known a priori to the measurements with an uncertainty σ_{Pj} (Waldfteufel, 2003, Gabarró, 2004). The uncertainty of each parameter, $\sigma_{Pj,}$ could change depending on the area of observation.

σ_{Tb}^2 is the uncertainty of the measurement used for each incidence angle:

$$\sigma_{Tb\_i}{}^2 = \sigma_{Tb\_meas\_i}{}^2$$

where the value of $\sigma_{Tb\_meas\_i}{}^2$ is given in the L1 output product.

For model 1, a global figure will be given as a linear function of auxiliary parameters (SST, SSS, wind speed – room must be kept for others parameters that might be needed) and of polarization, considering the assumptions and limitations specified in each module of the model.

Some experiments (Sabia et al., 2005) advise not using SSS as one of the constrained parameters P_j, as the retrieved value tends to the a priori value. Until this is clarified we propose using this term with a very big σ_{Pj} (e.g. 100) to remove its impact on equation 4.14.1.

- Case 2 – Model error taken into account

For a single measurement, the variance-covariance matrix for $T_b{}^{mod}$ ($C_{Earth}{}^{mod}$) is <u>diagonal in the Earth reference frame</u>:

$$C_{Earth}^{mod} = \begin{pmatrix} \sigma_{Th\_model}^2 & 0 & 0 & 0 \\ 0 & \sigma_{Tv\_model}^2 & 0 & 0 \\ 0 & 0 & \sigma_{T3\_model}^2 & 0 \\ 0 & 0 & 0 & \sigma_{T4\_model}^2 \end{pmatrix}$$

where $\sigma^2_{Th\_model}$, $\sigma^2_{Tv\_model}$, $\sigma^2_{T3\_model}$, $\sigma^2_{T4\_model}$ are the variances of the $T_b{}^{mod}$ components ($T_h{}^{mod}$, $T_v{}^{mod}$, $T_3{}^{mod}$, $T_4{}^{mod}$) in the Earth reference frame. The correlation of the model error between different measurements are neglected here.

The value of the model uncertainty is given by a global figure that takes into account the assumptions and limitations specified in each module of each model. In this version of ATBD, it is assumed to be constant and independent of polarization. Its value is given in the TGRD in the Earth reference frame.
In the future, σ_{Tb_model} could be given as an analytical function of auxiliary parameters (SST, wind speed – with room kept for others parameters that might be needed), incidence angle and polarization.

The method of transport of the error variances to the antenna reference frame is detailed below.

The variance/covariance matrix in the antenna reference frame ($C^{mod}{}_{Ant}$) for $T_b{}^{mod}$ is given in the antenna reference frame by:

$$C^{mod}{}_{Ant} = (MR4) \, C^{mod}{}_{Earth} \, (MR4)^T$$

where MR4 is the rotation matrix described in § 4.12.1.2 and ^{T} represents the transposition operation.

$C^{mod}{}_{Ant}$ is then given by:

$$C^{mod}_{Ant} = \begin{pmatrix} \sigma^2_{A1\_mod\,el} & c_{12} & c_{13} & c_{14} \\ c_{21} & \sigma^2_{A2\_mod\,el} & c_{23} & c_{24} \\ c_{31} & c_{32} & \sigma^2_{A3\_mod\,el} & c_{34} \\ c_{41} & c_{42} & c_{43} & \sigma^2_{A4\_mod\,el} \end{pmatrix}$$

with the variances:

$$\sigma^2_{A1\_model} = \sigma^2_{Th\_model} \cos^4(a) + \sigma^2_{Tv\_model} \sin^4(a) + \sigma^2_{T3\_model} \cos^2(a) \sin^2(a)$$
$$\sigma^2_{A2\_model} = \sigma^2_{Th\_model} \sin^4(a) + \sigma^2_{Tv\_model} \cos^4(a) + \sigma^2_{T3\_model} \cos^2(a) \sin^2(a)$$
$$\sigma^2_{A3\_model} = (\sigma^2_{Th\_model} + \sigma^2_{Tv\_model}) \sin^2(2a) + \sigma^2_{T3\_model} \cos^2(2a)$$
$$\sigma^2_{A4\_model} = \sigma^2_{T4\_model}$$

and the covariances:

$$c_{21} = (\sigma^2_{Th\_model} + \sigma^2_{Tv\_model} - \sigma^2_{T3\_model}) \cos^2(a) \sin^2(a)$$
$$c_{31} = \sigma^2_{Th\_model} \cos^2(a) \sin(2a) - \sigma^2_{Tv\_model} \sin^2(a) \sin(2a) - \sigma^2_{T3\_model} \cos(a) \sin(a) \cos(2a)$$
$$c_{41} = 0$$
$$c_{12} = c_{21}$$
$$c_{32} = \sigma^2_{Th\_model} \sin^2(a) \sin(2a) - \sigma^2_{Tv\_model} \cos^2(a) \sin(2a) + \sigma^2_{T3\_model} \cos(a) \sin(a) \cos(2a)$$
$$c_{42} = 0$$
$$c_{13} = c_{31}$$
$$c_{23} = c_{32}$$
$$c_{43} = 0$$
$$c_{14} = 0$$
$$c_{24} = 0$$
$$c_{34} = 0$$

Note that this matrix is not diagonal, leading to correlated model errors in the antenna reference frame.

As the measurement error is assumed to be uncorrelated in the antenna reference frame, the variance-covariance matrix for T_b^{meas} (C^{meas}) is <u>diagonal in the antenna reference frame</u>:

$$C^{meas} = \begin{pmatrix} \sigma^2_{A1\_meas} & 0 & 0 & 0 \\ 0 & \sigma^2_{A2\_meas} & 0 & 0 \\ 0 & 0 & \sigma^2_{A3\_meas} & 0 \\ 0 & 0 & 0 & \sigma^2_{A4\_meas} \end{pmatrix}$$

where $\sigma^2_{A1\_meas}$, $\sigma^2_{A2\_meas}$, $\sigma^2_{A3\_meas}$, $\sigma^2_{A4\_meas}$ are the variances of the T_b^{meas} components (A_1^{meas}, A_2^{meas}, A_3^{meas}, A_4^{meas}) in the antenna reference frame. The value of the measurement uncertainty is given in the L1 output product.

Finally, since errors are assumed to be Gaussian, the variance covariance matrix of Tb (C_{Tb}) in the antenna reference frame is given by:

$$C_{Tb} = C^{meas} + C^{mod}{}_{Ant}$$

In a first approach, the correlations are neglected and the C_{Tb} matrix is assumed to be diagonal:

$$C_{Tb} = \begin{pmatrix} \sigma^2_{A1\_meas} + \sigma^2_{A1\_model} & 0 & 0 & 0 \\ 0 & \sigma^2_{A2\_meas} + \sigma^2_{A2\_model} & 0 & 0 \\ 0 & 0 & \sigma^2_{A3\_meas} + \sigma^2_{A3\_model} & 0 \\ 0 & 0 & 0 & \sigma^2_{A4\_meas} + \sigma^2_{A4\_model} \end{pmatrix}$$

The cost function to be minimized is then the same than in eq. 4.14.1, with

$$\sigma^2{}_{Tb} = \sigma^2{}_{A\_meas} + \sigma^2{}_{A\_model}.$$

The theoretical error σ_{Pi} on the geophysical parameter P_i is computed by the Levenberg and Marquardt algorithm as follows:

$$\begin{bmatrix} \sigma_{P1} \\ ... \\ \sigma_{PM} \end{bmatrix} = \sqrt{diag(M^{-1})}.$$

M is the pseudo-Hessian, with:

$$M = F^T C_0^{-1} F,$$

where C_0 is the a posteriori covariance matrix (see above),

$$diag(C_0) = \begin{bmatrix} \sigma^2_{A1} \\ ... \\ \sigma^2_{AN} \\ \sigma^2_{P10} \\ ... \\ \sigma^2_{PM0} \end{bmatrix},$$

F is the Jacobian,

$$F = \left(\frac{\partial A_n^{mod}}{\partial P_i} \right)_{\substack{n=1,...,N \\ i=1,...,M}}$$

and the superscript ^{T} is the transpose operator.

4.14.1.1.1 Parameters to be retrieved:

Depending on the forward model used for the roughness effect different parameters P_j can be adjusted/retrieved (SSS + up to 5) in the iterative convergence. We list here those that for

each case are (or can be) adjusted during the iteration process, with a different impact on the SSS retrieval that depends on the weight (associated error) introduced in the cost function.

Roughness model	Dual pol	Dual pol + Stokes 1	Full pol	Full pol + Stokes 1
1. Two-scale	SSS SST TEC WSx WSy	SSS SST WSx WSy	SSS SST TEC WSx WSy	SSS SST WSx WSy
2. SSA	SSS SST TEC U* Ω Φ	SSS SST U* Ω Φ	SSS SST TEC U* Ω Φ	SSS SST U* Ω Φ
3. Empirical	SSS TEC WS Hs Ω U* MSQS	SSS WS Hs Ω U* MSQS	SSS TEC WS Hs Ω U* MSQS	SSS WS Hs Ω U* MSQS

The exact definition of these parameters, in terms of what auxiliary data (see ECMWF SMOS DPGS Interface, XSMS-GSEG-EOPG-ID-06-0002) will be used in the retrieval process, is indicated in the variables list (section 1.2 of this ATBD).

The User Data Product (see section 6) will contain, for each grid point, three salinity values (SSS1, SSS2, SSS3) retrieved through iterative convergence using the three roughness models, as well as one SST and one WS value that will be initially obtained from the ECMWF auxiliary data files, but that after analysis of the output quality (commissioning phase) can be substituted by the best retrieved values.

In the Data Analysis Product (see section 6) all the retrieved parameters in addition to SSS (e.g. SST, TEC, U*, …), and their associated theoretical uncertainties, will be listed as ParamX_MY with X 1 to 5 and Y 1 to 3 (the three roughness models).

Note: As mentioned in section 4.4 roughness model 3 is linearly dependent on the incidence angle. Then it is only possible to retrieve two roughness parameters for each polarisation. In the case of using H and V polarisation independently, the maximum number of retrieved is 4. If the first Stokes is used, then only 2 parameters can be retrieved. These 2 or 4 retrieved parameters will be selected from the roughness descriptors included in the table above.

In all these explainations we suppose that the cross polarisation measurements are used in the full polarisation mode. This can be modified in the future if they finally appear not to be usable due to being too noisy.

4.14.1.2. Mathematical description of algorithm

Mathematically equation 4.14.1 (including model error) can be written as follows:

$$\chi^2 = (T_b^{meas} - T_b^{mod}(\theta, \overrightarrow{P_j}))^T C_{T_B}^{-1}(T_b^{meas} - T_b^{mod}(\theta, \overrightarrow{P_j})) + (P_j^{prior} - P_j)^T C_{P_j}^{-1}(P_j^{prior} - P_j) \quad [4.14.2]$$

Where the T_b^{meas} are the N_m observations performed at different incidence angles, ^{T} represents the transposition operation, and C_{Tb} is the variance/covariance matrix for T_b. The diagonals of this matrix are the quadratic sum of the radiometric sensitivity of T_b measurements and of the model error. In this first approach, off diagonal elements are neglected in the antenna frame.

P_j are different parameters that should be retrieved, P_j^{prior} are the a priori knowledge of the parameters (obtained from models or satellites, the auxiliary information), and C_{Pj} is the variance/covariance matrix of these parameters. The diagonal of the matrix are the uncertainties on the a priori parameters.

Finally the above equation can be expressed as follows:

$$\chi^2 = (X - X \bmod)^T C_z^{-1}(X - X \bmod) \quad [4.14.3]$$

Where C_Z matrix is built by aligning along the main diagonal the matrixes C_{Tb} and C_{Pj}; the vector X has a Nm+Np length and consists on:

$$X = \begin{pmatrix} T_b(1) \\ T_b(2) \\ ..... \\ T_b(Nm) \\ P_{prior}(1) \\ p_{prior}(2) \\ ..... \\ p_{prior}(Np) \end{pmatrix} \quad [4.14.4]$$

Where P_{prior} is the a priori information of the parameter; X_mod has the same length as X and is defined as:

$$X\_mod = \begin{pmatrix} T_b^{mod}(1,p) \\ T_b^{mod}(2,p) \\ ..... \\ T_b^{mod}(Nm,p) \\ p(1) \\ p(2) \\ ..... \\ p(Np) \end{pmatrix} \qquad\qquad [4.14.5]$$

Where P is the parameter to be retrieved that will change at each iteration. It is the first guess value at the first iteration.

Let's call a the vector of Np parameters to be retrieved (for example a= [SSS, SST, WS, Hs, Ω]).

Sufficiently close to the minimum the cost function is approximated by a quadratic form:

$$\chi^2(a) = \gamma - d \cdot a + \frac{1}{2} \cdot a \cdot D \cdot a \qquad\qquad [4.14.6]$$

Then jumping from current trial parameters a_{cur} (equal to a first guess value for step 0) to a minimizing one a_{min} is done by the inverse Hessian method:

$$a_{min} = a_{cur} + D^{-1} \cdot \left[-\nabla \chi^2(a_{cur)} \right] \qquad\qquad [4.14.7]$$

But if the minimum functions couldn't be approximated by a quadratic form, a *steepest decent method* has to be used:

$$a_{next} = a_{cur} + constant \nabla \chi^2(a_{cur)} \qquad\qquad [4.14.8]$$

The gradient (d) and the Hessian (D) of χ^2 need to be calculated:

$$d = \frac{\partial \chi^2}{\partial a_k} \qquad\qquad D = \frac{\partial^2 \chi^2}{\partial a_k \partial a_l} \qquad\qquad [4.14.9]$$

Let,

$$\alpha_{kl} = \frac{1}{2} D \qquad \beta_k = -\frac{1}{2} d \qquad\qquad [4.14.10]$$

The *inverse Hessian method* can then be written as:

$$\sum_{i=0}^{Nm-1} \alpha_{kl} \delta a_l = \beta_K \qquad\qquad [4.14.11]$$

And the *steepest decent method* can be rewritten as:

$$\delta a_k = constant \times \beta_k \qquad\qquad [4.14.12]$$

With δa=a$_{min}$-a$_{cur}$ or δa=a$_{next}$-a$_{cur}$ and k∈[0:Np-1]

The Levenberg & Marquardt method put forth a method for varying smoothly between the extremes of the *Inverse-Hessian method* and the *steepest descent method* using a factor λ. This factor will replace the constant term in the *steepest descent method:*

$$\delta a_k = \frac{1}{\lambda \alpha_{kk}} \beta_k \quad with \quad k \in [0:Np-1] \qquad\qquad [4.14.13]$$

and then if we define a new matrix α', by the following prescription:

$$\begin{cases} \alpha'_{jj} = \alpha_{jj}(1+\lambda) \\ \alpha'_{jk} = \alpha_{jk} \quad (j \neq k) \end{cases} \qquad\qquad [4.14.14]$$

the two methods can be expressed as:

$$\sum_{i=0}^{Nm-1} \alpha'_{kl} \delta a_l = \beta_K \qquad\qquad [4.14.15]$$

When λ is very large, the matrix α' is forced into being diagonally dominant, so method is like *steepest descent method* and as λ approaches 0 method is like *Hessian gradient method*.

Given an initial guess for the set of fitted parameters *a*, the iterative method consists of:

1   Compute χ^2 (a).
2   Select an initial modest value for λini, say λini = 0.001.
3   Solve the linear equations for δa and evaluate χ^2 (a+δa).
4   If χ^2 (a+δa) ≥ χ^2 (a), increase λ by a factor Kd and go back to 3.
     If λ becomes greater than a threshold Tg_lambda_diaMax the iteration should be stopped and a flag Fg_ctrl_marq raised.

5   If $\chi^2(a+\delta a) < \chi^2(a)$, decrease λ by a factor Kd update the trial solution $a=a+\delta a$ and go back to 3.

(Press, 1986; Marquardt 1963). (See also 'Retrieval Concept and Architecture for Sea Surface Salinity Retrieval for SMOS Mission' document from the CNN2 of contract 16027/02/NL/GS):

This iteration loop should be stopped when both of these convergence tests are acomplished, logical 'AND':

- Convergence test 1: If χ^2 is decreased with respect the previous iteration by less than a threshold δ_χ as an absolute value:

$$\text{abs}\left(\chi^2_{i+1} - \chi^2_i\right)/\chi^2_i < \delta_\chi$$

where i is the iteration.

- Convergence test 2: If the relative parameter variation from one iteration to another is lower than the threshold δ_{sig} (i is the iteration):

$$\max[\text{abs}(p_{i+1}-p_i)/\sigma_{prior}] < \delta_{sig}$$

where i is the iteration.

These thresholds should be easy modifiable and should be calibrated once the satellite will be flying.

Also the step at the first iteration, this is λini, can be adjusted to better values, to optimize the computing time.

The maximum number of iterations allowed to the system is Tg_it_max, and should be also modifiable. It could be changed once the computing time for each grid point will be better known. If the number of iterations Dg_num_iter_X reaches Tg_it_max then the flag Fg_ctrl_reach_maxiter_X (X = 1, 2, 3, Acard as it can be different for the three forward models plus cardioid) should be set to true and the ouput value of the process, should be set to the value obtained in the last iteration.

No boundaries will be applied in the inversion process, therefore the retrieved parameters should be considered as effective values, since they could result in physically impossible values (i.e. negative wind speeds).

A test of retrieval quality will be performed, by comparing the value of the normalised cost function at the last iteration χ^2 with a threshold Tg_Qχ. If Dg_chi2_X (where X is 1,2 or 3 for the 3 different roughness models) = χ^2/NFD < Tg_Qχ then the flag Fg_ctrl_chi2_X should be set to 0 (good quality). Elsewhere it should be set to 1 remaking the low quality of the retrieval. NFD is the number of freedom degree (NFD = number of measurements – number of parameters to be retrieved).

Another test to be performed is: **Chi2_P**, main goodness of fit indicator; is the χ^2 high end acceptability probability. This is the probability that no anomaly occurred about the fit.

This figure is given by:

$$\text{Dg\_chi2\_P\_X} = \text{GAMM}_q(\text{NFD}/2, \text{Dg\_chi2\_X} \cdot \text{NFD}/2)$$

where GAMM_q is the upper tail of the incomplete gamma function.

With NFD in the range of several tens, Dg_chi2_P_X should go down to a small number of percent when Dg_chi2_X exceeds a figure around 1.3 to 1.4. Note that very high values of Dg_chi2_P_X (when Dg_chi2_X is "too small") are suspicious also, as they raise the possibility of correlated noise which would be unduly fitted by the direct model.

The table below illustrates the values of Chi2_P against χ^2/NFD (cost function normalized by the number of degrees of freedom) values.

χ^2/NFD \ NFD	0.50	0.55	0.60	0.65	0.70	0.75	0.80	0.85	0.90	0.95	1.00	1.05	1.10	1.15	1.20	1.25	1.30	1.35	1.40	1.45	1.50
8	.857	.819	.779	.736	.692	.647	.603	.558	.515	.473	.433	.395	.359	.326	.294	.265	.238	.213	.191	.170	.151
10	.891	.855	.815	.772	.725	.678	.629	.580	.532	.485	.440	.398	.358	.320	.285	.253	.224	.197	.173	.151	.132
12	.916	.883	.844	.801	.753	.703	.651	.598	.546	.495	.446	.399	.355	.314	.276	.241	.210	.182	.157	.135	.116
15	.942	.913	.878	.835	.787	.735	.679	.622	.564	.507	.451	.399	.350	.304	.263	.225	.192	.163	.137	.115	.095
20	.968	.946	.916	.877	.830	.776	.717	.653	.587	.522	.458	.397	.341	.289	.242	.201	.166	.135	.109	.088	.070
25	.982	.966	.941	.907	.863	.809	.747	.679	.607	.534	.462	.394	.331	.275	.224	.181	.144	.113	.088	.068	.052
30	.990	.978	.959	.929	.888	.835	.772	.700	.623	.544	.466	.391	.323	.261	.208	.163	.126	.096	.072	.053	.039
35	.994	.986	.970	.945	.908	.857	.794	.719	.638	.553	.468	.388	.314	.249	.193	.147	.110	.081	.058	.041	.029
40	.997	.991	.979	.957	.923	.875	.812	.736	.651	.561	.470	.384	.306	.238	.180	.134	.097	.069	.048	.033	.022
45	.998	.994	.985	.967	.936	.891	.829	.752	.663	.568	.472	.381	.298	.227	.168	.121	.085	.059	.039	.026	.017
50	.999	.996	.989	.974	.947	.904	.843	.765	.674	.574	.473	.377	.291	.217	.157	.110	.075	.050	.032	.020	.013
60	1.00	.998	.994	.984	.963	.925	.868	.790	.693	.586	.476	.371	.277	.199	.138	.092	.059	.037	.022	.013	.007
70	1.00	.999	.997	.990	.973	.941	.888	.810	.711	.596	.478	.364	.265	.183	.121	.077	.047	.027	.015	.008	.004
80	1.00	1.00	.998	.994	.981	.954	.904	.828	.726	.606	.479	.358	.253	.169	.107	.065	.037	.020	.011	.005	.003
90	1.00	1.00	.999	.996	.986	.963	.918	.844	.740	.615	.480	.352	.242	.156	.095	.054	.029	.015	.007	.003	.002
100	1.00	1.00	.999	.997	.990	.971	.930	.858	.753	.623	.481	.346	.232	.145	.084	.046	.024	.011	.005	.002	.001
110	1.00	1.00	1.00	.998	.993	.977	.939	.870	.765	.630	.482	.341	.223	.134	.075	.039	.019	.009	.004	.001	.001
120	1.00	1.00	1.00	.999	.995	.981	.948	.881	.776	.637	.483	.336	.214	.125	.067	.033	.015	.006	.003	.001	.000

For example, for NFD=120 and χ^2/NFD=1.25, the probability of a correct fit (with a Gaussian noise on the sample) amounts to 0.033. There are 96.7% of chances that a problem happened during the retrieval.

Then the following test will be done to control the quality of the retrieval: If Tg_chi2_P_min < Dg_chi2_P_X < Tg_chi2_P_max then the flag Fg_ctrl_chi2_P_X should be set to 0 (good quality). Elsewhere it should be set to 1 remarking the low quality of the retrieval.

4.14.1.3. Error budget estimates (sensitivity analysis)

The algorithm will iterate until χ^2 decreases less than a threshold between two consecutive iterations and the change in the parameter between successive iterations is lower than a threshold. Another reason to stop the iterative process is if the number of iterations is higher than a previously defined Tg_it_max .

Therefore it is impossible to obtain better results if any of the two conditions described above have been accomplished.

4.14.2. Practical considerations

An external file will provide what first guesses we want to use (maybe prior values + something else specified in this external file)

If the two polarizations are used in the retrieval, the vector Tb_i^{meas} should contain first the measured Tbh in different incidence angle and latter the Tbv for the different θi. The same for Tb_i^{model}.

In the case of performing the retrieval with the 1st Stokes, then Tb_i^{meas} is a vector that contains the 1st Stokes (Tbh+Tbv) for the different incidence angles. The same for Tb_i^{model}. The model uncertainty is then given by:

$$\sigma^2_{ST1\_model} = \sigma^2_{Th\_model} + \sigma^2_{Tv\_model}$$

The uncertainty is assumed to be the same in the Earth reference frame and in the antenna reference frame.

In ATBD issue 2.0 a new module has been introduced to retrieve a pseudo-dielectric constant using the cardioid model (see section 4.10). All the procedures described here for the SSS retrieval will be also applied to this new variable.

4.14.2.1. Calibration and validation

The adjustments to be done to the model once it is working with real values, as it is explained in 4.14.1.2, will have to do with:

- o first value of λini;
- o threshold δ_χ;
- o maximum number of iterations, Tg_it_max.

4.14.2.2. Quality control and diagnostics

If convergence is not achieved after Tg_it_max iterations, this is, if once Tg_it_max iterations are performed the condition $(\chi_{i+1}^2 - \chi_i^2)/\chi_i^2 < \delta_\chi$ is not true, then the flag Fg_ctrl_reach_maxiter_X should be raised, and the parameters given by the algorithms should be the value obtained in the last iteration.

For each of the roughness models run in parallel the following test should be done and raise the appropriate flags, which will be reported in the User Data Product:

1) Check if SSS retrieved is in the expected range (Tg_SSS_max, Tg_SSS_min). If the retrieved salinity value is outside the range then raise the flag Fg_ctrl_range_X (where X is 1, 2 or 3, for each roughness model).
2) Compute σ_{SSSret} of the retrieved SSS. Compare this σ_{SSSret} with a threshold, Tg_sigma_max. If σ_{SSSret} is higher than the threshold then the flag Fg_ctrl_sigma_X should be raised.
3) Compare the value of χ^2 at the last iteration, Dg_chi2_X, with the threshold Tg_Qχ. If Dg_chi2_X > Tg_Qχ (bad quality retrieval) then the flag Fg_ctrl_chi2_X should be raised.
4) Compare the value Dg_chi2_P_X, with the threshold Tg_chi2_P_max and Tg_chi2_P_min. If Dg_chi2_P_X < Tg_chi2_P_min or Dg_chi2_P_X > Tg_chi2_P_max (bad quality retrieval) then the flag Fg_ctrl_chi2_P_X should be raised.

An overall quality assessment for the three different salinities retrieved for each grid point (SSS1, SSS2 and SSS3) is needed to decide which of them is the best. It may happen that a unique performance ranking can not be established, since the behaviour of the roughness models might depend on regional or temporal characteristics (sea state, temperature, distance to coast, quality of auxiliary data ...). General quality descriptors (Dg_quality_SSS1, Dg_quality_SSS2, and Dg_quality_SSS3), incorporated into the User Data Product, are defined as follows:

We consider the following error categories:
- Effect of radiometric noise and *a priori* uncertainties
- Instrument, calibration, reconstruction
- External sources (galactic noise, sun, RFI, …)
- Forward models.

For each model, a quality index Dg_quality_SSSX is built by combining error contributions C_i, using scaling coefficients SC_i. Errors in terms of Tb are accounted for using the sensitivity function dSSS/dTb, noted dS_dT, estimated from nadir simulations with Klein and Swift model (Figure 3). Only the SST dependence is considered. We use a linear fit for dTb/dSSS, which results in:

dS_dT = 1/(dTb/dSSS) = 1/(dT_dS_0+ dT_dS_1*SST), with dT_dS_0 = - 0.224, and dT_dS_1 = - 0.0157
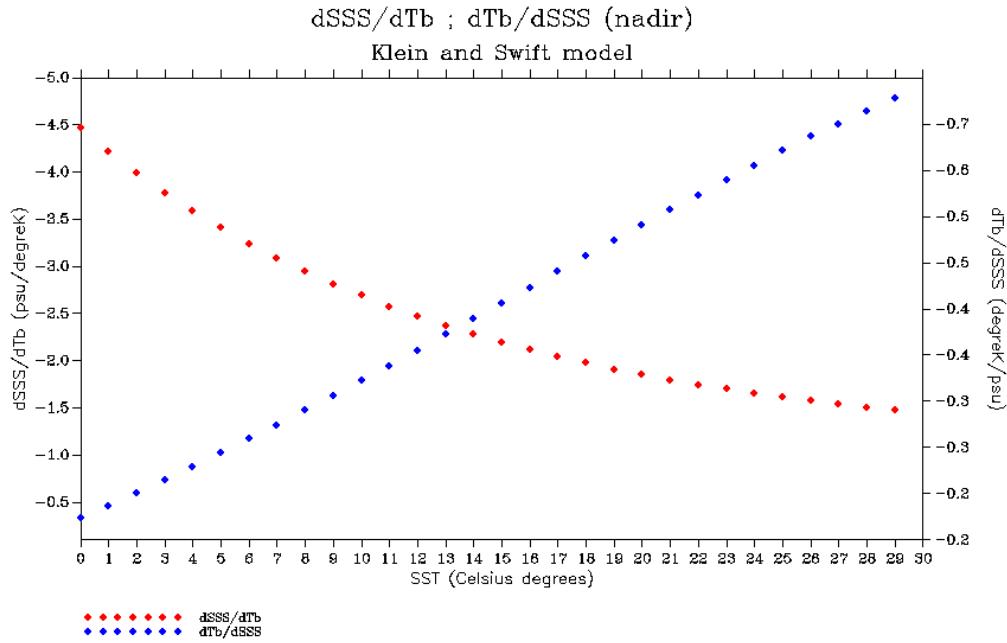
Figure 3 - Sensitivity functions dSSS/dTb and dTb/dSSS vs. SST at nadir from Klein and Swift model

Uncertainty origin	Driver D	Contribution Ci to Dg_quality_SSS	Init SCi value	SCi unit	Rand/ bias	Comments
Radiom ΔTB & prior	D=σ_{SSSx}	SC11*D	1	dl	R	
Instrument	Unknown for now	SC21*dS_dT	1	K	B?	
Instrument	D = abs(Dg_X_swath)	SC22*D*dS_dT	0	K km^{-1}	B?	
Calibration	Unknown for now	SC23*dS_dT	1	K	B?	
Reconstruction	Unknown for now	SC24*dS_dT	0.2	K	B?	
Reconstruction	D= Mean over dwell (L1c T25 field #22)	SC25*D	0	dl	B?	
Position in FOV	D=Dg_border_fov/ Dg_num_meas_l1c	SC26*D*dS_dT	0	K	??	
Position in FOV	D=Dg_af_fov/ Dg_num_meas_l1c	SC28*D*dS_dT	0	K	??	
Goodness of fit	Dg_chi2_P_X	SC31/D*dS_dT (watch division sign!)	0.05	K	R	1 K for 5% prob of no anomaly
Outliers	D=Dg_num_outliers / Dg_num_meas_l1c	SC32*D*dS_dT	10	K	R	1 K for 10%
RFI	Unknown for now					
Various L1C	Unknown for now					

flags						
SUN in front	D= Dg_sun_fov/ Dg_num_meas_l1c	SC33*D*dS_dT	0.5	K	B-	To be implemented in version 2
Sun glint	D=Dg_sunglint_L2/ Dg_num_meas_l1c	SC34*D*dS_dT	10	K	B	1 K for 10%
Moon glint	D=Dg_moonglint/ Dg_num_meas_l1c	SC35*D*dS_dT	10	K	B	1 K for 10%
Sky	D=Dg_sky/ Dg_num_meas_l1c	SC36*D*dS_dT	5	K	R	0.5 K for 10%
TEC	Unknown for now					
Coast	D=1 if Fg_sc_land_sea_coast1=T and Fg_sc_land_sea_coast2=T, D=0 otherwise	SC41*D*dS_dT	1	K	R?	
Rain	D=0/1 if Fg_sc_rain =F/T	SC42*D*dS_dT	0.2	K	B?	
Ice	D=Dg_suspect_ice/ Dg_num_meas_l1c	SC43*D*dS_dT	10	K	B?	1 K for 10%
High wind	D=1 if Fg_sc_low_wind = F and Fg_sc_high_wind = T, 0 otherwise	SC44*D*dS_dT	0.5	K	??	
Low wind	D=1 if Fg_sc_low_wind=F and Fg_sc_high_wind=F, 0 otherwise	SC45*D*dS_dT	0.5	K	??	
High SST	D=1 if Fg_sc_low_SST=F and Fg_sc_high_SST=T, 0 otherwise	SC46*D*dS_dT	0	K	??	
Low SST	D=1 if Fg_sc_low_SST=F and Fg_sc_high_SST=F, 0 otherwise	SC47*D*dS_dT	1	K	??	
High SSS	D=1 if Fg_sc_low_SSS=F and Fg_sc_high_SSS=T, 0 otherwise	SC48*D*dS_dT	0	K	??	
Low SSS	D=1 if Fg_sc_low_SSS=F and Fg_sc_high_SSS=F, 0 otherwise	SC49*D*dS_dT	0	K	??	
Sea state 1	D=1 if Fg_sc_sea_state_1=T, 0 otherwise	SC50*D*dS_dT	0	K	??	
Sea state 2	D=1 if	SC51*D*dS_dT	0	K	??	

	Fg_sc_sea_state_2=T, 0 otherwise					
Sea state 3	D=1 if Fg_sc_sea_state_3=T, 0 otherwise	SC52*D*dS_dT	0	K	??	
Sea state 4	D=1 if Fg_sc_sea_state_4=T, 0 otherwise	SC53*D*dS_dT	0	K	??	
Sea state 5	D=1 if Fg_sc_sea_state_5=T, 0 otherwise	SC54*D*dS_dT	0	K	??	
Sea state 6	D=1 if Fg_sc_sea_state_6=T, 0 otherwise	SC55*D*dS_dT	0	K	??	
SST front	D=0/1 if Fg_sc_SST_front=F/T	SC56*D*dS_dT	0	K	??	
SSS front	D=0/1 if Fg_sc_SSS_front=F/T	SC57*D*dS_dT	0	K	??	

Table 1 – Contributions to the global salinity quality index Dg_quality_SSS

The global salinity quality index Dg_quality_SSSX is given by the quadratic sum of all contributions listed in Table 1.

$$Dg\_quality\_SSSX = \sqrt{\sum_i Ci^2}$$

SCi coefficients values are given in the TGRD and will be updated during the mission. The SSSX with lowest value for this index will be considered the best one.

In addition to this global quality index in psu, a flag (Fg_ctrl_quality_SSSX) will be raised in case at least one of the following 'critical flags' is raised:
- Fg_ctrl_range_X
- Fg_ctrl_sigma_X
- Fg_ctrl_chi2_X
- Fg_ctrl_chi2_P_X
- Fg_ctrl_many_outliers
- Fg_ctrl_sunglint
- Fg_ctrl_moonglint
- Fg_ctrl_gal_noise
- Fg_sc_TEC_gradient
- Fg_sc_ice
- Fg_sc_rain
- Fg_ctrl_num_meas_low
- Fg_OoR_RoughX_Y

Waldteufel, P., Boutin, J., Kerr, Y. (2003) Selecting an optimal configuration for the Soil Moisture and Ocean Salinity mission. *Radio Science*, Vol. 38, No. 3, 8051, doi:10.1029/2002RS002744.

4.15. Brightness temperature at surface level

One of the outputs of the SMOS SSS L2 processor can be to provide, for each grid point, the set of brightness temperatures measured by MIRAS that have been used to compute salinity. But, unlike in L1c product, these have to be values at surface level (not antenna level) that can be used for example for assimilation in general circulation models, in validation exercises or in cross-calibration with Aquarius. Due to the singularity points and cross-correlated errors we do not transform measured Tb from antenna level to surface, but compute, with the forward models that correspond to the selected option, the different components of the Tb at surface level with the SSS and final auxiliary parameters as obtained during the retrieval.

Then the values will be those contributing to Tb_{BOA} , as explained in section 4.13.1.2

$$Tb_{BOA} = (Tb_{flat} + Tb_{rough})(1-F) + Tb_{foam} + (Tb_{DN}\Gamma + (Tgal\_refl)e^{-\tau_{atm}})$$

Due to operational constraints (size of the SMOS L2 output files), only one value ($Tb_{42.5H}$ and $Tb_{42.5V}$, with their associated uncertainties) corresponding to a fixed incidence angle (L2a_angle, 42.5°) will be regularly provided to users and using the default roughness model. The uncertainties will be computed using the theoretical uncertainties associated to the default forward model.

For a comparison between modeled and measured values, these $Tb_{42.5H}$ and $Tb_{42.5V}$ will be transported to antenna level with the same procedure used during the SSS retrieval, and the resulting $Tb_{42.5X}$ and $Tb_{42.5Y}$ values will be put in the UDP.

If the 42.5° angle is not included in the dwell line for the given point and given satellite pass, it will not be possible, due to model contraints, to compute these $Tb_{42.5H}$ and $Tb_{42.5V}$. Then a flag will be raised (Fg_ctrl_no_surface.true) and a warning value (999) will be put instead in the UDP.

The full set of modelled surface Tb values, and for the different modelling options, can be recovered by using processing tools based on the L2 SSS Prototype Processor made available by the SMOS Project

Note: The need for a complete set of measured (not modelled) Tb at surface is considered a key point for calibration/validation activities, as stressed by several participants to the First SMOS Cal/Val Experimenters Meeting (Avila, November 2005). This issue requires further attention and a satisfactory solution should be provided. An ESA funded study has been carried out by CLS, and results reported to L2 Mid Term Review on 19 Sept 2007. The decision at MTR was to keep the possible implementation of this TbBOA computation for a further stage, and do not introduce it in the processor before launch.

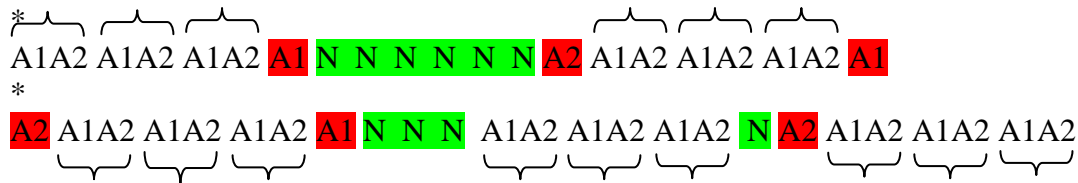## 4.16. Measurements selection (polarisation)

This module describes how to select the successive MIRAS measurements for the computation of SSS, according to the polarisation mode chosen.

To perform the iterative convergence, brightness temperature has to be taken in couples of H and V polarisations if the 1st Stokes parameter is used, otherwise the two polarisations are included independently in the computations. The way to extract proper measurements is as follows:

In case of Dual Polarisation: In a specific grid point all the snapshots that include it should be used, and this will include consecutively perpendicular polarisations. However, some of them can be invalid for SSS retrieval (either classified as bad by L1 or discarded in the L2 measurement discrimination) and as a consequence some pairs of horizontal (A1) and vertical (A2) measurements will not be formed.

In case of using the 1st Stokes parameter, and if the Scene Bias Correction (SBC, see module 4.11) is applied, the H+V pairs have always to be organised by taking first an H measurement and its immediately consecutive V. Then if the first snapshot that includes a grid point provides a V measurement, this will not be processed. In case of lack of one or more measurements in the sequence, the order should not be changed and continue by coupling first A1 and then A2. With this selection method it might happen that some measurements are not used, in spite of providing good data.

The following figure represents a couple of examples (grid points with very small number of measurements, for simplicity) from the first to the last view in a satellite overpass:

*⏜ ⏜ ⏜
A1A2 A1A2 A1A2 A1 N N N N N N A2 A1A2 A1A2 A1A2 A1
*
A2 A1A2 A1A2 A1A2 A1 N N N A1A2 A1A2 A1A2 N A2 A1A2 A1A2 A1A2

The brackets show the formed pairs of perpendicular polarisations in the most restrictive case (SBC with 1st Stokes), while N means invalid measurements and red marks measurements that will be lost due to the measurement selection (lack of companion polarisation). If SBC is not applied, only measurements marked with * in the examples above are lost with 1st Stokes option (end of a string with odd number of good data), as the order of complementary polarisations in a pair is not relevant. When the two polarisations are used separately, no good data have to be discarded, as pairs formation is not needed.

When a correct measurement is not used in the retrieval due to this selection method, a flag on the measurement should be raised (Fm_lost_data).

In case of Full Polarisation mode: do the same as dual polarisation, but taking into consideration only HH and VV measurements, not the mixed ones.

The first Stokes value (I) is computed as described in 4.13.1.1.1 and $\sigma^2 I = \sigma^2 A1 + \sigma^2 A2$

4.17. Auxiliary geophysical parameters bias correction

A separate document (SMOS ECMWF Pre-Processor, SO-TN-GMV-GS-4405) describes the geophysical auxiliary data needs of the L2 Ocean Surface Salinity Processor, and details how the data will be obtained from ECMWF and transformed into information usable by the inversion algorithm. A first version (at that moment named SMOS Level 2 Ocean Salinity Auxiliary Geophysical Data Processor Specification, hereafter AGDP) was incorporated as an annex to the OS L2 ATBD from draft 4 in October 2005, but from issue 1.1b the annex was removed and only a section dealing with bias correction is kept here.

Given the sensitivity of surface emissivity at L-band to SST and surface roughness, it is clear that we must ensure, to the extent possible, that auxiliary data be free of bias. Below we outline approaches to bias correction for SST and wind speed. Figure 1 shows the flow of data through the bias correction module.
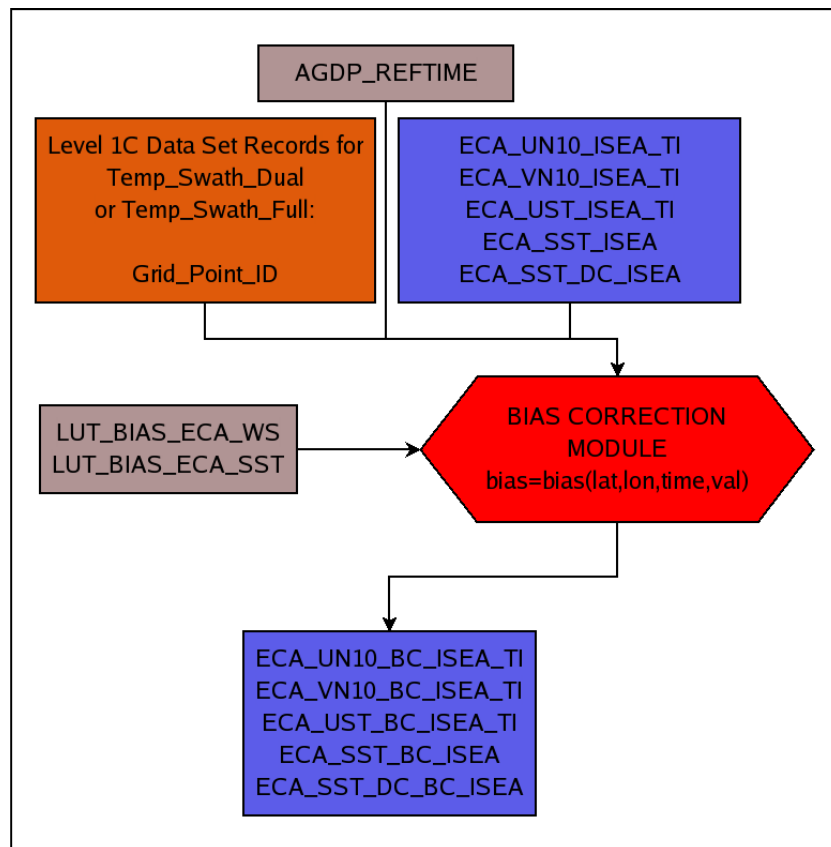

Figure 1: Schematic showing data flow through the bias correction module.

4.17.1 Sea Surface Temperature

Most SST analyses (including those obtained from ECMWF) are derived from much of the available in-situ and satellite observations, and many of these analyses have already been processed by bias-removal schemes. We propose including a lookup table of SST bias as a

function of latitude, longitude, time of year, and SST. The lookup table will be discretized into bins of 1.0º x 1.0º in space, monthly in time, and 2ºC in SST (0 – 30ºC). The table will consume 50 Mb assuming a 4 byte representation of bias values. Multilinear interpolation from this lookup table to the location and SST for each retrieval shall be performed using all 4 coordinates.

Table 1: Lookup Table for SST Bias Removal

LUT Dimension	Starting Value	Ending Value	Interval	Number of Values
Latitude	-90ºN	90ºN	1°	181
Longitude	0ºE	359ºE	1°	360
Time of year	January	December	1 month	12
SST	0ºC	30ºC	2ºC	16

4.17.2 Wind Speed

In general it is difficult to estimate error characteristics of numerical model output. In the IFS system, error variances and covariances for assimilated quantities are required to build covariance matrices for the variation data assimilation system. How to obtain such error covariance matrices is an area of active research at this time, however ECMWF routinely computes them using information from past forecasts. Bias removal in assimilated observations is also an integral part of the IFS assimilation system, but methods to obtain required bias adjustments are generally very approximate.

One approach to determining error characteristics is to compare ECMWF 10 m wind speed to that derived from other sources, such as buoys and scatterometers. Such comparisons have been performed in the past by various investigators.

One problem with such comparisons is the fact that all observation systems are potentially contaminated by random error and bias, and so simple model-buoy or model-scatterometer comparisons may not yield useful information on model bias and error variance. One of the more promising techniques that attempts to address this problem involves simultaneously comparing three noisy systems, which, with some assumptions, allows one to estimate the noise amplitude of all three and the bias in two of the systems.

One such "triple-collocation" technique is that of Freilich and Vanhoff (1999). In order to compare scatterometer, radiometer, and buoy derived wind speeds, they introduced the nonlinear noisy wind speed model

$$\hat{W}_i^2 = [(\alpha_i W_t + \beta_i)\cos(\varphi) + \delta_i n_{xi}]^2 + [(\alpha_i W_t + \beta_i)\sin(\varphi) + \delta_i n_{yi}]^2,$$

which maps a given true wind speed W_t and wind direction φ to an observed wind speed for observation system i. α_i is the wind speed gain, β_i is the wind speed bias, n_{xi} and n_{yi} represent normally distributed noise with zero mean and unit amplitude, and δ_i is the amplitude of the normally distributed random noise applied to each wind component. As shown by Freilich and Vanhoff, if we introduce 3 observing systems and if we assume that the true wind speed follows a two-parameter Weibull distribution of the form

$$P(W_t) = CW_t^{C-1}A^{-C} \exp\left\{-\left(\frac{W_t}{A}\right)^C\right\}$$

where A and C are free parameters known as the scale and shape parameters, respectively, then it is possible to uniquely resolve all of the calibration parameters as well as the Weibull scale and shape parameters, so long as one of the observing systems has known bias and gain (typically assumed to be zero and 1, respectively). The above error model together with the Weibull distribution yields the expressions for the second and fourth order moments and cross moments, which can be used to extract the calibration coefficients for three systems. In our case, since we are interested in obtaining calibration coefficients for ECMWF, we use ECMWF IFS wind speed as one of the observing systems and we use buoys and QuikSCAT as the other two.

Figure 2 shows the distribution of true wind for a given small range of ECMWF wind speed. The blue curves show the true wind speed distribution without adjusting ECMWF for bias and gain, while the red curves show the true wind speed distribution after adjusting ECMWF for bias and gain. The standard deviation of these true wind speed distributions are a measure of the uncertainty in the true wind speed.
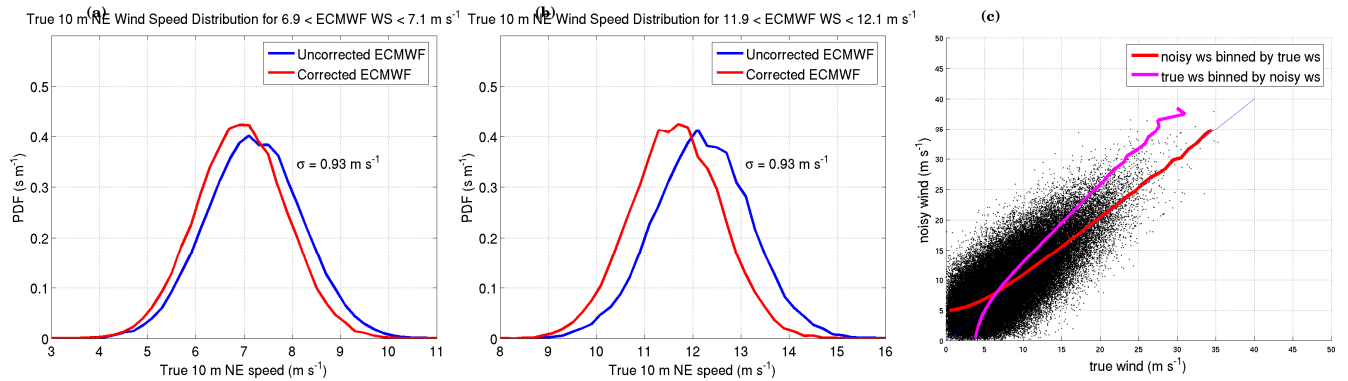

Figure 2: (a) Probability density function of the true 10 m neutral equivalent wind speed (m s^{-1}) for ECMWF IFS wind speed between 6.9 and 7.1 m s^{-1}). Blue curve shows the PDF for the uncorrected ECMWF wind speed with noise, gain, and bias derived from the triplet analysis. Red curve shows the distribution derived by retaining the noise but setting the gain to unity and bias to zero. Standard deviation of the true wind speed is shown. (b) Same as (a) except for an ECMWF wind speed range of 11.9 to 12.1 m s^{-1}. (c) Scatterplot of an idealized simulation in which a sequence of Weibull distributed true wind speed is used to generate a noisy sequency with a component noise level of 4 m s^{-1}. Red curve shows average bias of noisy wind relative to true wind averaged in true wind speed bins of 1 m s^{-1}. Magenta curve shows difference between true wind and noisy wind averaged in noisy wind speed bins of 1 m s^{-1}.

Note that there remains a residual bias associated with the noise in ECMWF wind speed, and it is anticipated that we may introduce a bias correction module to adjust for this. Figure 18c

illustrates how noise in an unbiased but noisy system can lead to an apparent bias in the noisy system when the true wind data are binned by the noisy data.

We anticipate providing bias correction as a function of space, time of year, and 10 m NE wind speed. The following table summarizes the structure of the lookup table. Assuming that the values are represented as 4 byte floating point variables, the lookup table will consume approximately 50 MB. Multilinear interpolation from this lookup table to the location and wind speed for each retrieval shall be performed using all 4 coordinates.

Table 2: Lookup Table for 10 m NE Wind Speed Bias Removal

LUT Dimension	Starting Value	Ending Value	Interval	Number of Values
Latitude	-90ºN	90ºN	1º	181
Longitude	0ºE	359ºE	1º	360
Time of year	January	December	1 month	12
10 m NE wind speed	0 m/s	30 m/s	2 m/s	16

4.17.3 Other parameters

Besides sea surface temperature and wind speed, other auxiliary parameters (wind direction, TEC, inverse wave age, mean square slope of waves, friction velocity, significant wave height) can be also affected by bias problems.

Then the processor has to be prepared to apply scale factor and offset corrections to these parameters. An approach based on Look-up Tables, similar to the one described for SST and wind speed, is expected to be used if necessary (see TGRD section 2.3.1.3). These additional parameters are:

LUT Dimension	Start value	End value	Interval	Number of values
Mean square slope (MSQS)	0	0.05	variable	16
Inverse wave age (omega)	0	12	variable	16
Neutral wind direction (phi_WSn)	0º	360º	5º	72
Sea surface salinity (SSS)	30 psu	40 psu	variable	10
Friction velocity from surface layer module (UST)	0 m/s	1 m/s	0.1	11
10 metre neutral equivalent wind – zonal & meridional components UN10, VN10	0 m/s	30 m/s	variable	16
Total electron count (TEC)	0 TECu	80 TECu	variable	16
Wave height (HS)	0	15m	1m	16
Cardioid model (Acard)				

4.17.4 Practical considerations

It might happen that during the computations some values in a grid point went out of range of the values defined in the LUTs above. In such cases warning flags will be raised: Fg_OoR_LUTAGDPT_lat (if at least one measurement went outside of the acceptable latitude limits in the auxiliary file), Fg_OoR_LUTAGDPT_lon (same for longitude), Fg_OoR_LUTAGDPT_month (if the month value went outside of acceptable limits), Fg_OoR_LUTAGDPT_param (same for value of the concerned parameter) and the parameter in the grid point will not be computed.

With the present information it is very difficult to evaluate the existence of these potential biases and their impact on the ovreall salinity retrieval. This will have to be analysed during the Commissioning Phase and beyond. Then, in the present configuration of the SMOS SSS L2 processor this auxiliary data bias correction will not be implemented and it will be addressed in the reprocessing ATBD.

5. Output Product

Two L2 Salinity Output files will be provided for each SMOS half orbit: a User Data Product (UDP), including information to be distributed to all users, and a Data Analysis Product (DAP), with auxiliary information on data processing for specific users working on algorithms improvement and products validation to allow analysing problems in the SSS retrieval. Both files have a unique Headers section plus a series of Binary fields (one per ISEA grid point, maximum 82257).

The Specific Product Header of both the UDP & DAP will contain information about retrieval quality. Each grid point will be classified as ocean, coast, or sea ice. Ocean grid points will be further classify by SSS, SST and wind speed into 27 (3 x 3 x 3) sub-classes: low, normal, or high SSS, SST & wind speed.

Grid points in each of these classifications may have poor quality flags set before retrieval is attempted, due to too many outliers, too much sun/moon glint, high galactic noise, possible sea ice, heavy rain, low number of measurements. For each grid point class & for each roughness model, the SPH will contain a set of values describing retrieval:

    number of grid points
    number flagged as poor quality
    for grid points not flagged as poor quality:
            number of successful retrievals & average sigma
            for failed retrievals, number failing because of:
                    poor SSS quality: outside valid range (Fg_ctrl_range)
                    poor SSS quality: sigma too high (Fg_ctrl_sigma)
                    poor fit quality: Fg_ctrl_chi2 or Fg_ctrl_chi2_P too large
                    lambda grew too large during iterations (Fg_ctrl_marq)
                    maximum number of iterations reached (Fg_ctrl_reach_Maxiter)
                    out-of-LUT range critical flag(s) raised
    for grid points flagged as poor quality:
            number of successful retrievals & average sigma

Additionally to this, information on intermediate processing steps, as the modelisation of the different components of Tb, will be accessible through the Breakpoints Reports that will allow recomputing these intermediate values with the prototype processor and complementary software tools

User Data Product

Origin	Name	Description	Units
L1c data	Latitude	Geodetic latitude	[deg]
	Longitude	Longitude	[deg]
L2 SSS processing	Equiv_ftprt_diam	Equivalent Footprint diameter	[m]
	Mean_acq_time	Mean acquisition time	[dd]
L2 SSS retrieval	SSS1	Sea surface salinity using roughness model 1	[psu]
	σ_{SSS1}	Theoretical uncertainty computed for SSS1	[psu]
	SSS2	Sea surface salinity using roughness model 2	[psu]

181

Origin	Name	Description	Units
	σ_{SSS2}	Theoretical uncertainty computed for SSS2	[psu]
	SSS3	Sea surface salinity using roughness model 3	[psu]
	σ_{SSS3}	Theoretical uncertainty computed for SSS3	[psu]
L2 A_card retrieval	A_card	Effective_Acard retrieved with minimalist model	
	σ_{A_card}	Theoretical uncertainty computed for Acard	
L2 Auxiliary Geophysical Data Processor	WS	Equivalent neutral wind speed as derived from ECMWF	[m.s^{-1}]
	σ_{WS}	Theoretical uncertainty associated with WS	[m.s^{-1}]
L2 Auxiliary Geophysical Data Processor	SST	Sea Surface Temperature as derived from ECMWF	[ºC]
	σ_{SST}	Theoretical uncertainty associated with SST	[ºC]
L2 SSS retrieval and default forward model	$Tb_{42.5H}$	Brightness Temperature at surface level derived with default forward model and retrieved geophysical parameters, H polarisation direction. Value is 999 if not possible to compute	[K]
	$\sigma_{Tb42.5H}$	Theoretical uncertainty computed for $Tb_{42.5H.}$ Value is 999 if not possible to compute	[K]
L2 SSS retrieval and default forward model	$Tb_{42.5V}$	Brightness Temperature at surface level derived with default forward model and retrieved geophysical parameters, V polarisation direction. Value is 999 if not possible to compute	[K]
	$\sigma_{Tb42.5V}$	Theoretical uncertainty computed for $Tb_{42.5V}$ Value is 999 if not possible to compute	[K]
L2 SSS retrieval and default forward model	$Tb_{42.5X}$	Brightness Temperature at antenna level derived with default forward model and retrieved geophysical parameters, X polarisation direction. Value is 999 if not possible to compute	[K]
	$\sigma_{Tb42.5X}$	Theoretical uncertainty computed for Tb42.5X. Value is 999 if not possible to compute	[K]
L2 SSS retrieval and default forward model	$Tb_{42.5Y}$	Brightness Temperature at antenna level derived with default forward model and retrieved geophysical parameters, Y polarisation direction. Value is 999 if not possible to compute	[K]
	$\sigma_{Tb42.5Y}$	Theoretical uncertainty computed for Tb42.5Y Value is 999 if not possible to compute	[K]

Note: After commissioning phase WS and SST values in UDP can be the retrieved values (using default model) if they are proven to be better than ECMWF information

Product confidence descriptor

Origin	Name	Description	Note	Size (bit)
		Confidence flags		
L2 measurement discrimination	Fg_ctrl_num_meas_low	Number of measurements valid for SSS retrieval is low		1
	Fg_ctrl_num_meas_min	Not processed due to too few valid measurements		1
	Fg_ctrl_valid	Grid point used in the retrieval		
L2 roughness models	Fg_ctrl_ECMWF_1	No missing ECMWF data for SS1 retrieval		1
	Fg_ctrl_ECMWF_2	No missing ECMWF data for SS2 retrieval		1
	Fg_ctrl_ECMWF_3	No missing ECMWF data for SS3 retrieval		1
	Fg_ctrl_ECMWF_4	No missing ECMWF data for Acard retrieval		1
	Fg_ctrl_roughness_M1	Roughness correction applied with model 1		1
	Fg_ctrl_roughness_M2	Roughness correction applied with model 2		1
	Fg_ctrl_roughness_M3	Roughness correction applied with model 3		1
	Fg_ctrl_foam_M1	Foam correction applied to model 1		1
	Fg_ctrl_foam_M2	Foam correction applied to model 2		1

Origin	Name	Description	Note	Size (bit)
L2 retrieval post-processing	Fg_ctrl_range_1	Retrieved value outside range using forward model 1		1
	Fg_ctrl_range_2	Retrieved value outside range using forward model 2		1
	Fg_ctrl_range_3	Retrieved value outside range using forward model 3		1
	Fg_ctrl_range_Acard	Retrieved value outside range using cardioid model		1
	Fg_ctrl_sigma_1	High retrieval sigma using forward model 1		1
	Fg_ctrl_sigma_2	High retrieval sigma using forward model 2		1
	Fg_ctrl_sigma_3	High retrieval sigma using forward model 3		1
	Fg_ctrl_sigma_Acard	High retrieval sigma using cardioid model		1
	Fg_ctrl_chi2_1	Poor fit quality using forward model 1		1
	Fg_ctrl_chi2_2	Poor fit quality using forward model 2		1
	Fg_ctrl_chi2_3	Poor fit quality using forward model 3		1
	Fg_ctrl_chi2_Acard	Poor fit quality using cardioid model		1
	Fg_ctrl_chi2_P_1	Poor fit quality from test Chi2_P using forw.model 1		1
	Fg_ctrl_chi2_P_2	Poor fit quality from test Chi2_P using forw.model 2		1
	Fg_ctrl_chi2_P_3	Poor fit quality from test Chi2_P using forw.model 3		1
	Fg_ctrl_chi2_P_Acard	Poor fit quality from test Chi2_P using cardioid.model		1
	Fg_ctrl_quality_SSS1	At least one critical flag was raised during SSS1 retrieval		1
	Fg_ctrl_quality_SSS2	At least one critical flag was raised during SSS2 retrieval		1
	Fg_ctrl_quality_SSS3	At least one critical flag was raised during SSS3 retrieval		1
	Fg_ctrl_quality_Acard	At least one critical flag was raised during pseudo-dielectric constant retrieval		1
	Fg_ctrl_marq_SSS1	Iteration stopped due to Marquardt increment too big		1
	Fg_ctrl_marq_SSS2	Iteration stopped due to Marquardt increment too big		1
	Fg_ctrl_marq_SSS3	Iteration stopped due to Marquardt increment too big		1
	Fg_ctrl_marq_Acard	Iteration stopped due to Marquardt increment too big		1
	Fg_ctrl_reach_maxiter_1	Maximum number of iterations reached before convergence using forward model 1		1
	Fg_ctrl_reach_maxiter_2	Maximum number of iterations reached before convergence using forward model 2		1
	Fg_ctrl_reach_maxiter_3	Maximum number of iterations reached before convergence using forward model 3		1
	Fg_ctrl_reach_maxiter_Ac	Maximum number of iterations reached before convergence using cardioid model		1
	Fg_ctrl_many_outliers	High number of outlier measurements		1
	Fg_ctrl_sunglint	High number of measurements flagged for sunglint		1
	Fg_ctrl_moonglint	High number of measurements flagged for moonglint		1
	Fg_ctrl_gal_noise	High number of measurements flagged for galact. noise		1
	Fg_ctrl_gal_noise_pol	High number of meas. flagged for polarised galact. noise		1
	Fg_ctrl_no_surface	42.5° angle not available to compute Tb at surface		
		spare		21
		Confidence descriptors		**byte**
L2 SSS retrieval post-processing	Dg_chi2_1	Retrieval fit quality index with forward model 1		1
	Dg_chi2_2	Retrieval fit quality index with forward model 2		1
	Dg_chi2_3	Retrieval fit quality index with forward model 3		1
	Dg_chi2_P_1	χ^2 high value acceptability probability with model 1		1
	Dg_chi2_P_2	χ^2 high value acceptability probability with model 2		1
	Dg_chi2_P_3	χ^2 high value acceptability probability with model 3		1
	Dg_quality_SSS1	Descriptor of SSS1 uncertainty		1
	Dg_quality_SSS2	Descriptor of SSS2 uncertainty		1
	Dg_quality_SSS3	Descriptor of SSS3 uncertainty		1
	Dg_num_iter_1	Number of iterations with forward model 1		1

Origin	Name	Description	Note	Size (bit)
	Dg_num_iter_2	Number of iterations with forward model 2		1
	Dg_num_iter_3	Number of iterations with forward model 3		1
	Dg_chi2_Acard	Retrieval fit quality index with cardioid model		1
	Dg_chi2_P_Acard	χ^2 high value acceptability probability with cardioid		1
	Dg_quality_Acard	Descriptor of Acard uncertainty		1
	Dg_num_iter_Acard	Number of iterations with cardioid model		1
L1c data	Dg_num_meas_l1c	Number of measurements available in L1c product		1
Measurement discrimination	Dg_num_meas_valid	Number of valid measurement available for retrieval		1
L1c data and measurement discrimination	Dg_border_fov	Number of measurements with BORDER_FOV flag raised.		1
	Dg_af_fov	Number of measurements with AF_FOV flag raised.		1
	Dg_sun_tails	Number of measurements with SUN_TAILS flag raised.		1
	Dg_sun_glint_area	Number of measurements with SUN_GLINT_AREA flag raised		1
	Dg_sun_glint_fov	Number of measurements with SUN_GLINT_FOV flag raised.	Not in L2 SM	1
	Dg_sun_fov	Number of measurements with SUN _FOV flag raised		1
L2 sunglint module	Dg_sunglint_L2	Number of measurements with L2 sunglint flag raised		1
L2 moonglint module	Dg_moonglint	Number of measurements with L2 moonglint raised		1
Measurement discrimination	Dg_suspect_ice	Number of measurements suspect of ice contaminated		1
	Dg_gal_noise_error	Number of meas. with galactic noise error flag raised.		1
	Dg_gal_noise_pol	Number of meas. with polarised gal. noise flag raised.		1

Science flags

Origin	Name	Description	Note	Size (bit)
L2 auxiliary data	Fg_sc_land_sea_coast1	Land / sea		1
	Fg_sc_land_sea_coast2	Coast / not coast		1
	Fg_sc_TEC_gradient	High TEC gradient along dwell for a grid point		1
SMOS ECMWF Pre-Processing	Fg_sc_ice	ECMWF give ice concentration > Tg_ice_concentration		1
	Fg_sc_in_clim_ice	Grid point within monthly climatological maximum extent of sea ice		1
	Fg_sc_suspect_ice	Fg_sc_in_clim_ice.true and SST < Tg_low_SST_ice and number of measurement with possible ice is larger than a threshold (Tg_num_suspect_ice)		1
	Fg_sc_rain	Rain rate is above the threshold.		1
	Fg_sc_high_wind	High or low wind condition.		1
	Fg_sc_low_wind	Low wind condition. To be combined with Fg_high_wind.		1
	Fg_sc_high_SST	High or low SST condition.		1
	Fg_sc_low_SST	Low SST condition. To be combined with Fg_high_SST.		1
	Fg_sc_high_SSS	High or low SSS condition.		1
	Fg_sc_low_SSS	Low SSS condition. To be combined with Fg_high_SST.		1
	Fg_ sc_sea_state_1	Sea state class 1		1

Origin	Name	Description	Note	Size (bit)
	Fg_ sc_sea_state_2	Sea state class 2		1
	Fg_ sc_sea_state_3	Sea state class 3		1
	Fg_ sc_sea_state_4	Sea state class 4		1
	Fg_ sc_sea_state_5	Sea state class 5		1
	Fg_ sc_sea_state_6	Sea state class 6		1
	Fg_sc_SST_front	Presence of a temperature front		1
	Fg_sc_SSS_front	Presence of a salinity front		1
	Fg_sc_ice_Acard	Ice flag from cardioid		1
		spare		21
		Science descriptors		**byte**
L2 measurement discrimination	Dg_sky	Count measurements with specular direction toward a strong galactic source.		1

Data Analysis Product

Origin	Name	Description	Units
L1c data	Grid_point_ID	Unique identified of the grid point in the DGG	[dl]
	Latitude	Geodetic latitude	[deg]
	Longitude	Longitude	[deg]
L2 preprocessing and L1c data	Fm_flags[NM]	Flags of measurements, see next table below. NM= Dg_num_meas_l1c < 256.	[dl]
L2 retrieval	Diff_TB_1[NM]	Difference between measurements and result of forward model 1. NM= Dg_num_meas_l1c <= 256. for 2 polarisations	[K]
	Diff_TB_2[NM]	Difference between measurements and result of forward model 2. NM= Dg_num_meas_l1c <= 256. for 2 polarisations	[K]
	Diff_TB_3[NM]	Difference between measurements and result of forward model 3. NM= Dg_num_meas_l1c <= 256. for 2 polarisations	[K]
	Diff_TB_Acard[NM]	Difference between measurements and result of cardioid model. NM= Dg_num_meas_l1c <= 256. for 2 polarisations	[K]
SMOS ECMWF Pre-Processing	Param1_prior_M1	Prior and sigma of seven parameters for retrieval with forward model 1. Seven placeholders.	
	Param1_sigma_prior_M1		
	Param2_prior_M1		
	Param2_sigma_prior_M1		
	Param3_prior_M1		
	Param3_sigma_prior_M1		
	Param4_prior_M1		
	Param4_sigma_prior_M1		
	Param5_prior_M1		
	Param5_sigma_prior_M1		
	Param6_prior_M1		
	Param6_sigma_prior_M1		
	Param7_prior_M1		
	Param7_sigma_prior_M1		
	Param1_prior_M2	Prior and sigma of seven parameters for retrieval with forward model 2. Seven placeholders.	
	Param1_sigma_prior_M2		
	Param2_prior_M2		

Origin	Name	Description	Units
	Param2_sigma_prior_M2		
	Param3_prior_M2		
	Param3_sigma_prior_M2		
	Param4_prior_M2		
	Param4_sigma_prior_M2		
	Param5_prior_M2		
	Param5_sigma_prior_M2		
	Param6_prior_M2		
	Param6_sigma_prior_M2		
	Param7_prior_M2		
	Param7_sigma_prior_M2		
	Param1_prior_M3		
	Param1_sigma_prior_M3		
	Param2_prior_M3		
	Param2_sigma_prior_M3		
	Param3_prior_M3		
	Param3_sigma_prior_M3	Prior and sigma of seven parameters for retrieval with forward model 3. Seven placeholders.	
	Param4_prior_M3		
	Param4_sigma_prior_M3		
	Param5_prior_M3		
	Param5_sigma_prior_M3		
	Param6_prior_M3		
	Param6_sigma_prior_M3		
	Param7_prior_M3		
	Param7_sigma_prior_M3		
SMOS ECMWF Pre-Processing	Param1_prior_Ac		
	Param1_sigma_prior_Ac		
	Param2_prior_Ac		
	Param2_sigma_prior_Ac		
	Param3_prior_Ac		
	Param3_sigma_prior_Ac	Prior and sigma of seven parameters for retrieval with cardioid model. Seven placeholders.	
	Param4_prior_Ac		
	Param4_sigma_prior_Ac		
	Param5_prior_Ac		
	Param5_sigma_prior_Ac		
	Param6_prior_Ac		
	Param6_sigma_prior_Ac		
	Param7_prior_Ac		
	Param7_sigma_prior_Ac		
L2 SSS retrieval	Param1_M1		
	Param1_sigma_M1		
	Param2_M1		
	Param2_sigma_M1		
	Param3_M1	Value and theoretical uncertainty of seven parameters retrieved with forward model 1. Seven placeholders. Set ParamX_sigma_M1 to 999 if parameter has not been retrieved, and the ECMWF prior value put for ParamX_M1. For the field names, "Param3" will be replaced by parameter name whenever it is known, e.g. SST, WS, etc.	
	Param3_sigma_M1		
	Param4_M1		
	Param4_sigma_M1		
	Param5_prior_M1		
	Param5_sigma_M1		
	Param6_M1		
	Param6_sigma_M1		
	Param7_prior_M1		
	Param7_sigma_M1		
L2 SSS retrieval	Param1_M2	Same as above for forward model 2.	
	Param1_sigma_M2		

Origin	Name	Description	Units
	Param2_M2		
	Param2_sigma_M2		
	Param3_M2		
	Param3_sigma_M2		
	Param4_M2		
	Param4_sigma_M2		
	Param5_M2		
	Param5_sigma_M2		
	Param6_M2		
	Param6_sigma_M2		
	Param7_M2		
	Param7_sigma_M2		
L2 SSS retrieval	Param1_M3	Same as above for forward model 3.	
	Param1_sigma_M3		
	Param2_M3		
	Param2_sigma_M3		
	Param3_M3		
	Param3_sigma_M3		
	Param4_M3		
	Param4_sigma_M3		
	Param5_M3		
	Param5_sigma_M3		
	Param6_M3		
	Param6_sigma_M3		
	Param7_M3		
	Param7_sigma_M3		
L2 Acard retrieval	Param1_Ac	Same as above for cardioid model	
	Param1_sigma_Ac		
	Param2_Ac		
	Param2_sigma_Ac		
	Param3_Ac		
	Param3_sigma_Ac		
	Param4_Ac		
	Param4_sigma_Ac		
	Param5_Ac		
	Param5_sigma_Ac		
	Param6_Ac		
	Param6_sigma_Ac		
	Param7_Ac		
	Param7_sigma_Ac		
Atmospheric contribution	Tbatm	Nadir atmospheric emissivity (only in polar 1)	
	tau	Nadir optical thickness	
	Tbgal_refl[NM]	Galactic noise reflected towards the radiometer	
Grid point descriptors			
Measurements discrimination	Dg_num_outliers	Number of outlier measurements discarded	
	Dg_num_high_resol	Number of measurements discarded due to excessive resolution	
	Dg_RFI_L1	Number of measurements discarded due to being flagged RFI at L1	
	Dg_sunglint_L1	Number of measurements discarded due to sunglint contamination at L1	

Origin	Name	Description	Units
	Dg_X_Swath	Distance (km) between satellite track and grid point, computed using stat vector of first measurement at grid point	
Out of LUT range flags			
	Fg_OoR_Sunglint_dim2_ThetaSun	ThetaSun went out of LUT range during retrieval	
	Fg_OoR_Sunglint_dim3_Phi	Phi went out of LUT range during retrieval	
	Fg_OoR_Sunglint_dim4_Theta	Theta went out of LUT range during retrieval	
	Fg_OoR_Sunglint_dim4_WS	WS went out of LUT range during retrieval	
	Fg_OoR_Rough1_dim1_SST	Prior or retrieved SST went outside of LUT range	
	Fg_OoR_Rough1_dim2_SSS	Prior or retrieved SSS went outside of LUT range	
	Fg_OoR_Rough1_dim3_U10	Prior or retrieved U1 went outside of LUT range	
	Fg_OoR_Rough1_dim4_Theta	Prior or retrieved Theta went outside of LUT range	
	Fg_OoR_Rough2_dim5_SST	Prior or retrieved SST went outside of LUT range	
	Fg_OoR_Rough2_dim4_SSS	Prior or retrieved SSS went outside of LUT range	
	Fg_OoR_Rough2_dim3_Theta	Prior or retrieved Theta went outside of LUT range	
	Fg_OoR_Rough2_dim1_Ust	Prior or retrieved Ust went outside of LUT range	
	Fg_OoR_Rough2_dim2_Omega	Prior or retrieved Omega went outside of LUT range	
	Fg_OoR_Foam_dim1_WS	WS went out of LUT range during retrieval	
	Fg_OoR_Foam_dim2_TseaAir	TseaAir went out of LUT range during retrieval	
	Fg_OoR_Foam_dim3_SSS	SSS went out of LUT range during retrieval	
	Fg_OoR_Foam_dim4_SST	SST went out of LUT range during retrieval	
	Fg_OoR_Foam_dim5_Theta	Theta went out of LUT range during retrieval	
	Fg_OoR_gam1_dec	Dec went out of LUT range during retrieval	
	Fg_OoR_gam1_ra	Ra went out of LUT range during retrieval	
	Fg_OoR_gam2_dec	Dec went out of LUT range during retrieval	
	Fg_OoR_gam2_psi	Psi went out of LUT range during retrieval	
	Fg_OoR_gam2_ra	Ra went out of LUT range during retrieval	
	Fg_OoR_gam2_theta	Theta went out of LUT range during retrieval	
	Fg_OoR_gam2_WSn	WSn went out of LUT range during retrieval	
	Fg_OoR_LUTAGDPT_lat	Latitude went out of LUT range in auxiliary file	
	Fg_OoR_LUTAGDPT_lon	Longitude went out of LUT range in auxiliary file	
	Fg_OoR_LUTAGDPT_month	Month value went out of LUT range in auxiliary file	
	Fg_OoR_LUTAGDPT_param	The value of parameters went out of LUT range in auxiliary file	

List of Measurement flags

Origin	Name	Description	Note	Size (bit)
		Measurement flags		
Preprocessing	Fm_suspect_ice	Difference between measured brightness temperature and flat sea model is greater than a threshold.		1
	Fm_out_of_range	Difference between measured brightness temperature and that derived with default forward model is greater than a threshold		1
	Fm_resol	Length of major axis of the footprint ellipse is greater than a threshold.		1
L1c data	Fm_L1c_sun			1
	FmL1c_border_fov			1
	FmL1c_eaf_fov			1
	FmL1c_af_fov			1
	FmL1c_sun_tails			1
	FmL1c_sun_glint_area			1
	FmL1c_sun_glint_fov			1
	FmL1c_RFI			1
Preprocessing	Fm_outlier	Measurement is an outlier		1
Sunglint module	Fm_high_sun_glint	High or low sun glint condition.		1
	Fm_low_sun_glint	Low sun glint condition. To be combined with Fm_high_sun_glint.		1
	Fm_sun_limit	Sun contamination above threshold		1
Moonglint module	Fm_moon_specdir	Specular direction close to target to Moon direction		1
Galactic noise module	Fm_gal_noise_error	Uncertainty on galactic noise source is large.		1
	Fm_high_gal_noise	Galactic noise is high		1
	Fm_gal_noise_pol	Polarised galactic noise is above threshold		1
Measurement discrimination	Fm_valid	Measurement is valid		1
	Fm_lost_data	Measurement not used due to lack of companion polarisation		1
		spare		14

ANNEX-1: Technical note on geometry conventions for SMOS

This annex aims at clarifying the conventions and formulae used for angles transformation in the SMOS L2 SSS ATBD, especially relevant in cases like Faraday rotation and change of coordinate frame from Earth to antenna.

The technical note has been generated as an independent document (smos-geom-jt-20080519.pdf) that will not be integrated in the Word working versions of the ATBD, but only in the formal PDF deliverables.

ANNEX-2: Technical note on the use of an effective L-band pseudo-dielectric constant for qualifying SMOS measurements over the ocean

L-band passive microwave radiometers provide information about surface soil moisture over land and about sea surface salinity (SSS) over the ocean. In case of the SMOS (Soil Moisture and Ocean Salinity) interferometer instrument, the retrieval of the geophysical parameters will be performed through the inversion of multiangular brightness temperatures (Tb) (typically 120 at the center of the swath). The retrieval of geophysical parameters is based on a minimization process between measured and modelled Tb and a knowledge (with some errors) of auxiliary parameters (e.g. sea surface temperature and wind speed over the ocean). However, the modelling of the radiometer signal is not straightforward: Tb reconstruction is a complex process, modelling of the sea surface emissivity is not completely under control (in particular roughness effects (Dinnat, Boutin et al. 2003)), external signal such as galactic noise reflected at the sea surface is still not completely understood (Vine, Abraham et al. 2004), auxiliary parameters may be poorly known (biased)… In addition the nature of the sea surface may be unknown at high latitude in presence of sea ice or drifting icebergs. Because of all these issues, a pseudo-cardioid model (Waldteufel, Vergely et al. 2004) has been developed to retrieve from SMOS multiangular Tb a single parameter, Acard, that synthesizes available information about surface dielectric caracteristics, thus avoiding the modelling of the link between geophysical parameters and surface dielectric properties.
In this paper we study to which extent the retrieval of this parameter over the ocean could be used 1) to detect the presence of ice and 2) to detect flaws in Tb, direct emissivity models or in auxiliary parameters.

The modelling of SMOS signal and the retrieval of Acard were performed using the SMOS Retrieval Simulator (SRS) described in (Boutin, Font et al. 2005). Main characteristics relevant for this study are described below.

Forward modeling of SMOS apparent temperature

The apparent temperature measured over sea surfaces by the SMOS radiometer is affected by four main processes:
-the emission of the surface

I

-the emission and attenuation by the atmosphere

-the emission of the sky reflected at the sea surface

-the Faraday rotation

Once all these contributions are modelled in horizontal and vertical polarizations, Tb are computed in SMOS antenna geometry according to geometric transformations described in (Waldteufel and Caudal 2002).

Sea water emissivity:

Dielectric constant of sea water is modelled according to (Klein and Swift 1977). Typical real and imaginary parts of sea water dielectric constant encountered over the open ocean are indicated on (Figure 1).
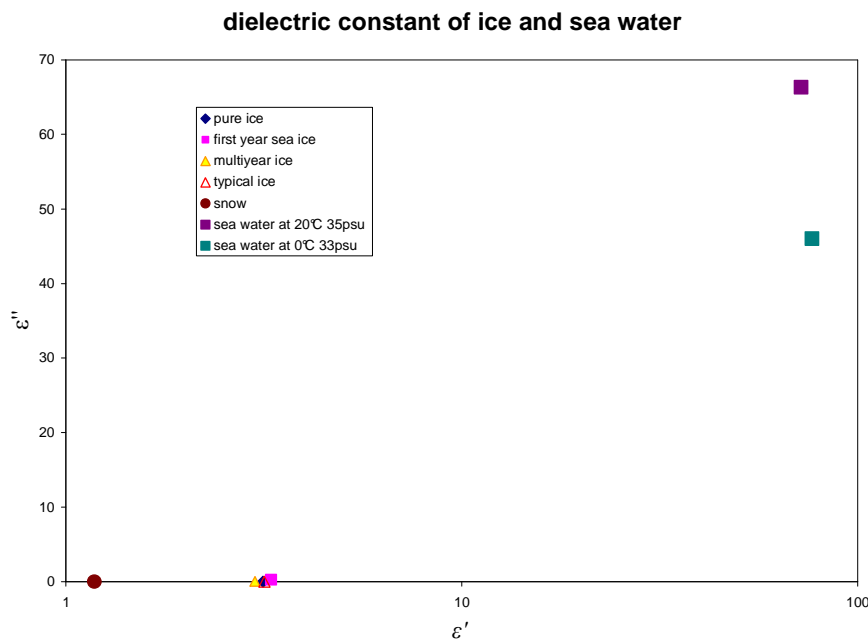
Figure 1: Imaginary and real parts of dielectric constants over various ice types and sea water

Brightness temperatures over a flat sea are deduced from dielectric constants using Fresnel equations. Additional signal coming from sea surface roughness is simulated using the two-scale model described in (Dinnat, Boutin et al. 2003) in which the wave spectrum is modeled using Durden and Vesecky parameterization (Durden and Vesecky 1985) multiplied by 2. With these models, for SST around 15°C and at nadir, the sensitivity of ocean Tb, Tb_ocean, to SSS is typically -0.5 K psu^{-1}, to wind speed (WS) 0.2 K m^{-1} s, and to SST close to 0 K °C^{-1}.

II

Sea ice emissivity:

At 1.4GHz, the penetration depth of sea ice ranges between 0.2 and 0.8m for first-year sea ice and between 0.8 and 2m for older sea ice ([*Ulaby et al.,* 1990], Figure E.24); for pure ice it reaches about 60m. In order to ease computations and given that the penetration depth increases with ice age, that the typical thickness of icebergs is several tens of meters and the typical thickness of first-year sea ice is typically 1m in winter (see for instance (Schodlok, Hellmer et al. 2006)), in the following we will always consider that the ice thickness is greater than the penetration depth (monolayer model).

Sea ice Tb, Tb_ice, are simulated using Fresnel relationships and ice dielectric constant, ε. We recall below values of ice ε as reviewed by [*Ulaby et al.,* 1990]:

-for pure ice :

$\varepsilon = 3.15 + j \ 10^{-3}$

-for sea ice, numerical values depend slightly whether it is first year sea ice or multiyear sea ice at -10°C :

$\varepsilon = 3.3 - j \ 0.25$ (first year sea ice) and

$\varepsilon = 3 - j \ 0.03$ (multiyear)

Given the strong contrast between sea water and sea ice dielectric constants (Figure 1), in the following we will model dielectric constant of ice selecting values intermediate between various sea ice dielectric constants:

$\varepsilon = 3.17 + j \ 0$

We will also neglect presence of snow; in presence of snow, the contrast between sea water and snow is greater than between sea water and ice (see Figure 1 where snow value has been taken as the minimalist value given by (Nedeltchev, Peuch et al.)).

Atmosphere and cosmic background

The atmospheric attenuation and emission are described using Liebe (Liebe, Hufford et al. 1993) model. The atmospheric attenuation of sea surface Tb is 0.7K at nadir. The atmospheric and cosmic background emissions are the dominant signal. Downward atmospheric emission and cosmic background emission are reflected at the sea surface. The

total contribution (atmospheric + cosmic background) ranges from 5.5K at nadir to 7K at 50° incidence angle. This contribution is not strongly affected by atmospheric parameters, in the absence of heavy rain.

Galactic Noise

In contrast to atmospheric emission and cosmic background emission (2.7K), which are homogeneous in space and time, galactic noise emissions are very inhomogeneous and they generate a signal reflected by the sea surface that may strongly vary inside the SMOS swath. Galactic noise reaching the sea surface are computed using a model developed at CETP (Delahaye, Golé et al. 2002). It makes use of Reich and Reich charts for the galactic sources at 0.25° resolution (Reich and Reich, pers. comm.). This map was weighted by weighted by an average of the synthetic antenna lobe weighting functions over the alias free field of view (Boutin, Font et al. 2004).

For this angular resolution, galactic sources vary from about 0.7K to more than 15K close to the galactic centre. These signals are reflected at the sea surface assuming a flat sea.

Retrieval of a pseudo-dielectric constant

As shown in (Waldteufel, Vergely et al. 2004), simultaneous retrieval of the real, ε', and imaginary part, ε'', of dielectric constant from SMOS Tb is an ill posed problem as the cost function, rather than a single minimum, exhibit a minimum valley, that can be represented analytically using a modified cardioid model (Figure 2, left)). After carrying out the following change of variable:

$\varepsilon' = A\_card \ (1 + \cos(U\_card) \ ) \cos (U\_card) + B\_card$

$\varepsilon'' = A\_card \ (1 + \cos(U\_card) \ ) \sin (U\_card)$

Eqn. 1

which is equivalent to:

$A\_card = m\_card^2 / (m\_card + \varepsilon' - B\_card)$ $U\_card = \tan^{-1}(\varepsilon''/(\varepsilon'-B\_card) \ )$

with: $m\_card = (\ (\varepsilon'-B\_card)^2 + \varepsilon''^2 \ )^{1/2}$

Eqn. 2

IV

	ICM-CSIC LOCEAN/SA/CETP IFREMER	SMOS L2 OS Algorithm Theoretical Baseline Document	Doc: SO-TN-ARG-GS-0007 Issue: 3 Rev: 7 Date: 22 June 2011 Page:A2- V

with B_card = 0.8, it is possible to retrieve the parameter Acard with good accuracy, as indicated on (Figure 2, right): a minimum of Chi2 is seen as a vertical line corresponding to a constant value of Acard and various values of Ucard. On (Figure 2, right), local minima of Chi2 are also observed for unrealistic negative values of Acard; as it will be described in the following, retrieval of such negative values are avoided by taking an error on prior Acard over the ocean of 20 units or by initiating the retrieval with low Acard value as low Acard are much better constrained.
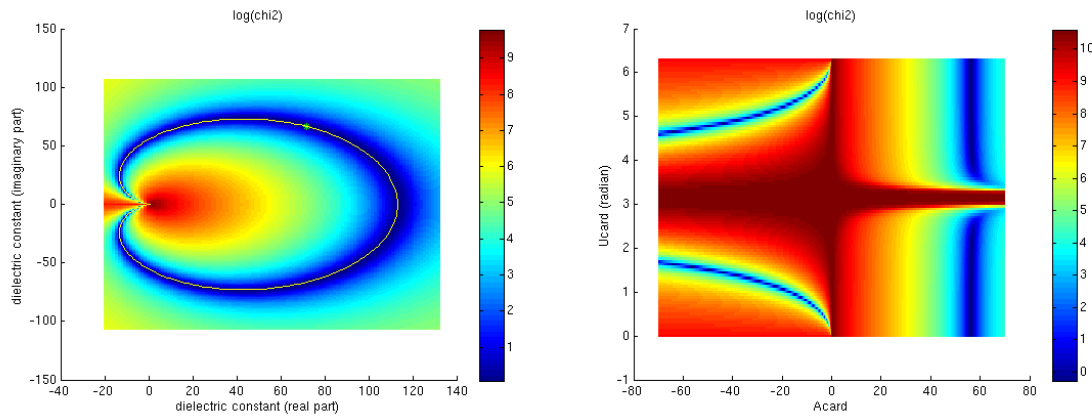
Figure 2. Chi2 (log value) in case of retrieval of (ε', ε") over sea water (left) plotted as function of (ε', ε"); the green cross indicates the true value of the dielectric constant. The yellow curve corresponds to a constant A_card with U_card varying between 0 and 360 °; (right) plotted as a function of (Acard, Ucard).

With these definitions and considering direct emissivity models described above: for sea ice, Acard=1.2 (Ucard=0); over a flat sea, Acard ranges between 48 and 67 depending on SSS and SST values (Figure 3) and U_card between -0.9 and -0.5 radians (not shown).
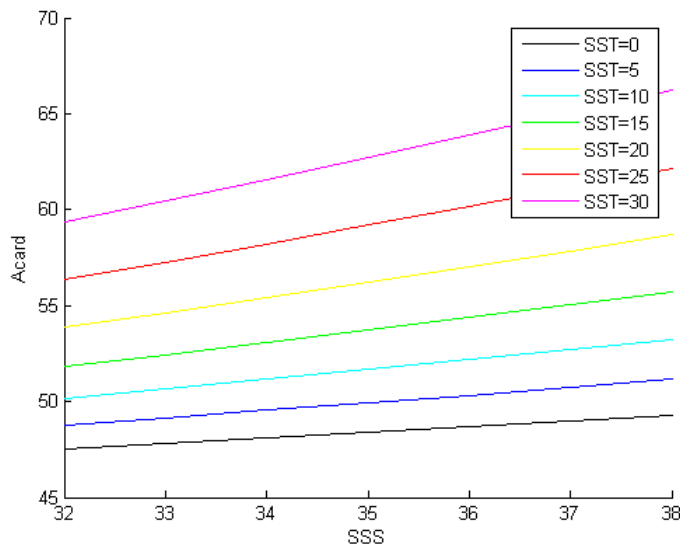
Figure 3: Variation of Acard as a function of SSS and SST

V

From Figure 2, it is clear that the minimization of Chi2 parameter does not allow to retrieve a single pair of (ε', ε") while it allows to retrieve a single value of Acard, Ucard remaining undetermined.

The retrieval is performed through the iterative Levenberg and Marquard (Marquardt 1963) algorithm. Minimization is done over Tb measured and modelled at the antenna level, using the following cost function:

$$chi2(P1, P2) = 1/N \sum_{i=0}^{Nm-1} \frac{\left[T_{bi}^{meas} - T_{bi}^{mod}(\theta_i, P1, P2) \right]^2}{\sigma_{T_{bi}}^2} + \sum_{P1,P2} \frac{\left[P^{prior} - P^{ret} \right]^2}{\sigma_P^2} \qquad \text{Eqn. 3}$$

where (P1, P2) are (Acard, surface temperature), Nm is the number of measurements in the pixel, T_{bi}^{meas}, radiometer measurements, T_{bi}^{mod} modelled Tb and $\sigma_{T_{bi}}$, radiometric errors; P^{prior}, P^{ret} and σ_P are a priori value, retrieved value and a priori error on P1 and P2 parameters. The error on surface temperature is set to 1.5°C. Over the ocean, Acard^{prior} is deduced from mean SSS and SST, and σ_{Acard} is taken as 20% of Acard a priori value (about 10). In case of sea-ice retrievals, several a priori values of Acard and σ_{Acard} were tested in order to avoid retrieval of negative Acard values while avoiding biases on low Acard values. We found that initiating the retrieval with low Acard prior value (Acard^{prior} =1) and large error on Acard (σ_{Acard} =50) meets this goal and gives the same result over ocean pixels as taking Acard^{prior} deduced from mean SSS and SST.

Two kinds of retrievals were performed: academic retrievals and semi-realistic retrievals:

Academic retrievals:

These retrievals were performed in order to look at the performance of the Acard retrieval, in case of ocean-ice heterogeneous pixels or in case of biases on auxiliary parameters or on Tb. Tb, entering in the retrieval, is modelled considering only parts of the direct model that are impacted by these biases. Atmospheric effects, galactic noise reflection and Faraday rotation are neglected.

VI

In case of sea-ice heterogeneous pixels, Tb are deduced as:

Tb=fr_ice.Tb_ice + (1-fr_ice).Tb_ocean

where fr_ice is the ice fraction determined following the same formalism as in (Zine, Boutin et al. 2007) for land fractions; Tb_ice and Tb_ocean are deduced from fresnel equations using ε given in IIA.1 and II.A.2. SST is taken equal to 2°C and ice temperature equal to -10°C. We consider a linear boundary between ice and ocean and the retrieval performed for pixels spaced every 4 km along a line perpendicular to this boundary (Figure 4).
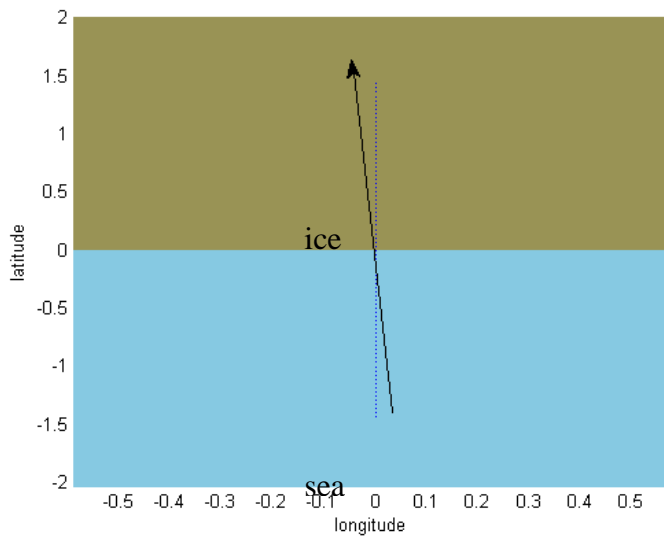
Figure 4 : Sea-Ice heterogeneous pixels : configuration of academic case. Retrievals are performed every 4km along grid nodes perpendicular to sea-ice boundary (blue points). Arrow represents sub-satellite track.

In order to look at the effect of wind speed variability, Tb were simulated with the direct model including the roughness contribution for SST of 20°C, SSS of 35psu and wind speed varying between 0 and 10m/s, while a flat sea is assumed in the retrieval (see below). The effect of a bias on SST was investigated at 0°C and 20°C with biases ranging between 0°C and 10°C.

In order to simulate a systematic bias in image reconstruction or coming from a drift of Noise Injection Radiometer, we add constant biases to modelled Tb with the flat sea model.

The retrieval is performed from these theoretical Tb after adding (or not) them a gaussian noise (1.5K) in order to look at the effect of radiometric noise and adding a random noise (1.5°C) on surface temperature. Retrievals are performed assuming homogeneous ocean pixels and a flat sea; a priori surface temperature is taken equal to noisy SST (even in case of mixed sea-ice pixel in order to simulate unexpected presence of ice).

VII

Semi-realistic retrievals:

In order to look at the effects of biases over various oceanic conditions, we perform retrievals over 462 selected pixels along a semi-orbit crossing the Pacific Ocean (Figure 5).
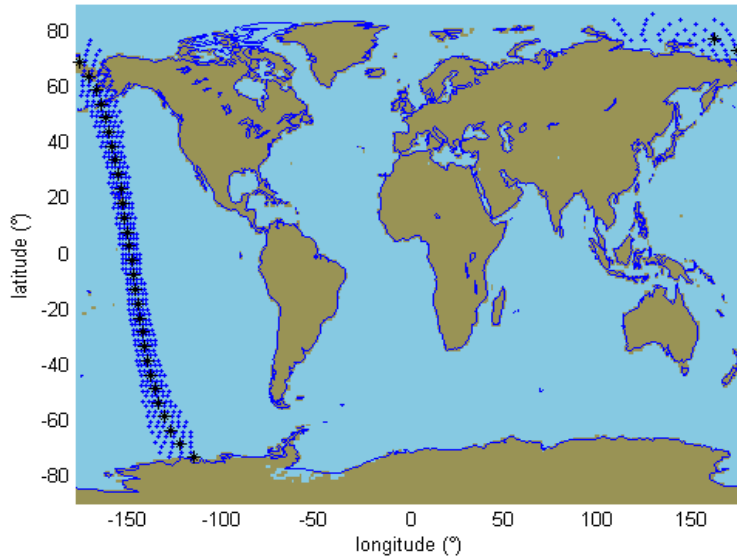
Figure 5 : Location of pixels used in retrievals in the semi-realistic case (stars represents sub-satellite track).

Data sources for SSS retrieval simulations are:

- for SSS: monthly climatological 1° Levitus field (January month) (Antonov, Levitus et al. 1998)

- for SST: weekly 1° Reynolds analysis (30decembre 2001-5janvier 2002) (Reynolds and Smith 1994)

- for wind components: daily 1° QSCAT map (02 Janvier 2002) generated from JPL-nudge level 2 wind product (25km resolution) using a simple objective analysis (Boutin and Etcheto 1997).

- for Total Electronic content (TEC): International Reference Ionosphere (Floury pers. comm.) years 1989, January.

with one simulated half orbit over the central Pacific ocean.

The selected data sets for the simulations are roughly representative of geophysical conditions encountered at global scale (see Table 1).

	Global ocean		Simulated SMOS ascending orbit	
	mean	standard deviation	mean	standard deviation
SSS (psu)	34.67	1.56	34.84	0.89
SST (K)	291.37	9.95	294.31	6.71
wind speed (m.s^{-1})	7.87	3.00	6.77	2.02

VIII

Table 1: Mean and standard deviation of distributions of SSS, SST and wind speed selected for the simulations and over the global ocean

Tb entering in the retrieval are simulated with all contributions described in section 2 in the direct model; a realistic Gaussian radiometric noise is added (see (Zine, Boutin et al. 2007) for a complete description).

Acard is retrieved, either assuming a flat sea and neglecting galactic noise reflection (minimalist model) or taking into account all contributions.

Results

Heterogeneous sea-ice pixels:

The retrieved Acard is very sensitive to the ice fraction present in the pixel (Figure 6, top). Retrieved Acard are much more noisy over the ocean (Acard error equal to 2) than over the ice (Acard error equal to 0.06) as the accuracy of Acard deteriorates as Acard increases (Waldteufel, Vergely et al. 2004). In case of almost pure pixel (sea fraction or ice fraction between 0.9 and 1) surface temperature is very well constrained by the retrieval: even in case of pure ice pixel, retrieved temperature is close to 263K (true value) while the retrieval was initiated with a temperature of 275K (Figure 6, middle). The presence of heterogeneous ice-ocean pixels is clearly demonstrated by low Acard values, very low surface temperature, and anomalously high Chi2 values (above 1.4) (Figure 6, bottom). The latter is a consequence of the radiative model being non linear ; for a mixed pixel, the retrieval attempts to adjust measured Tb using a "mean" dielectric constant, whereas Tb is actually the sum of two Tb estimated using two dielectric constants). Hence the quality of the fit deteriorates, as illustrated on Tb at the antenna level weighted by the antenna gain, adjusted over a mixed and pure pixel (Figure).

It is interesting to note that maximum of Chi2 is observed for sea fractions around .8 and .2. In cases where sea and ice fractions are close to 0.5, the best indicator of the presence of ice (in addition to Acard) is the surface temperature.

IX
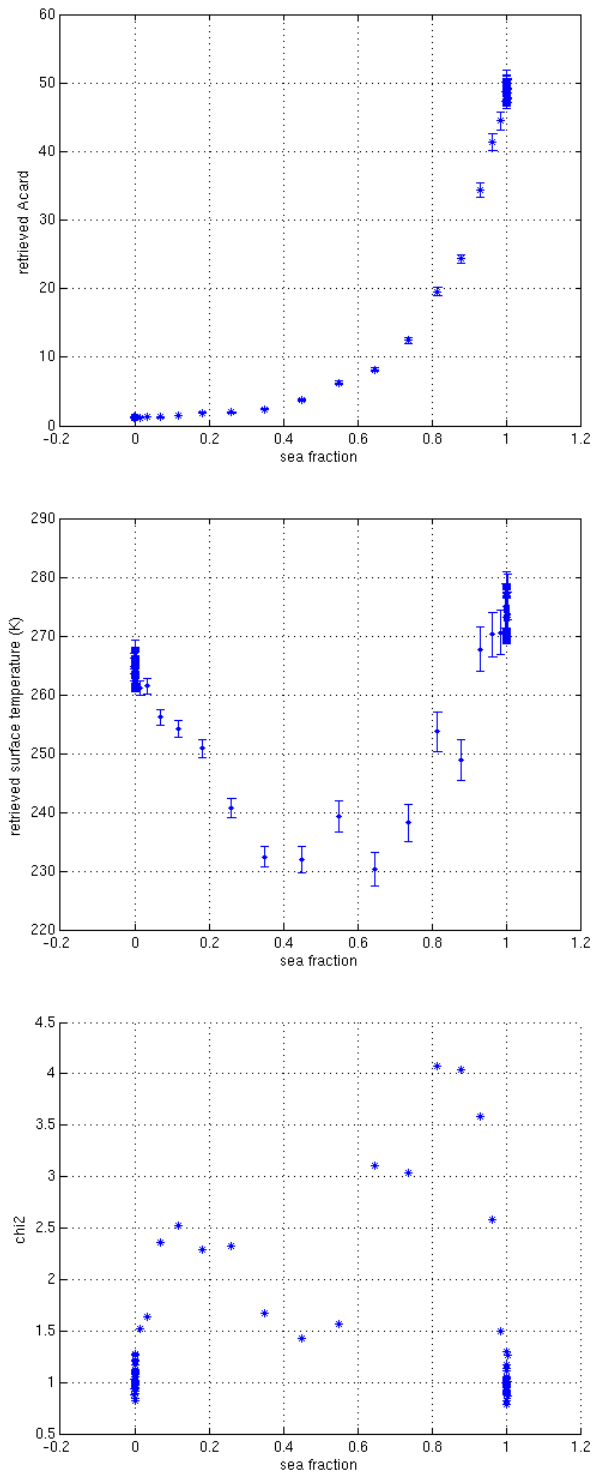
Figure 6: Top) Retrieved Acard as a function of sea-ice fraction. Middle) Retrieved surface temperature Bottom) Chi2 as a function of sea-ice fraction.

X
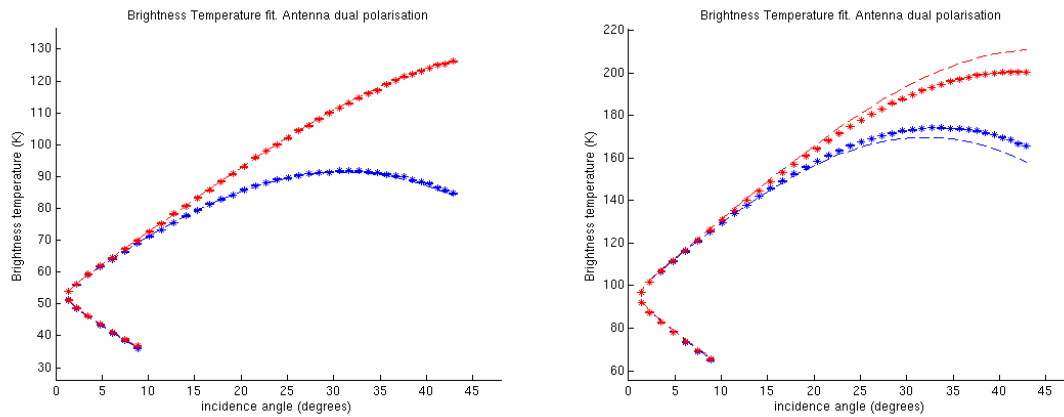
Figure7: Tb adjustement after retrieval of Acard on left)pure ocean pixel; right) mixed ocean-ice pixel(sea fraction=0.4). Radiometric noise has been taken very low (0.1K) in order to better see the adjustment. Crosses: true Tb, line : fitted Tb

Sensitivity of 'effective' pseudo-dielectric constant to geophysical variability and radiometric biases:

Academic case

A 1m/s wind speed variation is roughly equivalent to 0.7 unit bias on 'effective' Acard (Figure 8 top); in case a low noise is put on Tb, the flaw due to the assumption of a flat sea is clearly detectable on Chi2 value (Figure 8 middle). However, in case a more realistic noise (1.5K) is put on Tb, the flaw is no longer detectable on Chi2 (Figure 8 bottom); thence the bias will be detectable on individual retrievals only if the Acard bias is larger than the error on retrieved Acard (typically 2 units over the ocean) e.g. if the wind speed bias is larger than 3.5m/s. Lower biases could be detectable only on averaged Acard.

Retrievals performed with a bias on SST show that the bias on 'effective' Acard is weak (always less than 0.2units per degrees of SST bias; not shown) and greatly depends on SST value; in case a noise is put on Tb, the flaw due to a SST bias is not detectable on Chi2 nor Acard values.

In case a bias is put on Tb (as it could arise from a radiometer drift or from an imperfect knowledge of mean galactic noise impacting the pixel), retrieved Acard is biased by about 1.2unit per Kelvin of Tb bias (not shown). However, when a realistic noise (1.5K) is put on Tb, biases smaller than 5K are not detectable from chi2 values; above 5K, chi2 is slightly overestimated (chi2 above 1.14).

XI
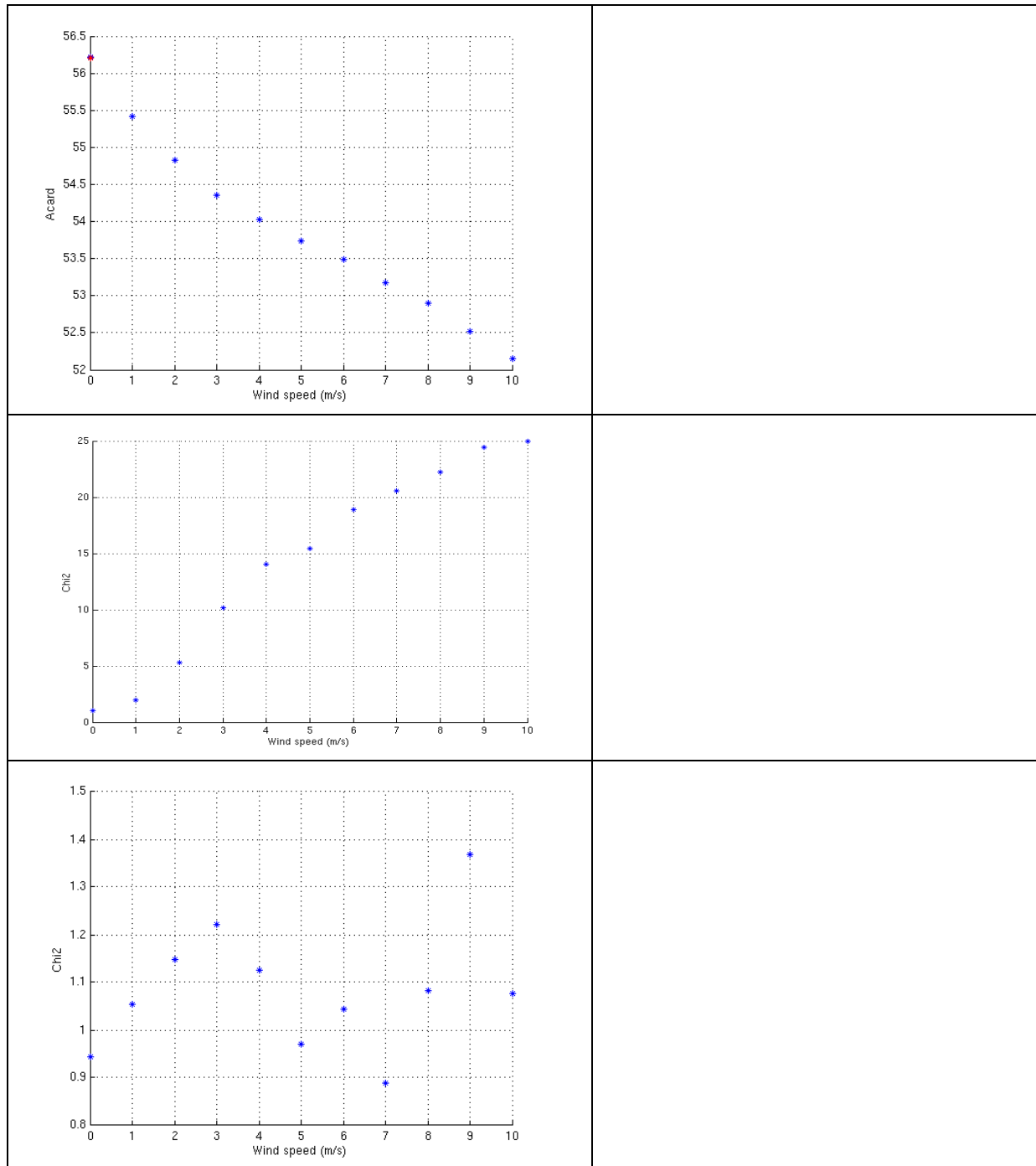
Figure 8: Top: Retrieved A_card as a function of wind speed bias; Red star is Acard value corresponding to true wind speed. noise on Tb is set to 0.1K in order to evidence biaises; middle: Chi2 as a function of wind speed bias ; noise on Tb set to 0.1K; bottom) Chi2 as a function of wind speed bias with a realistic noise put on Tb.

Semi_realistic case:

When roughness effect and galactic noise are not taken into account, 'effective' Acard is low biased on average by 7 units (Figure 9, left) (Acard close to 1 on that figure correspond to

sea ice pixels) which is clearly above the noise on retrieved Acard over the ocean (typically 2 units). Chi2 parameter gives very poor information about flaws in the direct models as Chi2 simulated with the minimalist model is very close to Chi2 simulated with the whole model (Figure 9, right).
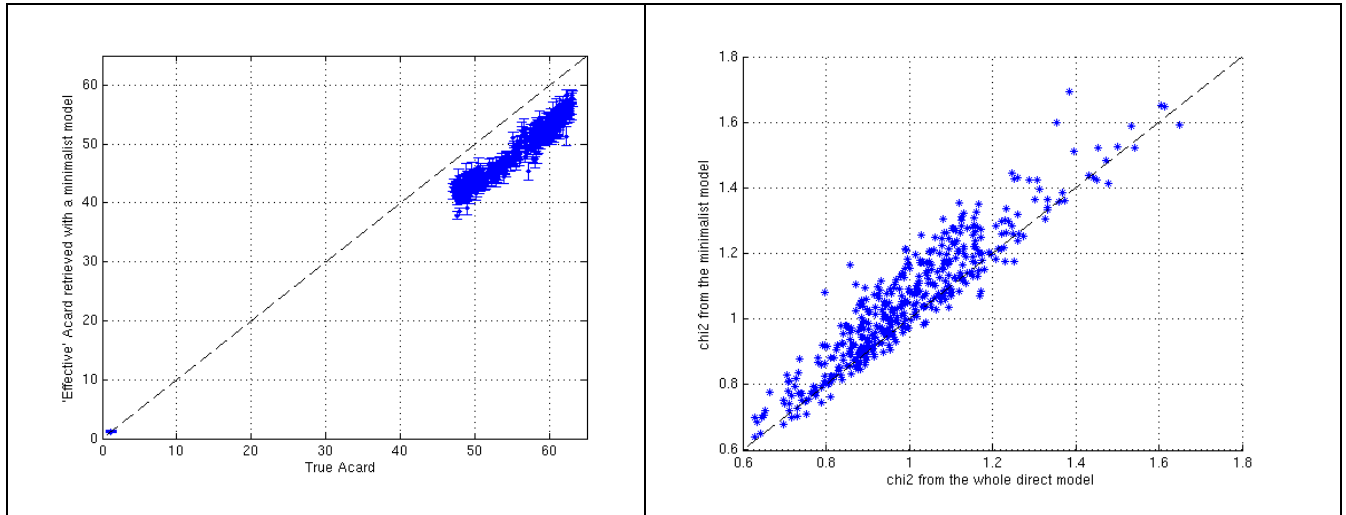
Figure 9: Left: Acard retrieved with a minimalist model (no roughness, no galactic noise) versus Acard retrieved with the whole direct model. Right) Chi2 of Acard retrieved with a minimalist model (no roughness, no galactic noise) versus Chi2 of Acard retrieved with the whole direct model.

Discussion and Conclusion:

In order to accurately retrieve SSS from SMOS measurements, it will be essential to well model the direct radiometric signal, characterize flaws coming from instrumental drifts and from auxiliary parameters inaccuracies and to detect the presence of surface heterogeneities in pixels like presence of sea ice.

A main difficulty for SMOS calibration/validation exercise will arise from the processing and the analysis of a great number of multiangular measurements performed in each pixel. In this paper we concentrate on the use of a pseudo-dielectric constant parameter to synthesize information contained in multiangular Tb. The retrieval of this parameter could be easily processed in parallel to the SSS retrieval and this parameter could be easily delivered together with retrieved SSS, contrary to all Tb measurements.

In order to stay as close as possible to the measurements and not to introduce errors coming from imperfect auxiliary parameters or from imperfect direct models, we choose to make the retrieval of Acard assuming a flat sea surface; in addition, given the linearity between SSS

and Acard, retrieving Acard with the whole direct model is rather equivalent to computing Acard from SSS and SST retrieved with the whole direct model. Given that the flat sea assumption is not valid over much of the ocean, the parameter such retrieved is biased towards high values (see Figure 9): on the half orbit average, Acard is biaseb by 7.3 units when neglecting galactic noise and wind roughness. Therefore, it rather represents an 'effective' pseudo-dielectric constant. As with the addition of a roughness effect Tb no longer follows a Fresnel law, Chi2 values are as large as 1.4, while there is not necessary anomalies in the measurements nor in the direct model.

Without any correction for geophysical effects, 'effective' Acard values should only allow to detect anomalies leading to very large positive Tb (e.g. mean bias on Tb larger than typically 10K) or to negative Tb (since all geophysical effects neglected in 'effective' Acard retrieval add a Tb signal). In order to use 'effective' Acard for detecting other anomalies, it will be first necessary to correct it for geophysical effects. From the dependency of 'effective' Acard with wind speed seen in academic tests (Figure 8, top), we anticipate that it should be possible to find the appropriate correction by fitting 'effective' Acard with geophysical parameters (like wind speed), after sorting Acard retrievals by dwell lines, eliminating large galactic noise events flagged in SMOS data product and averaging Acard over numerous retrievals to decrease noise. These empirical fits should also allow to validate the direct model used to retrieve salinity: if the model is correct, the dependencies of 'effective' Acard obtained by direct comparison with geophysical variables should be very close to the dependencies of the differences between 'effective' Acard and Acard computed from SSS and SST retrieved using the complete direct model, with geophysical variables. Additional constraint could come from comparisons with Acard deduced from SSS and SST independent of SMOS retrieval (e.g. climatology).

In presence of a sea-ice heterogeneous pixel, when proportion of ice or of ocean is larger than 10%, 1)Acard decreases by more than 15 units with respect to the expected ocean value, 2) retrieved surface temperature decreases by more than 10°C with respect to the true value; 3) the quality of Acard retrieval strongly deteriorates: Chi2 parameter becomes larger than 1.4 thus being in most cases larger than the one due to the computation of an 'effective' Acard. All these indices should allow to retrieve a raw sea-ice fraction from 'effective' Acard in cold waters; in case roughness effects are corrected for, presence of sea ice could be flagged from Acard and Chi2 values even in pixels containing 5% of ice.

XIV

Given the above discussion, it is recommended to perform the retrieval of an 'effective' Acard in the SMOS processing chain over the ocean, in parallel to the SSS retrieval, as it appears as a powerful tool for testing and assessing the validity of SMOS measurements and retrieved parameters.

References:

Antonov, J. I., S. Levitus, et al. (1998). World Ocean Atlas 1998. N. A. N. 27**: 166pp.

Arnal, E. M., E. Bajaja, et al. (2000). "A high sensitivity HI survey of the sky at d<=-25°." Astron. Astrophys. Suppl. Series **142**: 35-40.

Boutin, J. and J. Etcheto (1997). "Long term variability of the air-sea CO_2 exchange coefficient: Consequences for the CO_2 fluxes in the equatorial Pacific Ocean." Global Biogeochemical Cycles **11**: 453-470.

Boutin, J., J. Font, et al. (2004). Retrieval concept and Architecture Document for Sea Surface Salinity Retrieval for SMOS Mission, ESA**: 68.

Boutin, J., J. Font, et al. (2005). Sea Surface Salinity Retrieval for SMOS Mission Final Report, ESA**: 93.

Camps, A., J. Font, et al. (2004). "The WISE 2000 and 2001 Field Experiments in Support of the SMOS Mission:Sea Surface L-Band Brightness Temperature Observations and Their Application to Sea Surface Salinity Retrieval." IEEE Transactions on Geoscience and Remote Sensing **42**: 804-823.

Delahaye, J. Y., P. Golé, et al. (2002). "Calibration error of L-band sky-looking ground-based radiometers." radio science **37**: 10.1029/2001RS002490.

Dinnat, E., J. Boutin, et al. (2003). "Issues concerning the sea emissivity modeling at L-band for retrieving surface salinity." Radio Science **38, No. 4**: 10.1029/2002RS002637.

Durden, S. L. and J. F. Vesecky (1985). "A Physical Radar Cross-Section Model for a Wind-Driven Sea with Swell." IEEE Journal Of Oceanic Engineering **OE-10**: 445-451.

Etcheto, J., E. Dinnat, et al. (2004). "Wind speed effect on L-band brightness temperature inferred from EuroSTARRS and WISE 2001 field experiments." IEEE Transactions on Geoscience and Remote Sensing **42**: 2206-2214.

Etcheto, J., E. Dinnat, et al. (2003). Comparison of EUROSTARRS and WISE measurements with sea surface emissivity models. First Results Workshop on EuroSTARRS, WISE, LOSAC campaigns.

Hartmann, D. and W. B. Burton (1997). <u>Atlas of galactic neutral hydrogen</u>, Cambridge university press, New York.

Hollinger, J. P. (1971). "Passive Microwave Measurements of Sea Surface Roughness." <u>IEEE Transactions on Geoscience Electronics</u> **GE-9**: 165-169.

Kelly, K. A., S. Dickinson, et al. (2001). "Ocean currents evident in satellite wind data." <u>Geophysical Research Letters</u> **28**: 2469-2472.

Klein, L. A. and C. T. Swift (1977). "An improved model for the dielectric constant of sea water at microwave frequencies." <u>IEEE Transactions on Antennas and Propagation</u> **AP-25**: 104-111.

Le Vine, D. M. and S. Abraham (2002). "The Effect of the Ionosphere on Remote Sensing of Sea Surface Salinity From Space: Absorption and Emission at L Band." <u>IEEE Trans Antennas and Propagation</u> **40**(4): 771-782.

LeVine, D. M. and S. Abraham (2004). "Galactic noise and passive microwave remote sensing from space at L-Band." <u>IEEE Transactions on Geoscience and Remote Sensing</u> **42**: 119-129.

Liebe, H. J., G. A. Hufford, et al. (1993). <u>Propagation modelling of moist air and suspended water/ice particles at frequencies below 1000GHz</u>. AGARD 52nd Specialists meeting of the Electromagnetic Wave Propagation Panel, Palma de Mallorca, Spain.

Liu, W. T. and W. Tang (1996). Equivalent neutral wind. Pasadena, Calif., Jet Propul. Lab.**:** 8.

Marquardt, D. W. (1963). "An algorithm for least-squares estimation of non-linear parameters." <u>J. Soc. Ind. Appl. Math</u> **11**: 431-441.

Nedeltchev, N. M., J. C. Peuch, et al. "Polarimetric remote sensing of sea ice-from theory to practice." <u>IEEE Transactions on Geoscience and Remote Sensing</u>: 2182-2184.

Reich, P. and W. Reich (1986). "A radio continuum survey of the northern sky at 1420 MHz." <u>Astron. Astrophys. Suppl. Ser.</u> **63**: 205-292.

Reynolds, R. W. and T. M. Smith (1994). "Improved global sea surface temperature analyses using optimum interpolation." <u>Journal of Climate</u> **7**: 929-948.

Sasaki, Y., I. Asanuma, et al. (1987). "The dependence of sea-surface microwave emission on wind speed, frequency, incidence angle and polarization over the frequency range 1 to 40 GHz." <u>IEEE Transactions on Geoscience and Remote Sensing</u> **GE-25**: 138-146.

Schodlok, M. P., H. H. Hellmer, et al. (2006). "Weddell Sea iceberg drift: Five years of observations." <u>J. Geophys. Res.</u> **111, C06018**: doi:10.1029/2004JC002661.

XVI

Swift, C. T. (1974). "Microwave radiometer measurements of sea surface roughness." IEEE Transactions on Geoscience Electronics **9-no7**: 641-653.

Vine, D. L., S. Abraham, et al. (2004). "Comparison of Measured Galactic Background Radiation at L-Band with Model." IEEE Transactions on Geoscience and Remote Sensing: 1930-1932.

Waldteufel, P. and G. Caudal (2002). "Off-axis Radiometric Measurements; Application to Interferometric Antenna Designs." IEEE Transactions on Geoscience and Remote Sensing **40(6)**: 1435-1439.

Waldteufel, P., N. Floury, et al. (2004). "Ionospheric effects for L-Band 2-D interferometric radiometry." EEE Trans. Geosci. Remote Sens. **42**(1): 105-118.

Waldteufel, P., J. L. Vergely, et al. (2004). "A modified cardioid model for processing multiangular radiometric observations." IEEE Transactions on Geoscience and Remote Sensing **42**: 1059-1063.

Yueh, S. H., R. West, et al. (2001). "Error sources and feasibility for microwave remote sensing of ocean surface salinity." IEEE Transactions on Geoscience and Remote Sensing **39**: 1049-1060.

Zine, S., J. Boutin, et al. (2007). "Issues about retrieving sea surface salinity in coastal areas from SMOS data." IEEE Transactions on Geoscience and Remote Sensing **45**(7): 10.1109/TGRS.2007.894934.

ANNEX-3: Technical note on the calculation of Stokes 1 parameter in full polarisation mode

Introduction

The purpose of this technical note is to propose strategies which could be used for the calculation of Stokes 1 from the MIRAS full polarization measurement mode.

In next section, the sequence of available measurements in full polarization mode is described. The following section we present ways of exploiting this sequence and shows various possible strategies for computing Stokes 1. Finally the Stokes 1 radiometric noise computation is explained.

Polarisation sequence in full polarisation mode

Recalling dual polarization mode, correlations are obtained of antenna pairs in the same polarization state. This acquisition mode only allows deriving XX and YY brightness temperature maps from correlation products.

In addition to measuring temperatures in polarization XX and YY, full polarization mode includes measuring the cross-correlation of antenna pairs in different polarization states. In the latter case, three temperature maps are obtained (for one snapshot): XX or YY, XY and YX.

A cycle in full polarization mode exists of 26 steps spread over 4 snapshots:
1. step 1: XX measurements, as in dual pol mode
2. repeat 4 times:
   - step 2: YY, XY and YX measurements
   - step 3: YY, XY and YX measurements
   - step 4: YY, XY and YX measurements
3. step 1': YY measurements, as in dual pol mode
4. repeat 4 times:
   - step 2': XX, XY and YX measurements
   - step 3': XX, XY and YX measurements
   - step 4': XX, XY and YX measurements

Snapshot	Step	arm pol	measurements	
1	1	XXX	XX	

I

2	2	YYX	YY, XY, YX	} repeated 4 times
	3	XYY	YY, XY, YX	
	4	YXY	YY, XY, YX	
3	1'	YYY	YY	
4	2'	XXY	XX, XY, YX	} repeated 4 times
	3'	YXX	XX, XY, YX	
	4'	XYX	XX, XY, YX	

These steps concern MIRAS acquisitions and not the TB product itself. The latter one is an aggregation of information coming from several acquisitions.

Figure 1 shows the sequence of polarization measurements and the different steps.
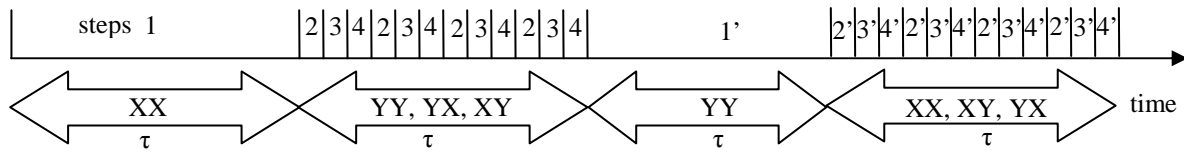
Figure 4 : Steps in one full polarization mode cycle.

In steps 2, 3 and 4, one third of the (u,v) domain is covered at each step for YY, XY and YX polarizations. At the end of the three steps (steps 2, 3 and 4), the full (u,v) domain is covered for YY, XY and YX polarizations.

Figure 2 presents, for a configuration close to that of SMOS, the first four steps.

If τ is the nominal integration time equal to 1.2 s, during one full polarization mode cycle the different steps have the following duration:

- step 1 : τ
- step 2 : 4 x $\tau/12 = \tau/3$
- step 3 : 4 x $\tau/12 = \tau/3$
- step 4 : 4 x $\tau/12 = \tau/3$
- step 1' : τ
- step 2' : 4 x $\tau/12 = \tau/3$
- step 3' : 4 x $\tau/12 = \tau/3$
- step 4' : 4 x $\tau/12 = \tau/3$

During step 1, on the full (u,v) domain, XX is observed during τ

During the step 2, 3 and 4, on full (u,v) domain, YY is observed during $\tau/3$, XY during $\tau/3$ and YX during $\tau/3$.

Because of the hermitian property XY=YX*, Stokes 3 and 4 are observed during $2\tau/3$ during one cycle.

Thus, during the steps 1, 2, 3, 4, 1', 2', 3', 4', on the full (u,v) domain and for the period 4 τ (complete cycle), this yields:

- XX is observed during $\tau +\tau/3=4\tau/3$
- YY is observed during $\tau +\tau/3=4\tau/3$
- XY is observed during $\tau/3 +\tau/3=2\tau/3$
- YX is observed during $\tau/3 +\tau/3=2\tau/3$

II

Consequently, during one complete cycle, XX, YY and XY temperatures are obtained with the same integration time.

In the L1c product, after aggregation, we obtain for four consecutive snapshots representing a full cycle:
- snap1: TB_XX1 (real number) -> corresponds to step 1
- snap2: TB_YY2 (real number) -> corresponds to step 2, 3 and 4 (repeated 4 times)
- snap2: TB_XY1 (complex number) -> corresponds to step 2, 3 and 4 (repeated 4 times)
- snap3: TB_YY1 (real number) -> corresponds to step 1'
- snap4: TB_XX2 (real number) -> corresponds to step 2', 3' and 4' (repeated 4 times)
- snap4: TB_XY2 (complex number) -> corresponds to step 2', 3' and 4' (repeated 4 times.

III
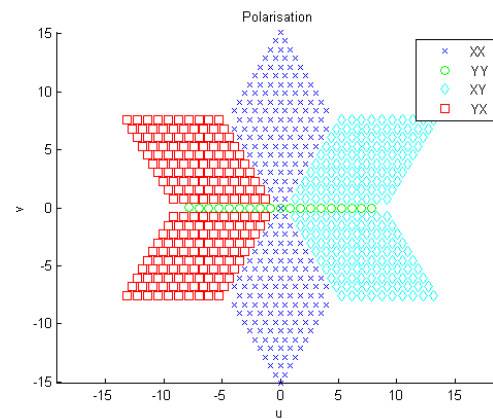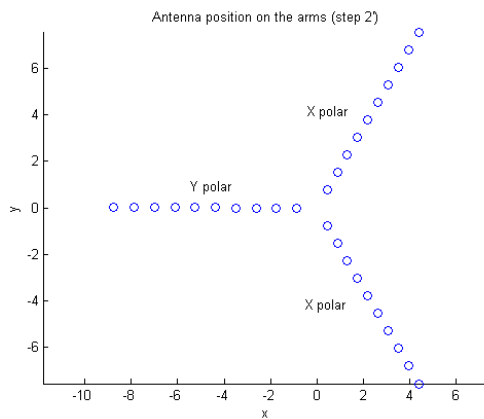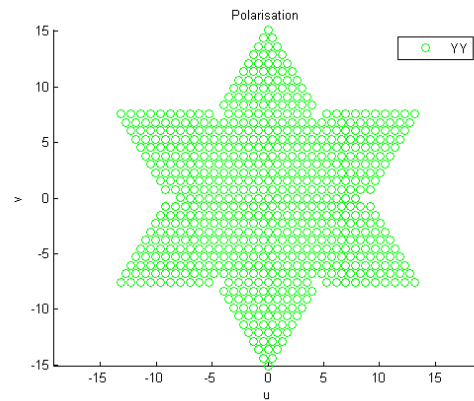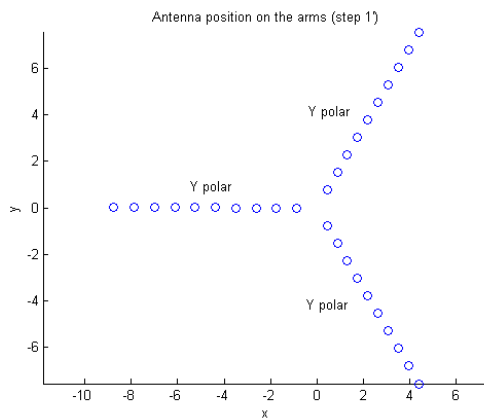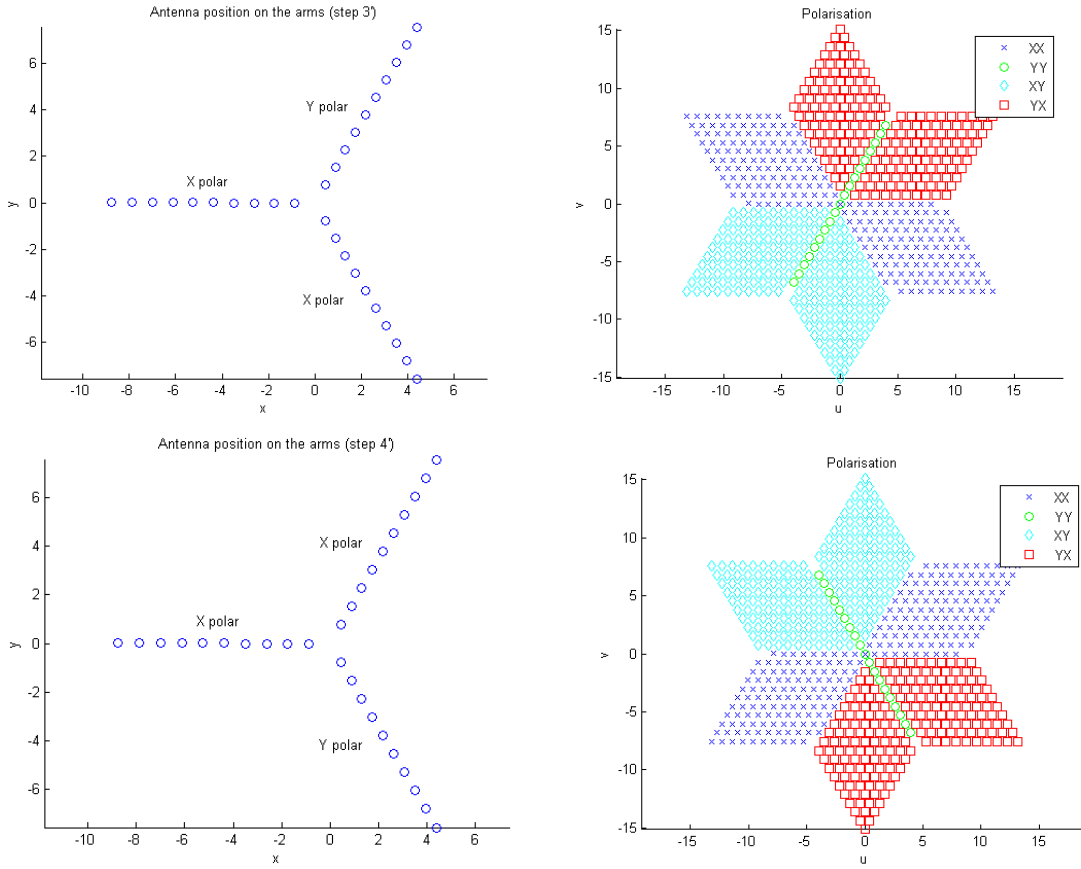
Figure 5 : Four steps (1',2',3' and 4') in full polarization mode. Top: the receivers of the three arms switch to Y polarisation. In the corresponding visibility domain, all baselines are YY. Middle and bottom: the receivers of two arms are in opposite polarisation as the receivers of the third arm. In such cases, baselines are XX, YY, XY or YX.

Stokes 1 computation strategy

In section 2, we noted that:

- A full cycle is described on a 4τ integration time, contrary to dual polarization mode which is described on a cycle of 2τ.
- In contrast to dual polarization, polarizations XX and YY (integrated over a period of τ) are never adjacent but are always separated by τ.
- The radiometric noise associated to XX and YY varies according to the integration time by a factor $\sqrt{3}$.

Three different strategies are suggested to compute Stokes 1:
1. to use measurements from a full cycle (i.e. four snapshots),
2. to use measurements coming from step 1 and 1' only,
3. to use successive measurements without taking into account the cycle which is associated to them.

1. Use of measurements of a full cycle.

IV

In this strategy, all the TB's in XX and YY polarizations are added during one full cycle in order to obtain a value of Stokes 1 per cycle. In the same way the Stokes 1 radiometric errors (quadratic sum) are obtained (Figure 6).
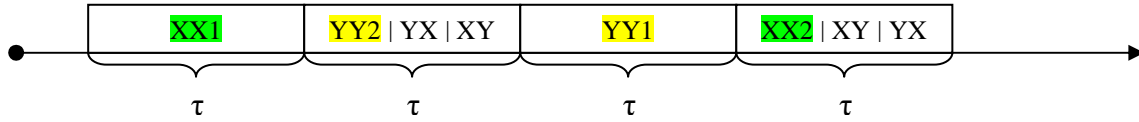
Figure 6: All measurements in XX pol (green) and all in YY pol (yellow) are summed up to yield Stokes 1.

In case of the absence of one measurement, either the measurements of the whole cycle are not processed (and then discarded), or else they are processed as follows:
- If the missing measurement is TB_XX2 or TB_YY2, only TB_XX1 and TB_YY1 are used.
- If the missing measurement is TB_XX1 or TB_YY1, only TB_XX2 and TB_YY2 are used.

In the case of the absence of two measurements, either the measurements of the whole cycle are discarded, or they are processed as follows:
- If the two missing measurements are TB_XX2 and TB_YY2, only TB_XX1 and TB_YY1 are used.
- If the two missing measurements are TB_XX1 and TB_YY1, only TB_XX2 and TB_YY2 are used.
- If the two missing measurements are TB_XX1 and TB_YY2 or TB_XX2 and TB_YY1, measurements of the whole cycle are not processed.

In case of one or more measurements missing from one whole cycle, a test could be implemented to decide whether different measurements can be added up:
A comparison between TB_XX1 and TB_XX2, TB_YY1 and TB_YY2 or TB_XX1+TB_YY1 and TB_XX2+TB_YY2 could be done. If the comparison yields results below a certain threshold the considered cycle (or pair of measurements) is rejected.

2. Use of measurements from step 1 and 1'.

In this strategy, only step 1 and step 1' measurements (XX1 and YY1) are used in order to compute Stokes 1 without using snapshots in cross polarisation mode (Figure 7). It allows adding measurements which have the same origin than in dual polarisation mode.
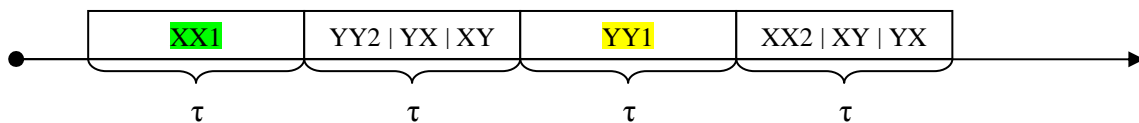

Figure 7: Only step 1 measurement (XX pol in green) and successive step 1' measurement (YY pol in yellow) are summed up to yield Stokes 1.

V

If one measurement is missing (step 1 or step 1'), the cycle could be shifted in order to loose the less possible of measurements.

3. Use of successive measurements

In this strategy, we do not consider a full cycle as the time basis of the measurement aggregation.

XX and YY are measurements separated by a maximal time interval between them. If the time interval between XX and YY or YY and XX is larger than some threshold, Stokes 1 is not calculated (Figure 8).
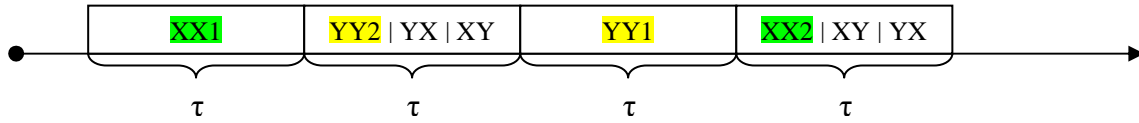
Figure 8: In this example, only successive XX and YY measurements (not necessarily from the same cycle) are selected to yield Stokes 1.

This strategy is similar to what is done in dual polarization mode, except that polarizations XX and YY can have a very different radiometric noise, depending from which step they originate (for instance, TB_XX1 could be combined with TB_YY2 and YY1 with XX2). No overlapping is considered.

Stokes 1 radiometric noise computation.

For all strategies, the Stokes 1 radiometric noise is computed using XX and YY radiometric noises added in a quadratic way:

$\sigma_{ST1} = \sqrt{\sigma_{XX1}^2 + \sigma_{YY2}^2 + \sigma_{XX2}^2 + \sigma_{YY1}^2}$, in nominal case of strategy 1

$\sigma_{ST1} = \sqrt{\sigma_{XX1}^2 + \sigma_{YY1}^2}$, in nominal case of strategy 2

$\sigma_{ST1} = \sqrt{\sigma_{XX1}^2 + \sigma_{YY2}^2}$ or $\sigma_{ST1} = \sqrt{\sigma_{XX2}^2 + \sigma_{YY1}^2}$, in nominal case of strategy 3

where $\sigma_{XX1}, \sigma_{XX2}, \sigma_{YY1}$ and σ_{YY2} are respectively the radiometric noises of XX1, XX2, YY1 and YY1 coming from L1c product.

Because no overlapping is considered, no error correlations are expected between successive Stokes 1.

References

« SMOS L1 Full Polarisation Data Processing ». ref : SO-TN-DME-L1PP-0024. Issue: 1.6. Date : 16/07/07. ESA/DEIMOS.

VI

PhD thesis: « Calibration, Validation and Polarimetry in 2D Aperture Synthesis: Application to MIRAS » , Serni Ribo Vedrilla, Univesitat Politecnica de Catalunya, 05/05

ANNEX-4: Secondary algorithm – empirical neural network

The following outline proposal for an empirical neural network is retained in this ATBD for future reference. There will not be an implementation of the algorithm in the Level 2 OS processor before launch.

1 Physics of the problem

One of the critical issues for SMOS ground segment is the inversion algorithm which can be used to retrieve the sea surface salinity (SSS) from the SMOS brightness temperatures. Most of the scientists have chosen an inversion processing based on a forward model, developed with theoretical or semi empirical models. This forward model allows simulating brightness temperatures, given a triplet of geophysical parameters (sea surface salinity, sea surface temperature and wind speed). The iterative method tries to minimize the cost function between the SMOS measured brightness temperatures and the simulated ones. One of the main drawbacks of such a method is the use of a forward model. We know that this model does not reproduce perfectly all the physics, especially the influence of the sea surface roughness (foam effects, swell…). All the studies performed with simulated data give errors which meet the GODAE requirements but, all the scientific community acknowledge that, once SMOS in-flight, the retrieval algorithm based on a forward model will provide inaccurate salinities. The improvement of the salinity retrieval can be performed only by improvement of the physics modelling in the forward model. This task represents a large amount of work and can not be achieved in reasonable delays in order to release SMOS products to the users, at the end of the commissioning phase.

In order to estimate realistic SSS, it could be useful to develop an empirical inversion algorithm. For that purpose, an algorithm using neural network methods could be built with SMOS data co-located with in-situ salinities. The neural network (NN) approach is well suited for such retrieval because of the large amount of brightness temperatures used for one retrieved SSS [1].

The aim is to retrieve salinity (*SSS*) for each simple grid point, based on the brightness temperatures Tb_i^{meas} available at all incidence angles θ_i, $i=1,Nm$ in the surface reference and with auxiliary data described by the vector **P** of size Np.

$$SSS = g(Tb_i^{meas}, \mathbf{P}), \quad i = 1, Nm \qquad (1)$$

The vector **P** will contain, at least, the sea surface temperature (SST), the wind speed (WS) and the salinity (SSS) plus all the sea surface descriptors available in the L1 processor. The aim is to describe the functional *g* with the NN algorithm. The error made on the retrieved SSS is also provided.

The algorithm is given for the SSS retrieval and the associated error but the number of retrieved parameters can be increased later.

2 Mathematical description of the algorithm

For the salinity retrieval, we use the multiplayer perceptron (MLP) network which is a nonlinear mapping model composed of parallel processors called "neurons". These neurons are organised in distinct layers. The first layer receives the input data X (input layer). The final layer (output layer) provides the network response Y. The intermediate layers are called the "hidden layers". Any neurons i and j between two consecutive layers are connected with a synaptic weight w_{ij}. A transfer function f is associated to each neuron and, for each neuron i of the hidden layers, the output s_i is computed taking into account the output of the precedent layer j, containing n neurons:

$$s_i = f(\sum_{j=1}^{n} w_{ij} s_j) + b_i \qquad (2)$$

Equation (3) gives the general formulation for the computation of the response Y, given an input vector X of size p, in the case of a single hidden layer, formed by n neurons.

$$Y = \sum_{i=1}^{n} W_i f_i \left(\sum_{j=1}^{p} W_{ij} X_j + b_{i0} \right) + b_0 \qquad (3)$$

b_{i0} are the bias values associated to the n neurons of the hidden layer and b_0 the bias value associated to the single output neuron.

In our case, X is a vector containing the input TBs and the vector P. Y is a scalar containing the retrieved SSS. The NN algorithm will be generalised for a MLP of several hidden layers.

One specific feature in the SMOS processing is that the values of the incidence angles will vary from a grid point to another, without any repetitive configuration. The NN algorithms cannot cope with such input variations and need always fixed inputs. Therefore, before doing the NN retrieval, a first step is performed in order to interpolate the TBs on fixed incidence angles.

The objective of this step is to transform the series of TBs corresponding to the grid point angles $\theta_i, i = 1, Nm$ into a series of TBs corresponding to the angles $\alpha_j, j = 1, Ns$, so that they are used as inputs of the network [2]. The interpolation method used is a locally weighted polynomial regression of order p [3]. It also acts as a smoother, which will be useful to reduce the high noise level on the SMOS TBs.

For every interpolation angle α, we search for the regression coefficients β_k, $k=1,p$, by minimizing the expression :

$$J = \sum_{i=1}^{Nm} \left(Tb^{meas}(\theta_i) - \left(\sum_{k=0}^{p} \beta_k \cdot (\theta_i - \alpha)^k \right) \right)^2 \cdot K\left(\frac{\theta_i - \alpha}{h} \right) \cdot I\left(\left| \frac{\theta_i - \alpha}{h} \right| \right)$$

Where:
- $Tb^{meas}(\theta_i)$ is the grid point SMOS brightness temperature (H-pol. or V-pol. or H+V pol) for the angle θ_i.
- K is a kernel function which assigns weights to each point. Here, we chose the Epanechnikov Kernel :
$$K(t) = \frac{3}{4}(1 - t^2) \text{ for } -1 < t < 1$$

II

$K(t) = 0 \qquad$ for $|t| \geq 1$

■ h is a positive real number, known as the bandwidth. It controls the smoothing procedure.

■ I is defined by :

$I(t) = 1$ for $0 \leq t \leq 1$

$I(t) = 0$ for $t > 1$

This means that we only take into account the angles θ_i that are in the interval [α-h ; α +h]. It is more convenient to work with matrix notation and the minimisation of J can be written as:

$$\underset{\beta}{Min} \left(\mathbf{Y} - \mathbf{X\beta}\right)^T \mathbf{W}\left(\mathbf{Y} - \mathbf{X\beta}\right)$$

where $\mathbf{W} = \text{diag}\left\{K_{\mathbf{H}}(\mathbf{\theta_i} - \mathbf{\alpha})\right\}$ is the (Nm x Nm) matrix of the weights

$$K_{\mathbf{H}}(\mathbf{\theta_i} - \mathbf{\alpha}) = \frac{1}{h} K\left(\frac{\mathbf{\theta_i} - \mathbf{\alpha}}{h}\right) = \frac{3}{4h}\left[1 - \left(\frac{\mathbf{\theta_i} - \mathbf{\alpha}}{h}\right)^2\right] \quad \forall \theta_i \in \left[\alpha - h, \alpha + h\right]$$

$\mathbf{\beta} = (\beta_0, \beta_1, ..., \beta_p)^T$ is the vector of the polynomial coefficients which is equivalent to the estimate of the derivatives $\mathbf{\beta} = (Tb_{\text{int}}, Tb'_{\text{int}}, ..., \beta_{\text{int}}^{(p)})^T$

$\mathbf{Y} = (Tb_0^{meas}, Tb_1^{meas}, ..., Tb_{Nm}^{meas})^T$ is the vector of the grid point Tbs

and

$$\mathbf{X} = \begin{pmatrix} 1 & \theta_1 - \alpha & \cdots & (\theta_1 - \alpha)^p \\ 1 & \theta_2 - \alpha & \cdots & (\theta_2 - \alpha)^p \\ \vdots & \vdots & \vdots & \vdots \\ 1 & \theta_{Nm} - \alpha & \cdots & (\theta_{Nm} - \alpha)^p \end{pmatrix}$$

The solution vector $\widehat{\mathbf{\beta}}$ is provided by the weighted least squares theory and the first component containing the interpolated value for the TB for angle α is given by the following equation:

$$Tb^{\text{int}}(\alpha) = \widehat{\beta}_0 = \mathbf{e_1^T}\left(\mathbf{X^T W X}\right)^{-1}\mathbf{X^T W Y}$$

where $\mathbf{e_1^T}$ is the (p x 1) unit vector: $\mathbf{e_1^T} = (1,0,...0)$

Another specific feature is that the grid point can be seen by different series of incidence angles: one extreme is all the range between 0° and 60° for pixels originally located on the dwell line or just a few angles between 50° and 60° for pixels far away from the dwell line. In order to deal with such a wide range of situations, several NN algorithms are provided. Their number has been determined with a classification method and is defined in the external file describing the weights and biases for each NN algorithm.

III

The NN inversion consists in 4 major steps, which are performed for each grid point:
1. Choice of the NN algorithm.
2. Formation of the input vector with interpolated brightness temperatures at fixed incidence angles.
3. Retrieval from these interpolated TBs with the NN algorithm (SSS).
4. Retrieval from these interpolated TBs with the NN algorithm (SSS error).

STEP 0 - Acquisition of the algorithms description

Each algorithm is characterised by:

- A series of fixed incidence angles α_j^k, $k = 1, Nc$, $j = 1, Ns$

  Nc is the number of algorithms (or classes).
  Ns is the number of fixed angles. It is different for each algorithm and can vary from 1 up to 50.

- A series of bandwidth values h_j^k, $k = 1, Nc$, $j = 1, Ns$

- NN architecture and coefficients (Mean and Std values for the input/output normalisation, weights, biases).

STEP 1 - Determination of the class of the NN algorithm

For each grid point, the NN algorithm is chosen depending on the values of the minimum and maximum values of the incidence angle series (θ_{min}, θ_{max}) available for the grid point.

The class of the algorithm c is defined for the grid point characterised by (θ_{min}, θ_{max}) with the following test:

Find $c \in [1, Nc]$ such that:

α_1^c is the closest angle to θ_{min} and $\theta_{min} \geq \alpha_1^c$ and

α_{Ns}^c is the closest angle to θ_{max} and $\theta_{max} \leq \alpha_{Ns}^c$

STEP 2 - Calculation of the interpolated Tbs

For each fixed angle α_j, $j = 1, Ns$ of the algorithm c, the brightness temperature is calculated with the following equation:

$$Tb^{int}(\alpha) = \widehat{\beta}_0 = \mathbf{e_1^T}(\mathbf{X^T W X})^{-1}\mathbf{X^T W Y}$$

which can be written under the simplified form:

$$Tb^{int}(\alpha) = \widehat{\beta}_0 = \mathbf{e_1^T \Sigma X^T W Y}$$

where the matrix $\mathbf{\Sigma}$ is the inverted matrix of size (p+1,p+1) with elements σ_{ij}. The different steps are detailed below.

1. Calculation of matrix $\mathbf{X^T W X}$

Since it is a symmetric matrix, only the diagonal and upper elements need to be calculated.

We recall the equation for the calculation of the weight associated to each θ_i for a given α_j:

$$K_H(\theta_i - \alpha_j) = \frac{1}{h_j}K\left(\frac{\theta_i - \alpha_j}{h_j}\right) = \frac{3}{4h_j}\left[1 - \left(\frac{\theta_i - \alpha_j}{h_j}\right)^2\right],$$

$$\forall i = 1, Nm \quad \theta_i \in [\alpha_j - h_j; \alpha_j + h_j]$$

IV

2. Calculation of matrix Σ by inversion of the (p+1,p+1) matrix $\mathbf{X^T W X}$

The matrix $\mathbf{X^T W X}$ will be either a (2x2) or a (4x4) matrix (p=1 or p=3).

3. Calculation of Tb at angle α with $Tb^{\text{int}}(\alpha) = \hat{\beta}_0 = \mathbf{e_1^T \Sigma X^T W Y}$

$$Tb^{\text{int}}(\alpha) = \sigma_{11}\sum_{i=1}^{Nm} K_H(\theta_i - \alpha)\cdot Tb(\theta_i) + \sigma_{12}\sum_{i=1}^{Nm} K_H(\theta_i - \alpha)\cdot Tb(\theta_i)\cdot(\theta_i - \alpha) + \cdots$$

$$+ \sigma_{1p+1}\sum_{i=1}^{Nm} K_H(\theta_i - \alpha)\cdot Tb(\theta_i)\cdot(\theta_i - \alpha)^p$$

STEP 3 - SSS retrieval

The input of the NN retrieval is the vector $\mathbf{X_{NN}}$ formed by the interpolated TBs and the auxiliary parameters $\mathbf{P}$, $\mathbf{X}_{NN} = (Tb_0^{\text{int}}, Tb_1^{\text{int}}, ..., Tb_{Ns}^{\text{int}}, P_1, ..., P_{Np})^T$ of size $Ni=Ns+Np$.

1) Input normalisation

$$XNorm(i) = \frac{X_{NN}(i) - Mean(i)}{Std(i)} \quad \forall i = 1, Ni$$

Where *Mean* and *Std* are provided in the NN description.

2) Hidden layers

Initialisation with the input data: *A[0:Ni-1]=XNorm[0:Ni-1]*
    NbNeu[0]=Ni

For all the hidden layers *k=1,NbHiddenLayer*

Acquisition of the number of neurons for the layer k: *Nb=NbNeu[k]*

Acquisition of the number of neurons for the previous layer: *Nb_in= NbNeu[k-1]*

    Acquisition of the weights between the current layer (neurons i) and the previous one (input j): W_{ij}^k

    Acquisition of the neuron biases for the layer: *Bias[0:Nb-1]*

    Input data for the considered neuron: *DataIn[0:Nb_in-1] =A*

For all the neurons *(i=0, Nb-1)* of the current layer

$$Temp[i] = 0$$

$$Temp[i] = Bias[i] + \sum_{j=1}^{Nb\_in} W_{ij}^k \cdot DataIn[j]$$

$$A[i] = a \cdot \tanh(c \cdot Temp[i])$$

(the values for a and c are provided in the algorithms description)

3) Output layer

$$Y = B + \sum_{i=1}^{n} W_i \cdot A(i)$$

where W_i is the weights vector between the last hidden layer and the output neuron.

n is the number of neurons in the last hidden layer

B is the bias associated to the output neuron

4) Ouput in the salinity range

$$SSS = (Y * StdSSS) + MeanSSS$$

V

Where *MeanSSS* and *StdSSS* are provided in the NN description.

STEP 4 – SSS error retrieval

The input of the error retrieval algorithm is the vector $\mathbf{X_{VAR}}$ formed by the vector $\mathbf{X_{NN}}$ and the SSS retrieved by the NN algorithm, $\mathbf{X}_{VAR} = (Tb_0, Tb_1, ..., Tb_{Nm}, P_1, ..., P_{Np}, SSS)^T$ of size $Ni=Ns+Np+1$.

The specifications are the same than the ones for the salinity retrieval except for the calculation of the output layer which uses an exponential function instead of the simple sum. The algorithm uses the NN coefficients specific to the error (variance) algorithm.

3 Practical considerations

If the two polarisations are used in the retrieval, the vector $\mathbf{X_{NN}}$ should contain first the measured Tbs in H polarisation at the different incidence angles and then the Tbs in V polarisation at the same angles.

In the case of full polarimetric retrieval, the vector $\mathbf{X_{NN}}$ should contain the sum of H and V Tbs.

An external file will provide the auxiliary parameters $\mathbf{P}$ and the associated errors to be used in the NN inversion.

Another external file will provide the values for the smoothing parameters (bandwidth values for each algorithm and each fixed angle) and the complete description of all the NN algorithms, for salinity and error retrieval.

The input and output data for the NN inversion are summarised below.

Input data

For each grid point of the Level 1c:
- Brightness temperatures in the surface reference frame, corrected for all effects.
- Error on the brightness temperatures (Instrumental, reconstruction errors…).
- Incidence angles
- Azimuth angles
- Grid point location (latitude, longitude)
- Grid point time tag

External file (Static Auxiliary Data):
- Auxiliary data P (or the a priori knowledge)
- Errors associated to the auxiliary data P
- NN description for all the algorithms
  - Number of algorithms (*Nc*)
  - For each algorithm:
    - Degree of the polynomial for the interpolation (*p*)
    - Number of fixed angle values (*Ns*)
    - Values of interpolated angles α_j, $j = 1, Ns$
    - Values of bandwidth h_j, $j = 1, Ns$
    - NN description for the SSS retrieval
      - Number of layers
      - Number of neurons per layer

VI

- Coefficients for the transfer function (*a* and *c*)
- Weights and biases
- Coefficient for the inputs and output normalisation
  - NN description for the SSS error retrieval
    - Number of layers
    - Number of neurons per layer
    - Coefficients for the transfer function (*a* and *c*)
    - Weights and biases
    - Coefficient for the inputs and output normalisation

Output data
For each grid point of the Level 1c:
- Retrieved salinity
- Error on the retrieved salinity

4 Calibration and validation

For pre-launch studies, the feasibility of neural network inversion could be demonstrated with simulated data sets. This simulation phase is very important because it allows fixing the architecture of the network and helps to identify the critical issues to build a reliable algorithm. Once SMOS is in-flight, the work will consist in two steps. First, the constitution of the database, using a suitable editing to make a representative dataset. In a second step, the coefficients of all the algorithms will be updated, keeping the architectures and strategy defined during the pre-launch study. The bandwidth values will also be tuned on SMOS data.

5 Quality control and diagnostics
The following tests should be performed and raise the associated flags, which will be reported in the User Data Product:
- Check if the retrieved SSS is in the expected range (SSS_Min,SSS_Max). If the retrieved salinity value is outside the range then raise the associated flag.
- Check if the error on retrieved SSS is in the expected range (SSS_Error_Min,SSS_Error_Max). If the error salinity value is outside the range then raise the associated flag.

6 Assumptions and limitations

Assumptions
N/A

Limitations
- If the number of measured Tbs for a grid point is less than a threshold (which can be different from the one used in the iterative scheme), then the inversion process (steps 0 to 4) is not performed.

- Check if the measured Tbs are in the expected range (Tb_Min,Tb_Max). If there is a percentage of the measured Tbs, for a given grid point, which are outside the range and this percentage exceeds a given threshold (Perc_Tb), the inversion process is not performed.
- Check if the interpolated Tbs are in the expected range (Tb_Min_Interp,Tb_Max_Interp). If there is a percentage of the inetrpolated Tbs, for a given grid point, which are outside the range and this percentage exceeds a given threshold (Perc_Tb_Interp), the SSS retrieval is not performed.

References

[1] Labroue S, E. Obligis, "WP3000 - Retrieval algorithms", Study on Salinity Data Processing, ESA Contract n°165/01/NL/SF.

[2] Ammar A, S. Labroue, E. Obligis, C. Mejia, S. Thiria and M. Crepon "Sea surface salinity retrieval throughout a SMOS half-orbit using neural networks", MicroRad '06 Proceedings.

[3] J.Fan, I.Gijbels, Local polynomial modelling and its applications, Chapman & Hall, 1996.

VIII

ANNEX-5: Pending actions on ATBD

Section	Details	Due date
3.1	Method to flag presence of SST and/or SSS fronts	
3.2	Method to weight (or not process) measurements outside AF_FOV	
4.3	Define $\sigma_{Tbmodel}^{2}$	
4.4.1.1	Define $\sigma_{Tbmodel}^{2}$	

Colors indicate action required from ESLs: ICM, IFREMER, IPSL, ACRI or ARGANS

After closing actions, the variables list (section 1.3) and change log have to be updated if necessary, as well as TGRD when applicable

I

ANNEX-6: Ocean Target Transformation (OTT)

ESL analysis of L1c and L2OS during commissiong showed that TBs from L2 forward models do not match those from L1c input products. The mis-match appears to be systematic in the xi-eta antenna frame, at least in regions far from land, such as the Pacific Ocean. To correct for these errors in order for the L2OS processor to retrieve salinity, ESL proposed and ESA agreed that an Ocean Target Transformation should be generated and applied to L1c TBs during L2OS processing. Each OTT contains TB offsets in a 2D array in xi/eta: during processing the L1c TBs are transformed into the xi/eta frame and the offset applied:

Tb used for retieval = L1c Tb – OTT offset

Before implementation, it was considered that the OTTs would be model dependent. Therefore a series of new ADFs were specified, one for each of the 3 retrieval configurations (surface roughness models). It was assumed that cardioid retrieval will use one of the other OTTs. For dual polarisation, OTTs are needed to correct TB in HH and VV; for full polarisation it was not known in advance if any of the snapshot OTTs would be the same, so OTTs are specified for HH, VV, short HH, short VV, VVH real and imaginary components, and HHV real and imaginary components. See the IODD for AUX_OTTxD/F_ file format specifications, and the TGRD for generation details.

OTT generation is perfomed by averaging snapshot error differences between each forward model and the L1c measured TBs, in the xi/eta antenna frame:

OTT offset = L1c measured Tb – forward model Tb

Averaging is performed over a large range of latitudes, far from land, using snapshots from one or more half-orbits.

I